Plasma Physics Reports, Vol. 27, No. 2, 2001, pp. 110–118. Translated from Fizika Plazmy, Vol. 27, No. 2, 2001, pp. 121–130.
Original Russian Text Copyright © 2001 by Dolgachev, Ushakov.

PLASMA DYNAMICS

Limiting Parameters of the Plasma Opening Switch

G. I. Dolgachev and A. G. Ushakov

Russian Research Centre Kurchatov Institute, pl. Kurchatova 1, Moscow, 123182 Russia

Received December 23, 1999

Abstract—Implementing programs for nuclear fusion research and X-ray generation requires the creation of superpower generators based on plasma opening switches (POSs) capable of commutating currents as high as several tens of megaamperes at output voltages of up to 5 MV and higher. The physical mechanisms limiting the POS voltage are investigated. It is shown that, as the generator voltage U_g increases, the voltage multiplication factor $k = U_{POS}/U_g$ (where U_{POS} is the POS voltage) decreases. An explanation for such a dependence is proposed, and the maximum value of the POS voltage is estimated. A POS design that enables operating in the above current and voltage ranges is considered. The design is based on applying an external magnetic field to the POS interelectrode gap, increasing the initial generator voltage, and decreasing the linear (along the perimeter of the outer electrode) density of the charge passing through the POS during the conduction phase. © *2001 MAIK "Nauka/Interperiodica".*

1. INTRODUCTION

The development of physical studies and the necessity of solving applied problems in the field of inertial controlled fusion have led to the creation of superpower megajoule pulsed generators, which makes it possible to achieve thermonuclear conditions in Z-pinches and imploding liners and to obtain intense bremsstrahlung X radiation. From the standpoint of both physics and cost-effectiveness, an inductive energy storage with a plasma opening switch (POS) is one of the most promising schemes for such a generator. The parameters of the largest existing POS-based generators, such as the GIT-16 and ACE-4 facilities, are the following: the current amplitude is 5 MA, the voltage at the instant of the break is 3 MV, and the break phase duration is 100 ns [1]. Although these parameters rank below those of generators based on water lines, such as the PBFA-Z facility (the current amplitude is 20 MA, the pulse voltage is 10 MV, and the pulse duration is 100 ns) [2], the possibility of creating a POS-based generator with a current of 50–100 MA and voltage of 5–10 MV is currently being considered [1, 3]. The present level of knowledge of POS physics does not provide an unambiguous answer to whether such a generator is possible to build. This paper is aimed at studying this problem and, in particular, investigating the main physical mechanisms and technological factors limiting the POS parameters.

2. MAIN PARAMETERS AND PHYSICAL MODELS OF THE POS

A POS-based generator consists of an *LC* circuit closed via a POS, which is a segment of a vacuum coaxial line whose electrodes are connected to each other via a plasma bridge over a fraction of the total length of the line (Fig. 1). One end of the line is connected to the capacitor bank of a Marx generator (MG), and the other end is connected to the load. After the generator is switched on, the growing current closes through the POS. During the first stage, which is called the conduction (or storage) phase, the POS impedance is low and the MG electric energy $W_e = CU^2/2$ converts into the magnetic energy of the line $LI^2/2$, where L is the total inductance of the line, generator, and connecting wires. Then, the POS impedance sharply increases and the stored energy of the magnetic field is released in the POS and shunting load. This process is called the break.

The properties and operating mode of a POS depend substantially on the electrode configuration, magnitude

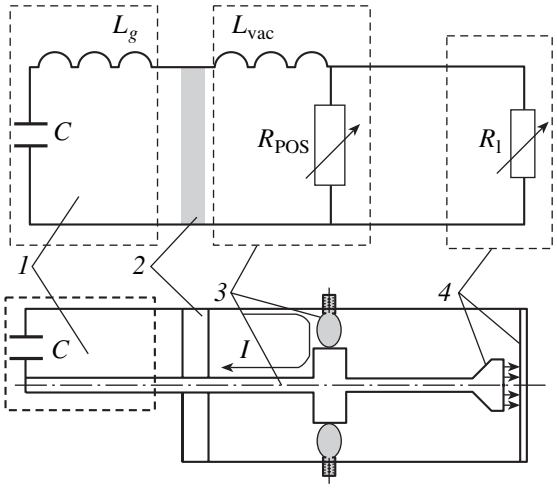

Fig. 1. Schematic of a POS-based generator: (*1*) Marx generator with capacitance C and inductance L_g, (*2*) high-voltage insulator, (*3*) vacuum feed line (L_{vac}) and POS (R_{POS}), and (*4*) electron diode load R_l.

1063-780X/01/2702-0110$21.00 © 2001 MAIK "Nauka/Interperiodica"

and distribution of the plasma density, amplitude and duration of the current, etc. The main parameters of present-day POS-based generators [4–21] vary within a wide range (see table): the conduction phase time is t_{con} = 0.2–3 μs; the current just before the break is I_{br} = 0.06–3 MA; the initial generator voltage is U_g = 0.05–1.5 MV; the POS voltage is U_{POS} = 0.5–4 MV; the voltage multiplication factor is $k = U_{POS}/U_g$ = 2–15; the anode radius is R_a = 1–20 cm; the cathode radius is R_c = 1–20 cm; the initial length of the plasma bridge is l = 1–60 cm; the charge densities per unit length of the circumference and per unit area of the surface of the outer electrode are q_1 = 0.2–30 mC/cm and q_2 = 0.2–5 mC/cm^2, respectively; and the initial plasma density is $n \le 5 \times 10^{17}$ cm^{-3}. Thus, a number of POS models taking into account specific conditions have been developed [22–25]. Three modes of POS operation can be specified depending on the characteristic scale a of the problem (e.g., the interelectrode gap) and the plasma density n: the magnetohydrodynamic (MHD), electron magnetohydrodynamic (EMHD), and erosion modes (Fig. 2).

The MHD mode is realized when

$$na^2 \gg Mc^2/Ze^2. \quad (1)$$

Under this condition, the POS operation can be described within the so-called "snow plow" model: under the action of the $\mathbf{F} = \mathbf{J} \times \mathbf{B}$ force, the plasma is displaced along the POS axis toward the load. If the magnetic field (or plasma density) in the gap is nonuniform, then the plasma displacement is also nonuniform; the higher the magnetic field (or the lower the density), the larger the displacement. The plasma displacement is accompanied by the formation of a vacuum gap in the shape of a wedge with a vertex on the load side. This gap is bounded with a denser plasma and propagates toward the load. The formation and expansion of the vacuum gap is caused by the magnetic pressure pushing the plasma apart. The MHD mode is completed when the gap vertex reaches the plasma boundary, where a region with a reduced plasma density is formed. For the coaxial configuration and linearly growing current, the snow plow model [26, 27] enables one to find the dependences of the conduction phase duration, current amplitude, and total charge passed through the POS on the plasma density. In a region with a reduced plasma density, which is formed due to the nonuniform motion of the plasma bridge, conditions can be satisfied for the transition to the EMHD mode (see below), in which the POS resistance sharply increases and the break occurs [28]. In this mode, the above-mentioned narrow wedge-shaped vacuum gap and extended region with a denser plasma still exist. The ion currents flowing across this region shunt the POS, thus limiting the POS voltage. The dense plasma at the gap boundary prevents the expansion of the gap caused by the escape of ions from the plasma surface.

The EMHD mode is realized at lower densities [25] such that

$$mc^2/e^2 < na^2 < Mc^2/ze^2. \quad (2)$$

The solution obtained in [23] describes the penetration of a fast convective magnetic-field wave, often referred to as a Kingsep–Mokhov–Chukbar (KMC) wave, into the plasma and allows an explanation of the measured high penetration velocities, which exceed the classical collisional penetration velocity by two to three orders of magnitude. One of the most remarkable EMHD effects is the universal expression for the POS (plasma-filled diode) impedance [24]:

$$R_{eff} = W/I^2 = 30u/c \ [\Omega], \quad (3)$$

where u is the characteristic current velocity averaged over the plasma volume. Note that, for the typical current velocities $u \simeq 10^8$ cm/s, we have $R_{eff} \simeq 0.1\ \Omega$, which is one or two orders of magnitude less than the POS impedance at the instant of the break. Involving other mechanisms may only increase the actual value of the switch impedance and voltage. It was noted in [29] that, assuming the ions to be immobile, the switch impedance by the end of the EMHD mode reaches the value given by expression (3), which corresponds to the Hall voltage

$$U_{Hall} = (H^2/8\pi en)\Pi_i^{-1}, \quad \Pi_i = \frac{4\pi e^2 zna^2}{Mc^2}. \quad (4)$$

Taking into account the ion motion allows us to estimate the limiting linear charge density during the conduction phase:

$$Q/r = Mc^2/e \simeq 0.6 \text{ mC/cm}. \quad (5)$$

The existence of the limiting charge density (q_1 = 2–5 mC/cm and q_2 = 1–3 mC/cm^2) has been observed experimentally [30, 31]. A decisive factor allowing one to relate the current wave propagation to the "electrotechnical" break of the current is the existence of the Hall electric field [32]: after the field in the form of a KMC wave has penetrated through the plasma and has magnetized the plasma electrons, the Hall erosion phase occurs, during which the radial Hall electric field $\mathbf{E} = [\mathbf{v}_e\mathbf{B}]/c$ accelerates the plasma ions toward the cathode. Such an ion acceleration in a quasineutral plasma with magnetized electrons looks like a rarefaction wave propagating from the cathode to anode. The POS voltage can be easily estimated when the load inductance is equal to the storage inductance. In this case, the POS impedance is

$$R = (1/2\pi ec^2)(I_g/nr^2)(2l\omega_{pi}/c)^2. \quad (6)$$

Although the electron component of the current shunts the POS gap, it is needed for the Hall erosion (the acceleration of ions and their escape from the plasma) to

Parameters of the most famous facilities [4–21]

Facility, reference	t_{con}, μs	I_{br}, MA	U_g, MV	U_{POS}, MV	k	R_a, cm	R_c, cm	l, cm	q_1, 10^{-3} C/cm	q_2, 10^{-3} C/cm^2	n, cm^{-3}	Note
Hawk [4]	~1	0.5	~0.7	2	3	7.5	1.3	8	5	0.6	4×10^{15}	
GIT-4 [5]	~1	2	0.6	1.76	3	28	24	24	5	0.2		
GIT-8 [6, 7]	0.8	1.5	0.48	1.1	2.2	10	8	30	20	0.6	2×10^{15}	
GIT-12 [8]	1.2	2–3	0.48	1.3	2.5	18	16	60	30	0.5		
DPM-1 [9, 10]	0.55	1	0.7	2.3	3.3						$>10^{15}$	
	0.6	1.2	0.7	2.7	4	7.5/10	6.5	2.5	12	5		Plasma anode
DM-1 [11]	0.28	1.3	1.3	2.4	2	18/24	9	2.5	1	0.4		″
Tesla [12]	0.55	0.35	1	2	2	12.5	18	10	1	0.1		Self-field B_z
DM-2 [13]	0.22	1.1	1.2	2.7	2.2	18	12.5	10	1.4	0.14		″
Ace-4 [14]	0.85	2.4	0.48	1.4	3	8	6	20	20	5	4×10^{15}	
Marina [15]	1	0.3	0.75	2.5	3.4	10		2	2.5	1.2		
Dubl [16]	1.2	0.24	0.48	1.5	3	15	2.25	2.5	2	1		
Taina [17]	1.8	0.18	0.45	1.5	3	18	3.5	2	2.5	1.2		
″	″	″	″	2.2	5	3.5	18	″	″	″		External field B_φ = 10 kOe
A-2C [18]	1.2	0.07	1.5	4	2.8	3	18	1	0.4	0.4		B_z = 3 kOe
GAMBLE2 [19]	0.05	0.9	3.4	4.6	1.4	4.5	2.4	10	1.8	0.18		
Tigr-1 [18]	3	0.12	0.04	0.5	12	3	18	1	1.5	1.5		B_z = 3 kOe
PC-20 [20]	0.6	0.06	0.8	3	4	20	15	1	0.17	0.17		B_z = 5 kOe
[21]	1	0.1	0.16	0.7	4.5	16	1	2	2	1		

occur and, consequently, the switch impedance to increase.

In some cases, the anomalous plasma resistance can make a substantial contribution to the POS impedance in the conduction phase [33]. The resistive effects are of importance at

$$a < mc^2/e(4\pi Tn)^{1/2}. \quad (7)$$

Under this condition, the anomalous plasma resistance is comparable with the EMHD impedance given by expression (3) and can attain 1 Ω. However, the main point here is that the anomalous resistance may affect the scaling law that follows from the EMHD model of switch operation.

As the density decreases further,

$$na^2 \ll mc^2/e^2 \quad (8)$$

the switch starts operating in the vacuum regime. In this range of parameters, the break can be described within the erosion model [22, 27]. The transition from the EMHD mode to the vacuum mode can occur via the Buneman instability, which is accompanied by the formation of electric double layers [34]. During the erosion process, the ions escaping from the anode boundary of the double layer are accelerated toward the POS cathode by the interelectrode electric field. The classical erosion model [22, 27] assumes the existence of four consecutive phases: conduction, erosion, enhanced erosion, and magnetic insulation. In the conduction phase, the electron and ion components of the current are related by the bipolar relationship

$$I_e/I_i = (M/zm)^{1/2}. \quad (9)$$

Neglecting the POS voltage, the maximum values of the total current and the ion current are determined by expression (9) and the ion drift velocity v_d:

$$I_{BP} \le (M/zm)^{1/2}(2\pi rl)n_i e v_d, \quad (10)$$

$$I_i \le (zm/M)^{1/2}(2\pi rl)n_i e v_d. \quad (11)$$

The inequalities opposite (10) and (11) correspond to the transition to the second (erosion) phase, in which the uncompensated ion loss results in the formation and growth of a vacuum gap. The growth rate of the gap width D is

$$dD/dt = I_i/(2\pi rl)rn_i e - v_d. \quad (12)$$

In this case, the POS voltage is equal to the gap voltage, which is determined by the Child–Langmuir law and, as a rule, does not exceed several ohms.

As soon as the gap width becomes equal to the electron Larmor radius, which corresponds to the critical current

$$I_c = 13.6(\gamma^2 - 1)^{1/2} r_c/D \text{ [kA]}, \quad (13)$$

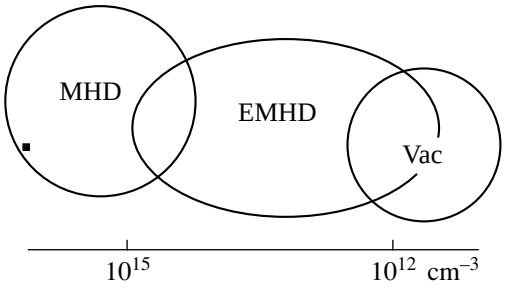

Fig. 2. POS operating modes: magnetohydrodynamic (MHD), electron magnetohydrodynamic (EMHD), and vacuum erosion (Vac) regimes. The modes partially overlap within the plasma density range 10^{12}–10^{15} cm^{-3}.

the transition to the phase of enhanced erosion occurs, during which the POS impedance sharply increases and the current switches to the load. The phase of magnetic insulation occurs in the case of a low-inductance load with a current exceeding the critical value (13). In [27], a modified condition for switching the current to the load was derived from expressions (12) and (13).

The erosion mechanism for the current break can be enhanced by applying an external magnetic field, which makes it possible to suppress the electron current through the POS and enables the most efficient use of the energy supplied to the POS for ion acceleration, i.e., plasma erosion.

The current scalings for the erosion models (both bipolar and modified bipolar), as well as for the EMHD and MHD modes, are given in [35]. The coefficients in the following formulas correspond to carbon plasma (C^{++}) and the ion velocity V_i = 3.6 cm/μs:

$$I_{BP} = 3.8 \times 10^{-10} rln, \quad (14)$$

$$I_{MBP} = 1.02 \times 10^{-2} rn^{1/2}, \quad (15)$$

$$I_{EMHD} = 1.64 \times 10^{-9} r(lndI/dt)^{1/2}, \quad (16)$$

$$I_{MHD} = 1.39 \times 10^{-5} 9r^2(l^2 ndI/dt)^{1/4}. \quad (17)$$

Supplementing expressions (14)–(16) with the limitations on the plasma density (2) and (8), we see that, in the vacuum and EMHD modes, the current and the density of the passed charge are limited.

Hence, for a limited POS volume, only the MHD mode, which is characterized by the lowest voltage multiplication factor, allows the accumulation of a large amount of energy in the inductive storage bank. In [28], the possibility of the division of a POS into two parts was considered, namely, the MHD region with a high plasma density, which allows a large charge to pass, and the EMHD (Hall) region, which enables a high impedance. In our opinion, this is not the only way to increase both the energy and the voltage. The EMHD or vacuum modes with an external magnetic field can

be used to attain a high voltage, and the current can be increased by increasing the area of the POS electrode surface. It is this method that will be considered below.

3. MAIN FACTORS DETERMINING THE POS VOLTAGE

Obviously, in the EMHD or erosion modes, the POS voltage is determined by the energy density spent on the ion acceleration, i.e., the Hall or electric plasma erosion. That the POS voltage U_{POS} at the instant of the break is a function of the input energy density w,

$$U_{POS} = f(w) \tag{18}$$

is of practical importance, because it enables the scaling of installations in which POSs are used for pulse sharpening.

Dependence (18) can easily be determined. Thus, for a planar configuration and magnetized electrons, the specific (per cm^2) energy dw_i spent on removing a plasma sheet with a thickness of dx is

$$dw_i = U_{POS} nzedx, \tag{19}$$

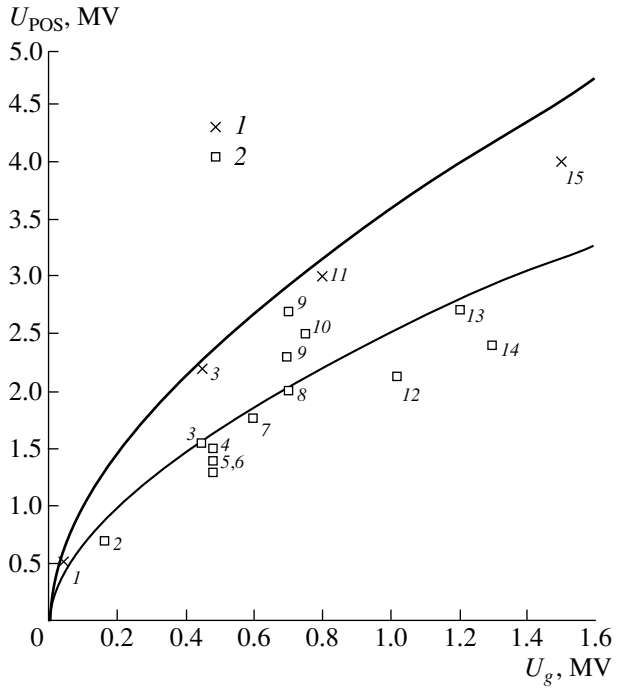

Fig. 3. Calculated dependence of U_{POS} on the generator voltage U_g, $U_{POS} = \alpha U_g^{4/7}$, and their real values from the table (*1*) with and (*2*) without an external magnetic field. Numerals stand for the installations: (*1*) Tigr-1, (*2*) Electron Beam Generator, (*3*) Taina, (*4*) Dubl, (*5*) GIT-12, (*6*) Ace-4, (*7*) GIT-4, (*8*) Hawk, (*9*) DPM-1, (*10*) Marina, (*11*) PC-20, (*12*) Tesla, (*13*) DM-2, (*14*) DM-1, and (*15*) A-2C.

where ze is the ion charge. If the energy storage inductance is so high that the voltage

$$U_{POS} = LdI/dt \tag{20}$$

is attained at a nearly constant ion current I (and, thus, at a nearly constant ion current density j), then, according to the "3/2 law" (Child–Langmuir law), the voltage increment is

$$dU_{POS} = j^{1/2}(4/9)\varepsilon_0(2ze/M)^{1/2}U_{POS}^{1/4}dx, \tag{21}$$

where $\varepsilon_0 = (8.85 \times 10^{-12}$ F/m and M is the ion mass. The voltage energy cost (i.e., the energy spent on increasing the voltage by one voltage unit) is

$$dw_i/dU_{POS} = U_{POS}^{3/4} n(zeM)^{1/2}/j^{1/2}(4/9)\varepsilon_0(2)^{1/2}. \tag{22}$$

Consequently, the dependence of the voltage on the input energy is

$$U_{POS} = [(7/4)(w_i/n(zeM)^{1/2})/j^{1/2}(4/9)\varepsilon_0(2)^{1/2}]^{4/7} \propto w_i^{4/7} \propto w^{4/7}, \tag{23}$$

where w is the density of the total energy loss, including the energy loss of the electron component of the current, which is actually more than 50% of the total POS current. Since, for most installations, the density of the charge passed through a POS is the same ($q_2 = \sim 10^{-3}$ C/cm^2), then, neglecting the energy loss during the conduction phase (i.e., assuming that the current increases to the amplitude value as $\sin\omega t$), we obtain that the specific energy loss is

$$w \propto q_2 U_g \tag{24}$$

and

$$U_{POS} = \alpha U_g^{4/7}. \tag{25}$$

The coefficient α can also account for a real configuration.

Figure 3 presents the values of U_{POS} versus U_g taken from the table and relation (25). The coefficients $\alpha_1 = 2.5$ and $\alpha_2 = 3.6$ ($MB^{3/7}$) were determined based on the data for the Taina facility [17] without (α_1) and with (α_2) an external magnetic field. It is seen that the calculated curves are fairly close to the experimental points. We note that the voltage $U_{POS} = 4.6$ MV obtained in the GAMBLE-2 facility coincides with $U_{POS} = \alpha_1 U_g^{4/7} = 5$ MV within an accuracy of about 10%. The U_{POS} values for the high-current facilities GIT and Ace-4, which operate mainly in the MHD mode, lie below the curve given by expression (25). The possible reason for this discrepancy comes from shunting the POS with the ion current flowing through the vacuum gap arising in a dense plasma pushed apart by the magnetic field. Applying an external magnetic field makes it possible to minimize the shunting effect of the electron current that is necessary for the existence of the EMHD mode

(Hall erosion). This allows one to attain high voltages. The fact that the voltages attained in facilities with an external magnetic field (such as A-2C [18] and PC-20 [20]) rank below the $\alpha_2 U_g^{4/7}$ values is caused by the electron leakage current bypassing the POS [20].

4. EXPERIMENT

The experimental dependence $U_{POS}(w)$ at a constant value of the passed charge

$$Q \sim CU_g \tag{26}$$

was measured in a facility [21] with a four-stage MG with the following parameters: C = 0.4 μF, U_g = 200 kV, I_g = 140 kA, and $T/4$ = 1 μs. The POS electrode diameters were 1.4 and 16 cm. Two methods of varying the input energy density w in a POS were used.

The first method is to vary the number of MG stages (from four to one), which changes the input energy density w and MG voltage U_g at a constant charge Q and charge density. The use of one stage instead of four increases the MG capacitance fourfold. In this case, the inductance of the MG–POS circuit decreases by approximately 20%; hence, the current amplitude decreases by ~50% and the period increases by ~80%.

The second method is to use an inductance load. In this case, the current I_l in the load and the energy W released in a POS are determined by the relation between the MG storage inductance L_g and the load inductance L_l

$$I_l = I_g L_g/(L_g + L_l), \tag{27}$$

$$W = W_g[(1 - L_g)/(L_g + L_l)], \tag{28}$$

where I_g and W_g are the initial current and energy in the MG storage inductance. Note that the experimental value of the current switched to the inductance load is, as a rule, less than the calculated current because of the partial shorting of the current through a POS. For this reason, the input energy was determined from the current waveform, namely, from the current values before and after the break. Both methods allowed us to change the input energy in a POS at a constant charge and charge density (Q = const and $q_{1,2}$ = const). The typical waveforms of the current and voltage for different input energies are shown in Fig. 4.

Figure 5 presents the dependence of the POS voltage on the input energy (the generator voltage) obtained based on waveforms similar to those in Fig. 4. The energy released in the POS in the absence of a load is taken as a unit input energy. Usually, during the break, the current decreases by $\Delta I = 0.5 I_g$; therefore, the unit input energy is

$$\begin{aligned} W_0 &= (L_g/2)[I_g^2 - (I_g - \Delta I)^2] \\ &= W_g(\Delta I/I_g)(2 - \Delta I/I_g) = 0.75 W_g, \end{aligned} \tag{29}$$

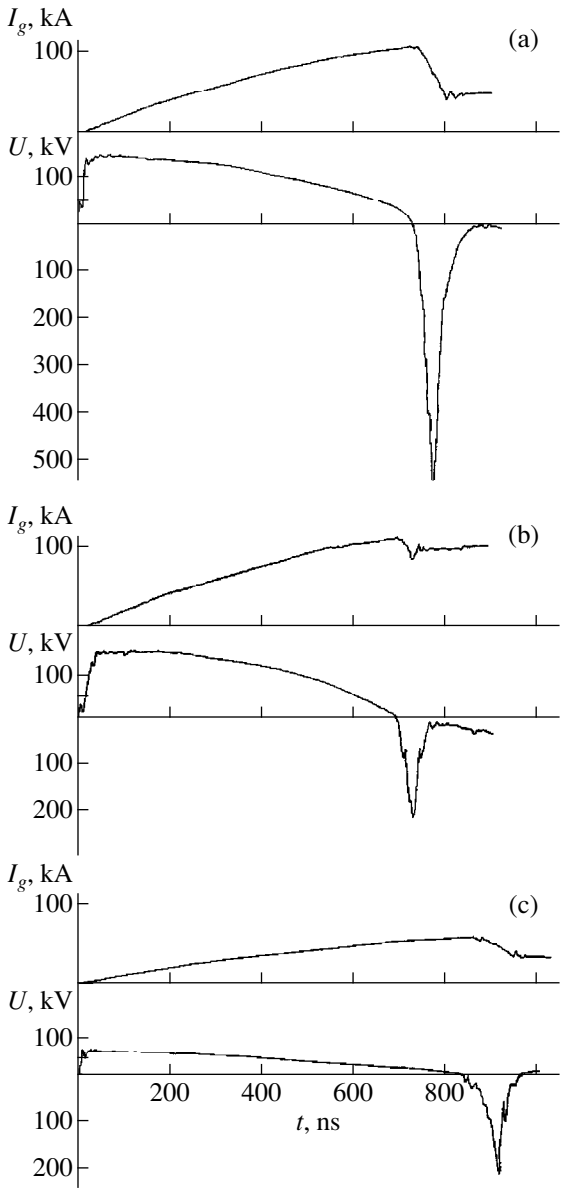

Fig. 4. Typical waveforms of the current I (measured with a shunt) and the voltage U (derived from the $d\Phi/dt$ signal measured with a magnetic loop) for different energy input densities (varied by changing the number of MG stages or the load type) and constant POS parameters: (a) four stages, high-impedance diode load, R_d = ~50 Ω; (b) four stages, inductance load, L = ~0.7 μH ($L\omega \approx 1$ Ω); and (c) one stage, high-impedance diode load, R_d = ~50 Ω.

where $W_g = QU_g$; i.e., the unit input energy W_0 corresponds to the voltage U_g = 168 kV. It is seen from Fig. 5 that the dependence $U_{POS}(U_g)$ agrees with expression (25). The voltage multiplication factor decreases with the generator voltage as

$$k = U_{POS}/U_g \propto U_g^{-3/7}. \tag{30}$$

Therefore, there is a limiting voltage $U_{g\,lim}$ at which $k \approx 1$. Thus, at higher generator voltages, applying a

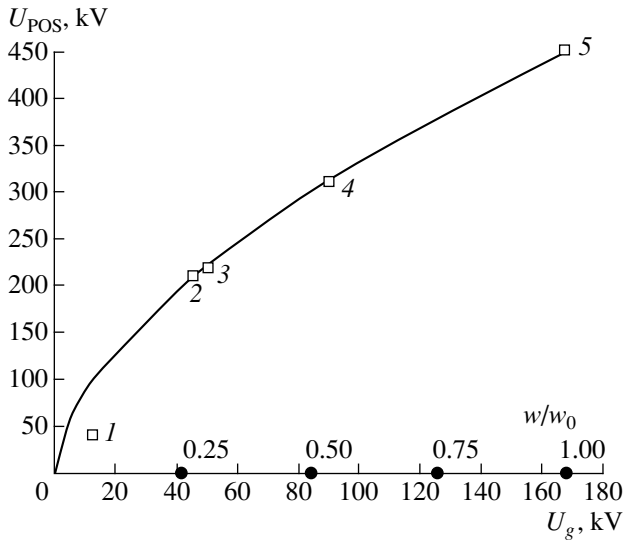

Fig. 5. POS voltage vs. the relative energy input density w/w_0 and the corresponding generator voltage U_g for (*1*) one-stage MG with an 0.7-μH inductance load, (*2*) one-stage MG in the idle running mode (high-impedance diode), (*3*) four-stage MG with an 0.7-μ H inductance load, (*4*) two-stage MG in the idle running mode (high-impedance diode), and (*5*) four-stage MG in the idle running mode (high-impedance diode).

POS as a voltage multiplier has no sense. This limiting voltage can be estimated by approximating the dependence $U_{POS}(U_g)$ obtained at higher voltages, e.g., in the PC-20 facility at a generator voltage of up to 1 MV.

5. INCREASING THE POS CURRENT AND VOLTAGE

The above result shows that one of the possible ways of increasing the voltage is to terminate each stage of the MG with its own POS and then sum up the POS voltages (Fig. 6) or magnetic fluxes (Fig. 7). However, the problems of synchronization, total efficiency of the device, etc. hardly allow one to use this method for creating powerful generators with megaampere currents.

It is seen from Fig. 3 that higher voltages can be attained in facilities with an external magnetic field and low densities of both the current and charge passed through a POS. However, the limited values of the charge densities q_1 = 2–5 mC/cm and q_2 = 1–3 mC/cm^2 used in such facilities at microsecond pulse durations and currents of ~80 MA make it necessary to use a POS with a diameter of ~12 m, which is not realistic. Nevertheless, the problem of increasing the charge and current at limited densities can be resolved by a more compact arrangement of several POSs, as is shown in Fig. 8. Four POSs with an external magnetic field can be connected in parallel. In this case, the overall diameter of the system will be ~3 m, which is quite reasonable. The magnetic field is created in the radial gap between two coils directed opposite to each other. This enables one to minimize the volume occupied by the magnetic field and, thus, reduce the energy spent on its production.

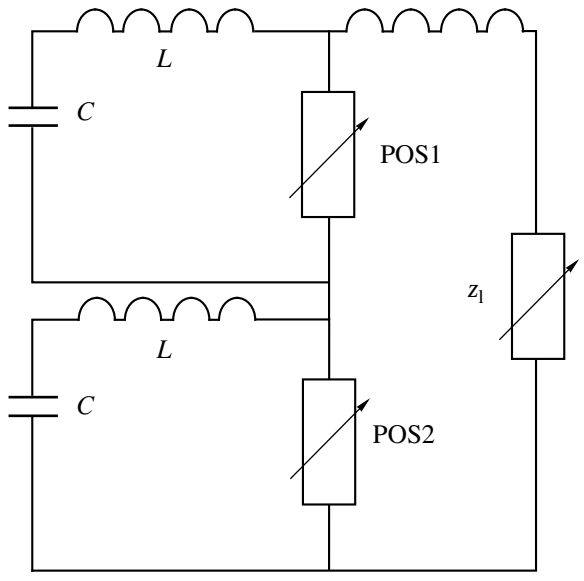

Fig. 6. Schematic of summing up the voltages from the two POSs (POS1 and POS2) at the load z_l; *C* is a capacitive storage, and *L* is an inductive storage.

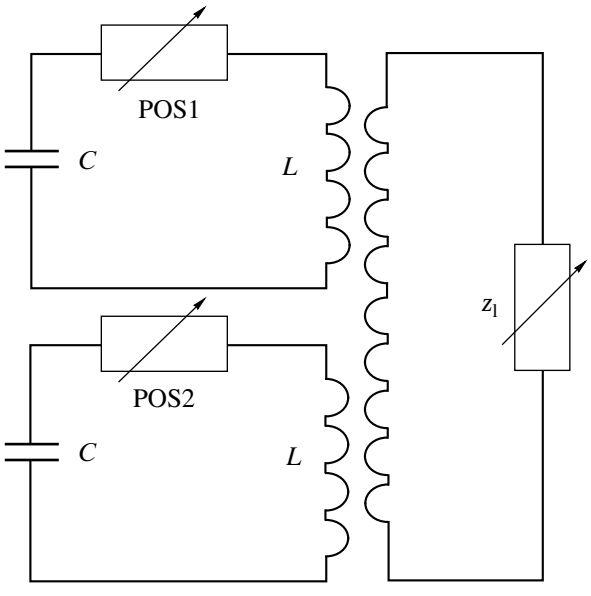

Fig. 7. Schematic of summing up the magnetic fluxes from the two inductive storages, switched by the two POSs (POS1 and POS2); *C* is a capacitive storage, and *L* is an inductive storage.

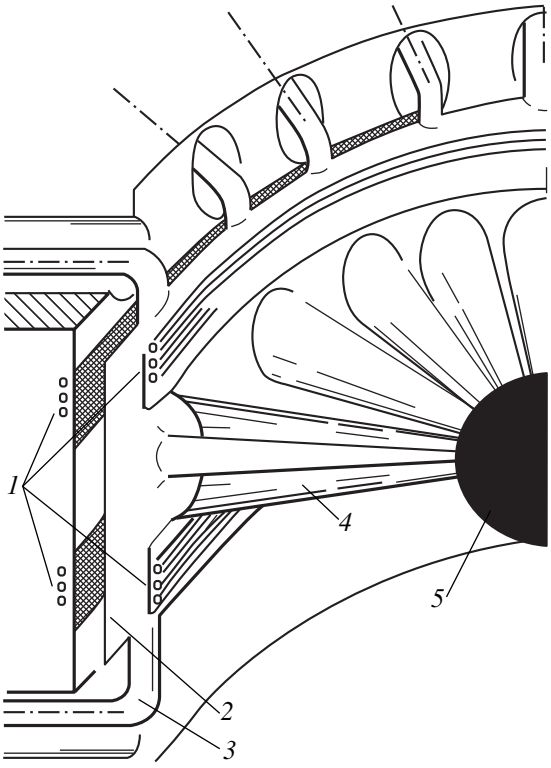

Fig. 8. Schematic of the four-sided feeding of a POS with an external magnetic field: (*1*) cathodes of the four POSs with magnetic coils, (*2*) common anode of the four POSs, (*3*) feed lines, (*4*) energy-to-load guide lines, and (*5*) load.

Estimates show that the energy spent on the production of the insulating magnetic field is at most 10% of the energy stored in the inductive storage bank. At the same time, applying the magnetic field makes it possible to reduce the current in the break phase to zero [32, 33] and almost completely utilize the inductive storage energy, whereas the ordinary scheme (without an external field) allows one to use no more than 75% of this energy. In the absence of an external magnetic field, a decrease in the current and accompanying magnetic field by one-half (or even lower) leads to the shorting of a POS; the remaining energy dissipates in the MG–POS circuit. The passed charge is to be limited not only in order to achieve the highest voltage but also to provide the possibility of repeatedly using the POS elements, because this decreases the energy release in the POS. Experiments with repetitive POSs [36] show that the use of pyrocarbon materials makes is possible to substantially prolong the lifetime of the main POS elements (electrodes and plasma guns) at a power density of up to 100 J/cm^2, a pulse duration of up to 100 ns, and a repetition rate of up to 4 Hz. In the single-pulse mode, the power density can be increased up to 200–300 J/cm^2.

Based on the available data (Fig. 3), we can deduce that a voltage of about 5 MV can be attained at a primary generator voltage of 2 MV, a POS interelectrode gap of 5 cm, and an external magnetic field of 20 kG. For the POS scheme shown in Fig. 8, at a charge density of 5 mC/cm^2, current rise time of 2 μs, an axial length of each POS of 5 cm (which is equal to the interelectrode gap), and a POS current of 80 MA, the area of the POS electrode surface should be 2×10^3 cm^2 and, accordingly, the diameter of the outer electrode (vacuum chamber) should be ~3 m. In this case, it is convenient to use a multimodule system as a primary storage bank. Since the four POSs are nearly integrated in space, the problem of synchronization disappears. The energy can be transported to the load with the use of a concentrator, as was done in [2].

6. CONCLUSIONS

An analysis of the parameters of POS-based facilities and the described experiments show that (i) the POS voltage is determined by the energy input density, (ii) the energy spent on increasing the voltage by one voltage unit increases as $U_{\mathrm{POS}}^{3/4}$, and (iii) there is a limiting voltage above which applying a POS has no sense. The limiting voltage can be estimated fairly accurately based on the dependence $U_{\mathrm{POS}}(U_g)$ measured within the megavolt range of voltages at the primary energy storage (MG). To obtain the maximum possible voltage, it is necessary to use an insulating magnetic field produced by an external power supply.

It is possible to compactly arrange four POSs connected in parallel, which allows one to increase the current to 80 MA at a limited density of the passed charge and a POS diameter of ~3 m.

ACKNOWLEDGMENTS

We are grateful to V.P. Smirnov for his continued interest in this work, discussion of the results, and productive remarks.

This work was supported on part by the U.S. Civilian Research and Development Foundation for the Independent States of the Former Soviet Union (CRDF), grant no. RP1-2113.

REFERENCES

1. W. J. Summa, R. L. Gillickson, M. P. Hebert, *et al.*, in *Proceedings of the 10th IEEE Pulsed Power Conference, Albuquerque, 1995*, p. 1.
2. R. B. Spielman, W. A. Stygar, J. F. Seamen, *et al.*, in *Proceedings of the 11th IEEE Pulsed Power Conference, Baltimore, 1997*, p. 709.
3. V. P. Smirnov, in *Abstracts of the 12th International Conference on High-Power Particle Beams, Haifa, 1998*, p. 19.
4. B. V. Weber, J. R. Boller, P. J. Commisso, *et al.*, in *Proceedings of the 8th International Conference on High-Power Particle Beams, Washington, DC, 1992*, p. 375.

5. B. M. Kovalchuk and G. A. Mesyats, in *Proceedings of the 9th International Conference on High-Power Particle Beams, Novosibirsk, 1990*, Vol. 1, p. 92.
6. A. A. Kim, B. M. Kovalchuk, V. A. Kokshenev, *et al.*, in *Proceedings of the 10th IEEE Pulsed Power Conference, Albuquerque, 1995*, p. 226.
7. A. Chuvatin, C. Roulle, B. Etlicher, *et al.*, in *Proceedings of the 11th International Conference on High-Power Particle Beams, Prague, 1996*, Vol. 2, p. 1203.
8. A. S. Chuvatin, A. A. Kim, V. A. Kokshenev, *et al.*, in *Proceedings of the 11th IEEE Pulsed Power Conference, Baltimore, 1997*, Vol. 1, p. 261.
9. J. Goyer, D. Kortbawi, K. Childers, *et al.*, in *Proceedings of the 10th International Conference on High-Power Particle Beams, San Diego, 1994*, p. 1.
10. S. B. Swanekamp, J. M. Grossmann, P. F. Ottinger, *et al.*, J. Appl. Phys. **76**, 2648 (1994).
11. J. R. Thompson, J. E. Rauch, J. E. Goyer, *et al.*, in *Proceedings of the 11th IEEE Pulsed Power Conference, Baltimore, 1997*, Vol. 1, p. 269.
12. M. E. Savage, E. R. Hong, W. W. Simpson, *et al.*, in *Proceedings of the 10th International Conference on High-Power Particle Beams, San Diego, 1994*, p. 41.
13. M. E. Savage, W. W. Simpson, C. W. Mendel, *et al.*, in *Proceedings of the International POS Workshop, Gramat, 1997*.
14. W. Rix, J. Thompson, R. Crumley, *et al.*, in *Proceedings of the 10th IEEE Pulsed Power Conference, Albuquerque, 1995*, p. 192.
15. É. N. Abdullin, G. P. Bazhenov, A. A. Kim, *et al.*, Fiz. Plazmy **12**, 1260 (1986) [Sov. J. Plasma Phys. **12**, 728 (1986)].
16. V. M. Bystritskiĭ, Ya. E. Krasik, I. V. Lisitsyn, *et al.*, in *Proceedings of the VIII All-Union Workshop on High-Current Electronics, 1990*, Part III, p. 112.
17. Yu. P. Golovanov, G. I. Dolgachev, L. P. Zakatov, *et al.*, Vopr. At. Nauki Tekh., Ser.: Termoyad. Sintez, No. 3, 56 (1990).
18. Yu. P. Golovanov, G. I. Dolgachev, L. P. Zakatov, *et al.*, Fiz. Plazmy **14**, 880 (1988) [Sov. J. Plasma Phys. **14**, 519 (1988)].
19. J. M. Neri, J. R. Boller, P. F. Ottinger, *et al.*, Appl. Phys. Lett. **50**, 1331 (1987).
20. N. U. Barinov, G. S. Belen'ki, G. I. Dolgachev, *et al.*, in *Proceedings of the 11th IEEE Pulsed Power Conference, Baltimore, 1997*, Vol. 2, p. 1222.
21. G. I. Dolgachev, M. S. Nitisyinski, and A. G. Ushakov, in *Proceedings of the 11th IEEE Pulsed Power Conference, Baltimore, 1997*, Vol. 1, p. 281.
22. P. F. Ottinger, S. A. Goldstein, and R. A. Meger, J. Appl. Phys. **56**, 774 (1984).
23. A. S. Kingsep, Yu. V. Mokhov, and K. V. Chukbar, Fiz. Plazmy **10**, 854 (1984) [Sov. J. Plasma Phys. **10**, 495 (1984)].
24. K. V. Chukbar and V. V. Yan'kov, Zh. Tekh. Fiz. **58**, 2130 (1988) [Sov. Phys. Tech. Phys. **33**, 1293 (1988)].
25. A. S. Kingsep, K. V. Chukbar, and V. V. Yan'kov, in *Reviews of Plasma Physics*, Ed. by B. B. Kadomtsev (Énergoizdat, Moscow, 1987; Consultants Bureau, New York, 1990), Vol. 16.
26. W. Rix, D. Parks, J. Shannon, *et al.*, IEEE Trans. Plasma Sci. **PS-19**, 400 (1991).
27. B. V. Weber, R. J. Commisso, P. J. Goodrich, *et al.*, IEEE Trans. Plasma Sci. **PS-19**, 757 (1991).
28. A. S. Chuvatin, A. A. Kim, V. A. Kokshenov, *et al.*, Izv. Vyssh. Uchebn. Zaved., Fiz., No. 12, 56 (1987).
29. A. V. Gordeev, A. V. Grechikha, A. V. Gulin, and O. M. Drozdova, Fiz. Plazmy **17**, 650 (1991) [Sov. J. Plasma Phys. **17**, 381 (1991)].
30. Yu. P. Golovanov, G. I. Dolgachev, L. P. Zakatov, *et al.*, Vopr. At. Nauki Tekh., Ser.: Termoyad. Sintez, No. 1, 61 (1988).
31. G. I. Dolgachev, L. P. Zakatov, and A. G. Ushakov, Fiz. Plazmy **17**, 1171 (1991) [Sov. J. Plasma Phys. **17**, 679 (1991)].
32. L. I. Rudakov, Fiz. Plazmy **19**, 835 (1993) [Plasma Phys. Rep. **19**, 433 (1993)].
33. G. I. Dolgachev, L. P. Zakatov, Yu. G. Kalinin, *et al.*, Fiz. Plazmy **22**, 1017 (1996) [Plasma Phys. Rep. **22**, 921 (1996)].
34. A. S. Kingsep and A. A. Sevast'yanov, Fiz. Plazmy **17**, 1183 (1991) [Sov. J. Plasma Phys. **17**, 685 (1991)].
35. B. V. Weber, R. J. Commisso, P. J. Goodrich, *et al.*, Phys. Plasmas **2**, 3893 (1995).
36. G. I. Dolgachev, L. P. Zakatov, M. S. Nitishinskiĭ, *et al.*, Fiz. Plazmy **24**, 1078 (1998) [Plasma Phys. Rep. **24**, 1008 (1998)].

Translated by N.N. Ustinovskiĭ

Plasma Physics Reports, Vol. 27, No. 2, 2001, pp. 119–128. Translated from Fizika Plazmy, Vol. 27, No. 2, 2001, pp. 131–140.
Original Russian Text Copyright © 2001 by Timofeev.

PLASMA OSCILLATIONS AND WAVES

Launching of Microwaves into a Dense Plasma in Open Confinement Systems

A. V. Timofeev

Russian Research Centre Kurchatov Institute, pl. Kurchatova 1, Moscow, 123182 Russia

Received June 1, 2000

Abstract—A study is made of the propagation of microwave beams in a plasma and their passage through the critical surface. It is shown that, in order for microwaves to penetrate deeply into a dense plasma, it is necessary to launch them through a magnetic mirror at a slight angle to the device axis. The characteristic features of ray trajectories are analyzed both ahead of and behind the critical surface. In a dense plasma behind the critical surface, microwaves tend to run out of the axial region toward the plasma periphery. This tendency may be unfavorable for heating plasmas whose radial density profiles are strongly peaked about the system axis. The problems under analysis are particularly important for assessing the prospects for ECR heating of dense plasmas in open confinement systems. *© 2001 MAIK "Nauka/Interperiodica".*

1. INTRODUCTION

It is well known that, in the absence of a magnetic field, electromagnetic oscillations do not penetrate into a plasma whose density exceeds the critical density, which is defined by the condition $\omega_{pe} = \omega$ (where ω_{pe} is the electron plasma frequency and ω is the oscillation frequency). However, in the presence of a magnetic field, microwaves whose wave vector is nearly parallel to the magnetic field ($\theta < \theta_{cr}$) can penetrate into a plasma with an arbitrary density. For $\omega_{pe} \gg \omega$, the critical angle is equal to $\theta_{cr} = \arccos(\omega/\omega_e)$. The electric field of such microwaves is essentially right-polarized; i.e., it has a significant circularly polarized component rotating in the same direction as the electrons. The electric field of microwaves propagating strictly along the magnetic field ($\theta = 0$) is completely right-polarized. Such right-polarized microwaves are attractive for electron-cyclotron resonance (ECR) heating of dense plasmas.

Microwaves propagating at small angles to the magnetic field are difficult to launch into closed magnetic confinement systems. On the other hand, such microwaves can naturally be employed for the ECR heating of a high-density plasma in open magnetic devices, into which they can be launched through magnetic mirrors along the magnetic field. This method for ECR heating of a low-density ($\omega_{pe} < \omega$) plasma was successfully implemented in experiments in the OGRA-4 open system [1]. In order to understand whether this method can actually be used to heat dense plasmas, we must answer some important questions.

Since the microwave power is launched from free space, microwaves should pass through the critical surface, at which $\omega_{pe} = \omega$. The critical surface is transparent to microwaves whose wave vector is parallel to the magnetic field. However, the transmission factor for microwaves, even those launched at comparatively slight angles to the magnetic field, can be negligibly small. Since microwave sources emit microwave beams in the form of a packet of waves with different wave vectors, the spectral width of the beam becomes an important parameter, which largely governs the beam passage through the critical surface. Note also that this parameter changes as the beam propagates from the source toward the critical surface. Here, we analyze the propagation of a microwave beam using the generalized geometrical-optics (GO) approximation proposed in [2]. The transmission factor is calculated using the formulas derived in [3].

In the vicinity of the critical surface, microwaves experience strong refraction. As a result, the ray trajectories of microwaves may deviate substantially from being straight (in contrast to the vacuum case). The refraction of microwaves that have passed through the critical surface and propagate in a dense plasma is also considerable. The effect of refraction on the propagation of microwaves can be described using the conventional GO approximation, as will be done in our study.

2. MICROWAVE PROPAGATION AHEAD OF THE CRITICAL SURFACE

2.1. General Dependence of the Refractive Index

Far from the critical surface, the plasma weakly affects the propagation of microwaves, so that their ray trajectories are almost straight. However, close to the critical surface, where the plasma plays a dominant role, the ray trajectories are fairly complex in shape. We analyze the ray trajectories using the plane plasma slab approximation and assuming a uniform magnetic field.

We introduce the local Cartesian coordinate system (ξ, ζ) with the ζ-axis directed along the density gradient

1063-780X/01/2702-0119$21.00 © 2001 MAIK "Nauka/Interperiodica"

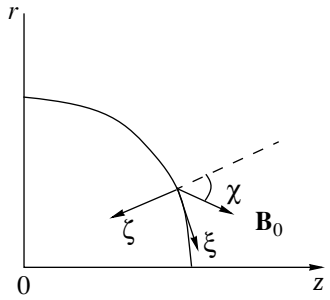

Fig. 1. Working coordinate systems.

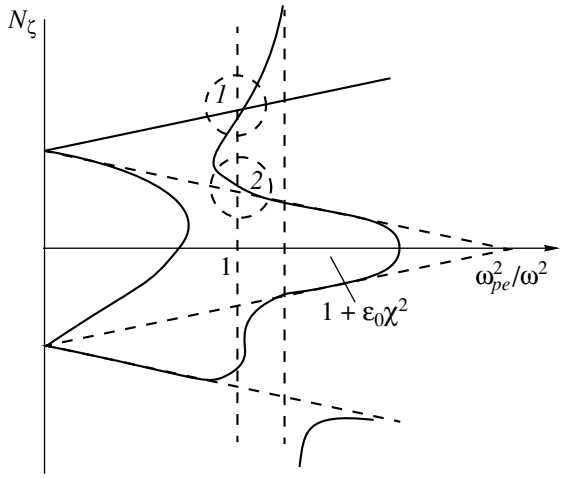

Fig. 2. Refractive-index component N_ζ vs. plasma density for $N_\xi = N_\xi^{(-)} = -N^{(-)}\sin\chi$. Numerals denote the regions where microwaves pass through the critical surface.

(Fig. 1) and denote the angle between ∇n_0 and $\mathbf{B}_0$ by χ. In order to better understand the general properties of the incident microwaves near the critical surface, we consider the dependence of N_ζ on the coordinate ζ or, equivalently, on the plasma density (Fig. 2). This is the only component of the refractive index that changes as microwaves propagate through a plane plasma slab; the component N_ξ remains constant.

Two possible ways in which microwaves pass through the critical surface are illustrated by the two points of intersection of the curve $N_\zeta(\zeta)$ with the vertical line $\omega_{pe}^2/\omega^2 = 1$ in Fig. 2 (see, e.g., [4]). At the first intersection point, the value of N_ζ is such that the wave vector is parallel to the magnetic field, in which case microwaves are either right-polarized waves (rotating in the same direction as the electrons) or left-polarized waves (rotating in the same direction as the ions). Figure 2 refers to right-polarized microwaves (region *1*). At the critical surface, the refractive index of the right-polarized microwaves is equal to $N^{(-)} = \sqrt{\Omega_e/(\Omega_e - 1)}$, where $\Omega_e = \omega_e/\omega$, with ω_e being the electron cyclotron frequency. Accordingly, the ξ-component of the refractive index is $N_\xi^{(-)} = -N^{(-)}\sin\chi$. This component does not change as microwaves propagate through a plane plasma slab. Consequently, if we prescribe $N_\xi = N_\xi^{(-)}$ at the slab boundary, then the refractive index of the incident microwaves at the critical surface will be such that the wave vector is parallel to the magnetic field [4, 3], in which case microwaves pass freely through the surface. For $N_\xi \neq N_\xi^{(-)}$, an opaque region should appear in zone *1* in Fig. 2. This is illustrated in Fig. 3. When passing through the opaque region via subbarrier tunneling, microwaves remain right-polarized.

The larger the difference $|N_\xi - N_\xi^{(-)}|$, the wider the opaque region. For $|N_\xi - N_\xi^{(-)}| \gg L^{-1/2}$, the fraction of microwaves that can pass through the critical surface is negligible [3]. (Here, L is the characteristic scale on which the plasma density varies; note also that all of the quantities having the dimensionality of length are nondimensionalized by multiplying by ω/c.) Near the critical surface, incident microwaves whose wave vector makes a small angle with the magnetic field experience an extremely strong refraction: their wave vector

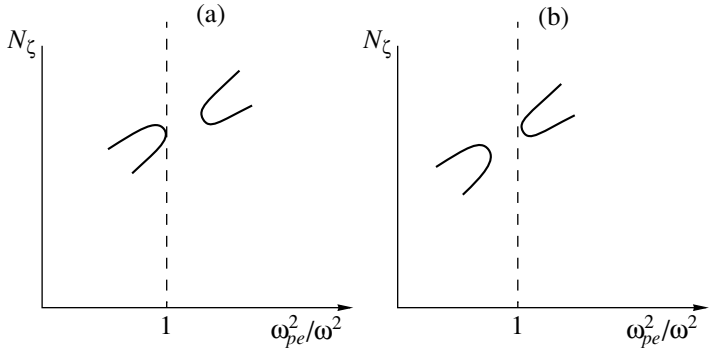

Fig. 3. The same as in Fig. 2, but in region *1* for (a) $N_\xi > N_\xi^{(-)}$ ($\Delta > 0$) and (b) $N_\xi < N_\xi^{(-)}$ ($\Delta < 0$).

changes from $N \approx N^{(-)}$ to $N \approx N^{(+)}$, where $N^{(+)} = \sqrt{\Omega_e/(\Omega_e + 1)}$ is the refractive index of the left-polarized microwaves at the critical surface (Fig. 2). As a result of refraction, electromagnetic rays abruptly change direction: on a reduced scale, the ray trajectories are seen to have a kink. Similar kinks in the ray trajectories have already been captured in simulations of the propagation of radio waves in the Earth's ionosphere (see, e.g., [5]). In Fig. 2, the zone in which the refractive index of microwaves changes as they pass through the critical surface is marked with the symbol *2*. Behind the critical surface, the microwaves are almost completely left-polarized. The transmitted microwaves propagate a comparatively short distance in a denser plasma; after reflection from the high-density plasma region, they start to move in the opposite direction and again pass through the critical surface (see the lower part of Fig. 2).

2.2. Refractive Index near the Critical Surface

Now, we examine the dependence $N_\zeta(\zeta)$ in the vicinity of the critical surface in more detail. Close to the critical surface, the propagation of electromagnetic waves in a cold magnetized plasma is described by the general dispersion relation

$$D = \varepsilon_0 N_\perp^2 (N^2 - 1) + \delta q\left(\frac{N^4}{\Omega_e^2 - 1} - \varepsilon_0 (N^2 - 1)(N_\parallel^2 - 1)\right) + 2\delta q^2 \frac{N^2}{\Omega_e^2 - 1} = 0, \quad (1)$$

where $\varepsilon_0 = \Omega_e^2/(\Omega_e^2 - 1)$, $\delta q = q - 1$, and $q = \omega_{pe}^2/\omega^2$.

Dispersion relation (1) implies that, at the critical surface ($\delta q = 0$), either the condition $N_\perp = 0$ or the condition $N = 1$ should hold (in Fig. 2, these conditions correspond to zones *1* and *2*).

Since the first condition is favorable for ECR plasma heating, we will analyze dispersion relation (1) assuming that $N_\parallel \gg N_\perp$, in which case the dispersion relation can be written in a somewhat simpler form:

$$D = \varepsilon_0 N_\perp^2 (N^2 - 1) - \delta q (N^2 - N^{(-)2})(N^2 - N^{(+)2}) + 2\delta q^2 \frac{N^2}{\Omega_e^2 - 1} = 0. \quad (2)$$

We transform this relation to the basic variables (N_ξ, N_ζ), where N_ξ is a constant quantity and N_ζ varies with the plasma density according to the equation

$$(\delta N_\zeta)^2 A + 2\delta N_\zeta B + C = 0. \quad (3)$$

Here, we introduce the notation $\delta N_\zeta = N_\zeta - N_\zeta^{(-)}$, $N_\zeta^{(-)} = N^{(-)}\cos\chi$, $\Delta = N_\xi - N_\xi^{(-)}$, $N_\xi^{(-)} = -N^{(-)}\sin\chi$, $A = \varepsilon_0 \sin^2\chi$, $B = \varepsilon_0 \Delta \sin\chi - 2\delta q \cos\chi N^{(-)} \frac{\Omega_e}{\Omega_e + 1}$, and $C = 2(\delta q)^2 \frac{\Omega_e}{\Omega_e + 1} + 4\delta q \Delta \tan\chi N^{(-)} \frac{\Omega_e}{\Omega_e + 1} + \Delta^2 \varepsilon_0$, in terms of which we have $N^2 \approx N^{(-)2} + 2N^{(-)}(\delta N_\zeta \cos\chi - \Delta \tan\chi)$ and $N_\perp \approx \Delta + \delta N_\zeta \sin\chi$.

We resolve dispersion relation (3) with respect to δN_ζ to obtain

$$\delta N_\zeta = \frac{-B \pm \sqrt{G}}{A}, \quad (4)$$

where

$$G = B^2 - AC = \frac{2\Omega_e^3}{(\Omega_e - 1)^2 (\Omega_e^2 - 1)^2} \times \delta q (\delta q (\cos^2\chi (\Omega_e + 1) - (\Omega_e - 1)) - 2\Delta \tan\chi N^{(-)} (\Omega_e - 1)).$$

The plasma is transparent to the microwaves under consideration ($\mathrm{Im}\,\delta N_\zeta = 0$) if $G > 0$. For this inequality to hold, it is necessary to satisfy the condition

$$\chi \le \chi_0 = \arccos\sqrt{\frac{\Omega_e - 1}{\Omega_e + 1}}$$

far from the critical surface ($|\delta q| \gg \Delta$).

For open confinement systems, the angle χ vanishes at the axis and increases with distance from the axis. If $N_\xi > N_\xi^{(-)}$ ($\Delta > 0$), the transparency region is adjacent to the critical surface (Fig. 3a). Under the opposite condition $N_\xi < N_\xi^{(-)}$ ($\Delta < 0$), microwaves are reflected before they reach the critical surface (Fig. 3b).

Microwaves with $N_\xi = N_\xi^{(-)}$ ($\Delta = 0$) pass freely through the critical surface (the corresponding ray trajectory has no singularity at the critical surface), still remaining right-polarized. The situation is radically different when N_ξ is not equal to $N_\xi^{(-)}$.

2.3. Ray Trajectories and Wave Polarization near the Critical Surface

Let us analyze ray trajectories with $N_\xi \neq N_\xi^{(-)}$ in the vicinity of the critical surface. In the $\xi 0 \zeta$ plane, the ray trajectories satisfy the differential equation

$$\frac{d\xi}{d\zeta} = \frac{V_{g\xi}}{V_{g\zeta}} = \frac{\partial D/\partial N_\xi}{\partial D/\partial N_\zeta} = -\frac{\partial N_\zeta}{\partial N_\xi}, \quad (5)$$

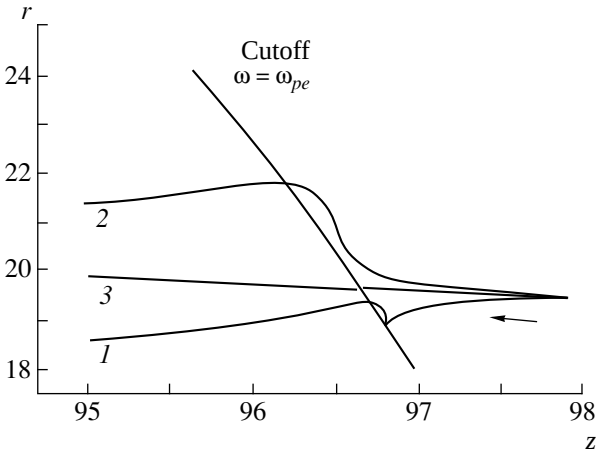

Fig. 4. Ray trajectories of microwaves with $N_\xi \approx N_\xi^{(-)}$ near the critical surface for (*1*) $N_\xi > N_\xi^{(-)}$ ($\Delta > 0$), (*2*) $N_\xi < N_\xi^{(-)}$ ($\Delta < 0$), and (*3*) $\Delta = 0$.

where V_g is the group velocity. The dependence $N_\zeta(N_\xi)$ is described by expression (4).

First, we assume that $\Delta > 0$ and consider the range of small $|\delta q|$ values ($|\delta q| \ll |\Delta|$). In this range, expression (4) yields

$$\delta N_\zeta \approx a\Delta \pm b\sqrt{-\Delta\zeta}, \tag{6}$$

where $a = -\dfrac{\Delta}{\sin\chi}$ and $b = \dfrac{2}{\Omega_e^2 - 1}\left(\dfrac{N^{(-)}}{\Omega_e \cos\chi \sin^3\chi}\dfrac{dq}{d\zeta}\right)^{1/2}$.

We integrate Eq. (5) to obtain

$$\xi \approx -a\zeta \pm \frac{b}{3}\frac{(-\zeta)^{3/2}}{\Delta^{1/2}}. \tag{7}$$

The ray trajectory (7) has a cusp at the point of reflection from the critical surface ($\zeta = 0$). This conclusion is confirmed by the numerical integration of the general dispersion relation (Fig. 4). Our simulations were carried out for conditions corresponding to planned experiments with the SME (Stabilizing Magnetic Element) open device, which is aimed at stabilizing the Drakon closed confinement system. The magnetic field was prescribed in terms of the magnetic potential

$$\Phi(\mathbf{r}) = B(0)\left(1 - \frac{r^2}{4}\frac{d^2}{dz^2}\right)\Phi_0(z),$$

$$\Phi_0(z) = \frac{1}{2}\left((R+1)z - (R-1)\frac{L_B}{\pi}\sin\left(\pi\frac{z}{L_B}\right)\right),$$

where we put $R = 3$ and $L_B = 170$. The coordinate-dependent plasma density was chosen to be $n_0(\mathbf{r}) = n_0(0)\exp\left(-\dfrac{\mathbf{r}^2}{L_n^2}\right)$ with $L_n = 65$. As before, the quantities having the dimensionality of length were normalized to c/ω. We also set $\omega_e(0) = \omega$ and $\omega_{pe}^2(0) = 10\omega^2$.

Ray trajectories having a cusp were also obtained by Piliya and Fedorov [6], who solved the problem of the propagation of electromagnetic waves near the plasma resonance surface. Analogous trajectories are characteristic of perturbations propagating near the interface between supersonic and subsonic plasma flows [7].

For $\Delta < 0$, there is an opaque region ahead of the critical surface. Near the boundary of the opaque region, we have

$$\delta N_\zeta \approx a\Delta \pm c(d\Delta - \zeta)^{1/2}, \tag{8}$$

where $c = \dfrac{1}{(\Omega_e - 1)\sin^2\chi}\left(2d\dfrac{\Delta}{\Omega_e}\dfrac{dq}{d\zeta}(\Omega_e - 1 - (\Omega_e + 1)\times\cos^2\chi)\right)^{1/2}$ and $d = \dfrac{2\tan\chi N^{(-)}}{(\Omega_e + 1)\cos^2\chi - (\Omega_e - 1)}\left(\dfrac{dq}{d\zeta}\right)^{-1}$.

The ray trajectories that satisfy Eq. (8) are described by the expression

$$\xi \approx a\Delta d \pm cd(\Delta d - \zeta)^{1/2}. \tag{9}$$

We can see that, after reflection from the opaque region ($\zeta > \Delta d$), the electromagnetic rays propagate along parabolic trajectories (see also Fig. 4).

Figure 4 shows that, regardless of the sign of Δ, the microwaves reflected from the boundary of the opaque region experience strong refraction: along a considerable portion of the ray trajectory, the wave vector of microwaves is nearly parallel to the critical surface. However, the ray trajectories inevitably intersect the critical surface. At the intersection points, the refractive index is equal to unity [see dispersion relations (1) and (2)].

The polarization of microwaves changes abruptly as they pass through the critical surface. It is convenient to analyze this issue in terms of the electric field components $E_\pm = (E_x \pm iE_y)/\sqrt{2}$ and $E_\parallel = E_z$ in a local Cartesian coordinate system with the *z*-axis directed along the magnetic field. According to [8], we have $E_\pm = C\dfrac{N_\pm}{\varepsilon_\pm - N^2}$ and $E_\parallel = C\dfrac{N_\parallel}{\varepsilon_\parallel - N^2}$, where $N_\pm = (N_x \pm iN_y)/\sqrt{2}$. In the plane plasma slab approximation, we can set $N_y = 0$.

Figure 5 illustrates the results of calculations of the polarization of microwaves along the two ray trajectories with $\Delta \neq 0$ that are shown in Fig. 4. Since, near the critical surface, the microwaves under consideration propagate at small angles to the magnetic field, they are almost completely right-polarized ($|E_-| \gg |E_+|, |E_\parallel|$).

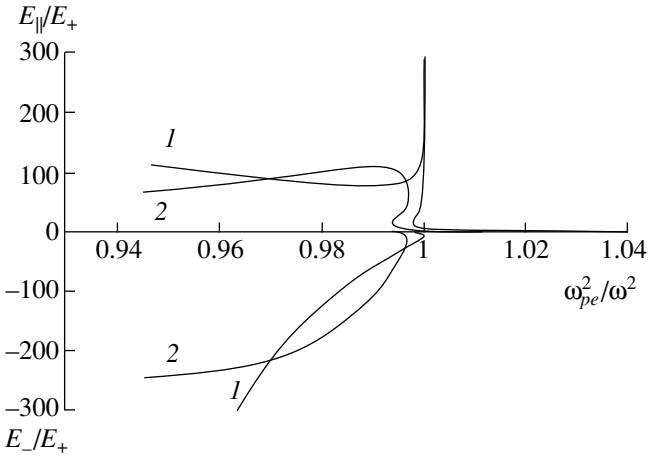

Fig. 5. Polarization of microwaves along the ray trajectories shown in Fig. 4. The numbers labeling the curves correspond to those in Fig. 4.

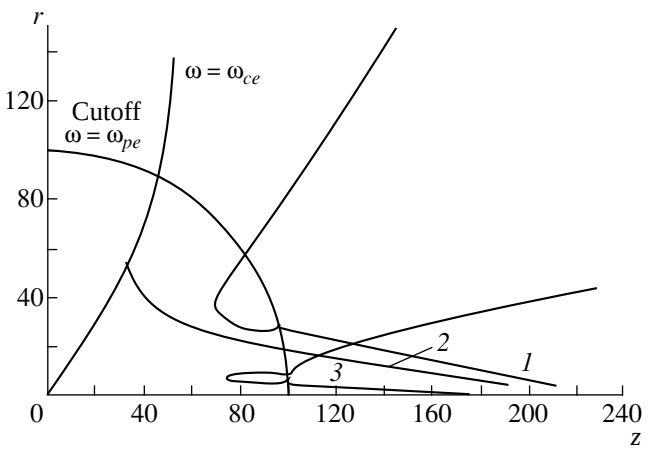

Fig. 6. Representative ray trajectories that intersect the critical surface for (*1*) $\Delta > 0$, (*2*) $\Delta = 0$, and (*3*) $\Delta < 0$.

After passing through the critical surface, the microwaves remain circularly polarized, but with the electric vector rotating in the opposite direction ($|E_+| \gg |E_-|$, $|E_\parallel|$). Near the critical surface, the microwave electric field acquires a considerable longitudinal component. Note that, at the cusp of the ray trajectory, the oscillations are nearly potential ($E_+ \approx E_- \approx 0$). In Fig. 5, we present only the lower part of the corresponding trajectory, because it runs beyond the frame of the figure. The result obtained is quite natural. In fact, dispersion relations (1) and (2) imply that the transverse component of the refractive index of the oscillations with $N \neq 1$ should vanish at the critical surface. It is well known that such oscillations should be either circularly or longitudinally polarized. The circular and longitudinal polarizations correspond to $\Delta = 0$ and $\Delta < 0$, respectively.

2.4. Choice of the Position of a Microwave Source

Numerical tracing of long portions of the ray trajectories shows that the transmitted microwaves with $\Delta \neq 0$ (which are almost completely left-polarized behind the critical surface) propagate a comparatively short distance in a dense plasma and then are reflected from the high-density plasma region. When moving away from the system axis, they again pass through the critical surface (see Fig. 6 and the lower part of Fig. 1).

Our analysis shows that, in order for the almost completely right-polarized incident microwaves to keep their original polarization behind the critical surface, their wave vectors should be nearly parallel to the magnetic field when they approach the surface (the extent to which the wave vector may be nonparallel to the magnetic field will be discussed below). The ray trajectories of such microwaves are illustrated in Fig. 7, which shows that the microwave source should be inclined at a slight angle to the device axis. Note that not all of the rays that pass through the critical surface reach the cyclotron resonance surface. The rays that make sufficiently large angles with the system axis are reflected from the high-density plasma region and occur again in the vicinity of the critical surface. Thereafter, they are either absorbed at the plasma resonance surface (if $\Delta > 0$) or pass through the critical surface into a lower density plasma (if $\Delta < 0$); in the latter case, the right-polarized microwaves become left-polarized (Figs. 2, 3).

The rays that are incident from the side of the lower density plasma can pass through the critical surface only if it is not too far from the system axis. The maximum distance between the critical surface and the axis is determined by the condition $\chi = \chi_0 = \arccos\sqrt{(\Omega_e - 1)/(\Omega_e + 1)}$ (see Section 2.3).

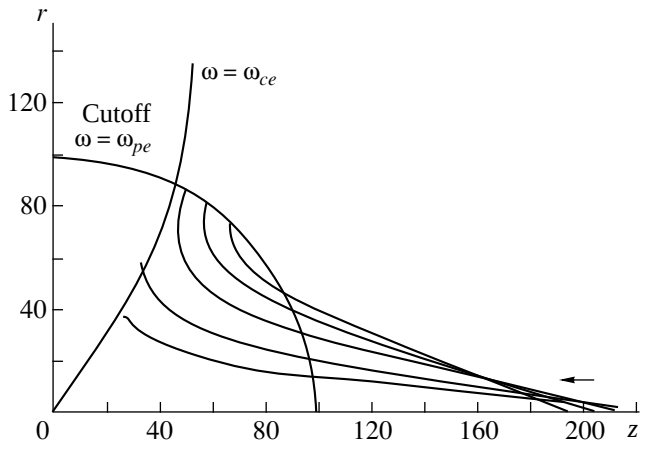

Fig. 7. Ray trajectories of microwaves whose wave vector is parallel to the magnetic field ($\Delta = 0$) when they pass through the critical surface.

3. PROPAGATION OF MICROWAVES BEHIND THE CRITICAL SURFACE

3.1. Ray Trajectories near the Axis of an Open Confinement System

In open confinement systems, the plasma density is highest near the axis. According to Fig. 7, microwaves can enter the central region only if they are launched at a slight angle to the axis. On the other hand, we can clearly see that the ray trajectories shown in this figure tend to deviate from the axis. Let us clarify the physical nature of this tendency.

In the axial region of an open confinement system, the coordinate dependence of the magnetic field and plasma density is described by the expressions

$$B_r(\mathbf{r}) \approx -\frac{r}{2}B_0'(z),$$

$$B_z(\mathbf{r}) \approx B_0(z) - \frac{r^2}{4}B_0''(z),$$

$$n_0(\mathbf{r}) \approx n_0^{(0)}(z) - r^2 n_0^{(1)}(z).$$

In order to analyze the ray trajectories in a dense plasma qualitatively, we assume that $\omega_{pe} \gg \omega$, in which case the microwaves under consideration (which are also referred to as whistlers) satisfy the approximate dispersion relation

$$N^2 \approx \frac{\omega_{pe}^2}{\omega(\omega_e\cos\theta - \omega)}. \quad (10)$$

With the above expressions for the coordinate dependence of the plasma density and magnetic field, dispersion relation (10) becomes

$$D = N_z^2\left(\Omega_e(z) - 1 - \frac{r^2}{4}\Omega_e''(z)\right) + N_z N_r\frac{r}{2}\Omega_e'(z) + N_r^2\left(\frac{1}{2}\Omega_e(z) - 1\right) - q_0(z) + r^2 q_1(z) = 0,$$

where $q_{0,1} = 4\pi e^2 n_0^{(0,1)}/m_e\omega^2$.

The desired ray-tracing equations can be derived from the equations of the GO approximation:

$$\frac{d\mathbf{r}}{dt} = \frac{\partial D}{\partial \mathbf{N}}\left(\frac{\partial D}{\partial \omega}\right)^{-1}, \qquad \frac{d\mathbf{N}}{dt} = -\frac{\partial D}{\partial \mathbf{r}}\left(\frac{\partial D}{\partial \omega}\right)^{-1}. \quad (11)$$

In order to simplify the calculations, we introduce the dimensionless time τ through the relationship $d\tau = dt(\partial D(\mathbf{r}(t), \mathbf{N}(t)/\partial\omega)^{-1})$, in which case the GO equations (11) become

$$\frac{d\mathbf{r}}{d\tau} = \frac{\partial D}{\partial \mathbf{N}}, \qquad \frac{d\mathbf{N}}{d\tau} = -\frac{\partial D}{\partial \mathbf{r}}. \quad (12)$$

We consider two equations from the complete set of four GO equations, specifically, the equations for r and N_r:

$$\dot{r} = \frac{1}{2}rN_z\Omega_e' + N_r(\Omega_e - 2), \qquad \dot{N}_r = -\frac{1}{2}N_r N_z\Omega_e' + r\left(\frac{1}{2}N_z^2\Omega_e'' - 2q_1\right). \quad (13)$$

Since, in open magnetic confinement systems, the plasma density experiences more abrupt spatial variations in comparison with the magnetic field, the coefficient q_1 is the largest among the coefficients in Eqs. (13). This circumstance enables us to take into account the variations of N_z, Ω_e, and q_1 along the ray trajectories parametrically and to specify the dependence of r and N_r on the dimensionless time in exponential form: $\propto\exp(\gamma\tau)$, where the instability growth rate is approximately equal to $\gamma \approx 2(q_1(1 - \Omega_e/2))^{1/2}$. By instability we mean an exponentially rapid deviation of the ray trajectories from the system axis. The sharper the radial decrease in the plasma density, the higher the instability growth rate; this tendency is illustrated by Fig. 8. For the narrowest radial density profile, the ray trajectory was traced numerically until it approached the critical surface from the side of the higher density plasma (curve *3*). For wider density profiles, the ray trajectories reached the ECR region (curves *1*, *2*). The behavior of these trajectories will be discussed below.

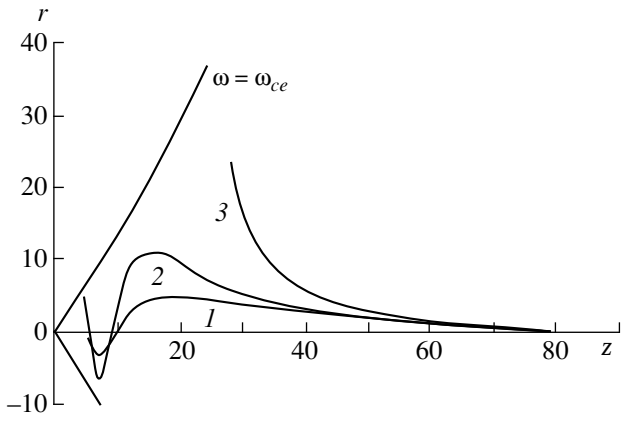

Fig. 8. Ray trajectories near the axis of an open confinement system for different radial density profiles: $n_0(\mathbf{r}) = \exp\left(-\left(\frac{z}{L_1}\right)^2 - \left(\frac{r}{L_2}\right)^2\right)$ with $L_1 = 65$ and $L_2 = (1)\ 65, (2)\ 32$, and $(3)\ 16$ (all of the normalizing quantities having the dimensionality of length are expressed in units of c/ω).

According to the widely held opinion based on geophysical studies, the whistlers under consideration propagate strictly along the geomagnetic field lines and can never deviate from them. Previous investigations [5] have shown that this opinion is to some extent valid in the case of a homogeneous plasma. However, our analysis indicates that, in an inhomogeneous plasma, the electromagnetic rays can make substantial excursions away from the magnetic field lines. It is interesting to note that Gershman *et al.* [9] attributed the propagation of ray trajectories strictly along the geomagnetic field lines to the plasma inhomogeneity, specifically to the appearance of plasma waveguides stretched along the geomagnetic field lines.

3.2. Ray Trajectories near the ECR Region

Here, we briefly investigate the specific features of the propagation of microwaves in the ECR region, where the ray trajectories behave in a very different manner: they do not move away from the axis, but rather approach the cyclotron resonance point, which lies at the axis of the system.

Since the refractive index of the right-polarized microwaves increases without bound when approaching the cyclotron resonance point, the variations of N_z (see above) can no longer be taken into account parametrically.

The problem can be treated analytically only under the assumption $\omega > \omega_e(0)(\Omega_e(0) > 1)$. In this case, the cyclotron resonance surface intersects the system axis at the point at which $\Omega_e' \neq 0$, so that the equation for $N_z(\tau)$ takes the form

$$\dot{N}_z \approx -N_z^2 \Omega_e',$$

which gives $N_z \approx 1/(\Omega_e'\tau)$. With this dependence, we can reduce Eqs. (13) to the equations

$$\dot{r} \approx \frac{1}{2}\frac{r}{\rho} - N_r,$$

$$\dot{N}_r \approx -\frac{1}{2}\frac{N_r}{\tau} + \frac{\Omega_e''}{2\Omega_e'^2}\frac{r}{\tau^2},$$

whose solution can be written in terms of the power functions $r = C_1\tau^{s_1} + C_2\tau^{s_2}$ with $s_{1,2} = \frac{1}{2} \pm i\sqrt{2\frac{\Omega_e''}{\Omega_e'^2}}$. The expression for $r(\tau)$ shows that the ray trajectories approach the cyclotron resonance point. Moreover, from Fig. 8, we can see that, near the resonance point, the behavior of the trajectories is oscillatory in character. It should be noted, however, that our calculations were carried out under the assumption that the cyclotron resonance point lies at the system axis, at which we have $\Omega_e' = 0$. As a result, the tendency of the ray trajectories to approach the system axis is even more pronounced, because the trajectories are bounded by the cyclotron resonance lines, which intersect at the axis.

Note also that, for the assumed magnetic field geometry of a simple mirror confinement system, the ray trajectories in a low-density ($\omega_{pe} < \omega$) plasma tend to move away from the axis [10]. However, because of the strong absorption of microwaves, the analysis of ray trajectories in the ECR region is a rather abstract issue.

4. PROPAGATION OF MICROWAVE BEAMS AND THEIR PASSAGE THROUGH THE CRITICAL SURFACE

The parameters of a propagating microwave beam change due to refraction, focusing (or defocusing), and diffraction. The first of these phenomena can be examined in the conventional GO approximation (see above). In [2], the remaining two phenomena were taken into account by supplementing the set of GO equations with the equations for the tensor elements $\partial k_i/\partial x_j$. The real part of the tensor determines how the phase of the beam varies over of its transverse cross section, and the imaginary part determines the variations of the beam amplitude (under the assumption that the amplitude obeys a Gaussian distribution over the transverse coordinates). Knowing the tensor elements $\partial k_i/\partial x_j$ along the ray trajectories of a microwave beam is sufficient to include both focusing (or defocusing) and diffraction processes. Note that the method used in [2] is a generalization of the approach developed by Bernstein and Friedland [11]. They assumed that the tensor elements $\partial k_i/\partial x_j$ are real, which made it possible to only investigate the focusing (or defocusing) of the spatially unbounded wave fields.

In [2, 11], the quantities $\partial k_i/\partial x_j$ were described by the equations

$$\begin{aligned}\frac{d}{d\tau}\left(\frac{\partial k_i}{\partial x_j}\right) = &-\frac{\partial^2 D}{\partial x_i \partial x_j} - \frac{\partial k_k}{\partial x_i}\frac{\partial^2 D}{\partial x_j \partial k_k} \\ &- \frac{\partial k_k}{\partial x_j}\frac{\partial^2 D}{\partial x_i \partial k_k} - \frac{\partial k_k}{\partial x_i}\frac{\partial k_l}{\partial x_j}\frac{\partial^2 D}{\partial k_k \partial k_l}.\end{aligned} \quad (14)$$

Equations (12) and (14) constitute the basic set of equations in the generalized GO approximation.

The initial values of $\partial k_i/\partial x_j$ are determined by the parameters of the microwave source. In calculations, we assumed that the source emits Gaussian beams, with an envelope of the form $\propto \exp(iQ_0\rho^2)$, where ρ is the distance from the beam axis. The beam width is determined by the imaginary part of Q_0; the real part of Q_0 characterizes either the convergence (focusing) of the beam (if $\mathrm{Re}\,Q_0 > 0$) or the divergence (defocusing) of the beam (if $\mathrm{Re}\,Q_0 < 0$). Due to diffraction, the beam propagating through the plasma becomes wider, but the

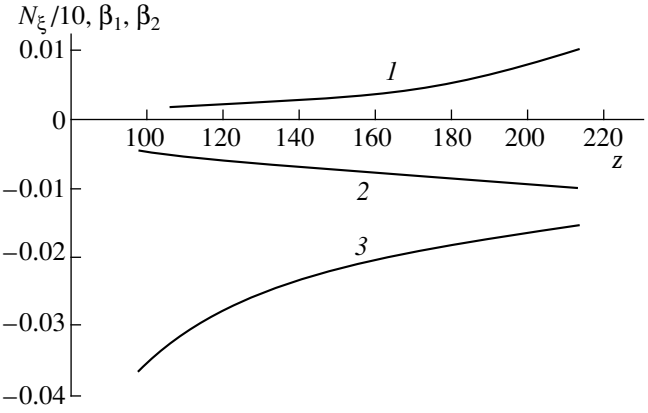

Fig. 9. Variation of the parameters (*1*) $N_\xi/10$, (*2*) β_1, and (*3*) β_2 of a microwave beam along a ray trajectory.

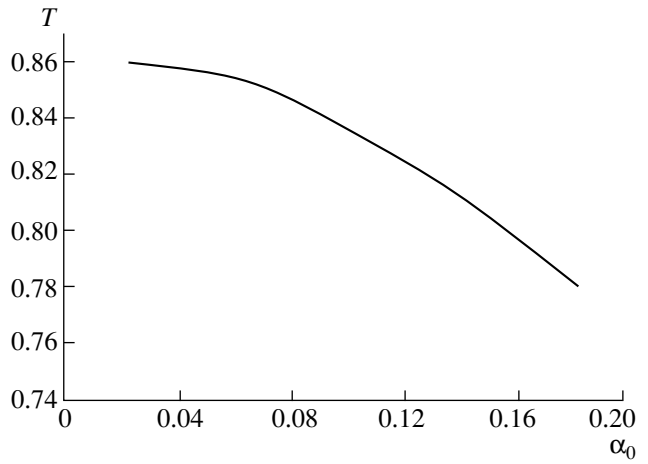

Fig. 10. Transmission coefficient vs. the initial angle between the ray trajectory and the system axis for $\mathrm{Re}\,Q_0 = \mathrm{Im}\,Q_0 = 0.01$, $z_0 = 212.81$, and $r_0 = 1.39$ (the coordinates are expressed in units of c/ω).

beam's divergence, which is characterized by the quantity $\delta k \approx \mathrm{Re}\,Q/\sqrt{\mathrm{Im}\,Q} > 0$, somewhat decreases (Fig. 9).

We consider the passage of a microwave beam through the critical surface by using the transmission coefficients derived in [3] for plane waves and wave beams:

$$T_0 = e^{-\tau}, \qquad T = \sigma^{1/2} e^{-\sigma\tau}, \tag{15}$$

where $\tau = \frac{1}{2}\pi L \varepsilon_-^{1/2}(N_\xi - N_\xi^{(-)})^2$ and $\sigma = \dfrac{\beta_1}{\beta_1 + \pi L \varepsilon_-^{1/2}/4}$. The parameter $\beta = \beta_1 + i\beta_2$ determines the spectral width of the beam: $E_\parallel(\mathbf{r}) = \int dN_\xi E_\parallel(\mathbf{r}, N_\xi) F(N_\xi)$, where $F(N_\xi) = \exp(-(N_\xi - N_{\xi 0})^2\beta)$ and $E_\parallel(\mathbf{r}, N_\xi)$ is the solution to the wave equation at a fixed N_ξ.

In [3], a plane plasma slab was analyzed using the same model as in Section 2 and microwaves propagating at a small angle to the magnetic field were studied under the assumption that the angle χ between the plasma density gradient and the magnetic field is also small.

In the plane plasma slab approximation, the parameters that remain unchanged during the propagation of microwaves are the refractive-index component N_ξ and the quantity β, which characterizes the spectral width of the beam. However, under the conditions adopted in our numerical simulations, these parameters change along the ray trajectories. The following question then arises: what are the values of these parameters that should be used in the transmission coefficients derived in [3]? In other words, at what point on the ray trajectory does the GO approximation fail making us to switch to the plane plasma slab approximation? To answer these questions, note that, in [3], the solution of the wave equation was found to approach the quasiclassical solution asymptotically in the limit $\zeta - \zeta_r \gg 1$ (where $\zeta_r = -\varepsilon_0 \chi^2 L$ is the coordinate of the plasma resonance surface). However, the quasiclassical approximation underlies the GO approach. Consequently, we must switch from the GO approximation to the plane plasma slab approximation when the difference $\Delta\zeta = \zeta - \zeta_r$ becomes a value on the order of unity. To be specific, we perform the switching at $\Delta\zeta = 3$, especially since switching at other $\Delta\zeta$ values between 2 and 10 will change the resulting transmission coefficients insignificantly. In fact, Fig. 9 shows that, along the portions of the ray trajectories immediately ahead of the critical surface, the parameters of interest vary relatively weakly. Note that the parameter Q is related to β by $\beta = \dfrac{1}{4Q}\left(\dfrac{V_{g\zeta}}{V_g}\right)^2$, where V_g is the group velocity. Since we are interested in microwaves that pass through the critical surface almost freely (the case of small angles θ and χ), we can assume that, near the critical surface, the ratio $V_{g\zeta}/V_g$ is close to unity.

Another condition for the validity of the asymptotic approach used in [3] is $\zeta \gg \chi L \Delta$. Since switching to the GO approximation implies that ζ is small, this condition imposes a fairly stringent restriction on the possible values of $\Delta = N_\xi - N_\xi^{(-)}$. The maximum value $|\Delta| = \Delta_c$ is determined from the approximate equality $\Delta_c \approx (\zeta_r + \Delta\zeta)/\chi L$, where $\Delta\zeta \approx 3$ (see above). The approach developed in [3] cannot be used to describe the ray trajectories with $|\Delta| > \Delta_c$ immediately ahead of the critical surface. In particular, this restriction is important in analyzing how the orientation of a microwave source affects the transmission coefficient (Fig. 10). When the orientation of the source is chosen to be optimum

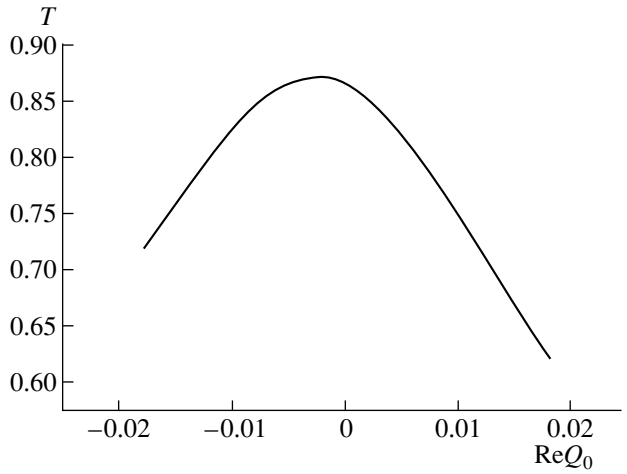

Fig. 11. Transmission coefficient vs. $\mathrm{Re}\,Q_0$ for $\mathrm{Im}\,Q_0 = 0.01$, $\alpha_0 = 0.15$, $z_0 = 212.81$, and $r_0 = 1.39$.

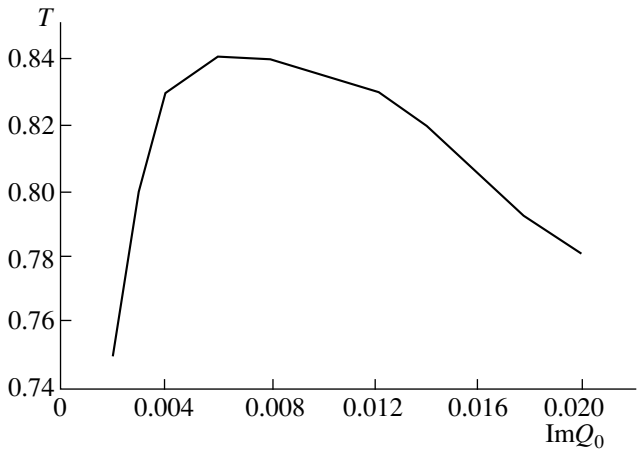

Fig. 12. Transmission coefficient vs. $\mathrm{Im}\,Q_0$ for $\mathrm{Re}\,Q_0 = 0.01$, $\alpha_0 = 0.15$, $z_0 = 212.81$, and $r_0 = 1.39$.

($\alpha_0 = \alpha_{0c} \approx 0.15$), the emitted microwaves approach the critical surface along the magnetic field lines. The transmission coefficient for such microwaves differs from unity due exclusively to the finite spectral width of the beam. With increasing α_0, the quantity $|\Delta|$ increases sharply and, accordingly, the transmission coefficient decreases. The maximum value $\alpha_0 \approx 0.18$ at which the transmission coefficients (15) are still valid is determined by the condition $|\Delta| = \Delta_c$. As α_0 decreases, the quantity Δ again increases but much more gradually than in the previous case, so that the critical value Δ_c is reached only at $\alpha_0 \approx 0.02$. Such asymmetry with respect to the sign of the difference $\alpha_0 - \alpha_{0c}$ stems from the straightening of the ray trajectories along the magnetic field at $\Delta > 0$ (see Section 2.3). On the trajectories with $\alpha_0 > \alpha_{0c}$ and $\alpha_0 < \alpha_{0c}$, the parameter Q, which characterizes the spectral width of the beam, also behaves in a different manner. For $\alpha_0 < \alpha_{0c}$, a decrease in this parameter leads to a slight increase in the transmission coefficient (Fig. 10).

The phenomena of diffraction and convergence (divergence) of a microwave beam affect the transmission coefficient via the quantity $Q = \frac{1}{4\beta}\left(\frac{V_{g\zeta}}{V_g}\right)^2$. Figures 11 and 12 show the transmission coefficient as a function of the initial values Q_0 of this quantity, which are determined by the parameters of the microwave source. According to Fig. 11, the transmission coefficient decreases as $|\mathrm{Re}\,Q_0|$ increases; moreover, the dependence $T(\mathrm{Re}\,Q_0)$ is almost insensitive to the sign of $\mathrm{Re}\,Q_0$. This result is quite natural, because the quantity $|\mathrm{Re}\,Q_0|$ determines the spectral width of the beam, while the sign of $\mathrm{Re}\,Q_0$ governs merely the spatial orientation of the wave vectors of microwaves in the beam.

Figure 12 presents the dependence of the transmission coefficient on $\mathrm{Im}\,Q_0$ at a fixed value $\mathrm{Re}\,Q_0 = 0.01$. In order to clarify the reasons for why this dependence is nonmonotonic, we analyze the spectrum of the function $F(x) = \exp(iQx^2)$, which models the envelope of the Gaussian microwave beam. Performing simple manipulations, we obtain $S(k) = |F(k)| = \frac{1}{|Q|}\exp\left(-\frac{\mathrm{Im}\,Q}{2|Q|^2}k^2\right)$. This expression implies that, as $\mathrm{Im}\,Q$ decreases, the spectrum narrows in the range $\mathrm{Im}\,Q > \mathrm{Re}\,Q$ and broadens in the range $\mathrm{Im}\,Q < \mathrm{Re}\,Q$. Consequently, there should exist an optimum value of $\mathrm{Im}\,Q$ at which the transmission coefficient is maximum. In order of magnitude, this value is equal to $|\mathrm{Re}\,Q|$.

5. CONCLUSION

We have shown that, in open magnetic confinement systems, microwaves that are launched through magnetic mirrors at a slight angle to the magnetic field can penetrate deeply into a dense plasma. When propagating through a dense plasma in the confinement system, microwaves tend to move away from the plasma axis toward the plasma periphery. This tendency may be unfavorable for heating plasmas whose radial density profiles are strongly peaked about the system axis.

ACKNOWLEDGMENTS

I am grateful to V.A. Zhil'tsov, A.V. Zvonkov, A.Yu. Kuyanov, and A.A. Skovoroda for fruitful discussions.

REFERENCES

1. V. A. Zhil'tsov, A. A. Skovoroda, and A. G. Shcherbakov, Fiz. Plazmy **17**, 785 (1991) [Sov. J. Plasma Phys. **17**, 456 (1991)]; V. A. Zhil'tsov, A. A. Skovoroda, A. V. Timofeev, *et al.*, Fiz. Plazmy **17**, 771 (1991) [Sov. J. Plasma Phys. **17**, 447 (1991)]; V. A. Zhil'tsov, A. Yu. Kuyanov,

A. A. Skovoroda, and A. V. Timofeev, Fiz. Plazmy **20**, 267 (1994) [Plasma Phys. Rep. **20**, 242 (1994)].

2. A. V. Timofeev, Fiz. Plazmy **21**, 646 (1995) [Plasma Phys. Rep. **21**, 610 (1995)].
3. A. V. Timofeev, Fiz. Plazmy **26**, 874 (2000) [Plasma Phys. Rep. **26**, 820 (2000)].
4. V. L. Ginzburg, *The Propagation of Electromagnetic Waves in Plasmas* (Nauka, Moscow, 1967; Pergamon, Oxford, 1970).
5. K. Davies, *Ionospheric Radio Waves* (Blaisdell, Waltham, 1969; Mir, Moscow, 1973).
6. A. D. Piliya and V. I. Fedorov, in *High-Frequency Plasma Heating*, Ed. by A. G. Litvak (Inst. Prikl. Fiz., Gorki, 1983), p. 281.
7. L. D. Landau and E. M. Lifshitz, *Fluid Mechanics* (Nauka, Moscow, 1986; Pergamon, New York, 1987).
8. A. V. Timofeev, Fiz. Plazmy **18**, 407 (1992) [Sov. J. Plasma Phys. **18**, 214 (1992)].
9. B. N. Gershman, L. M. Erukhimov, and Yu. A. Yashin, *Wave Phenomena in Ionospheric and Space Plasmas* (Nauka, Moscow, 1984).
10. A. V. Zvonkov and A. V. Timofeev, Fiz. Plazmy **14**, 1270 (1988) [Sov. J. Plasma Phys. **14**, 743 (1988)].
11. A. Bernstein and L. Freeland, in *Basic Plasma Physics*, Ed. by A. A. Galeev and R. N. Sudan (Énergoatomizdat, Moscow, 1983; North-Holland, Amsterdam, 1983), Vol. 1.

Translated by I.A. Kalabalyk

Plasma Physics Reports, Vol. 27, No. 2, 2001, pp. 129–136. Translated from Fizika Plazmy, Vol. 27, No. 2, 2001, pp. 141–148.
Original Russian Text Copyright © 2001 by Irzak, Tregubova, Shcherbinin.

PLASMA OSCILLATIONS AND WAVES

Modeling of the Excitation of Electron Bernstein Modes in Spherical Tokamaks

M. A. Irzak, E. N. Tregubova, and O. N. Shcherbinin

Ioffe Physicotechnical Institute, Russian Academy of Sciences, Politekhnicheskaya ul. 26, St. Petersburg, 194021 Russia

Received June 2, 2000; in final form, August 4, 2000

Abstract—The possibility is studied of using electron cyclotron waves to heat plasmas and to drive currents in spherical tokamaks when the cutoff layer for the waves is located at the plasma edge. It is shown that, by optimizing the method for the excitation of electron cyclotron waves, it is possible to achieve conditions corresponding to the so-called "radio window" effect, i.e., conditions under which the efficient conversion of incident waves into Bernstein modes propagating toward the plasma center occurs already at the plasma edge. As an example, the parameters of multiwaveguide antennas capable of emitting directed penetrating radiation are calculated. © *2001 MAIK "Nauka/Interperiodica".*

The interaction between electron cyclotron (EC) waves with plasmas confined in magnetic devices has been studied for nearly forty years (see [1]). EC waves are widely used in practical applications, e.g., for plasma heating, controlling the current density profile, and as diagnostic tools. The three types of EC waves that can exist in a plasma are as follows: two types of electromagnetic waves with different polarizations [namely, an ordinary wave (the O-mode) and an extraordinary wave (the X-mode)] and a short-wavelength electrostatic Bernstein wave (the B-mode). The excitation and propagation of these waves in magnetically confined plasmas is governed primarily by the value of the dimensionless parameter $\omega_{pe}^2/\omega_{ce}^2$ (the squared ratio of the plasma frequency to the electron cyclotron frequency at the center of the chamber). This parameter determines the spatial position of the cutoff surfaces for electromagnetic waves. Until recently, the problem of the wave–plasma interaction was studied for application in devices with comparatively strong magnetic fields such that the condition $\omega_{pe}^2/\omega_{ce}^2 \sim 1$ holds in the central plasma regions. This indicates that the O-mode can propagate to the central region, where EC waves are usually damped, in which case the distance between the singular surfaces—the cutoff surface for O- and X-modes and the upper hybrid resonance (UHR) surface—is much larger than the wavelength λ_0 of the wave in a vacuum. These are the conditions under which full-scale experiments on ECR plasma heating in the T-10 tokamak [2] were performed.

However, interest in EC waves has recently been renewed in connection with their possible use in spherical tokamaks—devices with comparatively weak magnetic fields such that $\omega_{pe}^2/\omega_{ce}^2 \gg 1$. In spherical tokamaks, the O- and X-modes can only propagate in a narrow peripheral region of the plasma, in which case the distance between the cutoff and UHR surfaces is much smaller than λ_0 and they are very close to the plasma boundary. On the other hand, the X-mode launched from the side of the weaker magnetic field converts easily into a B-mode in the UHR region (the so-called X–B conversion), and the O-mode near its cutoff surface can efficiently exchange energy with the X-mode, which then converts into a B-mode (the O–X–B conversion). The heating scenario based on these two mechanisms for the peripheral conversion of the O- and X-modes into a B-mode, which then propagates toward the region of denser plasma and is damped there, was proposed in [3, 4] for the small aspect ratio NSTX tokamak.

In this paper, we present the results from modeling the excitation of Bernstein modes for plasma heating in the Globus-M spherical tokamak [5], which has recently been constructed at the Ioffe Physicotechnical Institute. The tokamak parameters are as follows: R_0 = 36 cm, a_0 = 24 cm, $B_{0\text{vac}}$ = 0.3–0.5 T, $n_0 \le 5 \times 10^3$ cm^{-3}, T_{e0} = 500 eV, and T_{eb} = 20 eV. Inside the separatrix, we adopted a flattened electron density profile, characteristic of spherical tokamaks: $n_e = (n_{e0} - n_{eb})(1 - (r/a_0)^6) + n_{eb}$. Outside the separatrix, the electron density was assumed to decrease exponentially. The frequency was chosen to be 14 GHz, so that the ECR region was near the chamber axis, in which case Bernstein modes were damped in the central plasma region. In Fig. 1a, we plot the locations of the ECR surface (solid line) and the cutoff surfaces for the X- and O-modes (dashed line) in the minor cross section of the torus. The plots in Fig. 1 were calculated for the following discharge parameters: I_{pl} = 330 kA, $B_{0\text{vac}}$ = 0.4 T (the paramagnetic correction being $B_{0\text{par}}$ = 0.18 T), $n_{e0} = 5 \times 10^{13}$ cm^{-3}, and $n_{eb} = 2 \times 10^{12}$ cm^{-3}, so that $\omega_{pe}^2/\omega_{ce}^2 = 15$. The origin of the coordinates is located at the geometric center of

1063-780X/01/2702-0129$21.00 © 2001 MAIK "Nauka/Interperiodica"

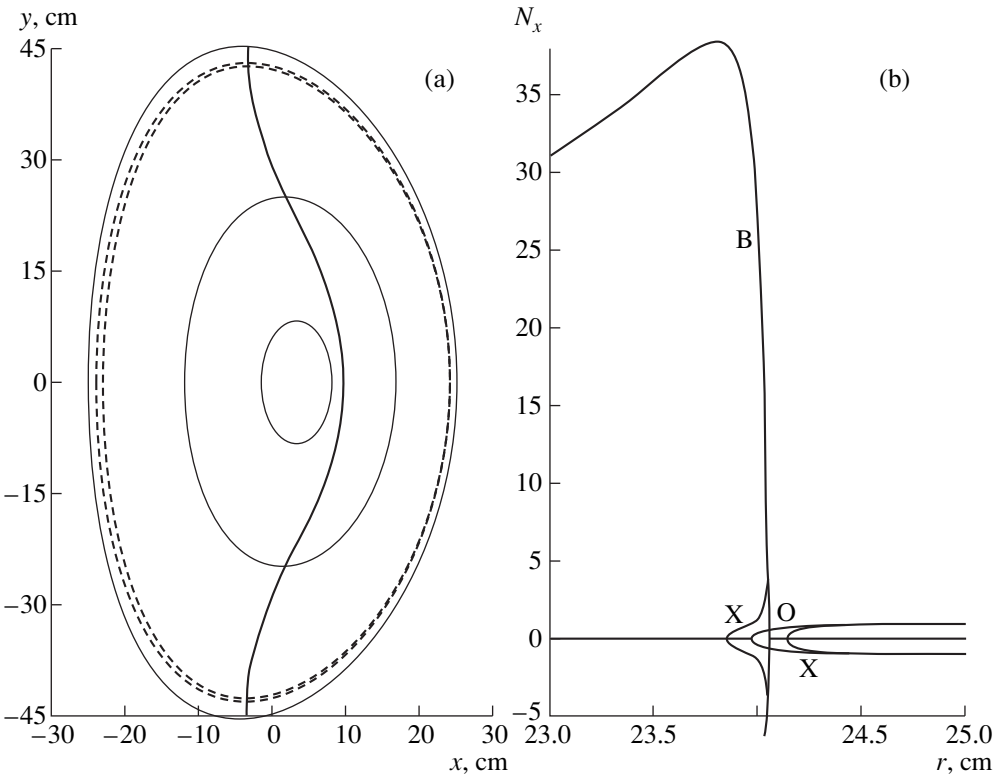

Fig. 1. (a) Locations of the ECR surface (solid line) and cutoff surfaces (dashed lines) in the minor cross section of the torus and (b) dispersion curves for the ordinary (O-mode), extraordinary (X-mode), and Bernstein (B-mode) waves in the peripheral plasma slab.

the transverse cross section of the chamber. The UHR surface, which lies between the cutoff surfaces is not plotted in Fig. 1a. More detailed information on the locations of the singular surfaces at the plasma periphery in the equatorial plane is given in Fig. 1b, which shows the dispersion curves for all of the modes in the case of normal incidence of the wave on the plasma surface. We emphasize that, since the spatial scale on which the plasma parameters vary is much shorter than λ_0, the Wentzel–Kramers–Brillouin (WKB) approximation fails to describe the case under investigation ($\omega_{pe}^2/\omega_{ce}^2 \gg 1$). For this reason, the dispersion curves, which can only be obtained in the WKB approximation, serve merely for illustration; nevertheless, they make it possible to describe the overall physical picture of the process qualitatively. Specifically, the X-mode easily overcomes a narrow (in comparison with the vacuum wavelength $\lambda_0 \approx 2$ cm) evanescence region, which occurs between the first cutoff surface and the UHR surface, and converts efficiently into the B-mode, which penetrates farther into the plasma provided that the condition $\omega < 2\omega_{ce}$ holds in the UHR region. Additionally, since the cutoff surfaces for the O- and X-modes are very close to one another, the O-mode is effectively coupled to the X-mode, thereby ensuring the subsequent conversion of the X-mode into a B-mode (the O–X–B conversion). It is important to note that, as the wave at the second harmonic of the electron cyclotron frequency enters the plasma, the Bernstein wave starts to propagate toward the chamber wall, in which case the proposed heating scenario becomes inapplicable.

In order to estimate the wave conversion efficiency, we constructed a model of a plane monochromatic wave incident obliquely from a vacuum onto a plane peripheral plasma slab that includes all of the singular surfaces for the incident wave; the electron density profile is assumed to be linear. The problem was solved in two steps. In the first step, we established the relationships between the components of the electric and magnetic fields of the incident wave at the plasma surface; i.e., we determined the surface impedance matrix by solving the wave equation for a one-dimensional plane inhomogeneous plasma slab. We assumed that the plasma parameters vary along the *x*-axis, which is perpendicular to the plasma surface, the *z*-axis being aligned with a constant magnetic field, which is parallel to the plasma surface. We solved the wave equation assuming that the spatial dispersion is weak (the "warm" plasma approximation) and retaining up to second order terms in the small parameter $\kappa\rho_L$, where κ is the wave vector and ρ_L is the electron gyroradius. This approach made it possible to describe the fundamental

and second cyclotron modes of the electron Bernstein wave. The plasma density variations were assumed to be small enough for the plasma particles to obey the local Maxwellian distribution [6]. At the inner boundary of the plasma slab, we imposed the radiation conditions toward the free half-space.

In the second step, we modeled the propagation of a plane wave in vacuum, using the calculated surface impedance matrix as the boundary condition. In order to calculate the reflection coefficient R defined as the ratio of the power reflected from the plasma slab to the incident power, we separately considered the longitudinally and transversely polarized waves (i.e., the waves that are polarized parallel and perpendicular to the magnetic field) incident from the vacuum at all possible angles. Note that, in a plasma, a wave with longitudinal or transverse polarization, being incident at a nonzero angle, converts into O- and X-modes, so that we generally should take into account both of the conversion mechanisms, X–B and O–X–B. We found that optimum ranges of incidence angles exist in which the reflection coefficient R is the smallest. Figure 2a shows the reflection coefficient R calculated as a function of the refractive index N_z (at $N_y = 0$) in the case of an obliquely incident, longitudinally polarized wave for different density gradients in a plasma slab: (*1*) 0.2×10^{12}, (*2*) 1.2×10^{12}, (*3*) 2×10^{12}, (*4*) 3.2×10^{12}, and (*5*) 10^{13} cm^{-4}. The values of the incidence angle that were calculated for the corresponding values of N_z are plotted on the additional horizontal axis under the frame in Fig. 2a. Figure 2b displays the dispersion curves for the O- and X-modes, calculated at $N_{zopt} = 0.66$ (which corresponds to curve *1* in Fig. 2a). We can see that the dispersion curves gradually merge, reflecting a strong coupling between the O- and X-modes. This explains why the efficiency with which the Bernstein wave is excited increases considerably. In connection with tokamaks, Preinhaelter and Kopecky [7] were the first to point out the existence of the optimum incidence angle. However, this was actually revealed earlier in ionospheric experiments aimed at investigating the effect of the reflected-signal tripling (the so-called "radio window" effect) [8].

Figure 3 shows the reflection coefficient calculated as a function of N_y (at $N_z = 0$) in the case of an obliquely incident, transversely polarized wave for different density gradients: (*1*) 0.4×10^{12}, (*2*) 2×10^{12}, (*3*) 3.2×10^{12}, (*4*) 6×10^{12}, and (*5*) 16×10^{12} cm^{-4}. The asymmetry of the curves with respect to the sign of N_y cannot be explained in the context of the WKB approximation [9]. In Fig. 4, the solid curves present the reflection coefficients calculated with the reference parameter values (see Fig. 1) in the plane of the parameters (N_z, N_y) for both longitudinally and transversely polarized waves. The dashed curves (semicircles) are drawn through the points corresponding to the incidence angles 20°, 40°, 60°, and 80°. One can see the regions of the optimum incidence angles (for which the reflection coefficient is the smallest). This situation is typical of a fairly broad range of experimental parameters.

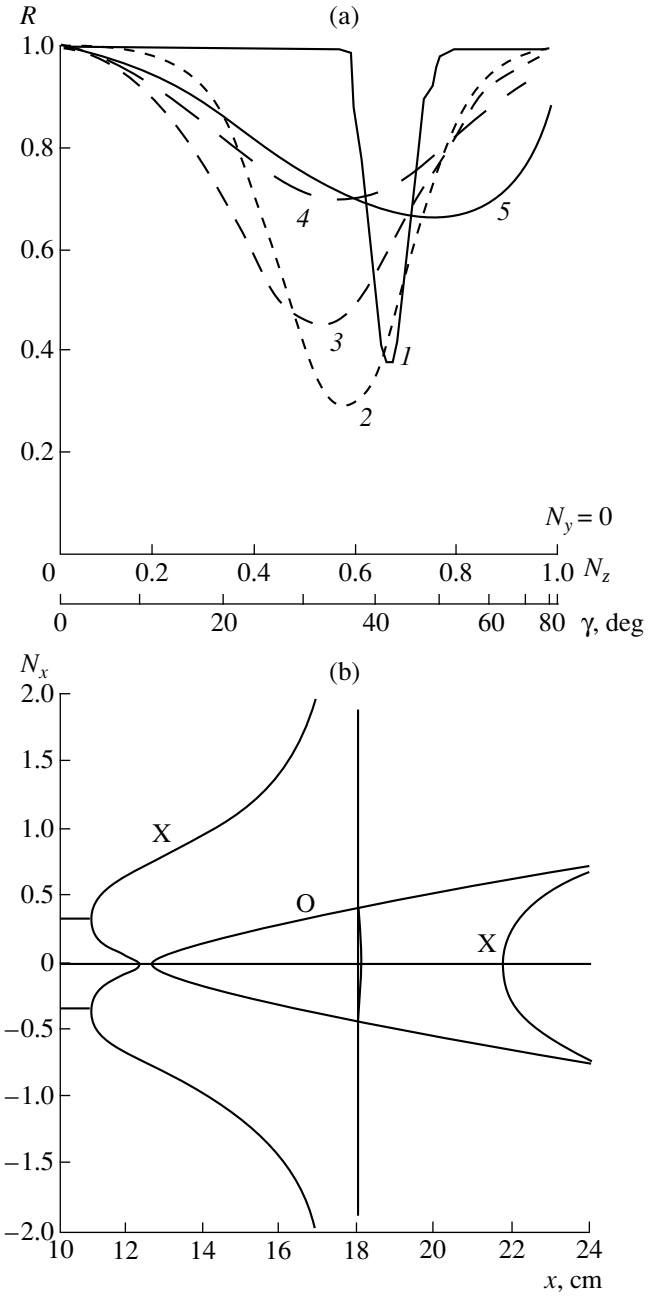

Fig. 2. (a) Reflection coefficient for a longitudinally polarized wave vs. the incidence angle γ (or, equivalently, the refractive index N_z) for different plasma density gradients: (*1*) 0.2×10^{12}, (*2*) 1.2×10^{12}, (*3*) 2×10^{12}, (*4*) 3.2×10^{12}, and (*5*) 10^{13} cm^{-4} and (b) dispersion curves for the case represented by curve *1* and for $N_z = 0.66$.

We also calculated the effective coupling impedance between the plasma and the antennas emitting waves with different polarizations. For this purpose, the incidence of waves in a certain spectral range on a plasma

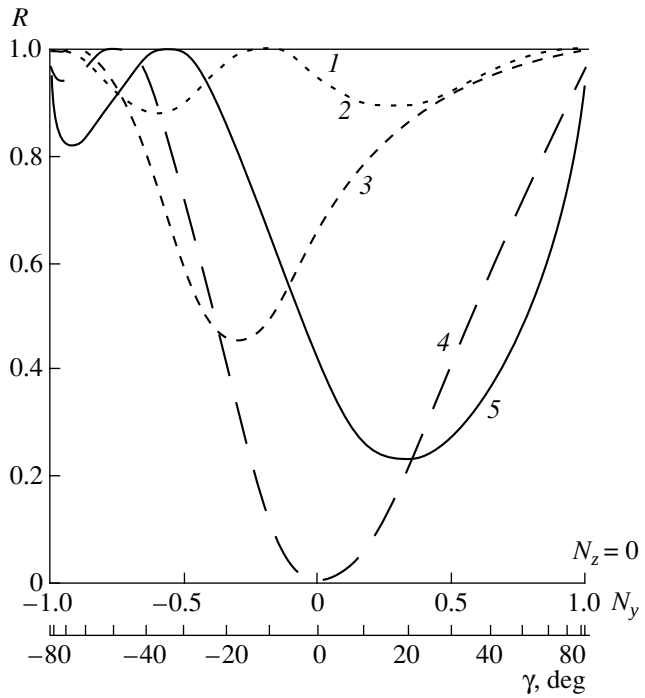

Fig. 3. Reflection coefficient for a transversely polarized wave vs. the incidence angle (or, equivalently, the refractive index N_y) for different plasma density gradients: (*1*) 0.4×10^{12}, (*2*) 2×10^{12}, (*3*) 3.2×10^{12}, (*4*) 6×10^{12}, and (*5*) 16×10^{12} cm^{-4}.

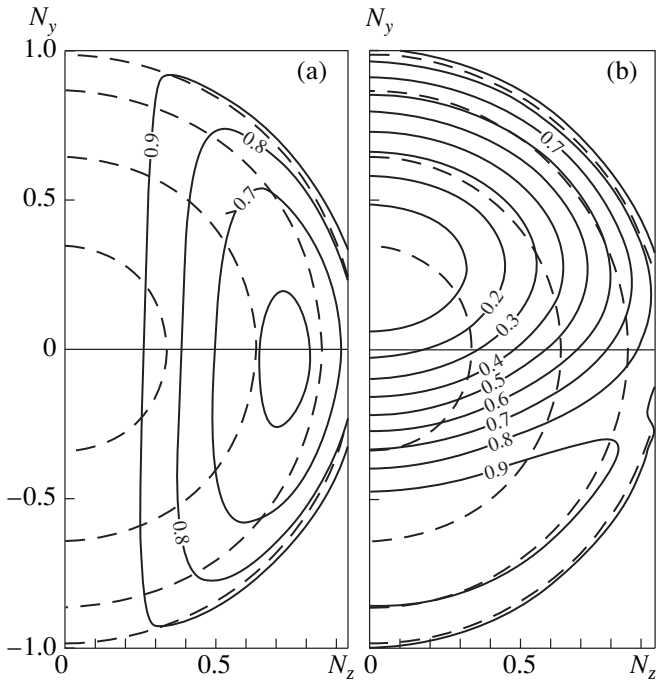

Fig. 4. Two-dimensional plots of the reflection coefficient calculated with the reference parameter values for (a) longitudinally and (b) transversely polarized waves.

slab was modeled with the GRILL3D code [10], which is capable of calculating the spectrum of waves emitted from a waveguide antenna and the coefficient of their reflection from the slab. The impedance matrix, which contains complete information on the processes occurring in the plasma, served to impose the boundary conditions for the code. We analyzed two types of waveguide antennas: (i) a two-waveguide antenna imitating a small-size horn antenna with a wide directional diagram (the waves emitted from the waveguides are inphase) and (ii) a multiwaveguide grill emitting a wave beam with a small divergence in the direction corresponding to the smallest reflection coefficient. The first antenna, which was capable of exciting waves with different polarizations, could be rotated about its axis. Figure 5 illustrates the total reflection coefficient of the slab for waves emitted from the two-waveguide antenna versus the angle of rotation α (the angle between the magnetic field and the wider wall of the waveguide) for three electron densities: n_{e0} = (*1*) 5×10^{12}, (*2*) 10^{13}, and (*3*) 5×10^{13} cm^{-3}. For $\alpha = 90°$, the reflection coefficient is seen to be less than 20% over the entire density range under consideration. For a high electron density, the reflection coefficient is small for all of the angles of rotation. Figure 6 depicts the spectra of waves excited in a plasma with the density $n_{e0} = 5 \times 10^{13}$ cm^{-3} (in the half-space $N_z \geq 0$) by waves emitted from the two-waveguide antenna for $\alpha = 0°$ and $\alpha = 90°$.

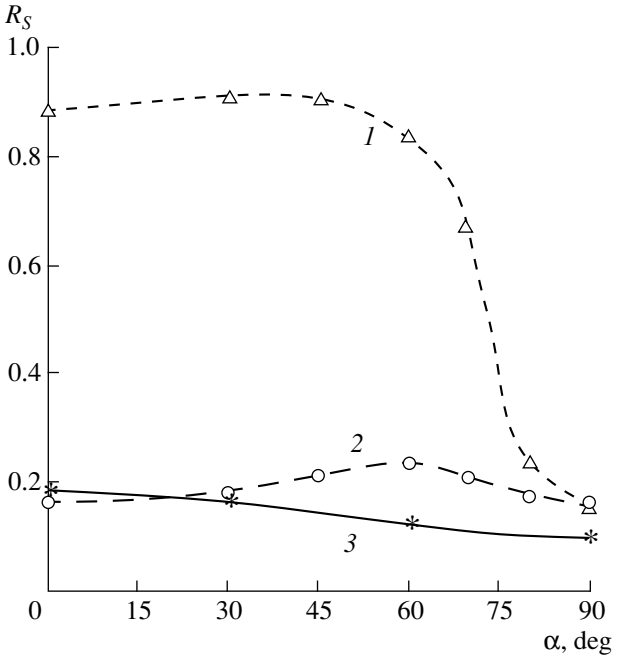

Fig. 5. Total reflection coefficient for waves from a two-waveguide antenna vs. the angle of rotation α for different electron densities at the plasma center: (*1*) 5×10^{12}, (*2*) 10^{13}, and (*3*) 5×10^{13} cm^{-3}.

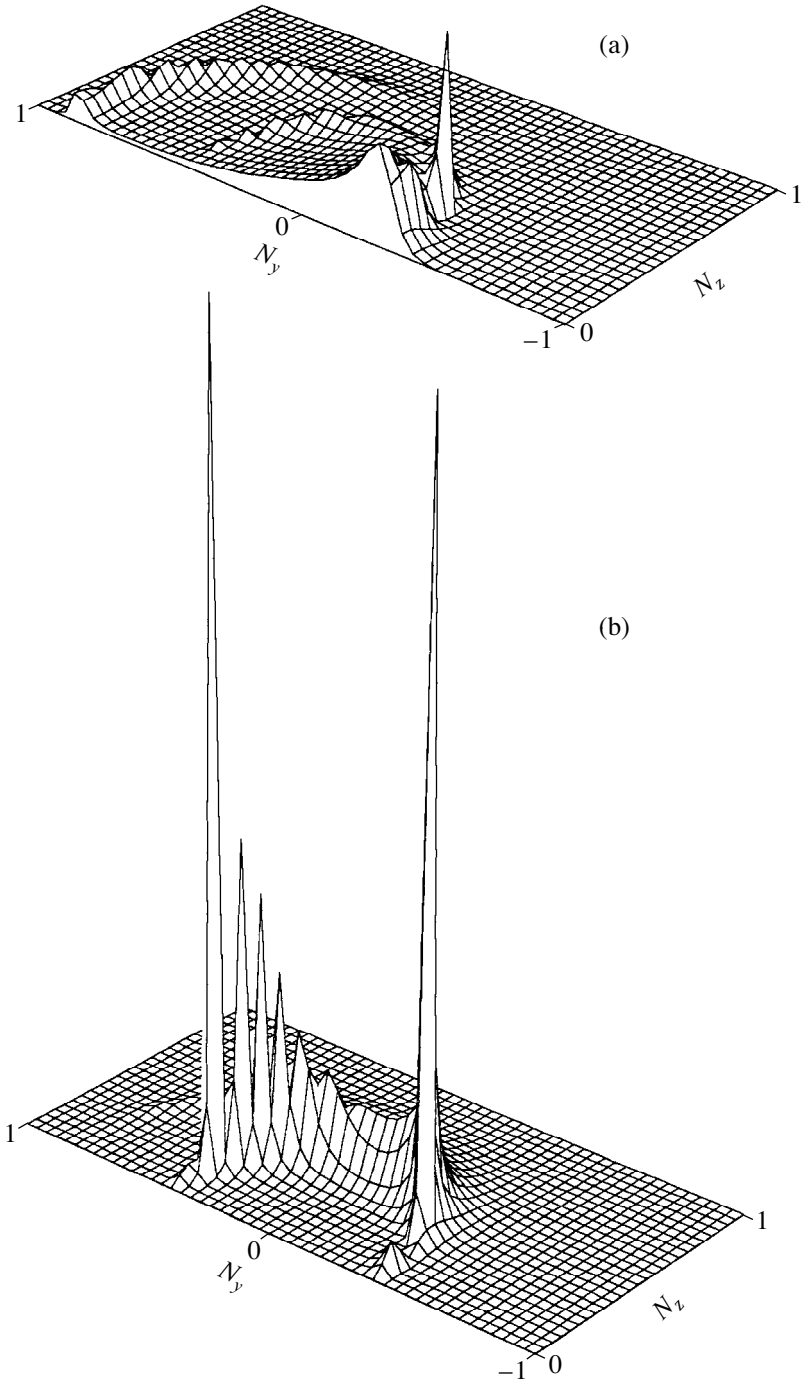

Fig. 6. Spectra of the waves excited in a plasma by the waves emitted from a two-waveguide antenna for different angles of rotation: α = (a) 0° and (b) 90°.

Numerous resonance peaks in the spectra are attributed to the fact that the electromagnetic waves are partially reflected from the cutoff surfaces.

As an example, Figs. 7b and 7c illustrate the results obtained by analyzing the structures of the electric fields and power fluxes for the Fourier harmonic with N_y = –0.32 and N_z = 0.32, which corresponds to the highest peak in the spectrum of waves emitted by the two-waveguide antenna for α = 90°. Figure 7a shows the corresponding dispersion curves, which determine the locations of singular surfaces. We can see that the short-wavelength field component E_x, generated in plasma after the passage of the emitted wave through

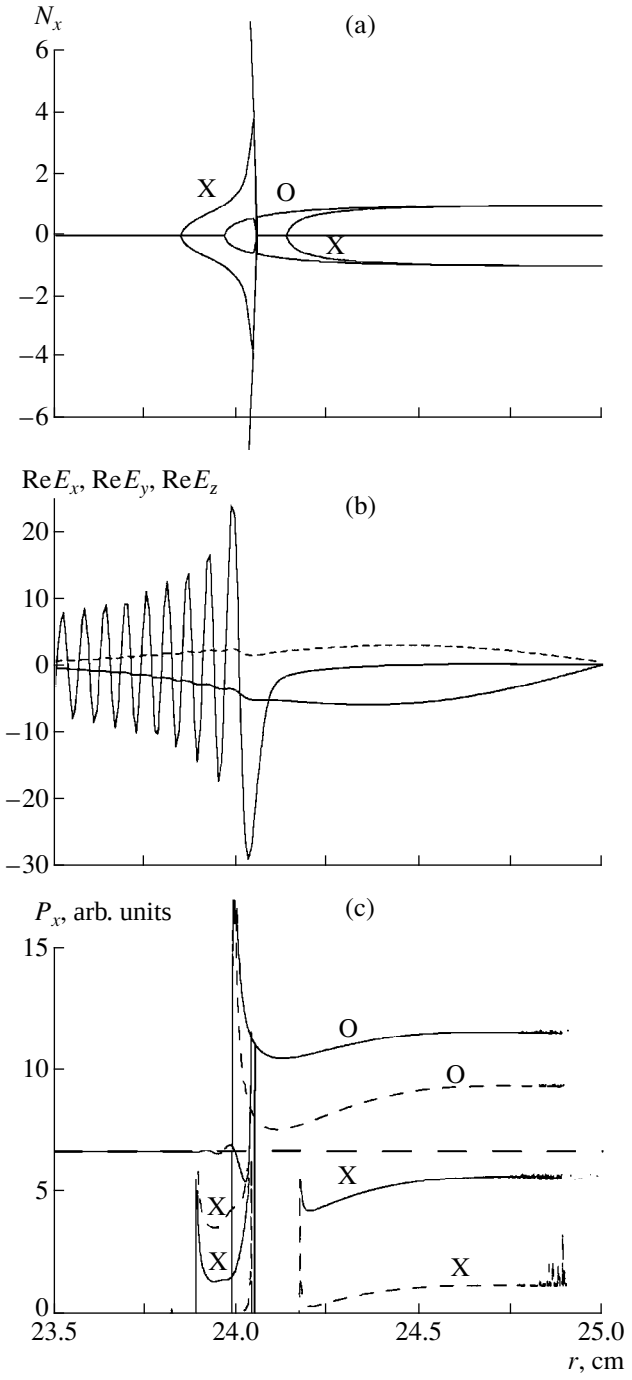

Fig. 7. (a) Dispersion curves, (b) electric fields, and (c) partial power fluxes for the Fourier harmonic with $N_y = -0.32$ and $N_z = 0.32$ in the wave spectrum shown in Fig. 6b.

the UHR surface, corresponds to the Bernstein wave, which is excited in the UHR region. The long-wavelength field components E_y and E_z correspond to electromagnetic waves and obey the spatial distributions characteristic of resonators.

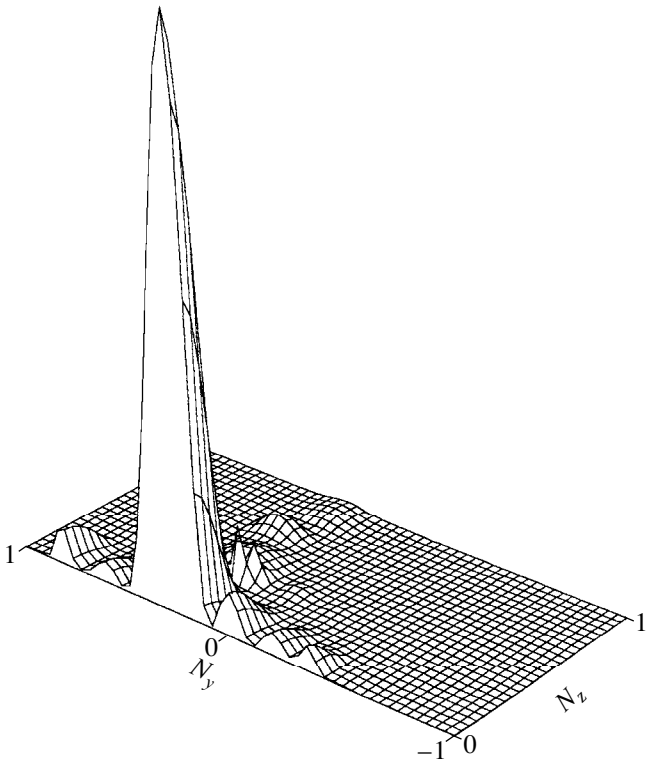

Fig. 8. Spectrum of the waves emitted by a grill composed of four waveguide arrays, with 4×12 waveguides in each (the angle of rotation being $\alpha = 0°$).

We have also attempted to describe the total electric field in the WKB approximation as the superposition of the partial fields corresponding to the forward and backward O-, X-, and B-modes. To do this, we formally regarded the dispersion relation corresponding to the "warm" wave equation at each spatial point. Solving this equation in the WKB approximation, we found the refractive indices and polarizations of the partial waves. Then, we used these parameters to calculate the fields of these waves and the related partial power fluxes. Figure 7c shows the forward (solid curves) and backward (dashed curves) power fluxes for each of these partial waves. Although this approach is not quite correct (especially near the singular surfaces, where the obtained power fluxes are far from being monotonic), it is very illustrative and may be helpful in analyzing the processes under discussion. Thus, we can see that, behind the UHR region, the O-mode is partially reflected from its cutoff surface and exchanges energy with the X-mode, which in turn partially converts into a Bernstein wave. Simultaneously, the X-mode emitted by the antenna overcomes the evanescence barrier and also exchanges energy with the Bernstein wave. The flux density of the input power, calculated from the total field (large dashes), remains almost constant across the entire plasma slab (because the absorption inside the slab is insignificant) and is equal to the flux density of the outgoing Bernstein wave.

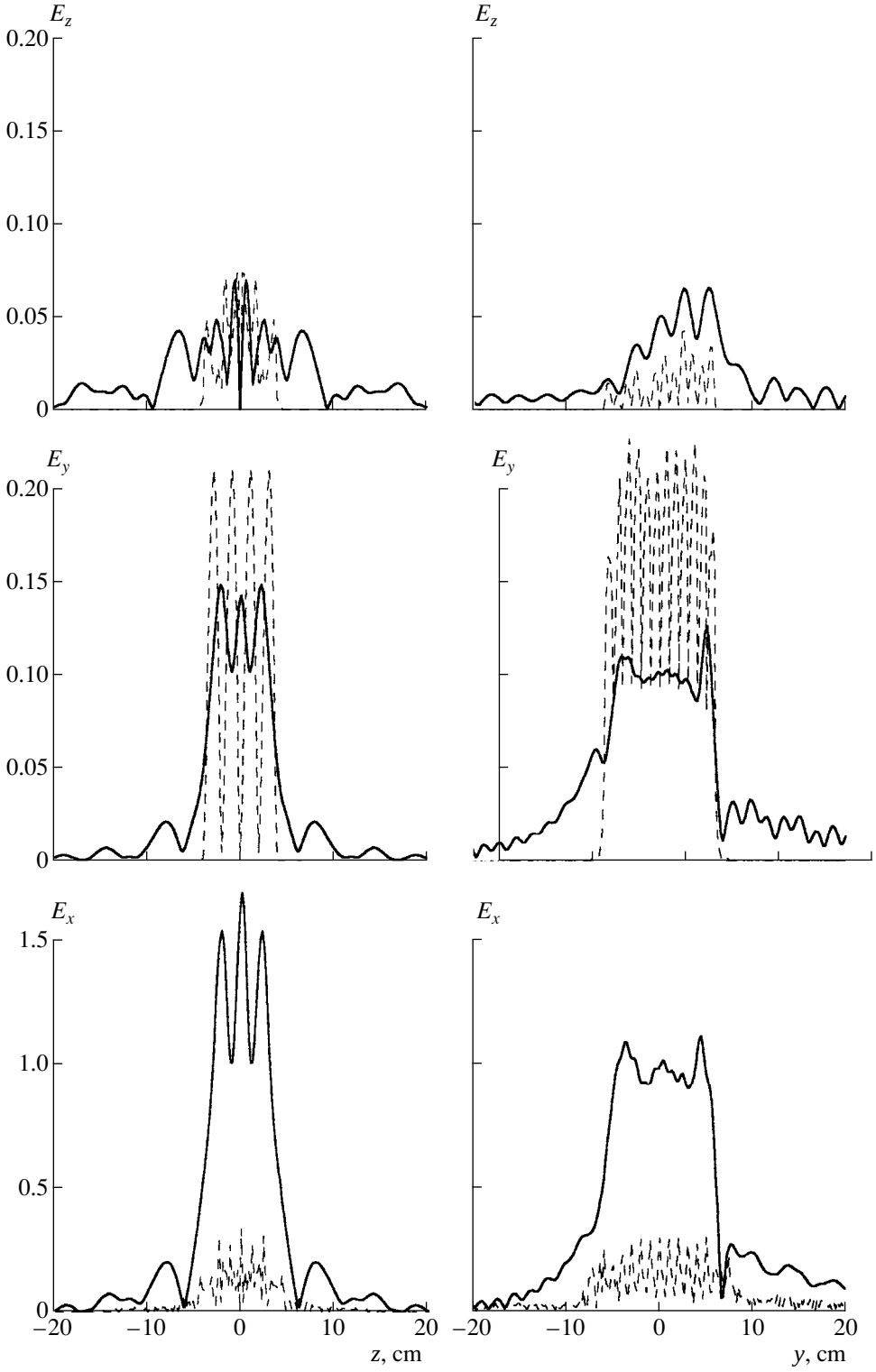

Fig. 9. Spatial distributions of the total field excited by a 4×12 grill at the plasma surface (solid curves) and inside the UHR region (dashed curves).

The situation with a multiwaveguide grill capable of emitting radiation with a small divergence is somewhat different. Figure 8 shows the spectrum of waves emitted from a grill composed of four waveguide arrays, with 12 waveguides in each. The wider walls of the waveguides are oriented along the magnetic field, the phase shift between the waves emitted from the neighboring waveguides being 45°. One can see that the grill

emits an almost monochromatic wave corresponding to the spectral "window" shown in Fig. 4b. The total reflection coefficient in this case is less than 4% (cf. 10–20% in the case of a two-waveguide antenna), the field structure is nonresonant, and the efficiency of the excitation of Bernstein waves is high. Note that, for practical purposes, it might be expedient to use a 2×8 grill (or smaller) or even an appropriately oriented horn antenna inclined at the required angle. Figure 9 illustrates how the spatial distribution of the wave fields changes as the wave propagates deeper into the plasma (the spatial profiles were calculated by summing up all of the excited partial fields). The dashed curves are for the field distributions at the plasma surface, and the solid curves are for the field distributions inside the UHR region. The origin of the coordinates is located at the geometric center of the grill. We can see that the electric field of a well-focused incident wave beam spreads out only slightly as the beam propagates through the plasma. This allows us to conclude that the efficiency of a single-pass conversion of the fast wave into a Bernstein wave is high.

Our calculations encourage the hope that EC waves can be effectively launched into the plasmas of spherical tokamaks. In order to gain insights into the further propagation of the Bernstein wave and to determine the place where it should be absorbed, it is necessary to carry out more detailed studies based on the ray tracing method.

ACKNOWLEDGMENTS

We are grateful to A.D. Piliya for his continuing interest in this work and useful discussion of the results.

REFERENCES

1. V. E. Golant and V. I. Fedorov, *High-Frequency Methods of Plasma Heating in Toroidal Thermonuclear Facilities* (Énergoatomizdat, Moscow, 1986).
2. V. V. Alikaev, A. A. Bagdasarov, *et al.*, Fiz. Plazmy **13**, 3 (1987) [Sov. J. Plasma Phys. **13**, 1 (1987)].
3. A. Bers, A. K. Ram, and S. D. Schultz, in *Proceedings of the 2nd European RF Conference, Brussels, 1998*, p. 237.
4. M. D. Carter, T. S. Bigelow, and D. B. Batchelor, in *Proceedings of the 13th RF Conference, Annapolis, 1999*, p. 407.
5. V. K. Gusev, V. E. Golant, E. Z. Gusakov, *et al.*, Zh. Tekh. Fiz. **69** (8), 58 (1999) [Tech. Phys. **44**, 1054 (1999)].
6. M. A. Irzak, E. N. Tregubova, and O. N. Shcherbinin, Fiz. Plazmy **25**, 659 (1999) [Plasma Phys. Rep. **25**, 601 (1999)].
7. J. Preinhaelter and V. Kopecky, J. Plasma Phys. **10**, 1 (1973).
8. V. L. Ginzburg, *The Propagation of Electromagnetic Waves in Plasmas* (Nauka, Moscow, 1960; Pergamon, Oxford, 1970).
9. A. R. Esterkin, E. Z. Gusakov, M. A. Irzak, and A. D. Piliya, in *Proceedings of the 22nd EPS Conference on Controlled Fusion and Plasma Physics, Bournemouth, 1995* [ECA **19C** (4), 389 (1995)].
10. M. A. Irzak and O. N. Shcherbinin, Nucl. Fusion **35**, 1341 (1995).

Translated by O.E. Khadin

Plasma Physics Reports, Vol. 27, No. 2, 2001, pp. 137–142. Translated from Fizika Plazmy, Vol. 27, No. 2, 2001, pp. 149–154.
Original Russian Text Copyright © 2001 by Kostrov, Strikovskiy, Shashurin.

PLASMA OSCILLATIONS AND WAVES

Plasma Turbulence near the Lower Hybrid Resonance

A. V. Kostrov, A. V. Strikovskiy, and A. V. Shashurin

Institute of Applied Physics, Russian Academy of Sciences, ul. Ul'yanova 46, Nizhni Novgorod, 603600 Russia

Received March 13, 2000; in final form, July 19, 2000

Abstract—Plasma turbulence at frequencies near the lower hybrid resonance is studied experimentally with the KROT device. Nonlinear effects during the interaction of intense lower hybrid waves with a magnetoactive plasma are investigated, with the focus on the formation and evolution of nonlinear plasma structures (cavitons). Macroscopic consequences of plasma turbulence are considered, including nonlinear plasma heating, particle acceleration, and its effect on transport processes. © *2001 MAIK "Nauka/Interperiodica".*

1. INTRODUCTION

At present, interest in the problem of strong plasma turbulence in the frequency range near the lower hybrid (LH) resonance frequency stems from the widely accepted view that LH waves play an important role in many geophysical and astrophysical processes. In particular, the generation of flows of accelerated particles observed in the Earth's ionosphere and magnetosphere is attributed to the development of turbulence [1, 2]. One the most interesting effects of LH turbulence is the appearance of cavitons (regions with a reduced plasma density in which intense LH oscillations are trapped) and their subsequent collapse resulting in flows of accelerated particles.

Since the theoretical model [3] describing LH turbulence and collapse is fairly complicated (in particular, because the equations are, in principle, non-one-dimensional), almost all of the investigations in this field involve numerical simulations. In [4, 5], the possibility of the collapse of plasma waves trapped in collapsing cavities extended along the external magnetic field was demonstrated.

Experimental studies [6–9] of plasma turbulence in the LH frequency range have usually been carried out under the condition $\omega_{He} \gg \omega_{pe}$ (where ω_{pe} is the plasma electron frequency and ω_{He} is the electron gyrofrequency), which corresponds to the parameters of a thermonuclear plasma. These studies were focused on weak-turbulence effects caused by the parametric decay of quasipotential waves and subsequent electron heating. A few laboratory experiments [10–12] aimed at investigating strong turbulence obviously cannot clarify the mechanism for the onset of the modulational instability in the LH resonance region, although the theoretically predicted threshold for this instability is very low in comparison with the case of Langmuir collapse in an isotropic plasma.

In this paper, we present the results of an experimental study of the excitation of intense LH waves and their interaction with a magnetoactive plasma under the condition $\omega_{pe} \gg \omega_{He}$ (in this case, the LH resonance frequency is equal to $\omega_{LH} = \sqrt{\omega_{Hi}\omega_{He}}$, where ω_{He} and ω_{Hi} are the electron and ion gyrofrequencies, respectively). This condition corresponds to the parameters of the Earth's ionosphere and magnetosphere. The experiments were carried out in the unique large-sized KROT device. Particular attention is drawn to the time evolution of nonlinear plasma structures and macroscopic consequences of plasma turbulence, such as particle acceleration and fast plasma thermodiffusion.

2. EXPERIMENTAL DEVICE AND DIAGNOSTIC TECHNIQUES

The experimental device is a large vacuum chamber 3 m in diameter and 10 m in length. A plasma was created by an RF pulsed discharge ($f = 5$ MHz, $\tau_p \approx 1.6$ ms) in argon at a pressure of 5×10^{-4} torr. The magnetic field was created by a solenoid 3.5 m in length and 1.5 m in diameter positioned inside the chamber. The field produced by the solenoid had a magnetic-mirror configuration with a mirror ratio of about 2.3. The experiments were carried out in the plasma-decay regime. The plasma decay was governed by ambipolar diffusion along the magnetic field with a characteristic time on the order of 10 ms.

An RF voltage pulse ($f_{pump} \approx 3$ MHz, $\tau \approx 1$ ms) was applied to a frame antenna of radius 10 cm positioned in the center of the magnetic confinement system. During the action of the pump field, the inequality $\left(\frac{\omega_{pe}}{\omega_{He}}\right)^2 \gg 1$ was satisfied in the chamber and, consequently, the LH resonance frequency was independent of the plasma density and only depended on the magnetic field: $\omega_{LH} = \sqrt{\omega_{Hi}\omega_{He}}$.

For the operating plasma parameters, the condition $\omega_{pump} = \omega_{LH}$ was fulfilled inside the confinement system at a distance of ~1 m from the emitting frame. It was this region in which most of the diagnostic detectors

The main plasma parameters in the KROT device

Physical quantity	Value
N_e, cm^{-3}	5×10^{10}
$T_e = T_i$, eV	1
$\sqrt{M/m}$	250
r_{He}, cm	1.5×10^{-2}
r_{Hi}, cm	3
ν_{em}, s^{-1}	7×10^4
ν_{im}, s^{-1}	10^4
ν_{ei}, s^{-1}	1.5×10^6
$\beta = \dfrac{8\pi NT}{H^2}$	3×10^{-5}

were installed. The magnetic field was $H \approx 260$ Oe, and the unperturbed value of the plasma density was $N \approx 5 \times 10^{10}$ cm^{-3}. The maximum voltage at the exciting antenna was 600 V. Under our experimental conditions, the initial ion and electron temperatures were equal to 1 eV. The main plasma parameters achieved in the experiment are presented in the table.

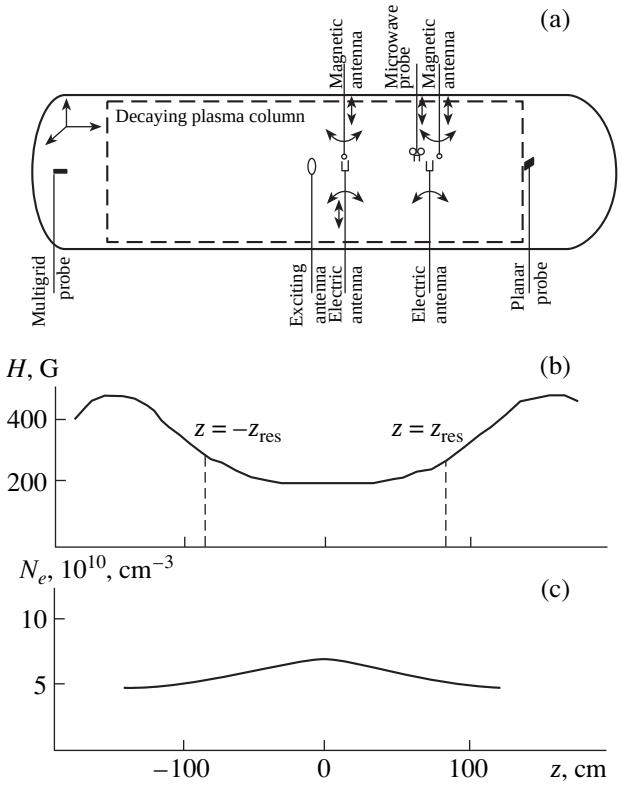

Fig. 1. Schematic of the KROT device: (a) arrangement of diagnostic detectors, (b) magnetic field profile, and (c) plasma-density distribution at the instant of switching on the RF pumping.

The experimental layout is shown in Fig. 1. To measure RF fields in the plasma, we used conventional electric and shielded magnetic antennas about 1 cm in diameter, which could be moved in the radial direction. The antennas were covered by an insulating film to prevent the plasma from having an influence on their input impedance. The flows of accelerated electrons were measured with a flat probe.

To diagnose the density fluctuation in a turbulent plasma, we used a compact microwave probe [13], which was a resonance system whose eigenfrequency depended on the plasma permittivity. The sensitivity of this technique to density perturbations was on the order of 1%. Small dimensions of the probe permitted local plasma-density measurements. This resonance technique is free of many of the disadvantages typical of similar measurements with the help of conventional Langmuir probes, such as the detection of intense RF oscillations in the double layer and their influence on the *I–V* characteristic of the probe [14]. Figure 2 shows the time behavior of the density during plasma decay and typical signals obtained with the resonance microwave probe.

In these experiments, the microwave probe was also used to detect potential LH oscillations excited in the plasma. The measurements were possible because the probe was a sensitive detector able to detect density fluctuations with frequencies satisfying the condition $\omega \ll \omega_{res}/Q$, where Q is the quality factor of the resonant system and ω_{res} is the probe resonance frequency in the plasma. The presence of potential oscillations in the plasma results in the modulation of the probe resonance curve at the frequency of these oscillations. If, when analyzing the oscillations, the operating point in the resonance curve is chosen to be in the region where the curve is the steepest, then the signal-modulation amplitude δA is related to the value of the density perturbation δn by the following relationship: $\delta A/A \approx Q/2(1 + \omega_0^2/\omega_{pe}^2)/(\delta n/n)$, where ω_0 is the probe resonance frequency in vacuum. Therefore, the amplitude of low-frequency modulation of the microwave-probe resonance curve can provide information about the amplitude and frequency spectrum of quasipotential waves excited in the plasma.

In the experiment, low-frequency density fluctuations were measured by a narrow-band receiver tuned to the frequency of these oscillations.

3. EXPERIMENTAL RESULTS

1. An analysis of signals from different detectors shows that the interaction of the pumping wave with the plasma at frequencies close to the LH resonance frequency is substantially nonlinear (Fig. 3). The threshold for the nonlinear interaction of the pumping wave

with the plasma corresponds to the inductor voltage $U_{pump} \approx 100$ V. For $U_{pump} > 400$ V, we observed the saturation of the amplitudes of the detector signals.

The most interesting results were obtained with a microwave probe at the inductor voltage $U_{pump} \approx 200$ V. In this case, the characteristic oscillations were observed on the microwave-probe resonance curve (Fig. 4), which pointed to the presence of the low-frequency modulation of the plasma density ($\delta n/n \geq 10\%$).

Figure 5 shows the radial profiles of the plasma density at a distance of 1 m from the inductor.[1] In the time evolution of density perturbations, we can distinguish two characteristic time intervals: the first 300 μs after the switching-on of the pumping pulse and $t \geq 500$ μs.

For the first 300 μs, we observed the formation of small-scale quasiperiodic structures (in the region $R < 10$ cm) with a characteristic density-modulation depth of 10–20% and a length of several centimeters. Further, the formed density cavities became blurred and, by the end of the pumping pulse, merged together to form a global minimum in the plasma density in the center of the plasma column ($R < 10$ cm) at $t \geq 500$ μs.

The quasiperiodic density modulation (Fig. 5c) with a characteristic period of $L \approx 3$ cm evidences the onset of the modulational instability of the excited LH waves in the plasma. The excitation of quasipotential LH waves was established by the modulation at a frequency of $f_{mod} = 3$ MHz of the high-frequency ($f = 8.3$ GHz) signal from the microwave probe. Thus, the experimental results show that the action of the pumping wave on the plasma results in the modulational instability of the excited LH waves. The characteristic transverse spatial scale length of the instability corresponds to $L \approx 3$ cm. However, further narrowing (collapse) of cavitons did not occur, but the density cavities broadened with time in the transverse direction. The condition of the pressure balance along the magnetic field $\delta n/n \approx (\omega_{pe}/\omega_{LH})^2|E_\parallel|^2/16\pi(T_e + T_i)$ allowed us to determine the longitudinal component of the electric field. This component was found to be on the order of $E_\parallel = 0.5$ V/cm (for $\delta n/n \approx 20\%$).

During caviton formation ($\tau \approx 100$ μs), the characteristic longitudinal size of cavitons reaches the value of $L_\parallel = V_s\tau \approx 20$ cm, where V_s is the ion acoustic velocity. In this case, during nonadiabatic flight (during one phase of the RF field) through such a caviton along the magnetic field, a thermal electron ($V_{Te} = 6 \times 10^7$ cm/s) can gain an energy on the order of 10 eV.

The measurements of the distribution function of accelerated electrons by a flat probe (Fig. 6) demonstrate the presence of fast electrons with characteristic energies of 20–30 eV, which agrees well with the above

[1] Note that the nonuniform radial profile of the plasma density in the absence of pumping is caused by the inductor shadow; i.e., it is caused by the depletion (recombination) of the plasma on the antenna surface ($R = 10$ cm).

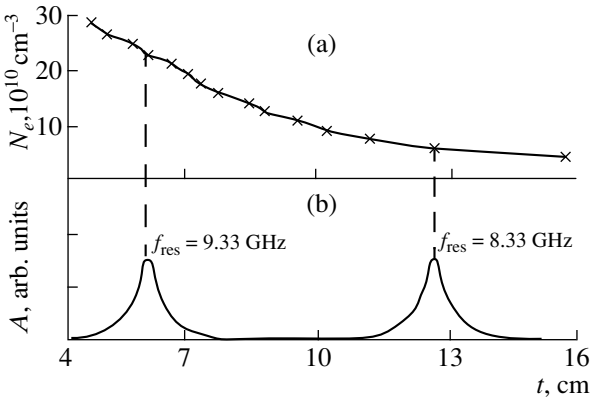

Fig. 2. (a) Decay of the plasma density and (b) typical signals from the resonance microwave probe for two values of the resonance frequency.

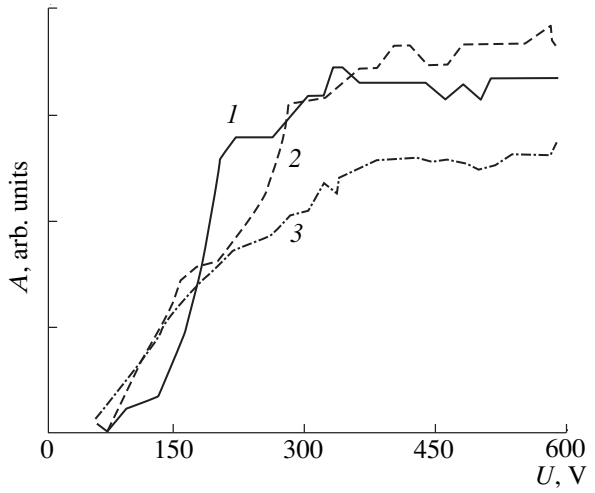

Fig. 3. Amplitudes of signals from different detectors vs. the exciting-antenna voltage: (*1*) amplitude of LH density fluctuations (microwave probe), (*2*) fast-electron current (multigrid probe), and (*3*) high-frequency magnetic-field oscillations (magnetic frame).

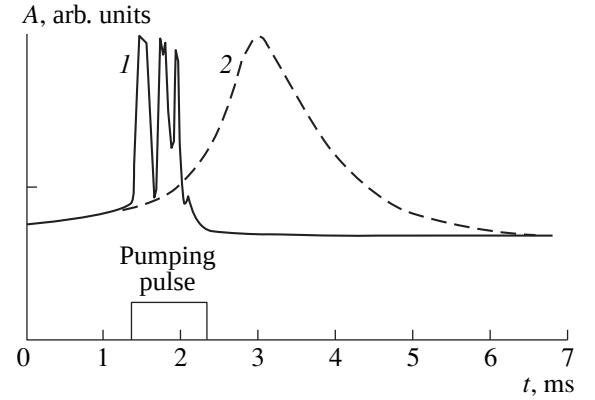

Fig. 4. Typical waveforms of signals from the microwave probe (*1*) with and (*2*) without RF pumping.

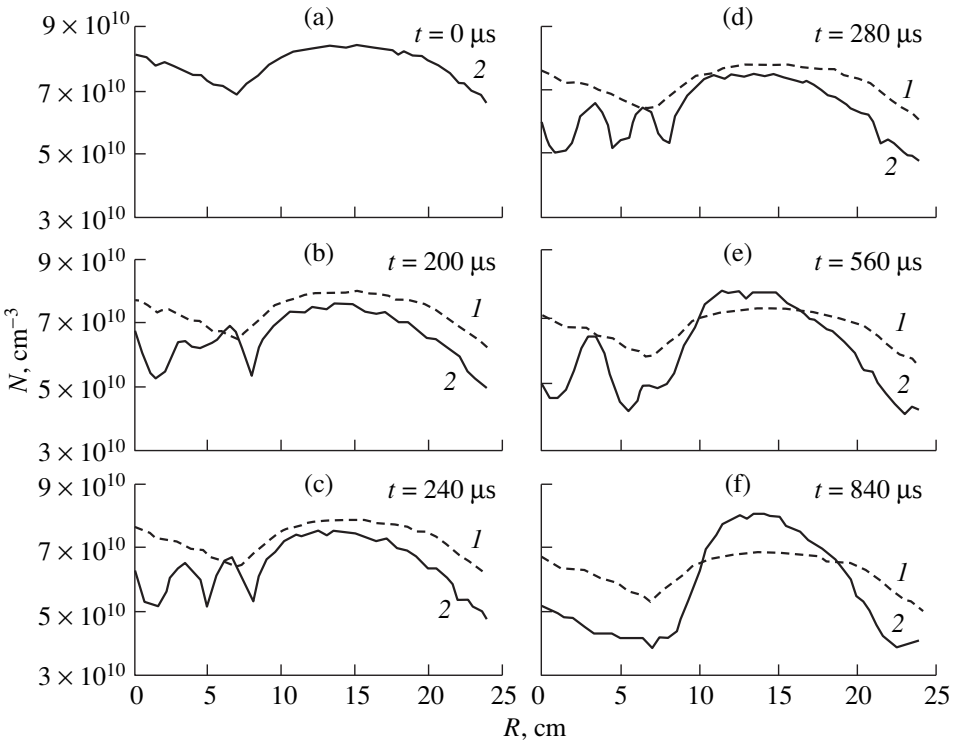

Fig. 5. Radial profiles of the plasma density at different instants (*1*) with and (*2*) without RF pumping.

estimate. Note that the decrease in the plasma density in the cavity correlates with the increase in the current of accelerated electrons along the magnetic field (Fig. 7).

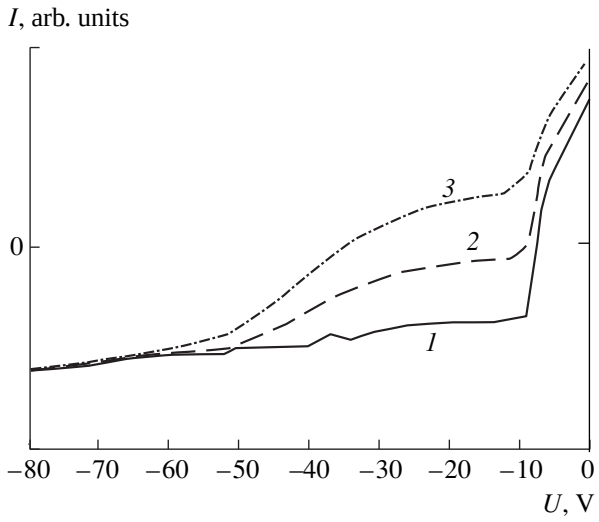

Fig. 6. *I–V* characteristic of the flat probe (the ion branch) at different instants after switching on the RF pumping: t = (*1*) 0, (*2*) 30, and (*3*) 40 μs. The appearance of current perturbations (for $|U| \sim 10$–40 V) corresponds to the appearance of the high-energy tail with a typical temperature of about 30 eV in the electron distribution function.

Hence, we have found that, for the first 300 μs after the switching-off of the pumping RF pulse, the onset of the modulation instability results in the formation of the density cavities (cavitons) in the plasma. However, the collapse of LH cavitons, predicted theoretically for a collisionless plasma, was not observed. Evidently, under our experimental conditions, the intense LH field trapped in cavitons results (in addition to striction effects) in the heating of the plasma electrons in the cavity. In this case, the thermal nonlinearity stabilizes the cavity collapse and then leads to the broadening and merging of the cavities (Figs. 5e, 5f).

We note that the experimental data obtained (Fig. 5) can be easily reproduced. Apparently, this is because the structure of the RF field was prescribed by a number of factors: the spatial distribution of the plasma density in the chamber, the geometry of an axially symmetric exciting antenna, etc. As a result, the onset of the modulational instability was accompanied by the formation of spatially ordered (according to the field structure) cavitons, rather than randomly oriented ones. The further development of the modulational instability, which, according to theoretical predictions, leads to the localization of energy in a great number of randomly oriented collapsing cavitons (i.e., to strong turbulence), was hampered by thermal nonlinearity. When the pump wave amplitude was increased to $U_{\text{pump}} = 600$ V, no cavities were observed, whereas, as early as 200 μs after the switching-on of the pumping, we observed a large-

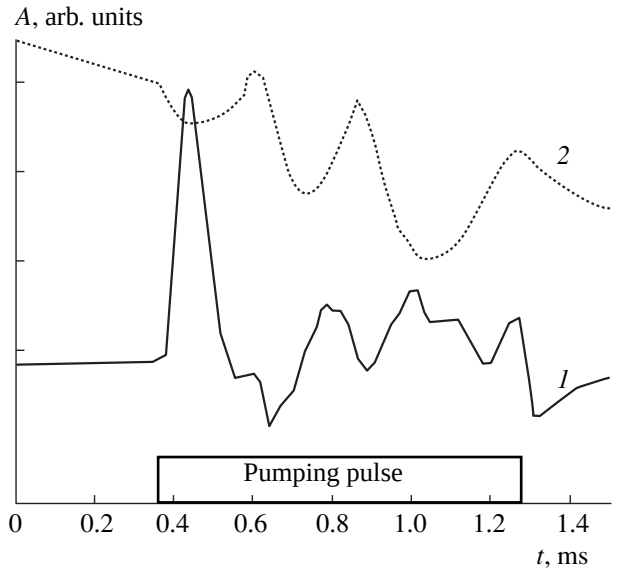

Fig. 7. Time correlation of signals from the detectors measuring (*1*) the fast-electron current and (*2*) plasma density.

scale (of the size of the exciting frame) depression in the plasma density.

2. The experimental data show that a significant transverse plasma loss occurs during periods on the order of 500 μs after the switching-on of the pumping RF pulse (Figs. 5e, 5f). Such a fast density redistribution cannot be explained by the transverse transport due to electron thermal diffusion, but it may attributed, as shown in [15, 16], to the unipolar plasma diffusion in the magnetic field. In this case, the electrons diffuse along the magnetic field and the ions diffuse across it, whereas the current circuit is closed through the background plasma. This results in the redistribution of the background plasma and in the appearance of regions with a reduced plasma density. The characteristic time of the density redistribution is determined by the longest time between those determined by the longitudinal electron and transverse ion unipolar diffusion.

Under our experimental conditions, the characteristic time of transverse ion diffusion substantially exceeds that of longitudinal electron diffusion. Hence, it is ions that govern the evolution of the system: $\tau_d = \tau_{i\perp} \approx L_\perp^2 \tau_{im}/r_{Hi}^2$, where τ_{im} is the ion–molecule collision time and r_{Hi} is the ion gyroradius. The characteristic time during which the plasma escapes from the central region of the chamber (R = 10–15 cm) is estimated to be on the order of 500 μs, which coincides with the experimentally observed value.

4. CONCLUSIONS

The study of the interaction of an intense RF field at a frequency near the LH resonance frequency with a magnetoactive plasma reveals the following:

(i) When the voltage amplitude at the exciting antenna increases to $U_{\text{pump}} \approx 100$ V, accelerated electrons appear in the plasma; the energies of these electrons exceed the initial thermal plasma energy by a factor of 20–30, which points to the nonlinear character of the interaction of the pumping wave with the plasma.

(ii) The interaction of the pumping wave with the plasma is accompanied by the onset of the modulational instability resulting in the formation of cavities—regions (seemingly, extended along the magnetic field) with a reduced plasma density ($\delta n/n \approx 20\%$), in which intense LH oscillations are trapped.

(iii) The appearance of electrons accelerated along the external magnetic field is related to the nonadiabatic energy gain in the longitudinal electric field of cavities ($\mathbf{E}_\parallel \parallel \mathbf{H}_0$, $E_\parallel = 0.5$ V/cm, and $L_\parallel \approx 20$ cm).

(iv) The collapse of LH cavitons, predicted theoretically for a collisionless plasma, is not observed. Under our experimental conditions, the intense LH cavity field results (in addition to striction effects) in the heating of the plasma in the cavities. In this case, the thermal nonlinearity stabilizes the collapse and leads to the broadening and merging of the cavities.

(v) The observed fast plasma thermodiffusion during electron heating is determined by the unipolar diffusion coefficients. The electrons diffuse along the magnetic field, the ions diffuse across it, and the current is closed through the background plasma.

ACKNOWLEDGMENTS

This work was supported in part by the Russian Foundation for Basic Research (project no. 98-02-17177) and the Russian Department of Science under the Program for Financing of Unique Devices (registration no. 01-18).

REFERENCES

1. T. Chang and B. Coppi, Geophys. Res. Lett. **8**, 1253 (1981).
2. J. La Belle, P. M. Kintner, A. W. Yau, and B. A. Whalen, J. Geophys. Res. **91**, 7113 (1986).
3. B. I. Sturman, Zh. Éksp. Teor. Fiz. **71**, 614 (1976) [Sov. Phys. JETP **44**, 322 (1976)].
4. V. D. Shapiro, V. I. Shevchenko, G. I. Solov'ev, *et al.*, Phys. Fluids B **5**, 3148 (1993).
5. J. M. Retterer, Phys. Plasmas **4**, 2357 (1997).
6. L. L. Pasechnik and V. F. Semenyuk, Zh. Tekh. Fiz. **45**, 779 (1975) [Sov. Phys. Tech. Phys. **20**, 491 (1975)].
7. G. M. Batanov, L. M. Kovrizhnykh, L. V. Kolik, *et al.*, Tr. Fiz. Inst. Akad. Nauk **160**, 122 (1985).
8. B. Bryusekhaber, E. Z. Gusakov, M. Kremer, *et al.*, Pis'ma Zh. Tekh. Fiz. **21** (13), 38 (1995) [Tech. Phys. Lett. **21**, 508 (1995)].

9. V. N. Budnikov, V. V. D'yachenko, L. A. Esipov, *et al.*, Pis'ma Zh. Tekh. Fiz. **21** (10), 34 (1995) [Tech. Phys. Lett. **21**, 366 (1995)].
10. W. Gekelman and R. L. Stenzel, Phys. Rev. Lett. **35**, 1708 (1975).
11. H. Inuzuka, Y. Takeda, and K. Yamagiwa, Phys. Lett. A **234**, 219 (1997).
12. S. N. Gromov, L. L. Pasechnik, and V. F. Semenyuk, Pis'ma Zh. Tekh. Fiz. **4**, 762 (1978) [Sov. Tech. Phys. Lett. **4**, 306 (1978)].
13. R. L. Stenzel, Rev. Sci. Instrum. **47**, 603 (1976).
14. V. A. Godyak and O. A. Popov, Zh. Tekh. Fiz. **47**, 766 (1977) [Sov. Phys. Tech. Phys. **22**, 461 (1977)].
15. S. V. Egorov, A. V. Kostrov, and A. V. Tronin, Pis'ma Zh. Éksp. Teor. Fiz. **47**, 86 (1988) [JETP Lett. **47**, 102 (1988)].
16. G. Yu. Golubyatnikov, S. V. Egorov, A. V. Kostrov, *et al.*, Fiz. Plazmy **14**, 482 (1988) [Sov. J. Plasma Phys. **14**, 285 (1988)].

Translated by N.F. Larionova

Plasma Physics Reports, Vol. 27, No. 2, 2001, pp. 143–152. Translated from Fizika Plazmy, Vol. 27, No. 2, 2001, pp. 155–164.
Original Russian Text Copyright © 2001 by Pal', Starostin, Filippov.

DUSTY PLASMA

Charging of Dust Grains in a Nuclear-Induced Plasma at High Pressures

A. F. Pal', A. N. Starostin, and A. V. Filippov

Troitsk Institute for Innovation and Thermonuclear Research, Troitsk, Moscow oblast, 142092 Russia

Received June 29, 2000; in final form, September 7, 2000

Abstract—The process of dust-grain charging in plasmas produced by radioactive decay products or spontaneous fission fragments in air and xenon at high pressures is studied numerically in the hydrodynamic approximation. It is shown that, at sufficiently high rates of gas ionization, the dust grains in air are charged by electrons rather than ions, so that the grain charge in air is comparable to that in electropositive gases. The results of numerical calculations based on a complete model agree well with the experimental data. The time evolution of the grain charge is investigated, and the characteristic time scales on which the grains acquire an electric charge are established. The validity of approximate theories of dust-grain charging in electropositive and electronegative gases at high pressures is examined. © *2001 MAIK "Nauka/Interperiodica".*

1. INTRODUCTION

In recent years, attention has been attracted to studies of dusty plasmas produced by radioactive decay products or spontaneous fission fragments [1–3] (below, we will refer to such plasmas as nuclear-induced plasmas). In experiments carried out by Fortov *et al.* [1, 3], dust grains in air at atmospheric pressure acquired an unexpectedly large electric charge. According to the established views [4], the grains in air become negatively charged, because negative ions are more mobile than positive ones. The charge of micron-size dust grains is estimated to be on the order of several tens of electron charges, which is one or two orders of magnitude smaller than the grain charges observed in [3]. Therefore, it becomes relevant to investigate the physical processes of dust-grain charging in a nuclear-induced plasma. From the standpoint of aerospace and other applications, such investigations are of interest for the development and fabrication of compact radioisotope batteries based on plasma–dust structures [2]. In such batteries, the radioactive-decay energy is converted into ultraviolet radiation and, then, into electric energy by wide-band-gap photovoltaic energy converters, in which case the problem of transporting photons through a dust cloud should be resolved by creating ordered plasma–dust structures. The main parameter determining whether such structures can be created is the charge of aerosol grains. The study of aerosol plasmas is also important for developing explosive and solid-fuel MHD generators.

The objective of this paper is to numerically investigate the process of dust-grain charging in a nuclear-induced plasma produced in air at atmospheric pressure, treating the charged plasma components in the hydrodynamic approximation. We also check the validity of simplified theories of dust-grain charging in electropositive and electronegative gases at high pressures [4]. As a typical example of an electropositive gas, we consider xenon, because it is expected to serve as a working medium in a radioisotope battery based on plasma–dust structures [2].

2. HYDRODYNAMIC THEORY OF DUST-GRAIN CHARGING

The transport of charged particles to the surface of a dust grain is treated in the drift–diffusion approximation, which is valid under the conditions [5–9]

$$\lambda_e \ll r_0 + d; \quad \lambda_i \ll r_0 + d, \tag{1a}$$

where λ_e and λ_i are the electron and ion mean free paths, r_0 is the dust-grain radius, and d is the characteristic spatial scale on which plasma quasineutrality is violated. At gas pressures equal to the atmospheric pressure and higher, the characteristic ion mean free path is ordinarily about 10^{-5}–10^{-6} cm. At the same pressures and in the absence of an electric field, the electron mean free path in xenon is about $\lambda_e = 10^{-5}$ cm and, in air, it is approximately equal to $\lambda_e = 10^{-4}$ cm. In xenon, the behavior of the electron mean free path as a function of the electric field is rather complicated, but the mean free path itself never exceeds 10^{-4} cm. In air, the stronger the electric field, the shorter the mean free path λ_e. Calculations show that, for grains of radius 10^{-4} cm, the characteristic spatial scale on which plasma quasineutrality is violated is about 10^{-3} cm. Consequently, in both atomic and molecular gases at pressures equal to the atmospheric pressure and higher, conditions (1a) are usually satisfied for dust grains with a radius larger than 10^{-4} cm.

1063-780X/01/2702-0143$21.00 © 2001 MAIK "Nauka/Interperiodica"

Under a stronger condition for the electrons, specifically,

$$\lambda_u \ll r_0 + d, \tag{1b}$$

where λ_u is the electron-energy relaxation length, electron parameters such as the mobility, diffusion coefficient, and creation and loss rates can be calculated using the local approximation [5]. Estimates show that, in molecular gases at atmospheric pressure, condition (1b) almost always holds for grains with a radius on the order of 10^{-4} cm and larger. For atomic gases at atmospheric pressure, the opposite condition is usually satisfied,

$$\lambda_u \gg r_0 + d, \tag{1c}$$

in which case the electric field of a charged dust grain perturbs the electron distribution function only slightly, so that atomic gases can be approximately described by the electron parameters of a plasma that is unperturbed by the dust component.

We model the process of dust-grain charging by the Seitz–Wigner cell method; i.e., we consider the charging of a test spherical grain of radius r_0 located at the center of a spherically symmetric cell whose radius a_d is determined by the dust density n_d:

$$a_d = \left(\frac{4}{3}\pi n_d\right)^{-1/3}. \tag{2}$$

We assume that the gas consists of one positive and one negative ion species (the equations presented below can be easily generalized for the case of electropositive gases). Under these assumptions, the grain charge and charged-particle density in a nuclear-induced plasma or a plasma produced by an electron beam in an electronegative gas are described by the following three continuity equations:

$$\begin{aligned}
\frac{\partial n_e}{\partial t} + \operatorname{div}\mathbf{j}_e &= Q + k_{\text{ion}} n_e N - \beta_{ei} n_e n_+ - \alpha n_e,\\
\frac{\partial n_+}{\partial t} + \operatorname{div}\mathbf{j}_+ &= Q + k_{\text{ion}} n_e N - \beta_{ei} n_e n_+ - \beta_{ii} n_- n_+,\\
\frac{\partial n_-}{\partial t} + \operatorname{div}\mathbf{j}_- &= \alpha n_e - \beta_{ii} n_- n_+.
\end{aligned} \tag{3}$$

Here, the subscripts "+," "–," and *e* stand for positive ions, negative ions, and electrons, respectively; *n* denotes the charged-particle density; *N* is the neutral density; *Q* is the rate of gas ionization by an external ionizing source; k_{ion} is the rate constant of gas ionization by the plasma electrons; β_{ei} and β_{ii} are the electron–ion and ion–ion recombination coefficients; α is the rate of electron losses due to dissociative and/or three-body attachment to gas particles; and the flux densities of the electrons, positive ions, and negative ions ($\mathbf{j}_e$, $\mathbf{j}_+$, and $\mathbf{j}_-$) have the form

$$\begin{aligned}
\mathbf{j}_e &= -n_e k_e \mathbf{E} - \operatorname{grad}(D_e n_e),\\
\mathbf{j}_+ &= n_+ k_+ \mathbf{E} - D_+ \operatorname{grad} n_+,\\
\mathbf{j}_- &= -n_- k_- \mathbf{E} - D_- \operatorname{grad} n_-,
\end{aligned} \tag{4}$$

where *k* and *D* denote the mobilities and diffusion coefficients of charged particles (for electrons, these parameters are field-dependent). Clearly, the basic set of continuity equations for electropositive gases contains neither the continuity equation for the negative ions nor the terms describing them. The electric field **E** satisfies Poisson's equation

$$\operatorname{div}\mathbf{E} = 4\pi e(n_+ - n_e - n_-), \tag{5}$$

where *e* is the absolute value of the electron charge. We assume that the probability of a dust grain absorbing plasma electrons and ions that are incident on its surface is unity. Under this assumption, Eqs. (3)–(5) should be supplemented with the boundary conditions

$$\begin{aligned}
&n_e|_{r=r_0} = 0, \quad n_+|_{r=r_0} = 0, \quad n_-|_{r=r_0} = 0,\\
&j_e|_{r=a_d} = 0, \quad j_+|_{r=a_d} = 0, \quad j_-|_{r=a_d} = 0,\\
&E|_{r=a_d} = 0.
\end{aligned} \tag{6}$$

(For the hydrodynamic description of the charged plasma components, these boundary conditions on the grain surface were justified by Chekmarev [10].) In boundary conditions (6), the secondary electron emission is neglected because, on the one hand, thermal emission from the "cold" grains plays a negligible role and, on the other hand, taking into account ion–electron emission under conditions when the electric field is insufficiently strong for the avalanche ionization of the gas (even near the grain surface, where the electric field is the strongest) will only result in multiplying the steady-state fluxes of charged particles by a factor approximately equal to unity minus the secondary ion–electron emission coefficient. These circumstances and the fact that the secondary ion–electron emission coefficient is usually on the order of 10^{-2} or smaller enable us to neglect the secondary electron emission under the conditions adopted here. Note that the grain charge is determined by the electric field at the grain surface and, accordingly, can be found from the boundary condition

$$E|_{r=r_0} = \frac{qe}{r_0^2}. \tag{7}$$

Belov *et al.* [11, 12] further developed the model proposed by Smirnov [4] and constructed an approximate theory of dust-grain charging in an electropositive gas at high pressures. For low dust densities, the model and theory yield the same expression for the grain charge:

$$q = -\frac{T_e r_0}{e^2}\ln\left(1 + \frac{k_e}{k_+}\right) \tag{8}$$

(if $T_e = T_+$, the unity drops out of the argument of the logarithm).

Under the same assumptions as those used for electropositive gases, an analogous approximate solution can be constructed for electronegative gases or their mixtures. Thus, under the condition $T_e \gg T_+$, for the grain charge and the charged-particle densities far from the grain, we have

$$\begin{aligned} N_{p0} + qn_d - N_{e0} - N_{n0} &= 0, \\ Q - \beta_{ei}N_{e0}N_{p0} - \beta_{ii}N_{n0}N_{p0} + 4\pi e k_+ q n_d N_{p0} &= 0, \\ Q - \beta_{ei}N_{e0}N_{p0} - \alpha N_{e0} & \\ - qn_d N_{e0}\frac{4\pi e k_e}{1 - \exp(-qe^2/r_0T_e)} &= 0, \\ q = -\frac{T_e r_0}{e^2}\ln\left(1 + \frac{k_e N_{e0}}{k_+ N_{p0}}\right), & \end{aligned} \tag{9}$$

where N_{e0} is the electron density and N_{p0} and N_{n0} are, respectively, the densities of positive and negative ions far from the dust grain. In Eqs. (9), the first equation is a consequence of the charge conservation law, the second and third equations describe the balance of positive ions and electrons, and the fourth equation follows from the condition that the total steady-state current equals zero. The main condition for the validity of Eqs. (9) is that the drift current of the negative ions be low in comparison with the electron drift current, specifically, $k_- N_{n0} \ll k_e N_{e0}$ or

$$Q \gg \frac{1}{\beta_{ii}}\left(\frac{k_-\alpha}{k_e}\right)^2. \tag{10}$$

Under condition (10), the grains are charged primarily by the electrons. Note that Smirnov [4] disregarded this possible charging process. The solutions to Eqs. (9) satisfy the following scaling relations:

$$\begin{aligned} N_{e0} &= f_1(n_d r_0, Q), \\ N_{p0} &= f_2(n_d r_0, Q), \\ N_{n0} &= f_3(n_d r_0, Q), \\ q/r_0 &= f_4(n_d r_0, Q). \end{aligned} \tag{11}$$

Equations (9) are easy to solve when the dust density is so low that, at large distances from the test grain, the electron and ion densities are perturbed by its electric field only slightly, in which case the grain charge is equal to

$$q = -\frac{T_e r_0}{e^2}\ln\left(1 + \frac{k_e}{k_+}\frac{\sqrt{\beta_{ii}Q}}{\alpha}\right). \tag{12}$$

Note that, under the condition $T_e = T_+ = T_- = T$, the fourth equation in set (9) becomes

$$q = -\frac{T r_0}{e^2}\ln\left(\frac{k_e N_{e0} + k_- N_{n0}}{k_+ N_{p0}}\right), \tag{13}$$

so that the grain charge in a plasma with low dust density has the form

$$q = -\frac{T r_0}{e^2}\ln\left(\frac{k_-}{k_+} + \frac{k_e}{k_+}\frac{\sqrt{\beta_{ii}Q}}{\alpha}\right). \tag{14}$$

With ionization rates low enough for the second term within the logarithm to be negligible, the grain charge (14) passes over to the corresponding expression derived in [4].

The results of solving Eqs. (9) numerically with allowance for scaling relations (11) are shown in Fig. 1. The quantities needed to perform calculations (namely, mobilities, diffusion coefficients, and production and loss rates of the charged components of the plasma) were taken from [13–18]. An analysis of both the charge exchange of ions with neutral gas particles and ion conversion shows that, in dry air at atmospheric pressure, the dominant positive ions are O_4^+ or N_4^+ ions, and the dominant negative ions are O_3^- or O_4^- ions. For plasmas in which other ion species dominate, the error in determining the grain charge would not be too large because of the weak logarithmic dependence on the ion mobility. This series of calculations was carried out with the following parameter values: $k_e = 1.91 \times 10^4$ cm^2/(V s), $D_e = 495$ cm^2/s, $T_e = 300$ K, $k_+ = 2.2$ cm^2/(V s), $k_- = 2.5$ cm^2/(V s), $T_+ = T_- = 300$ K, $\beta_{ei} = 2.0 \times 10^{-6}$ cm^3/s, $\alpha = 1.2 \times 10^7$ s^{-1}, and $\beta_{ii} = 2.2 \times 10^{-6}$ cm^3/s. Note that the values of the electron parameters correspond to the case in which the electric field is absent. Inequality (10) implies that, for the parameter

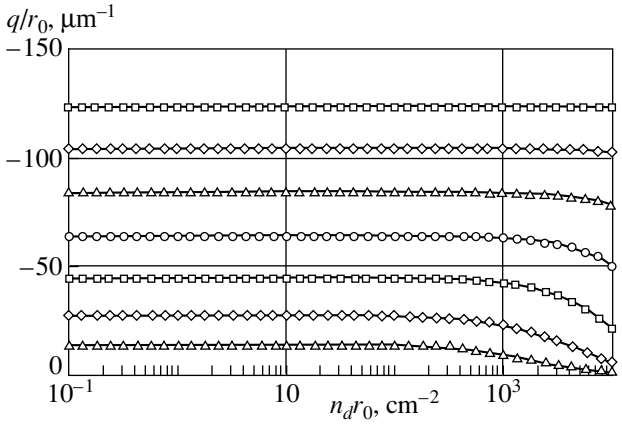

Fig. 1. Grain charge as a function of the parameters of a dusty plasma produced in air at atmospheric pressure for the ionization rates $Q = 10^{12}, 10^{13}, \ldots, 10^{18}$ cm^{-3} s^{-1} (from bottom to top).

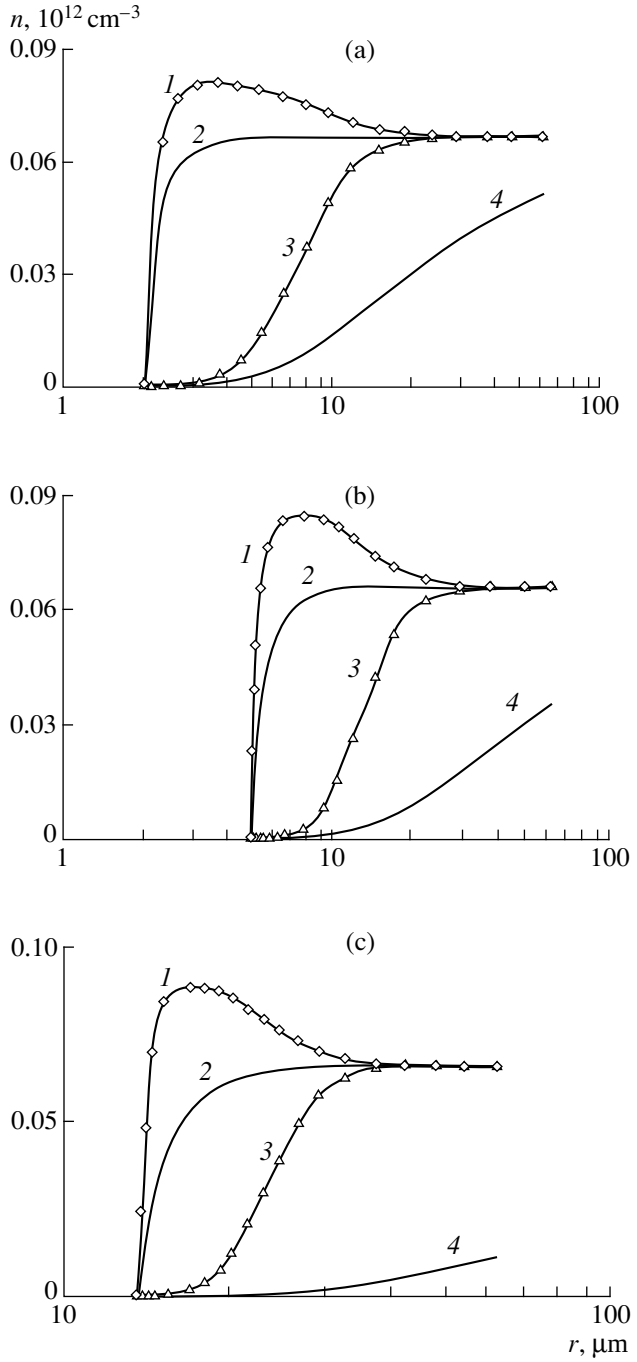

Fig. 2. Steady-state profiles of the densities of positive ions (curves *1*, *2*) and electrons (curves *3*, *4*) in xenon for $n_d = 10^6$ cm^{-3} and $Q = 10^{16}$ cm^{-3} s^{-1} and for different grain radii: r_0 = (a) 2, (b) 4.8, and (c) 13.6 μm. Profiles *1* and *3* are calculated by the establishment method (the number of intervals being $M = 200$), the symbols show some of the numerous points obtained by the relaxation method (the number of intervals being $M = 1000$), and profiles *2* and *4* are computed using the approximate theory of grain charging.

values adopted, the above approximate solution is valid if the ionization rate of air molecules satisfies the condition $Q \gg 10^{12}$ cm^{-3} s^{-1}.

Below, we will show that the results obtained from the approximate theory are insufficiently accurate. Moreover, using this theory makes it virtually impossible to incorporate field-dependent electron parameters in a reasonable manner. However, despite these drawbacks, the approximate theory can yield important results because it provides the possibility of both evaluating the grain charge as a function of the plasma parameters and recalculating the charge obtained with specific values of n_d, r_0, and Q in terms of other values of these three parameters by using the scaling relations and formulas (12) and (14).

3. SOLUTION OF THE PROBLEM OF GRAIN CHARGING BY A FINITE-DIFFERENCE METHOD

The numerical scheme for solving the nonlinear boundary-value problem as formulated is based on the method of integral identities [19] (see Appendix). The algorithm for solving the set of finite-difference equations (A.12) on the basis of this method is as follows. At each time step in the difference method, the values of the field and charged-particle densities calculated at the preceding ith time step are taken as the initial approximation. Let the values $n_{e,k}^m$, $n_{+,k}^m$, and E_k^m ($k = 1, \ldots, M$) approximating the exact solution at a certain iteration step be known. Then, at the next iteration step, the approximate solution is calculated in two stages. First, using the matrix sweep method [20], we solve the linearized continuity equations for the charged particles. Second, using the newly calculated densities of the electrons and positive ions, we determine the electric field from Poisson's equation (5). After achieving the desired accuracy, we stop the iterative procedure. If the solution of the difference equations requires many iterations, we shorten the time step by a factor of 2, and, in the case of a small number of iterations, we increase the time step by 10%.

The convergence of the numerical scheme is controlled by calculating the charged-particle fluxes with the help of expressions (A.4) at given times. When approaching the steady solution, the sum of the electron and ion fluxes over the entire elementary cell tends to zero. In order to control the accuracy of the calculations, we calculate the grain charge by using boundary conditions (6) and by numerically integrating the differential equation

$$\frac{dq}{dt} = -4\pi(J_{+,0} - J_{e,0} - J_{-,0}). \qquad (15)$$

Here, the charged-particle fluxes $J_{a,0}$ at $r = r_0$ were extrapolated from formula (A.4) with $k = 1/2$ and 3/2:

$$J_{a,0} = J_{a,k=1/2} - \frac{1}{2}\frac{h_0}{\hbar_1}(J_{a,k=3/2} - J_{a,k=1/2}). \qquad (16)$$

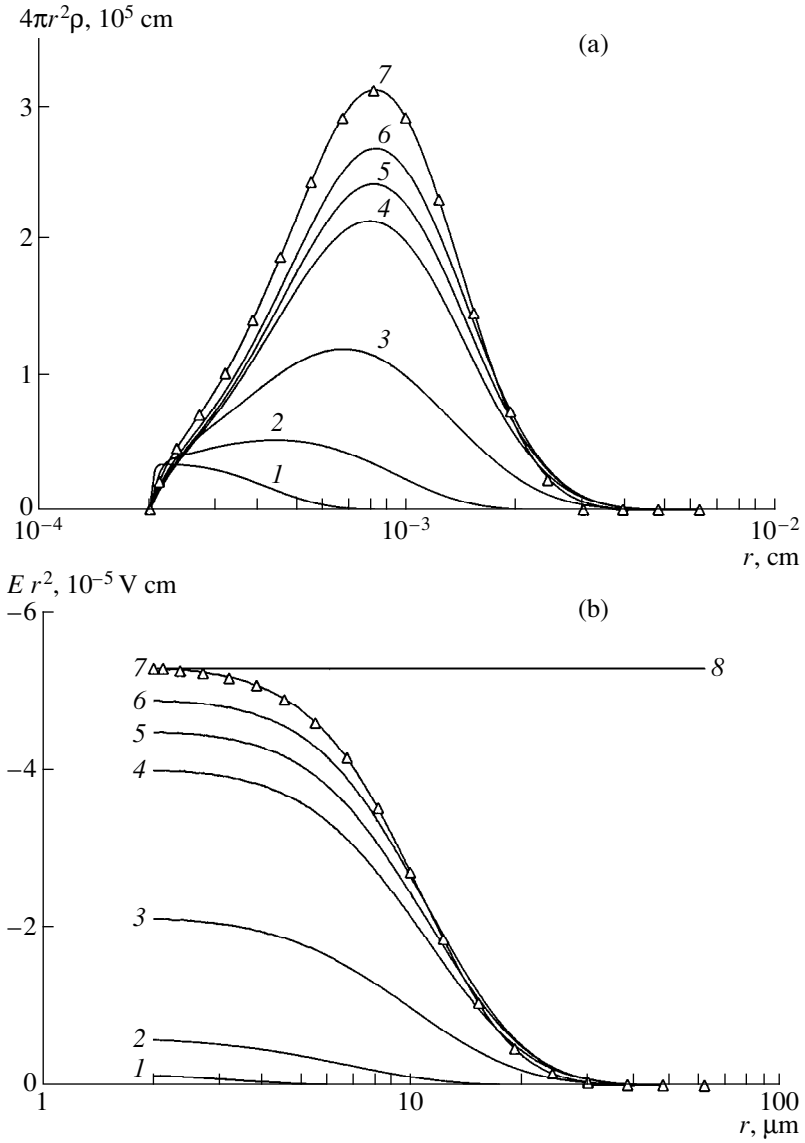

Fig. 3. Time evolutions of (a) the charge density and (b) electric field strength in xenon for $n_d = 10^6$ cm^{-3}, $r_0 = 2$ μm, and $Q = 10^{16}$ cm^{-3} s^{-1} at the times t = (*0*) 0, (*1*) 0.4 ns, (*2*) 4 ns, (*3*) 0.04 μs, (*4*) 0.4 μs, (*5*) 0.8 μs, (*6*) 1.6 μs, and (*7*) 25 μs. Profiles (*8*) are computed using the approximate theory of grain charging, and the triangles show some of the numerous points obtained by the relaxation method (the number of intervals being $M = 1000$).

4. DISCUSSION OF THE SIMULATION RESULTS

In Figs. 2 and 3, we compare the results of numerically solving the boundary problem of grain charging in a nuclear-induced Xe plasma by the relaxation method and the initial problem by the finite-difference method on a radially uniform grid, assuming that the electron parameters are field-independent (below, the latter method will be referred to as the establishment method). In the relaxation method, the results obtained from the approximate theory are used as the initial approximation when solving the time-independent boundary problem. The parameters of the problems were chosen to correspond to the conditions of experiments carried out in [1, 3] with plasmas produced in atmospheric-pressure air by α-particles and fission fragments of ^{252}Cf nuclei, the spontaneous-fission rate being 10^5 fission/s. In those experiments, the plasma contained spherical monodisperse melamine-formaldehyde grains with diameters of 1.90 [1, 3], 4.8, and 13.6 μm [1]. The grain charge was determined from the balance between the gravitational, electric-field, and friction forces and was found to be 900–1300 elementary charges [3]. Notably, in the conclusion of [1], the authors mentioned that they observed dust grains with charges as large as (1000–5000)*e*.

For such a low gas ionization rate as in the experiments of [1, 3], it is necessary to take into account the track structure of the produced plasma (see, e.g., [21,

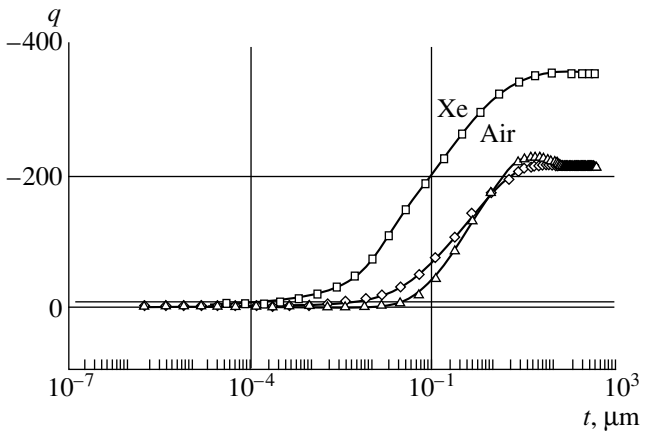

Fig. 4. Time evolutions of the grain charge in a nuclear-induced plasma produced in xenon and air for $n_d = 10^6$ cm^{-3}, $r_0 = 2$ μm, and $Q = 10^{16}$ cm^{-3} s^{-1}. The dashed curve refers to the results obtained for zero initial densities of the charged particles, which corresponds to instantaneous switching-on of an ionization source.

22]). In fact, in the gas volume under investigation, there are only a few tracks (cylindrical plasma formations with a length of about 2 cm and radius of up to 100 μm). Consequently, the gas ionization cannot be regarded as being uniform. However, inside the tracks, the plasma is essentially homogeneous over the characteristic lifetime of the track. Dyuzhov and Poletaev [23] studied the luminescence of nuclear-induced plasmas created in nitrogen–argon and nitrogen–helium mixtures in a way similar to that in [1, 3]. With the data obtained in [23] on the electron density in nitrogen–argon mixtures at a pressure of 2 atm, the ionization rate is estimated as 6×10^{17}–10^{20} cm^{-3} s^{-1}. The higher the pressure, the higher the rate of ionization losses and the smaller the track radii. Consequently, in the first approximation, the mean ionization rate depends on the cube of the pressure. That is why, in simulations, we set the ionization rate to be $Q = 10^{16}$ cm^{-3} s^{-1}, which is of the same order of magnitude as the ionization rate in the working medium (xenon) of the proposed compact radioisotope electric energy source based on wide band-gap photovoltaic converters [3].

From Figs. 2 and 3, we can see that the relaxation and establishment methods yield essentially the same results. In Table 1, we summarize the results obtained in calculating the charges of dust grains of different sizes by means of the approximate theory [11, 12] and by the relaxation and establishment methods. One can see that the methods based on the complete model of grain charging yield essentially the same results, whereas the approximate theory gives smaller values of the grain charge; moreover, the larger the grain radius (at a constant dust density), the larger this discrepancy. Note also that the humplike positive-ion density profiles shown in Fig. 2 cannot be captured by the approximate theory.

The time evolution of the grain charge is illustrated in Fig. 4. The characteristic time scale τ_q on which the grains are charged completely is governed by slower ions. For spherical aerosol grains, this time scale can be estimated as (see, e.g., [24])

$$\tau_q \simeq \frac{d^2}{\pi^2 D_+}, \qquad (17)$$

where d is the spatial scale on which the plasma is nonquasineutral. For the problem under consideration, the charging time is estimated as $\tau_q = 7$ μs, which agrees well with the data of Fig. 4.

Figure 4 also illustrates the results of simulation of the grain charging process in air by the establishment method for constant electron parameters. Note that aerosol grains in air acquire nearly the same charge as in xenon, which is an electropositive gas (see also Table 2). Let us discuss this point in more detail.

An analysis of the radial profiles of charged-particle fluxes shows that, at any point of the calculation region, the flux of negative ions at each instant is negligible in comparison with the flux of electrons or positive ions. Recall that this circumstance, which is the major condition for the applicability of the approximate theory of grain charging in electronegative gases, explains the fact that, in air, the dust grains are charged by electrons. This effect can be explained as follows: in the vicinity of a grain, electrons are lost primarily due to diffusion onto the grain surface rather than due to attachment to oxygen molecules. Because of the latter process (rather than because of the diffusion onto the grain surface), the density of negative ions decreases toward the grain surface more sharply than the density of positive ions.

We also simulated grain charging in air, assuming the electron parameters to be field-dependent. We processed the data presented in the tables in [13, 15–17] using the least squares method and derived simple approximate functions for the electron parameters. We

Table 1. Calculated charges of dust grains of different sizes in xenon for $n_d = 10^6$ cm^{-3} and $Q = 10^{16}$ cm^{-3} s^{-1}

r_0, μm	2.0	4.8	13.6
Calculations by the approximate theory	−289.8	−695.0	−1964.3
Calculations by the relaxation method ($M = 200$)	−361.3	−1106	−5088
Calculations by the establishment method ($M = 1000$)	−366.0	−1111.2	−5095.7

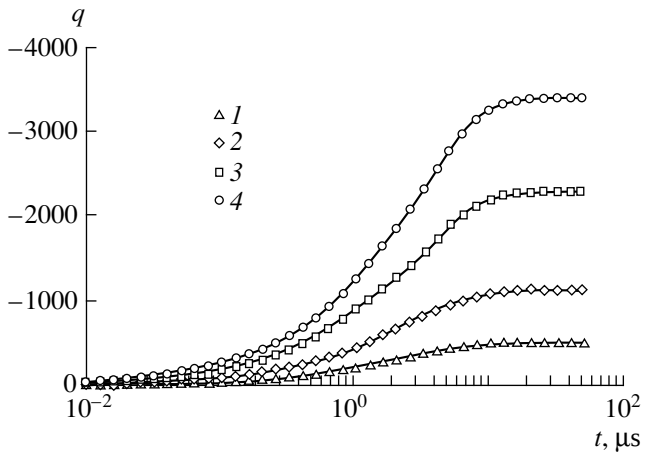

Fig. 5. Time evolutions of the charge of dust grains with different radii (*1*) 1.0, (*2*) 2.4, (*3*) 4.8, and (*4*) 6.8 μm for $n_d = 10^5$ cm^{-3} and $Q = 10^{16}$ cm^{-3} s^{-1} and for electron parameters dependent on the reduced electric field.

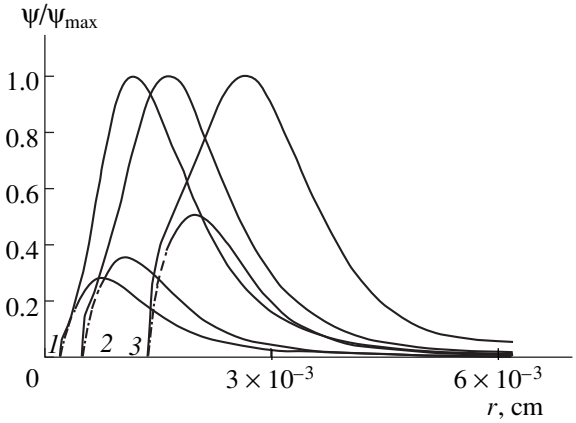

Fig. 6. Radial profiles of the charge density $\Psi = 4\pi r^2\rho$ of dust grains with different radii r_0 = (*1*) 2, (*2*) 4.8, and (*3*) 13.6 μm in air for $n_d = 10^6$ cm^{-3} and $Q = 10^{16}$ cm^{-3} s^{-1}. The dashed curves were obtained with constant electron parameters, and the solid curves were obtained with electron parameters dependent on the reduced electric field. For grains of different sizes, the charge density is normalized to its maximum value calculated for the field-dependent electron parameters (the maximum charge densities for profiles *1–3* are in the ratio 1 : 2.22 : 6.83).

tried to construct continuous approximate functions having (if possible) continuous first derivatives. In Fig. 5, we plot representative time evolutions of the grain charge that were calculated for field-dependent electron parameters. The final charges of grains of different sizes calculated for both field-dependent and constant electron parameters are summarized in Table 2. From Fig. 5 and Table 2, one can see that the grain charges obtained with field-dependent electron parameters are markedly larger. Note also that the radial profiles of the grain charge computed for field-dependent electron parameters are peaked at larger distances from the grain (Fig. 6).

The results listed in Table 2 allow us to check the validity of scaling relations (11). First, we emphasize that the dust density plays an important role only when the characteristic region where the plasma quasineutrality is violated is larger than an elementary cell, in which case, however, the Seitz–Wigner method is unlikely to be applied and it is necessary to use at least a two-dimensional model. In calculations carried out for $Q = 10^{16}$ cm^{-3} s^{-1} and for two different dust densities, $n_d = 10^5$ and 10^6 cm^{-3}, we revealed essentially no difference between the final charges of dust grains with the sizes adopted here. Consequently, under these conditions, the grain charge is almost independent of the parameter $n_d r_0$ and is primarily governed by the grain radius. From Table 2, we can see that, for field-dependent electron parameters, the grain charge-to-radius ratio q/r_0 remains essentially constant, except for the grains with the radius r_0 = 13.6 μm. This result indicates that scaling relations (11) are approximately valid.

It is also of interest to determine the fraction of positive ions that recombine at the grain surfaces. The surface recombination losses of positive ions are described by the quantity $\eta = 4\pi J_{+,0} n_d/Q$, where the positive ion flux onto the grain surface is determined by expression (16). Table 2 shows that, although the surface recombination losses increase almost proportionally to the

Table 2. Calculated charges of dust grains of different sizes in air for $n_d = 10^5$ cm^{-3} and $Q = 10^{16}$ cm^{-3} s^{-1} (the problem was solved on a nonuniform spatial grid with the spacing $\delta = 0.05$ by the finite-difference method, the number of intervals being $M = 200$)

r_0, μm			1.0	2.0	2.4	4.8	6.8	13.6
Calculations by an analytic theory			−84.4	−168.7	−202.5	−404.9	−573.6	−1147
Calculations by the difference method	Constant electron parameters		−92.3	−206.3	−257.3	−624.4	−1069	−2807
	Field-dependent electron parameters	q	−492.7	−937.2	−1116	−2282	−3380	−8045
		$\lvert q\rvert/r_0$	493	469	465	475	497	591
		$\eta \times 10^3$	1.156	2.140	2.532	5.055	7.349	17.18
		ξ	0.872	0.850	0.845	0.824	0.819	0.805

Table 3. Electron energy relaxation length $\lambda_{e,u}$, electron mean free path $\lambda_{e,m}$, and characteristic length of the region where quasineutrality of the plasma produced in air at atmospheric pressure is violated for aerosol grains of different sizes and for $n_d = 10^5$ cm^{-3} and $Q = 10^{16}$ cm^{-3} s^{-1}

r_0, μm	2	4.8	13.6
$\lvert E_0\rvert$, V/cm	3374	1426	626
$\lambda_{e,m}$, μm	0.23	0.29	0.30
$\lambda_{e,u}$, μm	3.1	4.6	5.4
d, μm	11.7	14.1	26.7

grain radius, they remain insignificant. That the ratio η/r_0 remains essentially constant is explained by the following two circumstances: the coefficient of the recombination of positive ions on the grain surfaces is approximately equal to the Langevin coefficient $\beta_{id} = 4\pi e k_+$ [14], and scaling relations (11) are approximately valid. In Table 2, we also present the values of the quantity $\xi = 4\pi J_{+,0}/\beta_{id} q n_{+,M}$, which is seen to be smaller than unity because the Langevin theory is only approximately applicable to our problem. The quantity ξ depends weakly on the grain radius: it decreases at most by 10% as the grain radius increases by more than one order of magnitude. The positive ion flux onto the grain surface is found to be less intense than the Langevin flux, because the electric field decreases much more rapidly with distance than the Coulomb field (Fig. 3b).

To conclude this section, let us again discuss the applicability condition for the validity of the hydrodynamic description of a plasma. The electron energy relaxation length is described by the expression

$$\lambda_u \approx \sqrt{D_e/\nu_u}, \tag{18}$$

where ν_u is the inelastic collision rate. Table 3 presents the electron energy relaxation lengths in an electric field near an aerosol grain in air and the characteristic dimensions of the region where the plasma quasineutrality is violated. The results given in Table 3 were calculated at the peak of the radial profile of the grain charge. A comparative analysis of these results shows that, for dusty plasmas with the parameters adopted here, condition (1b) for the applicability of a hydrodynamic approach is satisfied.

5. CONCLUSION

We have developed a numerical model of the process of dust-grain charging in nuclear-induced dusty plasmas produced in air at high pressures, treating the charged plasma components in the hydrodynamic approximation. We have shown that, at a sufficiently high ionization rate, aerosol grains in air are charged by electrons and not by ions, as was thought previously. For this reason, the dust grains in air can acquire an electric charge comparable with that in electropositive gases. We have found that the simplified theory based on the assumption that dust grains are charged primarily by ions [4] leads to quite large errors in determining the grain charge. Although refined theories yield better results, they are too crude to ensure the desired accuracy of predictions and can only be used to obtain rough estimates, whereas the results of numerical calculations based on the complete model agree well with the experimental data of [1, 3].

We have also investigated the time evolution of the grain charge. This problem is also of interest because it has been little studied in the literature (most papers deal with steady-state problems). We have determined the characteristic time scales on which the dust grains are charged. The results obtained will be useful in interpreting data from experiments with unsteady nuclear-induced dusty plasmas.

ACKNOWLEDGMENTS

This work was supported in part by the Russian Foundation for Basic Research, project nos. 99-02-18176 and 00-15-96539 (under the program "Leading Scientific Schools").

APPENDIX

The difference scheme for solving the nonlinear boundary-value problem numerically is constructed using the method of integral identities [19]. We introduce a spherical coordinate system with the origin at the center of a dust grain. On the closed interval $[r_0, a_d]$ inside an elementary cell, we introduce two nonuniform grids, specifically, a reference grid with mesh points r_k and an auxiliary grid with mesh points $r_{k+1/2}$ (the mesh points of the reference grid alternate with those of the auxiliary grid):

$$r_{k+1} = r_k + h_k, \quad r_{k=0} = r_0, \quad r_{k=M} = a_d,$$

$$r_{k+1/2} = \frac{r_{k+1} + r_k}{2} = r_k + \frac{h_k}{2}$$

$$= r_{k+1} - \frac{h_k}{2} = r_{k-1/2} + \hbar_k,$$

where $h_k = (1+\delta)^k h$, $h = \dfrac{\delta}{(1+\delta)^{M-1} - 1}(a_d - r_0)$, and $\hbar_k = \dfrac{h_{k-1} + h_k}{2}$. The grids with $\delta = 0$ are uniform, with a regular spacing h.

Taking into account the spherical symmetry of the problem, we introduce the fluxes

$$J_a = r^2\left(n_a k_a E - \frac{\partial(D_a n_a)}{\partial r}\right), \tag{A.1}$$

where $J_a = \{J_e, J_+, J_-\}$, $n_a = \{n_e, n_+, n_-\}$, $k_a = \{-k_e, k_+, -k_-\}$, and $D_a = \{D_e, D_+, D_-\}$ for electrons, positive ions, and negative ions, respectively.

We integrate continuity Eqs. (3) from $r_{k-1/2}$ to $r_{k+1/2}$ to obtain

$$J_{a,k+1/2} - J_{a,k-1/2} = \int_{r_{k-1/2}}^{r_{k+1/2}} \left(R_a - \frac{\partial n_a}{\partial t}\right) r^2 dr, \qquad (A.2)$$

where the symbol R_a stands for the right-hand sides of Eqs. (3). Now, we integrate Eqs. (3) from $r_{k-1/2}$ to r and use definition (A.1) for the particle fluxes. As a result, we find

$$r^2\left(k_a n_a E - \frac{\partial (D_a n_a)}{\partial r}\right) = J_{a,k-1/2} + \int_{r_{k-1/2}}^{r} \left(R_a - \frac{\partial n_a}{\partial t}\right) r^2 dr. \qquad (A.3)$$

Then, we integrate Eq. (A.3) from r_{k-1} to r_k and retain terms up to second order in the maximum distance between the mesh points to arrive at the following expression for the charged-particle fluxes at the point $r_{k-1/2}$:

$$J_{a,k-1/2} = r_k r_{k-1}\left(-\frac{D_{a,k} n_{a,k} - D_{a,k-1} n_{a,k-1}}{h_{k-1}} + \frac{k_{a,k} n_{a,k} E_k + k_{a,k-1} n_{a,k-1} E_{k-1}}{2}\right). \qquad (A.4)$$

We substitute fluxes (A.4) into expressions (A.2) and switch from the integrals over closed intervals between the mesh points of the reference grid to the sums according to the trapezoid rule, by factoring the function $R_a - \partial n_a/\partial t$ out of the integral sign and replacing this function with its value at the point r_k. As a result, to second order in the maximum distance between the mesh points, we obtain

$$\frac{\partial n_{a,k}}{\partial t} = R_{a,k} + \frac{1}{\hbar_k r_k}\left[r_{k+1}\frac{D_{a,k+1} n_{a,k+1} - D_{a,k} n_{a,k}}{h_k} - r_{k-1}\frac{D_{a,k} n_{a,k} - D_{a,k-1} n_{a,k-1}}{h_{k-1}} - r_{k+1}\frac{k_{a,k+1} n_{a,k+1} E_{k+1} + k_{a,k} n_{a,k} E_k}{2} + r_{k-1}\frac{k_{a,k} n_{a,k} E_k + k_{a,k-1} n_{a,k-1} E_{k-1}}{2}\right]. \qquad (A.5)$$

The electric field can be found by integrating Poisson's equation (5) from right to left according to the trapezoid rule:

$$F_k = F_{k+1} + 4\pi e \frac{r_k - r_{k+1}}{2} \times (r_k^2 (n_{+,k} - n_{e,k} - n_{-,k}) + r_{k+1}^2 (n_{+,k+1} - n_{e,k+1} - n_{-,k+1})), \qquad (A.6)$$

where $F = r^2 E$.

The initial densities of charged particles can be obtained, e.g., by solving the corresponding problem for a plasma without dust grains, which corresponds to the case of instantaneous injection of dust grains into the plasma. We can also set the initial plasma density to zero, which corresponds to the instantaneous switching-on of an ionization source. Note that in a plasma produced in air at ionization rates lower than 10^{20} cm^{-3} s^{-1}, the electron–ion recombination plays a negligible role. Consequently, without any serious loss of accuracy, we can simplify the problem by setting the electron–ion recombination coefficient equal to the ion–ion recombination coefficient, in which case the problem for a grain-free plasma has the solution

$$N_{e0} = Q/(\beta_{ii} N_{p0} + \alpha), \quad N_{p0} = \sqrt{Q/\beta_{ii}}, \quad N_{n0} = N_{p0} - N_{e0}. \qquad (A.7)$$

In order to specify the boundary conditions at the right end of the calculation interval, we supplement the grid with the mesh point r_{M+1} and set

$$J_{a,M+1/2} = 0. \qquad (A.8)$$

With allowance for relationships (A.3) and (A.8), Eqs. (A.5) yield the following equation for the charged-particle densities at the right boundary:

$$\frac{\partial n_{a,M}}{\partial t} = R_{a,M} + \frac{r_{M-1}}{\hbar_M r_M} \times \left[-\frac{D_{a,M} n_{a,M} - D_{a,M-1} n_{a,M-1}}{h_{M-1}} + \frac{k_{a,M} n_{a,M} E_M + k_{a,M-1} n_{a,M-1} E_{M-1}}{2}\right]. \qquad (A.9)$$

Note that the resulting difference equations (A.5) and (A.9) are monotonic and, consequently, well-posed under the conditions [20]

$$\frac{1}{h_k} - \frac{k_{a,k+1}}{D_{a,k+1}}\frac{E_{k+1}}{2} > 0, \quad k = 1, \quad M-1, \qquad (A.10a)$$

$$\frac{1}{h_k} + \frac{k_{a,k-1}}{D_{a,k-1}}\frac{E_{k-1}}{2} > 0, \quad k = 1, \quad M. \qquad (A.10b)$$

Since ordinary dust grains are usually charged negatively and $E < 0$, conditions (A.10) lead to the following

restriction on the grid size:

$$h_k < \min\left(\frac{2D_{e,k+1}}{k_{e,k+1}|E_{k+1}|}, \frac{2D_-}{k_-|E_{k+1}|}, \frac{2D_+}{k_+|E_{k-1}|}\right). \quad \text{(A.11)}$$

In the calculations described here, all of these conditions were satisfied by a large margin.

Differential equations (A.5) and (A.9) were solved using the semi-implicit scheme

$$n_{a,k=0}^{i+1} = 0,$$

$$\frac{n_{a,k}^{i+1} - n_{a,k}^{i}}{\tau} = R_{a,k}^{i+\sigma} + \frac{r_{k+1}}{\hbar_k r_k}\left(\frac{D_{a,k+1}^{i+\sigma} n_{a,k+1}^{i+\sigma} - D_{a,k}^{i+\sigma} n_{a,k}^{i+\sigma}}{h_k}\right.$$

$$\left. - \frac{k_{a,k+1}^{i+\sigma} n_{a,k+1}^{i+\sigma} E_{k+1}^{i+\sigma} + k_{a,k}^{i+\sigma} n_{a,k}^{i+\sigma} E_k^{i+\sigma}}{2}\right)$$

$$- \frac{r_{k-1}}{\hbar_k r_k}\left(\frac{D_{a,k}^{i+\sigma} n_{a,k}^{i+\sigma} - D_{a,k-1}^{i+\sigma} n_{a,k-1}^{i+\sigma}}{h_{k-1}}\right.$$

$$\left. - \frac{k_{a,k}^{i+\sigma} n_{a,k}^{i+\sigma} E_k^{i+\sigma} + k_{a,k-1}^{i+\sigma} n_{a,k-1}^{i+\sigma} E_{k-1}^{i+\sigma}}{2}\right), \quad \text{(A.12)}$$

$$k = 1, \quad M-1,$$

$$\frac{n_{a,M}^{i+1} - n_{a,M}^{i}}{\tau} = R_{a,M}^{i+\sigma}$$

$$- \frac{r_{M-1}}{r_M \hbar_M}\left[\frac{(D_{a,M}^{i+\sigma} n_{a,M}^{i+\sigma} - D_{a,M-1}^{i+\sigma} n_{a,M-1}^{i+\sigma})}{h_{M-1}}\right.$$

$$\left. - \frac{k_{a,M}^{i+\sigma} n_{a,M}^{i+\sigma} E_M^{i+\sigma} + k_{a,M-1}^{i+\sigma} n_{a,M-1}^{i+\sigma} E_{M-1}^{i+\sigma}}{2}\right],$$

where the lower index a stands for the charged-particle species (e, "+," or "–" for electrons, positive ions, or negative ions, respectively), $R_{e,k}^{i+\sigma} = Q + (\nu_{\text{ion},k}^{i+\sigma} - \alpha_k^{i+\sigma}) n_{e,k}^{i+\sigma} - \beta_{ei,k}^{i+\sigma} n_{e,k}^{i+\sigma} n_{+,k}^{i+\sigma}$, $R_{+,k}^{i+\sigma} = Q + \nu_{\text{ion},k}^{i+\sigma} n_{e,k}^{i+\sigma} - \beta_{ei,k}^{i+\sigma} n_{e,k}^{i+\sigma} n_{+,k}^{i+\sigma} - \beta_{ii} n_{+,k}^{i+\sigma} n_{-,k}^{i+\sigma}$, $R_{-,k}^{i+\sigma} = \alpha_k^{i+\sigma} n_{e,k}^{i+\sigma} - \beta_{ii} n_{+,k}^{i+\sigma} n_{-,k}^{i+\sigma} = R_{+,k}^{i+\sigma} - R_{e,k}^{i+\sigma}$, $n_{e,k}^{i+\sigma} = \sigma n_{e,k}^{i+1} + (1-\sigma) n_{e,k}^{i}$, $n_{+,k}^{i+\sigma} = \sigma n_{+,k}^{i+1} + (1-\sigma) n_{+,k}^{i}$, $n_{-,k}^{i+\sigma} = \sigma n_{-,k}^{i+1} + (1-\sigma) n_{-,k}^{i}$, $E_k^{i+\sigma} = \sigma E_k^{i+1} + (1-\sigma) E_{e,k}^{i}$, $\nu_{\text{ion},k}^{i+\sigma} = \nu_{\text{ion}}(E_{e,k}^{i+\sigma})$, $\beta_{ei,k}^{i+\sigma} = \beta_{ei}(E_{e,k}^{i+\sigma})$, $k_{e,k}^{i+\sigma} = k_e(E_{e,k}^{i+\sigma})$, and $D_{e,k}^{i+\sigma} = D_e(E_{e,k}^{i+\sigma})$. The parameter σ determines the degree to which the difference scheme is implicit: the scheme with $\sigma = 1$ is fully implicit; for $\sigma = 1/2$, we deal with the Crank–Nicholson scheme; and the scheme with $\sigma = 0$ is an explicit scheme, which is convergent if the time step satisfies the condition $\tau < \min(h_k^2/2D_{e,k})$.

REFERENCES

1. V. E. Fortov, A. P. Nefedov, V. I. Molotkov, *et al.*, Izv. Akad. Nauk, Ser. Fiz. **63**, 2221 (1999).
2. V. Yu. Baranov, I. A. Belov, A. V. Dem'yanov, *et al.*, in *Isotopes*, Ed. by V. Yu. Baranov (IzdAT, Moscow, 2000), p. 626.
3. V. E. Fortov, V. I. Vladimirov, L. V. Deputatova, *et al.*, Dokl. Akad. Nauk **366**, 184 (1999).
4. B. M. Smirnov, *Aerosols in Gases and Plasma* (Inst. Vys. Temp. Akad. Nauk SSSR, Moscow, 1990).
5. L. D. Tsendin, Zh. Éksp. Teor. Fiz. **66**, 1638 (1974) [Sov. Phys. JETP **39**, 805 (1974)].
6. N. L. Aleksandrov, A. P. Napartovich, and A. N. Starostin, Fiz. Plazmy **6**, 1123 (1980) [Sov. J. Plasma Phys. **6**, 618 (1980)].
7. N. L. Aleksandrov, A. M. Konchakov, A. P. Napartovich, and A. P. Starostin, in *Plasma Chemistry*, Ed. by B. M. Smirnov (Énergoatomizdat, Moscow, 1984), Vol. 11, p. 3.
8. Yu. B. Golubovskiĭ, V. M. Zakharov, V. N. Pasunkin, and L. D. Tsendin, Fiz. Plazmy **7**, 620 (1981) [Sov. J. Plasma Phys. **7**, 340 (1981)].
9. N. A. Gorbunov, N. B. Kolokolov, and A. A. Kudryavtsev, Fiz. Plazmy **15**, 1513 (1989) [Sov. J. Plasma Phys. **15**, 881 (1989)].
10. I. B. Chekmarev, Zh. Tekh. Fiz. **50** (1), 48 (1980) [Sov. Phys. Tech. Phys. **25**, 25 (1980)].
11. I. A. Belov, A. S. Ivanov, D. A. Ivanov, *et al.*, Pis'ma Zh. Tekh. Fiz. **25** (15), 89 (1999) [Tech. Phys. Lett. **25**, 630 (1999)].
12. I. A. Belov, A. S. Ivanov, D. A. Ivanov, *et al.*, Zh. Éksp. Teor. Fiz. **117**, 105 (2000) [JETP **90**, 93 (2000)].
13. J. Dutton, J. Chem. Phys. Ref. Data **4**, 577 (1975).
14. B. M. Smirnov, *Ions and Excited Atoms in Plasma* (Atomizdat, Moscow, 1974).
15. J. B. A. Mitchell, Phys. Rep. **186** (5), 215 (1990).
16. A. V. Phelps, ftp://jila.colorado.edu/collision_data/eletrans.txt.
17. N. L. Aleksandrov, F. I. Vysikaĭlo, R. Sh. Islamov, *et al.*, Teplofiz. Vys. Temp. **19**, 22 (1981).
18. B. M. Smirnov, *Complex Ions* (Nauka, Moscow, 1983).
19. G. I. Marchuk, *Methods of Numerical Mathematics* (Nauka, Moscow, 1989; Springer-Verlag, New York, 1975).
20. A. A. Samarskiĭ and A. V. Gulin, *Numerical Methods* (Nauka, Moscow, 1989).
21. M. Suzuki, J. Ruan (Gen), and S. Kubota, Nucl. Instrum. Methods **192**, 565 (1982).
22. A. P. Budnik and I. V. Dobrovol'skaya, Kvantovaya Élektron. (Moscow) **24**, 506 (1997).
23. Yu. A. Dyuzhov and E. D. Poletaev, in *Proceedings of the Mathematical Conference on Low Temperature Plasma, Petrozavodsk, 1998*, Part 1, p. 175.
24. Yu. P. Raizer, *Gas Discharge Physics* (Nauka, Moscow, 1987; Springer-Verlag, Berlin, 1991).

Translated by O.E. Khadin

Plasma Physics Reports, Vol. 27, No. 2, 2001, pp. 153–157. Translated from Fizika Plazmy, Vol. 27, No. 2, 2001, pp. 165–169.
Original Russian Text Copyright © 2001 by Soldatov.

PLASMA KINETICS

Distribution Function of Relativistic Electrons Produced by the Tunneling Ionization of a Gas by an Intense Electromagnetic Wave

A. V. Soldatov

All-Russia Research Institute of Experimental Physics, Russian Federal Nuclear Center, Sarov, Nizhni Novgorod oblast, 607190 Russia

Received May 10, 2000

Abstract—The distribution function of the relativistic electrons produced in the interaction between an intense electromagnetic wave and a neutral gas is derived and is shown to be nonequilibrium and anisotropic. The drift plasma current is calculated, and the applicability conditions for the results obtained are determined.
© 2001 MAIK "Nauka/Interperiodica".

1. INTRODUCTION

Recently developed high-power lasers capable of generating pico- and femtosecond pulses open new possibilities for studying the fundamental properties of matter [1, 2] and hold great promise for practical applications [3]. In a plasma produced in the interaction of the electromagnetic field of a laser pulse with a gas, the electron distribution is nonequilibrium and may give rise to various plasma instabilities [4]. The most important features of this interaction are the high rate of gas ionization and the relatively minor role of hydrodynamic processes during the laser pulse. The key role in the plasma processes is played by the kinetic effects associated with the specific features of the electron distribution; because of the short interaction times, these features are governed completely by the pump pulse parameters. The interaction between the laser pulse and the plasma produced gives rise to a number of interesting phenomena, such as wakefield excitation [5–7] and laser frequency upshift during the propagation of a pulse through a plasma [8].

In calculating the electron distribution function (EDF), Bychenkov and Tikhonchuk [4] restricted their study to the nonrelativistic case. Here, we consider relativistic effects that occur during gas ionization by an intense laser pulse. A similar problem was treated by Glazov and Rukhadze [9–11] in connection with breakdown in a low-pressure gas and the electron-impact ionization of a gas. Here, we use a somewhat different approach to solving the kinetic equation and describe the effects associated with the generation of the longitudinal current in a laser-produced plasma.

Relativistic effects come into play when the kinetic energy of the electron oscillations in an electromagnetic field becomes comparable with the electron rest mass energy. For laser pulses with a wavelength of about 1 μm, this condition holds at laser intensities of about 10^{18} W/cm^2.

This circumstance gives rise to one of the challenges in determining the properties of a laser-produced plasma. Specifically, since the electric field of such laser pulses is much stronger than the atomic field $E_a = 5.1 \times 10^9$ V/cm, the ionization rate of gas atoms cannot be calculated rigorously (the Keldysh formula for the tunneling ionization rate [12, 13] was derived perturbatively and fails to produce the desired result). Additionally, it is necessary to take into account the effects of multiple ionization, because multiply ionized gases with ion charge numbers up to 10 have already been observed in laser experiments (see, e.g., [14, 15]). For this reason, we restrict ourselves to a model description of the ionization of a gas by a laser pulse.

Our purpose here is to calculate the relativistic EDF for a plasma produced in the interaction of an intense ($I \geq 10^{18}$ W/cm^2, the field amplitude being $E_0 \geq 2 \times 10^{10}$ V/cm) ultrashort ($\tau \leq 10^{-12}$ s) laser pulse with a monatomic gas. To do this, we derive a model expression for the ionization rate without allowance for the reverse effect of the produced plasma on the laser pulse. We also discuss the applicability conditions for our approach.

2. ELECTRON MOTION IN THE FIELD OF A PLANE ELECTROMAGNETIC WAVE

We consider a free electron that originates at a certain time and moves in the field of a plane electromagnetic wave propagating through a gas. We assume that the wave propagates along the z-axis and represent the wave field as

$$\begin{aligned} \mathbf{E} &= (E_x, E_y, 0), \\ \mathbf{H} &= (H_x, H_y, 0) = (-E_y, E_x, 0). \end{aligned} \tag{1}$$

1063-780X/01/2702-0153$21.00 © 2001 MAIK "Nauka/Interperiodica"

We also assume that the field components are harmonic functions of the wave phase:

$$\begin{aligned} E_x &= E_0 \cos\psi, \\ E_y &= \alpha E_0 \sin\psi, \\ \psi &= \omega_0(t - z/c), \end{aligned} \tag{2}$$

where ω_0 is the angular frequency and α is the parameter characterizing the ellipticity of polarization of the wave field ($\alpha = 0$ for linear polarization, and $\alpha = 1$ for circular polarization). The electric field amplitude E_0 describes the slowly varying (over the field period) laser-pulse envelope. We assume that the amplitude of the dimensionless vector potential is comparable with unity:

$$a_0 = \frac{eE_0}{mc\omega_0} \geq 1, \tag{3}$$

so that the electron motion is relativistic. The quantity a_0 is related to the laser pulse parameters by

$$a_0 = 0.85\sqrt{I_{18}}\lambda_{\mu m},$$

where I_{18} is the pulse intensity in units of 10^{18} W/cm^2 and $\lambda_{\mu m}$ is the laser wavelength in microns.

The solutions to the equations of electron motion in the field of a plane electromagnetic wave are well known [16–18]. Assuming that the electrons originate with a zero kinetic energy (in any case, the initial electron kinetic energy is much lower than the electron oscillatory energy), we write the solutions for the components of the momentum of a test electron (in units of *mc*) as

$$\begin{aligned} \tilde{p}_x &= -a_0(\sin\psi - \sin\psi_0), \\ \tilde{p}_y &= \alpha a_0(\cos\psi - \cos\psi_0), \\ \tilde{p}_z &= \frac{1}{2}\tilde{p}_\perp^2 = \frac{1}{2}(\tilde{p}_x^2 + \tilde{p}_y^2), \\ \tilde{\gamma} &= \sqrt{1 + \tilde{\mathbf{p}}^2} = 1 + \tilde{p}_z, \end{aligned} \tag{4}$$

where ψ_0 is the field phase at which the test electron originates. For convenience of further analysis, some of the quantities are marked by a tilde. Note that the *z*-component of the electron momentum is always positive, which is characteristic of the drift in crossed fields. The electron motion is relativistic ($\tilde{\mathbf{p}}_{\max}^2 = 1$) already at

$$a_0 = (\sqrt{5} - 2)^{1/2} \approx 0.49,$$

which corresponds to the laser pulse intensity $I = 0.96 \times 10^{18}\lambda_{\mu m}^{-2}$ W/cm^2.

Note also that the solutions obtained apply to the field switched on adiabatically in the infinite past.

3. DISTRIBUTION FUNCTION

We will solve the following kinetic equation for the distribution function of the electrons that originate during gas ionization by laser light:

$$\frac{\partial f}{\partial t} + \mathbf{v}\frac{\partial f}{\partial \mathbf{r}} - \frac{e}{mc}\left(\mathbf{E} + \frac{1}{c}\mathbf{v}\times\mathbf{H}\right)\frac{\partial f}{\partial \mathbf{p}} = S_i\delta(\mathbf{p}), \tag{5}$$

where **E** and **H** are the electric and magnetic fields of a laser pulse and S_i is the production rate of electrons per cubic centimeter.

Solving Eq. (5) by the method of characteristics, we obtain the EDF in terms of the integral over the field phases at which the electrons originate:

$$f(\mathbf{p}, \psi) = \frac{1}{\omega_0}\int^{\psi} d\psi_0(1 + p_z)S_i\delta(\mathbf{p} - \tilde{\mathbf{p}}). \tag{6}$$

That this expression is valid can be verified by simply substituting it into Eq. (6). Assuming that free electrons are produced exclusively through the ionization of gas atoms by the wave field (i.e., neglecting the processes of recombination and electron-impact ionization), we can write the production rate per cubic centimeter as

$$S_i = \sum_{k=0}^{Z-1} w_k n_k, \tag{7}$$

where n_k is the density of ions in the *k*th ionization state, w_k is the probability of ionization of these ions, and *Z* is the maximum ion charge number.

When the oscillatory energy of a free electron is higher than the ionization energy, the probability of the tunneling ionization of an atom in an external field is usually calculated from the Keldysh formula [12, 13], which was derived for fields much weaker than the intra-atomic field and thereby cannot be directly applied to our problem. Moreover, in external fields much stronger than the intra-atomic field, the electron shells of the gas atoms are deformed so much that, on a time scale of about the revolution period, the electrons leave the outer atomic shells and start to move freely in a gas. Consequently, we can assume that the probability for a neutral atom to be ionized is $w_0 \sim \omega_a$, where $\omega_a = 4.1 \times 10^{16}$ s^{-1} is the atomic frequency, which is much higher than the laser frequency,

$$w_0 \gg \omega_0$$

(for the laser wavelength $\lambda = 1$ μm, the laser frequency is equal to $\omega_0 = 2 \times 10^{15}$ s^{-1}). Under these conditions, we can consider the ionization to be threshold in nature: when the field amplitude (or the pulse propagation time) exceeds a certain critical value, all of the gas atoms are ionized instantaneously. In other words, we set

$$w_0 = \delta(t - t_{th}) = \omega_0\delta(\psi_0 - \psi_{th}).$$

Of course, the higher the ionization state of an ion, the higher its ionization energy, so that the probability of multiple ionization is lower, but we assume that it is still higher than ω_0. Under this assumption, we can write

$$S_i = \omega_0 n_a \sum_{k=0}^{Z-1} \delta(\psi_0 - \psi_{th}^k), \tag{8}$$

where n_a is the neutral atom density and ψ_{th}^k is the threshold field phase corresponding to ionization to the kth state. Substituting expression (8) into formula (6) for the EDF, we find

$$f(\mathbf{p}, \psi) = n_a \int^{\psi} d\psi_0 (1 + p_z) \delta(\mathbf{p} - \tilde{\mathbf{p}}) \times \sum_k \delta(\psi_0 - \psi_{th}^k). \tag{9}$$

Note that, if we integrate the EDF weighted by 1 and $-eV_z$ over momenta, we immediately obtain the electron density and electron current density:

$$n_e = n_a \int^{\psi} d\psi_0 \sum_k (1 + \tilde{p}_z) \delta(\psi_0 - \psi_{th}^k),$$
$$J_z = -e n_a c \int^{\psi} d\psi_0 \sum_k \tilde{p}_z \delta(\psi_0 - \psi_{th}^k). \tag{10}$$

3.1. Circularly Polarized Wave ($\alpha = 1$)

For a circularly polarized wave, we can readily show that the product of two δ-functions, $\delta(p_x - \tilde{p}_x)\delta(p_y - \tilde{p}_y)$, is independent of ψ_0. In fact, introducing the notation

$$P_x = -p_y + a_0 \cos\psi,$$
$$P_y = p_x + a_0 \sin\psi,$$

we obtain

$$\delta(p_x - \tilde{p}_x)\delta(p_y - \tilde{p}_y) = \delta(P_x - a_0 \cos\psi_0)\delta(P_y - a_0 \sin\psi_0) = \frac{1}{2\pi a_0}\delta(P_\perp - a_0),$$

$$P_\perp^2 = P_x^2 + P_y^2 = p_\perp^2 + a_0^2 + 2a_0(p_x \sin\psi - p_y \cos\psi).$$

Integrating the last δ-function yields the final expression for the EDF:

$$f(\mathbf{p}, \psi) = n_a \frac{\delta(P_\perp - a_0)}{2\pi a_0} \times \sum_k (1 + \tilde{p}_z)\delta(p_z - \tilde{p}_z) U(\psi - \psi_{th}^k) = n_a \frac{\delta(P_\perp - a_0)}{2\pi a_0} \sum_k \left(1 + 2a_0^2 \sin^2 \frac{\psi - \psi_{th}^k}{2}\right) \times \delta\left(p_z - 2a_0^2 \sin^2 \frac{\psi - \psi_{th}^k}{2}\right) U(\psi - \psi_{th}^k), \tag{11}$$

where U is the Heaviside step function. Plasmas with such nonequilibrium EDFs are subject to various instabilities, in particular, the Weibel instability (which is associated with the anisotropic character of the electron distribution), a parametric decay of the pump wave, and the excitation of longitudinal waves (the latter two are associated with the beamlike character of the electron distribution).

From EDF (11), we find the electron density,

$$n_e = n_a \sum_k \left(1 + 2a_0^2 \sin^2 \frac{\psi - \psi_{th}^k}{2}\right) U(\psi - \psi_{th}^k) \tag{12}$$

and the electron current density in the plasma,

$$J_z = -e n_a c \sum_k 2a_0^2 \sin^2 \frac{\psi - \psi_{th}^k}{2} U(\psi - \psi_{th}^k). \tag{13}$$

We can see that, first, the electron density and electron current density are both modulated at the laser frequency and, second, the electron density in the wave is higher than the density of the produced electrons. The latter effect can be explained as follows. The electrons that originate with a zero energy are entrained by the wave in a certain phase and are accelerated to relativistic velocities, so that the accelerated electrons move essentially in phase with the wave. Then, this process repeats for the electrons originating over the next time interval, and so on.

We also consider the EDF averaged over the pump wave period,

$$\langle f \rangle = \frac{1}{2\pi} \int_{\psi}^{\psi + 2\pi} d\psi f. \tag{14}$$

The projection of the phase portrait of the electrons onto the (p_x, p_y) plane is as follows. The electron trajectories uniformly cover a circle of radius a_0, whose center precesses about the origin of the coordinates and describes a circumference of the same radius at a rate equal to the laser frequency. Consequently, the averaging procedure can be performed separately for the longitudinal and transverse momentum components. As a

result, we obtain

$$\langle f\rangle = Zn_a\frac{U(2a_0-p_\perp)}{4\pi a_0\sqrt{4a_0^2-p_\perp^2}} \times\frac{(1+p_z)U(p_z)U(2a_0^2-p_z)}{\pi\sqrt{p_z(2a_0^2-p_z)}}. \quad (15)$$

It is interesting to note that the longitudinal and transverse electron "temperatures" are proportional to $\propto a_0^2$ and $\propto a_0$, respectively.

3.2. Linearly Polarized Wave ($\alpha = 0$)

For a linearly polarized wave, the EDF has the form

$$f = n_a\delta(p_y)\delta\left(p_z-\frac{1}{2}p_x^2\right), \sum_k(1+p_z)\delta(p_x+a_0\sin\psi-a_0\sin\psi_{th}^k)U(\psi-\psi_{th}^k). \quad (16)$$

The electron density and electron current calculated from EDF (16) are equal to

$$n_e = n_a\sum_k\left(1+\frac{1}{2}a_0^2(\sin\psi-\sin\psi_{th}^k)^2\right)U(\psi-\psi_{th}^k), \quad J_z = -en_ac\sum_k\frac{1}{2}a_0^2(\sin\psi-\sin\psi_{th}^k)^2U(\psi-\psi_{th}^k). \quad (17)$$

We can see that they are both modulated at the doubled laser frequency. Clearly, the quantities averaged over the wave phase depend on the threshold phases for ionization, i.e., the threshold values of the field phase that correspond to the ionization states under consideration. However, we can assume that these threshold phases are sufficiently randomly distributed over the laser field period. Indeed, if the field is assumed to be switched on adiabatically in the infinite past, then, because of the smallness of the parameter $(\omega_0\tau)^{-1}$, the field amplitude changes only slightly over the wave period, so that it is not *a priori* clear at which wave phase the field amplitude will exceed the level corresponding to the ionization energy for each successive electron removed. Therefore, we can also average expressions (17) over the random phases ψ_{th}^k:

$$\langle n_e\rangle = Zn_a\left(1+\frac{1}{2}a_0^2\right), \quad \langle J_z\rangle = -Zen_ac\frac{1}{2}a_0^2. \quad (18)$$

Now, we can average the EDF over both the laser field period and threshold phases:

$$\langle f\rangle = Zn_a\frac{1}{\pi^2a_0}(1+p_z)K\left(\sqrt{1-\frac{p_x^2}{4a_0^2}}\right) \times U(4a_0^2-p_x^2)\delta(p_y)\delta\left(p_z-\frac{1}{2}p_x^2\right), \quad (19)$$

where K is the complete elliptic integral.

4. APPLICABILITY RANGE OF OUR APPROACH

The induced polarization wake field that remains in the plasma after the passage of a laser pulse of duration τ has the form

$$E_{pz} = -4\pi\langle J_z\rangle\tau. \quad (20)$$

In order for our model to be valid, the polarization field should have a much smaller impact on the electron motion than the laser field, at least over the laser field period. This requirement imposes the restriction

$$E_p|_{\tau=2\pi/\omega_0} \ll E_0,$$

which reduces to the following condition on the gas and laser-pulse parameters:

$$\frac{1}{2}(1+\alpha)a_0 \ll \frac{\omega_0^2}{2\pi\omega_p^2}, \quad (21)$$

where $\omega_p = (4\pi Ze^2n_a/m)^{1/2}$ is the electron Langmuir frequency of the produced plasma. Condition (21) can be rewritten as the following constraints on the laser pulse intensity:

$$I_{18} \ll \frac{4.8}{(Zn_a[10^{19}\ \mathrm{cm}^{-3}])^2\lambda_{\mu m}^6}$$

for a linearly polarized laser ($\alpha = 0$),

$$I_{18} \ll \frac{2.4}{(Zn_a[10^{19}\ \mathrm{cm}^{-3}])^2\lambda_{\mu m}^6}$$

for a circularly polarized laser ($\alpha = 1$).

5. CONCLUSION

Using the simplest model assumptions, we have calculated the relativistic EDF for a plasma produced in the interaction between an intense laser pulse and a neutral gas. The resulting EDF, which can be derived analytically for linearly and circularly polarized laser fields, depends on the only dimensionless parameter—the amplitude of the vector potential. The EDF is found to be highly anisotropic, which indicates that laser-driven plasmas are subject to the Weibel instability. The degree to which the EDF is anisotropic is proportional to $\sqrt{I}$, so that it would be worthwhile to carry out fur-

ther theoretical and experimental investigations into the possibility of diagnosing intense laser pulses by processing the measured data on the anisotropic relativistic EDF.

The field of an intense laser pulse accelerates the produced electrons in such a manner that they form a relativistic beam propagating in the direction of the pulse. Such a beamlike character of the relativistic EDF should manifest itself as a parametric decay of the pump wave and the generation of longitudinal plasma waves as well as the onset of such specific current instabilities as Buneman and Pierce instabilities (in finite-length systems). Presumably, the processes of nonlinear interaction related to these plasma instabilities will play a governing role in the propagation of a laser radiation and the conversion of its energy into other forms (plasma waves, microwave radiation, the generation of fast particles, etc.).

ACKNOWLEDGMENTS

I am grateful to V.T. Tikhonchuk for his continuing interest in this work and his valuable remarks and to the participants of the Rukhadze seminar for fruitful discussions.

REFERENCES

1. A. J. Taylor, C. R. Tallman, J. P. Roberts, *et al.*, Opt. Lett. **15**, 39 (1990).
2. J. H. Eberly, P. Maine, D. Strickland, *et al.*, Laser Focus **23**, 84 (1987).
3. S. A. Akhmanov, V. A. Vysloukh, and A. S. Chirkin, *The Optics of Femtosecond Pulses* (Nauka, Moscow, 1988).
4. V. Yu. Bychenkov and V. T. Tikhonchuk, Laser Phys. **2**, 525 (1992).
5. B. Luther-Davies, E. G. Gamaliĭ, V. T. Tikhonchuk, *et al.*, Kvantovaya Élektron. (Moscow) **19**, 313 (1992).
6. L. M. Gorbunov and V. I. Kirsanov, Zh. Éksp. Teor. Fiz. **93**, 509 (1987) [Sov. Phys. JETP **66**, 290 (1987)].
7. P. Sprangle, E. Esaray, A. Ting, and G. Joyce, Appl. Phys. Lett. **53**, 2146 (1988).
8. N. Bloembergen, Opt. Commun. **8**, 285 (1973).
9. L. G. Glazov and A. A. Rukhadze, Fiz. Plazmy **15**, 1484 (1989) [Sov. J. Plasma Phys. **15**, 863 (1989)].
10. L. G. Glazov and A. A. Rukhadze, Fiz. Plazmy **15**, 1491 (1989) [Sov. J. Plasma Phys. **15**, 867 (1989)].
11. L. G. Glazov and A. A. Rukhadze, Fiz. Plazmy **19**, 1289 (1993) [Plasma Phys. Rep. **19**, 679 (1993)].
12. L. V. Keldysh, Zh. Éksp. Teor. Fiz. **47**, 1945 (1964) [Sov. Phys. JETP **20**, 1307 (1964)].
13. A. M. Perelomov, V. S. Popov, and M. V. Terent'ev, Zh. Éksp. Teor. Fiz. **51**, 617 (1966) [Sov. Phys. JETP **24**, 401 (1967)].
14. T. S. Luk, V. Johan, H. Egger, *et al.*, Phys. Rev. A **32**, 214 (1985).
15. A. McPherson, G. Gibson, H. Jara, *et al.*, J. Opt. Soc. Am. B **4**, 595 (1987).
16. L. D. Landau and E. M. Lifshitz, *The Classical Theory of Fields* (Nauka, Moscow, 1988; Pergamon, Oxford, 1975).
17. V. A. Buts and A. V. Buts, Zh. Éksp. Teor. Fiz. **110**, 818 (1996) [JETP **83**, 449 (1996)].
18. C. J. McKinstrie and E. A. Startsev, Phys. Rev. E **54**, R1070 (1996).

Translated by O.E. Khadin

Plasma Physics Reports, Vol. 27, No. 2, 2001, pp. 158–163. Translated from Fizika Plazmy, Vol. 27, No. 2, 2001, pp. 170–175.
Original Russian Text Copyright © 2001 by Kuzelev, Rukhadze.

PLASMA KINETICS

Microwave and Optical Gas Discharges in Superstrong Pulsed Fields

M. V. Kuzelev and A. A. Rukhadze

Institute of General Physics, Russian Academy of Sciences, ul. Vavilova 38, Moscow, 117942 Russia

Received August 14, 2000

Abstract—A review is given of theoretical papers on gas breakdown in high-power pulsed microwave and optical fields under conditions such that the electron oscillatory energy in the wave field is much higher than the ionization energy of gas atoms. In microwave fields, which are much weaker than the atomic field, the ionization mechanism for gas atoms is governed by electron-impact avalanche ionization. In high-power optical fields that are comparable in strength to the atomic field, the gas atoms are ionized via the tunneling of the bound electrons. It is shown that, in both cases, the electrons obey similar, highly anisotropic distributions, thereby strongly affecting the stability of the discharge plasma. *© 2001 MAIK "Nauka/Interperiodica".*

1. INTRODUCTION

In the late 1960s, the development of high-power pulsed lasers capable of generating radiation with intensities above 10^{14} W/cm^2 raised questions concerning both the ionization mechanisms for gas atoms in the fields of such a high-power radiation and the electron distribution function in plasmas created by such lasers. In such a strong wave field, the electron oscillatory energy ε_0 is much higher than the ionization energy I_i of gas atoms,

$$\varepsilon_0 = \frac{e^2 E_0^2}{2m\omega_0^2} \gg I_i, \quad (1)$$

where ω_0 is the radiation frequency and E_0 is the electric field strength, which is comparable to the atomic field strength $E_a \simeq 5.1 \times 10^9$ V/cm. Clearly, in such strong radiation fields, the tunneling of the bound electrons is so intense that it becomes an important mechanism for the direct ionization of gas atoms. The tunneling mechanism was studied quite thoroughly in earlier papers [1–3]. As for the electron distribution function in a plasma produced by laser breakdown, the first attempt to calculate it was unsuccessful [4]. The electron distribution function was calculated correctly only much later [5–8]. However, the authors of [5–8] probably did not know that gas breakdown in a strong microwave field had been studied in theoretical works that were published in the early 1980s, and in which not only was the electron distribution function in a discharge plasma calculated but the stability of such a plasma was also thoroughly investigated (see [9, 10] and the literature cited therein). In contrast to optical fields, microwave electric fields generated by present-day pulsed radiation sources are far weaker than the atomic field, in which case the gas atoms are primarily ionized by the impact of oscillating electrons, so that ionization is governed by the development of an electron avalanche. Nevertheless, in both optical and microwave discharge plasmas, the electrons obey similar distribution functions, while the ionization mechanism primarily affects the time evolution of the electron density.

At microwave frequencies ($\omega_0 \approx 2 \times 10^{10}$–$2 \times 10^{11}$ s^{-1}), modern-day pulsed radiation sources are capable of generating radiation with an intensity of about 10^8 W/cm^2, the electric field being $E_0 \lesssim 10^6$ V/cm, which is much weaker than the atomic field E_a. At optical frequencies ($\omega_0 \approx 2 \times 10^{15}$–$2 \times 10^{16}$ s^{-1}), the situation is radically different: the laser pulse intensities are as high as 10^{14}–10^{18} W/cm^2, the electric field being $E_0 \approx 10^9$–10^{10} V/cm, which is comparable with the atomic field E_a or even stronger. In both cases, condition (1) is satisfied by a large margin; moreover, the oscillating electrons may acquire relativistic energies ε_0.

Nevertheless, below we will restrict ourselves to a comparative analysis of papers [7, 9], which survey the results of studying the electron distribution function and the stability of the discharge plasma in optical and microwave frequency ranges at nonrelativistic electron oscillatory energies ε_0. In the nonrelativistic limit, the problem is far simpler to treat; moreover, most of the experiments carried out so far have been related just to this case. The role of relativistic effects (see [8, 10]) is briefly discussed in the Appendix, in which we solve exactly the related problem for a circularly polarized radiation field.

2. ELECTRON DISTRIBUTION FUNCTION AND TIME EVOLUTION OF THE DISCHARGE PLASMA DENSITY

Under condition (1), stochastic (thermal) electron motion in a discharge plasma can be neglected in com-

1063-780X/01/2702-0158$21.00 © 2001 MAIK "Nauka/Interperiodica"

parison with the electron oscillations in the radiation field. Since collisions are very infrequent, we can also ignore the collisional stochastization of the forced electron oscillations. In addition, we can neglect the effect of the polarization electric fields on the radiation field until the electron density $n_e(t)$ of the plasma produced during gas breakdown is below the critical density ($\omega_0^2 > \omega_{Le}^2 = 4\pi e^2 n_e/m$). The plasma density is assumed to be low in comparison with the neutral gas density n_0, so that the latter can be considered to be constant.

The kinetic equation for plasma electrons produced during gas breakdown in a strong pulsed field can be written as

$$\frac{\partial f_0}{\partial t} + \mathbf{v}\frac{\partial f_0}{\partial \mathbf{r}} + e\left\{\mathbf{E}_0 + \frac{1}{c}[\mathbf{v}\times\mathbf{B}_0]\right\}\frac{\partial f_0}{\partial \mathbf{p}} = n_0 w_i \delta(\mathbf{p}), \quad (2)$$

where $\mathbf{E}_0(\xi)$ and $\mathbf{B}_0(\xi)$ are the electric and magnetic fields of a wave propagating along the z-axis, $\xi = \omega_0 t - \mathbf{k}_0\mathbf{r} = \omega_0(t - z/c)$, and w_i is the ionization probability for gas atoms.

In the nonrelativistic limit, the magnetic field in Eq. (2) can be neglected and the electric field can be assumed to depend only on time. Under these assumptions, Eq. (2) becomes

$$\frac{\partial f_0}{\partial t} + e\mathbf{E}_0\frac{\partial f_0}{\partial \mathbf{p}} = n_0 w_i \delta(\mathbf{p}). \quad (3)$$

In the case of microwave breakdown, we deal with electron-impact ionization, so that the ionization probability w_i has the form [9]

$$w_i = \int \nu_i(|\mathbf{p}'|) f_0(\mathbf{p}', t) d\mathbf{p}', \quad (4)$$

where $\nu_i(|\mathbf{p}|) = \frac{|\mathbf{p}|}{m}\sigma_i(|\mathbf{p}|)$ is the rate of ionizing collisions and $\sigma_i(|\mathbf{p}|)$ is the cross section for ionization of a gas atom by electron impact. In the case of optical breakdown, we have [11]

$$w_i = 4\omega_a\left(\frac{I_i}{I_a}\right)^{5/2}\frac{E_a}{|\mathbf{E}_0|}\exp\left[-\frac{2}{3}\left(\frac{I_i}{I_a}\right)^{3/2}\frac{E_a}{|\mathbf{E}_0|}\right], \quad (5)$$

where $I_a = \hbar\omega_a/2 \approx 13.6$ eV is the ionization energy of a hydrogen atom and $\omega_a = 5\times 10^{15}$ s^{-1} is the atomic frequency. Expression (5) was derived under the assumption that the tunneling time of an electron is short in comparison with the period of the field $\mathbf{E}_0(t)$, so that the latter was assumed to be constant. Additionally, expression (5) is valid for a plasma containing singly charged ions (taking into account multiply charged ions is not of fundamental importance and does not qualitatively change the results obtained below).

Substituting expressions (4) and (5) into Eq. (3) makes it possible to reveal the difference in the phenomena of gas breakdown in the pulsed fields of microwave and optical ranges. For a microwave discharge, Eq. (3) for $f_0(\mathbf{p}, t)$ is a homogeneous integrodifferential equation whose positive eigenvalue $\gamma(E_0)$ determines the avalanche ionization constant:

$$\frac{\partial n_e}{\partial t} = \gamma(E_0) n_e = n_0\int\frac{|\mathbf{p}'|}{m}\sigma_i(|\mathbf{p}'|) f_0(\mathbf{p}', t) d\mathbf{p}'. \quad (6)$$

For an optical discharge, Eq. (3) is an inhomogeneous equation with a prescribed source and describes the time evolution of the plasma density during gas breakdown:

$$n_e(t) = n_0\int_0^t dt' w_i(t') = 4\omega_a n_0\left(\frac{I_i}{I_a}\right)^{5/2}\int dt'\frac{E_a}{|\mathbf{E}_0|}\exp\left[-\frac{2}{3}\left(\frac{I_i}{I_a}\right)^{3/2}\frac{E_a}{|\mathbf{E}_0|}\right]. \quad (7)$$

However, we can neglect the right-hand sides of Eqs. (2) and (3) in the first approximation and calculate the electron distribution function directly by solving the Vlasov equation if the following conditions[1] are satisfied:

$$\omega_0 \gg \gamma, \quad w_i(E_0), \quad (8)$$

where the avalanche ionization constant $\gamma(E_0)$ is to be determined and, for optical breakdown, the probability $w_i(E_0)$ is described by expression (5). In this approximation, for $\mathbf{E}_0(t) = \mathbf{E}_0\cos\omega_0 t$, the solution to Eq. (3) can be sought as a function of the characteristic of this equation:

$$\frac{d\mathbf{v}}{dt} = \frac{e\mathbf{E}_0}{m}\cos\omega_0 t, \qquad \mathbf{v} = \frac{e\mathbf{E}_0}{m\omega_0}(\sin\omega_0 t - \sin\varphi), \quad (9)$$

where φ is the field phase at which an electron originates. For the solution of the form $f_0(\mathbf{v}, t) = n_e(t)\,\tilde{f}_0(\mathbf{v})$, we obtain

$$\tilde{f}_0(\mathbf{v}) = \delta(\mathbf{v}_\perp)\delta[v_\parallel - v_E(\sin\omega_0 t - \sin\varphi)], \quad (10)$$

[1] The electron distribution function in a discharge plasma may, in principle, be calculated under the conditions opposite to (8), in which case the breakdown occurs almost instantaneously (on a time scale shorter than the field period), so that the field $\mathbf{E}_0(t)$ can be assumed to be constant. If the gas pressure is sufficiently low and a fully ionized plasma is subcritical, then we can again solve the homogeneous Vlasov equation (3), in which case there is no need to average solution (10) over the field phases at which the electrons originate, because the breakdown occurs at a fixed phase of the field. However, this problem goes beyond the scope of this paper. Under the conditions opposite to (8), the problem under discussion was treated by Soldatov [8], who took into account the effects of multiple ionization and performed averaging over the field phases.

where $v_E = eE_0/m\omega_0$ is the electron oscillatory velocity in an alternating electric field and the function $\tilde{f}_0(\mathbf{v})$ satisfies the normalization condition $\int d\mathbf{v}\tilde{f}_0(\mathbf{v}) = 1$.

Taking into account conditions (8), we can average distribution function (10) over the field phases φ in order to arrive at the following expression, which is known as the equipartition in phases [9]:

$$\langle \tilde{f}_0(v)\rangle = \frac{1}{\pi\sqrt{v_E^2 - (v_\parallel + v_E\cos\omega_0 t)^2}}\delta(\mathbf{v}_\perp). \quad (11)$$

Now, we can describe the time evolution of $n_e(t)$. Recall that, in an optical discharge plasma, the electron density $n_e(t)$ is described by integral expression (7) taken with the field $\mathbf{E}_0(t) = \mathbf{E}_0\cos\omega_0 t$. In the case of microwave breakdown, Eq. (6) implies that the avalanche ionization develops in an exponential manner:[2]

$$n_e = n_{e0}e^{\gamma t}, \quad \gamma = \frac{n_0}{\pi}\int_0^\infty dv\frac{v\sigma_i(v)}{\sqrt{v_E^2 - v^2}}. \quad (12)$$

Here, the ionization cross section $\sigma_i(v)$ can be described with good accuracy in the Born approximation [11]:

$$\sigma_i = \frac{\alpha}{v^2}\ln\left(\frac{v}{\sqrt{2I_i/m}}\right)\eta(v - \sqrt{2I_i}/m), \quad (13)$$

where α, as well as I_i, differs between different gases (for hydrogen, we have $\alpha = 16.3$).

To conclude this section, we briefly discuss the applicability ranges of conditions (8). For an optical discharge plasma, conditions (8) hold for electric fields $E_0 < E_a = 5.1 \times 10^9$ V/cm and are essentially independent of the neutral gas pressure (up to pressures of several tens of atmospheres). For a microwave discharge plasma, conditions (8) depend strongly on the neutral gas density and are well satisfied up to gas pressures of $P_0 \approx 10$–100 torr.

Hence, under conditions (1) and (8), the electron velocity distribution function for both microwave and optical discharge plasmas is well described by equipartition (11), which implies that the instants at which the electrons originate are evenly distributed in phases of the electric field.

[2] Note that, for microwave discharges in hydrogen, helium, and air, Glazov and Rukhadze [9] solved Eq. (3) numerically using the experimentally measured values of $\sigma_i(v)$ at electric fields of up to $E_0 \approx 10^6$ V/cm. The function $\tilde{f}_0(v)$ obtained in [9] differs by no more than 20% from the function in expression (11), and the discrepancy between the computed values of $\gamma(E_0)$ and the avalanche ionization constant in formula (12) does not go beyond the computational error.

3. STABILITY OF THE PLASMA PRODUCED DURING GAS BREAKDOWN IN A STRONG WAVE FIELD

3.1. Above, we have shown that distribution function (11) for electrons in a discharge plasma is highly anisotropic with respect to the direction of the radiation field, which, first of all, should result in the onset of the well-known Weibel instability [12] (see also [13]). In order to convince ourselves that this conclusion is valid and to find the instability growth rate, we turn to the adiabatic approximation, assuming that the instability grows faster than the plasma density. In this approximation, we can use the following dispersion relation for small perturbations:

$$\left|k^2\delta_{ij} - k_i k_j - \frac{\omega^2}{c^2}\varepsilon_{ij}(\omega, \mathbf{k})\right| = 0, \quad (14)$$

where the dielectric tensor elements $\varepsilon_{ij}(\omega, \mathbf{k})$ have the form [13]

$$\varepsilon_{ij}(\omega, \mathbf{k}) = \left(1 - \frac{\omega_{Li}^2}{\omega^2}\delta_{ij}\right) + \frac{\omega_{Le}^2}{\omega^2}\int d\mathbf{v}\left[v_i\frac{\partial\tilde{f}_0}{\partial v_j} + v_i v_j\frac{\mathbf{k}\dfrac{\partial\tilde{f}_0}{\partial\mathbf{v}}}{\omega - \mathbf{kv}}\right]. \quad (15)$$

Dielectric function (15) was derived in the approximation of cold ions. The kinetic equation for the perturbed electron distribution function was solved without considering the strong external high-frequency field, which is valid in a short-wavelength limit ($kv_0 \approx \omega_{Le} \gg \omega_{Li}$).

The nonzero contributions of the electron distribution function to dielectric tensor (15) are equal to [9]

$$\delta\varepsilon_{11} = \delta\varepsilon_{22} = -\frac{\omega_{Le}^2}{\omega^2},$$

$$\delta\varepsilon_{13} = \delta\varepsilon_{31} = \frac{\omega_{Le}^2}{\omega^2}\frac{k_\perp}{k_\parallel}\left(1 - \frac{s}{\sqrt{1 - k^2 v_E^2/\omega^2}}\right), \quad (16)$$

$$\delta\varepsilon_{33} = -\frac{\omega_{Le}^2}{\omega^2}\frac{k_\perp^2}{k_\parallel^2} + \frac{\omega_{Le}^2}{k_\parallel^2}\left(\frac{2k_\perp^2}{\omega^2} + \frac{k_\perp^2 + k_\parallel^2}{\omega^2 - k_\parallel^2 v_E^2}\right)\frac{s}{\sqrt{1 - k^2 v_E^2/\omega^2}},$$

where

$$s = \begin{cases} \operatorname{sgn}\operatorname{Re}\omega \cdot \operatorname{sgn}\operatorname{Im}\omega \\ 1 \quad \text{for} \quad \operatorname{Re}\omega = 0 \\ 1 \quad \text{for} \quad \operatorname{Im}\omega = 0, \quad k^2 v_E^2 < \omega^2 \\ \operatorname{sgn}\omega \quad \text{for} \quad \operatorname{Im}\omega = 0, \quad k^2 v_E^2 > \omega^2. \end{cases} \tag{17}$$

Substituting expressions (15)–(17) into Eq. (14) yields the following dispersion relation for electron perturbations propagating across the radiation field ($k_\parallel = 0$):

$$k^2 c^2 = \omega^2 \left[1 - \frac{\omega_{Le}^2}{\omega^2} \left(1 + \frac{k^2 v_E^2}{2\omega^2} \right) \right]. \tag{18}$$

From Eq. (18), we obtain the following expression, which characterizes the growth rate of the Weibel instability in the frequency range $\omega^2 \ll \omega_{Le}^2$ [13]:

$$\omega^2 = -\frac{\omega_{Le}^2 k^2 v_E^2}{2(\omega_{Le}^2 + k^2 c^2)} \lesssim -\omega_{Le}^2 \frac{v_E^2}{2c^2}. \tag{19}$$

Clearly, transverse electron perturbations are unstable only when the growth rate determined by expression (19) exceeds the avalanche ionization constant $\gamma(E_0)$ in the case of microwave breakdown or the ionization probability w_i in the case of optical breakdown.

Electron perturbations propagating strictly along the radiation field are stable.

3.2. In contrast to the Weibel instability, which is characteristic of a discharge plasma with an arbitrary anisotropic electron distribution function (in particular, with a distribution function whose anisotropy is associated with the high-frequency field), the instability that we will analyze in this section occurs in the range $\omega_0 \gg k v_E \approx \omega_{Le}$ and is peculiar only to equipartition distribution function (11) having a positive (nonequilibrium) slope along the energy axis. Recall that, for an equilibrium (Maxwellian) electron energy distribution, the instability to be studied here never occurs in this frequency range (see [14]).

The dispersion relation for purely potential electron–ion oscillations in a strong high-frequency ($\omega_0 \gg \omega_{Le}$) field has the form [14]

$$\begin{aligned} &1 + \delta\varepsilon_e^l(\omega, \mathbf{k}) + \delta\varepsilon_i^l(\omega, \mathbf{k}) \\ &+ \left[1 - J_0^2\left(\frac{k_\parallel v_E}{\omega_0} \right) \right] \delta\varepsilon_e^l(\omega, \mathbf{k}) \delta\varepsilon_i^l(\omega, \mathbf{k}) = 0, \end{aligned} \tag{20}$$

where J_0 is a Bessel function. With allowance for equipartition distribution function (11), the partial longitudinal dielectric functions $\delta\varepsilon_{e,i}^l(\omega, \mathbf{k})$ for electrons and ions are equal to [9]

$$\begin{aligned} \delta\varepsilon_i^l(\omega, \mathbf{k}) &= -\omega_{Li}^2/\omega^2, \\ \delta\varepsilon_e^l(\omega, \mathbf{k}) &= -\frac{\omega_{Le}^2}{k^2} \int d\mathbf{v} \frac{\mathbf{k} \dfrac{\partial \tilde{f}_0(\mathbf{v}, t)}{\partial \mathbf{v}}}{\omega - \mathbf{k}\mathbf{v}} \\ &= -\frac{\omega_{Le}^2 s}{\omega^2 (1 - k_\parallel^2 v_E^2/\omega^2)^{3/2}}. \end{aligned} \tag{21}$$

We substitute expressions (21) into dispersion relation (20) to obtain unstable solutions corresponding to low-frequency ion oscillations:

$$\omega = \begin{cases} \omega_{Li}^2 \left[1 + i \dfrac{\omega_{Le}^2 \omega_{Li}}{|k_\parallel v_E|^3} J_0^2\left(\dfrac{k_\parallel v_E}{\omega_0} \right) \right] \\ k_\parallel^2 v_E^2 \gg \omega_{Le}^2 \\ |k_\parallel v_E| \left(\dfrac{m}{M} \right)^{1/3} \dfrac{\sqrt{3} + i}{2}, \quad k_\parallel^2 v_E^2 \ll \omega_{Le}^2. \end{cases} \tag{22}$$

We can see that the instability under analysis is governed by the positive slope of distribution function (11) along the energy axis and can be interpreted as stimulated Cherenkov excitation of the low-frequency ion oscillations by the electrons oscillating in the radiation field. Of course, this instability can only grow at a rate faster than that at which the plasma density increases; i.e., the growth rate should exceed the avalanche ionization constant $\gamma(E_0)$ in the case of microwave breakdown or the ionization probability w_i in the case of optical breakdown.

3.3. Finally, we discuss the instability resulting from stimulated Raman scattering (SRS) of the incident radiation by electron-density waves in a plasma created by the radiation itself. Since the SRS instability is described in many textbooks (see, e.g., [13]) and was discussed in detail by Soldatov [8] for conditions typical of optical breakdown, we will not derive the relevant dispersion relation and will simply present the final expression for the instability growth rate, which is highest for direct backscattering:

$$\operatorname{Im}\omega = \frac{v_E}{2c} \sqrt{\omega_{Le} \omega_0}. \tag{23}$$

Of course, in order for this instability to occur, growth rate (23) should exceed the rate at which the plasma density increases during gas breakdown.

Hence, we can conclude that discharge plasmas in superstrong pulsed wave fields are subject to a number of instabilities caused by such factors as the anisotropic nature of equipartition distribution function (11), its positive (nonequilibrium) derivative with respect to velocity, and the SRS of the radiation field by electron-density waves.

4. BRIEF DISCUSSION OF THE RESULTS OBTAINED

The above analysis allows us to draw the following conclusions:

(i) When the radiation frequency exceeds the rate at which the plasma density increases, the electron distribution functions in both microwave and optical discharges in gases are described with good accuracy by equipartition distribution function (11), which implies that the instants at which the electrons originate are evenly distributed in the field phases. Microwave and optical discharges differ only in the time evolution of the electron density, which is governed by the ionization mechanism: during microwave breakdown, the gas atoms are ionized by electron impact, whereas, during optical breakdown, the plasma is produced via tunneling ionization.

(ii) In both microwave and optical discharges, the plasma electrons experience rapid oscillations along the wave electric field, the electron oscillatory energy being much higher than the ionization energy of the gas atoms. As a result, fast electrons can escape from the region of the wave electric field and ionize the surrounding gas, so that it becomes possible to produce even overdense plasmas. Additionally, after the microwave (or optical) pulse has come to an end, the plasma recombination is hindered by the high mean energy of the electrons in a discharge plasma. In other words, during gas breakdown in superstrong pulsed fields, a long-lived plasma formation should be created.

(iii) Discharge plasmas in superstrong pulsed fields are subject to instabilities associated with such factors as the anisotropic nature of the electron distribution function (the Weibel instability), its positive (nonequilibrium) derivatives with respect to velocity (kinetic excitation of the ion oscillations), and periodic temporal variations of the mean electron energy (the parametric instability, or SRS of the wave field by electron-density waves).

(iv) If the induced motion of electrons is relativistic, then they acquire a mean velocity in the propagation direction of the ionizing radiation as a result of a drift motion in the crossed electric and magnetic fields of the wave.

ACKNOWLEDGMENTS

We are grateful to A.V. Soldatov, since this study was stimulated by discussions in reviewing his paper [8]. This work was supported in part by the Ministry of Science and Technology of the Russian Federations (under the grants “Russian Universities” and “Microwaves”).

APPENDIX

Relativistic Effects during Gas Breakdown in Intense Wave Fields

Relativistic effects can be described by solving complete equation (2). Under conditions (8), the characteristics of Eq. (2) with zero on the right-hand side can be written as

$$\tilde{p}_{x,y} = \pm m v_E \begin{cases} \sin\psi - \sin\psi_0 \\ \cos\psi - \cos\psi_0, \end{cases} \qquad \tilde{p}_z = \frac{\tilde{p}_x^2 + \tilde{p}_y^2}{2mc}. \tag{A.1}$$

Here, the wave field has the form

$$\mathbf{E}_0 = (E_{0x} = E_0\cos\psi,\ E_{0y} = \alpha E_0 \sin\psi,\ 0), \qquad \mathbf{B}_0 = (-E_{0y},\ E_{0x},\ 0), \tag{A.2}$$

where $\psi = \omega_0(t - z/c)$ is the field phase (the wave is assumed to propagate along the z-axis), α is the parameter characterizing the ellipticity of polarization of the wave field ($\alpha = 0$ for linear polarization, and $\alpha = 1$ for circular polarization), and ψ_0 is the field phase at which an electron originates.

We represent the electron distribution function $f_0(\mathbf{p}, t)$ as $f_0(\mathbf{p}, t) = \tilde{f}_0(\mathbf{p})n_e(t)$, where the electron density $n_e(t)$ is described by formulas (6) and (7), with the corresponding relativistic expressions for $\sigma_i(|\mathbf{p}|)$ and $w_i(E_0)$, and the function $f_0(\mathbf{p})$, which is normalized to 1, has the form

$$\tilde{f}_0(\mathbf{p}) = \delta(\mathbf{p} - \tilde{\mathbf{p}}) = \delta(p_x - \tilde{p}_x)\delta(p_y - \tilde{p}_y)\delta(p_z - \tilde{p}_z). \tag{A.3}$$

Averaging function (A.3) over the initial phases ψ_0 leads to a fairly lengthy expression, which, however, can be considerably simplified for a circularly polarized wave ($\alpha = 1$). In this case, the product $\delta(p_x - \tilde{p}_x)\delta(p_y - \tilde{p}_y)$ is independent of ψ_0 and is equal to

$$\delta(p_x - \tilde{p}_x)\delta(p_y - \tilde{p}_y) = \frac{1}{2\pi m v_E}\delta(P_\perp - m v_E), \tag{A.4}$$

where

$$P_\perp^2 = p_x^2 + p_y^2 + m^2 v_E^2 + 2m v_E(p_x\sin\psi - p_y\cos\psi). \tag{A.5}$$

As a result, function (A.3) reduces to

$$\tilde{f}_0(\mathbf{p}) = \frac{1}{2\pi m v_E}\delta(p_\perp - m v_E)\delta\left[p_z - 2m\frac{v_E^2}{c}\sin^2\frac{(\psi - \psi_0)}{2}\right]. \tag{A.6}$$

Finally, we average function (A.6) over ψ_0 to obtain

$$\tilde{f}_0(\mathbf{p}) = \frac{1}{2\pi m v_E}\delta(p_\perp - m v_E)\frac{1}{\sqrt{p_z(2m v_E^2/c - p_z)}}. \quad \text{(A.7)}$$

In order to relate our results to those of [8, 10], we also average function (A.7) over the microwave period. We thus arrive at the following expression, which corrects for the misprinted formula (9) in [10]:

$$\langle \tilde{f}_0(\mathbf{p})\rangle = \frac{1}{2\pi^2 p_\perp}\frac{1}{\sqrt{4m^2 v_E^2 - p_\perp^2}} \times \frac{1}{\sqrt{p_z(2m v_E^2/c - p_z)}}. \quad \text{(A.8)}$$

Having derived expressions (A.7) and (A.8), we can draw an important conclusion: if the electron motion is relativistic, then the electrons acquire a nonzero longitudinal (with respect to the propagation direction of the wave) momentum $\bar{p}_z \approx 2m v_E^2/c$ as a result of their drift in the crossed electric and magnetic fields of the ionizing radiation. Note also that function (A.8), in which the longitudinal electron velocity is nonzero and which has a positive derivative with respect to the velocity component, makes it possible to describe the onset of new electron–ion instabilities analogous to the Buneman and ion acoustic instabilities as well as to the instabilities analyzed in Subsection 3.2.

REFERENCES

1. F. V. Bunkin and A. M. Prokhorov, Zh. Éksp. Teor. Fiz. **46**, 1090 (1964) [Sov. Phys. JETP **19**, 739 (1964)].
2. L. V. Keldysh, Zh. Éksp. Teor. Fiz. **47**, 1945 (1964) [Sov. Phys. JETP **20**, 1307 (1964)].
3. A. M. Perelomov, V. S. Popov, and M. V. Terent'ev, Zh. Éksp. Teor. Fiz. **50**, 1393 (1966) [Sov. Phys. JETP **23**, 924 (1966)].
4. Yu. A. Afanas'ev, É. M. Belenov, O. N. Krokhin, and I. A. Poluéktov, Zh. Éksp. Teor. Fiz. **63**, 121 (1972) [Sov. Phys. JETP **36**, 64 (1973)].
5. V. V. Korobkin and M. Yu. Romanovskiĭ, Pis'ma Zh. Éksp. Teor. Fiz. **53**, 493 (1991) [JETP Lett. **53**, 517 (1991)].
6. B. N. Chichkov, S. A. Shumsky, and S. A. Uryupin, Phys. Rev. A **45**, 7475 (1992).
7. V. Yu. Bychenkov and V. T. Tikhonchuk, Laser Phys. **2**, 525 (1992).
8. A. V. Soldatov, Fiz. Plazmy **27**, 165 (2001) [Plasma Phys. Rep. **27**, 153 (2001)].
9. L. G. Glazov, A. V. Ignat'ev, and A. A. Rukhadze, in *High-Frequency Discharge in Wave Fields* (Inst. Prikl. Fiz., Gorki, 1988), p. 63.
10. L. G. Glazov and A. A. Rukhadze, Fiz. Plazmy **19**, 1289 (1993) [Plasma Phys. Rep. **19**, 679 (1993)].
11. L. D. Landau and E. M. Lifshitz, *Quantum Mechanics: Non-Relativistic Theory* (Nauka, Moscow, 1963; Pergamon, New York, 1977).
12. E. Weibel, Phys. Rev. **2**, 83 (1959); Phys. Fluids **2**, 52 (1959).
13. A. F. Alexandrov, L. S. Bogdankevich, and A. A. Rukhadze, *Principles of Plasma Electrodynamics* (Vysshaya Shkola, Moscow, 1988; Springer-Verlag, Berlin, 1984).
14. V. P. Silin, *Interaction of High-Power Radiation with Plasmas* (Nauka, Moscow, 1973).

Translated by I.A. Kalabalyk

Plasma Physics Reports, Vol. 27, No. 2, 2001, pp. 164–171. Translated from Fizika Plazmy, Vol. 27, No. 2, 2001, pp. 176–183.
Original Russian Text Copyright © 2001 by Akishev, Dem'yanov, Karal'nik, Pan'kin, Trushkin.

LOW-TEMPERATURE PLASMA

Pulsed Regime of the Diffusive Mode of a Barrier Discharge in Helium

Yu. S. Akishev, A. V. Dem'yanov, V. B. Karal'nik, M. V. Pan'kin, and N. I. Trushkin

Troitsk Institute for Innovation and Thermonuclear Research, Troitsk, Moscow oblast, 142092 Russia

Received May 19, 2000

Abstract—Periodic pulsations of the active current component are revealed experimentally in transversely homogeneous barrier discharges in helium at small values of the parameter *Pd* (below 500 torr mm) and moderate frequencies of the applied voltage ($f < 100$ kHz). The frequency of the current pulsations is higher than the frequency of the well-studied pulsations in a transversely inhomogeneous streamer barrier discharge in air by a factor of approximately 100. Numerical calculations show that the physical nature of the observed pulsations can be explained in terms of the negative differential resistance of the cathode fall region, which occupies essentially the entire interelectrode gap in each half-period of the applied voltage. © *2001 MAIK "Nauka/Interperiodica".*

1. INTRODUCTION

Barrier discharges are low-frequency (lower than 1 MHz) ac discharges between the plates of a gas-filled capacitor in which either one or both of the electrodes are coated with a dielectric material. At present, barrier discharges are widely applied in many areas of practical activity such as ozone generation, light sources, plasma displays, modification of surfaces, etc. Therefore, it becomes relevant to study the spatial structure and current characteristics of barrier discharges.

Plane barrier discharges are frequently encountered in experimental studies. In planar geometry, several modes of barrier discharge have been revealed, depending on the interelectrode distance d, the frequency f and amplitude U_0 of the applied voltage, and also the sort and pressure P of the working gas.

The most familiar mode is the streamer mode of a barrier discharge in an electronegative gas (air or oxygen) at pressures equal to atmospheric pressure or higher [1, 2]. The waveforms of the discharge current in the streamer mode show a fairly regular series of sharp and rare (about ten) spikes of approximately the same amplitude in each half-period of the applied voltage. Every current spike corresponds to numerous streamers (or microdischarges) that are excited simultaneously in the interelectrode gap when the applied voltage becomes higher than the breakdown voltage and rapidly decay due to attachment and ion–ion recombination when the applied voltage becomes lower than the breakdown voltage. Since the steamers are randomly distributed in space, a barrier discharge in this mode looks diffusive and transversely homogeneous.

In electropositive gases at large values of the parameter *Pd* (≥500–1000 torr mm) and low frequencies of the applied voltage ($f < 100$ kHz), barrier discharges are actually observed to be diffusive and transversely homogeneous and resemble quasisteady glow discharges [3–6]. The waveforms of the current in this discharge mode show a single spike, which corresponds to the transversely uniform breakdown of a gas in the interelectrode gap when the applied voltage exceeds the breakdown voltage. Under these conditions, the voltage drop across the homogeneous discharge column is higher than that across the cathode fall of a glow discharge. After the breakdown, no decay processes are observed: the plasma is maintained in a quasisteady manner until the total current falls off almost to zero.

At small values of *Pd* (≤500–1000 torr mm) and high frequencies of the applied voltage ($f \geq 100$ kHz), a barrier discharge in an electropositive gas usually evolves into current filaments regularly distributed over the interelectrode gap. The filaments are observed to be diffusive, and their transverse sizes are larger than those of streamers in electronegative gases [7]. The waveforms of the current in this discharge mode also show a single spike, corresponding to the breakdown of the interelectrode gap. Two-dimensional simulations [7] of the discharge evolving into this mode reveal that, several tens of microseconds after the external voltage is turned on, the gas breakdown over each half-period of the applied voltage occurs in a transversely homogeneous fashion and the voltage drop across the cathode fall (which is in a subnormal state) exceeds that across the discharge plasma column. Over each of the subsequent half-periods, the discharge after breakdown is observed to be structured; the current filaments are regularly distributed over the interelectrode gap and persist until the total current falls off almost to zero. A transversely homogeneous discharge evolves into a transversely inhomogeneous state within a very short time scale (about 1 μs). In a structured discharge mode, the volt-

1063-780X/01/2702-0164$21.00 © 2001 MAIK "Nauka/Interperiodica"

age across the current filament is comparable to or even higher than the voltage across the cathode fall, which evolves into a nearly normal state.

In this paper, we report the results of our experiments with barrier discharges in an electropositive gas (helium) at small values of the parameter Pd (<500 torr mm) and low frequencies of the applied voltage ($f < 100$ kHz). Under these conditions, the voltage across the plasma column after the breakdown of a gas in the interelectrode gap is much lower than the voltage drop across the cathode fall. Consequently, the breakdown and post-breakdown discharge stages are governed primarily by the way in which the cathode fall evolves into a steady state and then decays. This discharge mode, which was discovered for the first time in our experiments [8], is characterized by regular current pulsations during each half-period of the applied voltage. Below, we will describe the experimental results and propose a simplified model for calculating the waveforms of the current in the pulsed regime of a barrier discharge.

In order to illustrate the above considerations, we present an illustrative and useful diagram of the modes of barrier discharge in the parameter plane (f, Pd). In Fig. 1, this plane is conditionally divided into four regions each corresponding to one of the above discharge modes. Of course, this is merely a qualitative diagram, because the parameter values corresponding to the boundaries between these regions depend largely on the content of the gas and its pressure.

2. EXPERIMENTAL DEVICE

Our experiments were carried out with the device shown schematically in Fig. 2. We used 2-mm-thick quartz plates 70 × 70 mm in size as the barriers, the interelectrode gap being 1.2 mm. The areas of the metal films with which the plates were vacuum-coated and which played the role of the capacitor plates were both equal to 14 cm^2. The measured capacitances of the barriers and interelectrode gap were 17.23 and 10.37 pF, respectively.

Barrier discharges were initiated in high-purity helium at the pressure P = 100 torr. To maintain the high degree of purity, helium was pumped through the gas-discharge chamber at a slow rate. A high-voltage generator made it possible to vary the amplitude and frequency of the sinusoidal voltage applied to the capacitor plates from zero to 4 kV and 120 kHz, respectively. The oscilloscope traces of the current and voltage were recorded by S8-9 and Tektronix TDS-520 oscillographs. The discharges between two opaque electrodes can be observed visually in two mutually perpendicular directions, parallel to the barrier planes.

3. EXPERIMENTAL RESULTS AND DISCUSSIONS

Figures 3 and 4 show several typical waveforms of the current in the pulsed regime of a barrier discharge at different frequencies f and amplitudes U_0 of the voltage applied to the interelectrode gap. We can see that, the higher the amplitude U_0, the larger the number of regular current spikes in each series (i.e., in each half-period of the applied voltage). At a fixed amplitude U_0, the number of current spikes in each series increases as the frequency of the applied voltage decreases, because the interval Δt between successive current spikes depends weakly on the frequency f. Since this interval is characteristically equal to $\Delta t \simeq 10$–20 μs, only one current spike was observed at high frequencies. For comparison, note that the characteristic interval

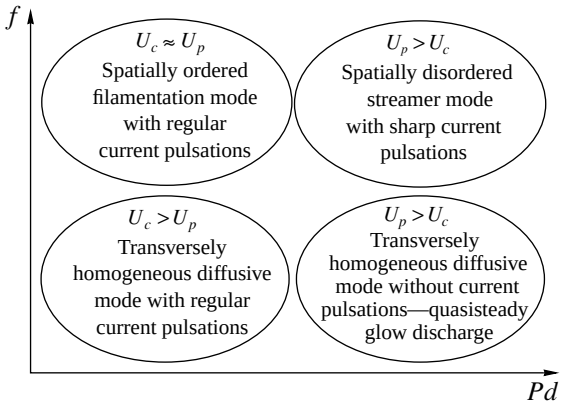

Fig. 1. Diagram of the modes of a barrier discharge: U_c is the voltage drop across the cathode fall and U_p is the voltage drop across the plasma column.

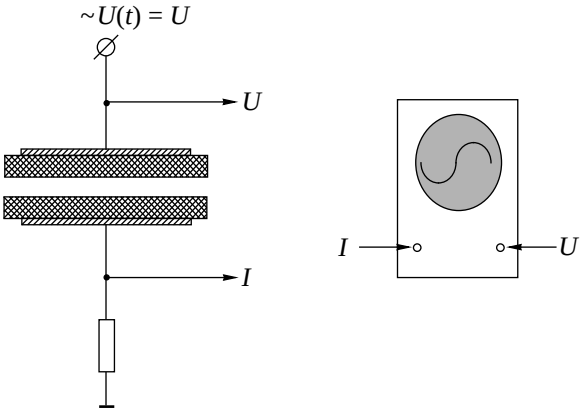

Fig. 2. Schematic of the experimental device for studying barrier discharges.

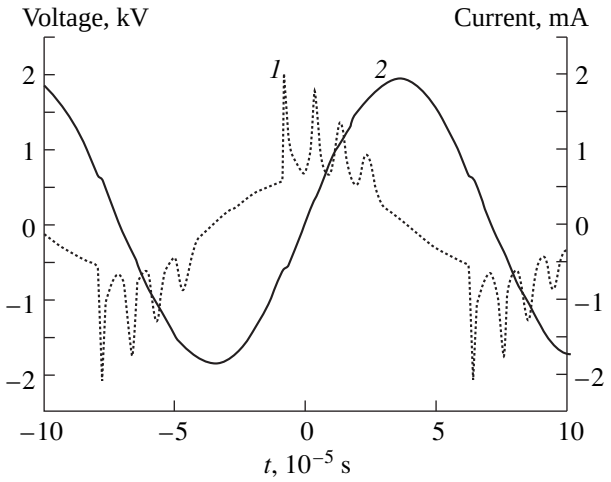

Fig. 3. Waveforms of (*1*) the current and (*2*) applied voltage in the pulsed regime of a barrier discharge for $f = 7$ kHz and $U_0 = 1.9$ kV. The amplitude of the first spike in each series of current spikes is reduced by an oscillograph by a factor of approximately 2.

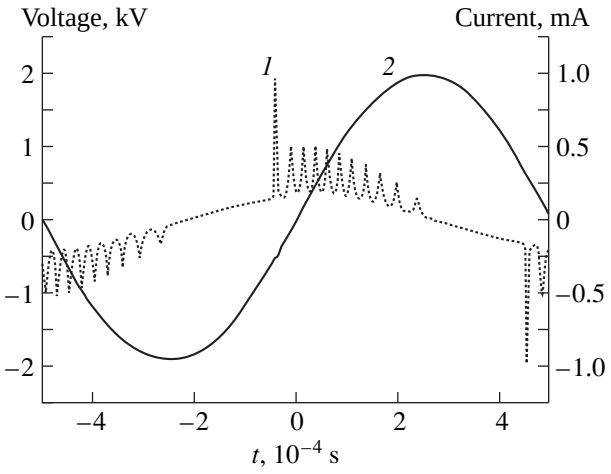

Fig. 4. Waveforms of (*1*) the current and (*2*) applied voltage in the pulsed regime of a barrier discharge for $f = 1$ kHz and $U_0 = 1.9$ kV.

between current spikes in the streamer mode of a barrier discharge in air (at $f = 50$ Hz) is 0.5–1.5 ms, the spike duration being 10–100 ns. In other words, the frequency of the newly discovered current pulsations in the diffusive mode of a barrier discharge in He is about two orders of magnitude higher than that of the well-studied current pulsations in the streamer mode of a barrier discharge in an electronegative gas.

When the amplitude of the applied voltage is close to the minimum amplitude $U_{0\,\min}$ at which the breakdown occurs, the waveform of the current shows a single small spike near the peak of the applied voltage. The lowest breakdown voltage, reconstructed from $U_{0\,\min}$, was found to be about 295 V, which agrees with the published data on the breakdown voltage (reconstructed from the Paschen curves) for He at Pd = 120 torr mm [9].

Note that the first (highest) current spike corresponds to the breakdown of a gas in the interelectrode gap and the appearance of the cathode fall. The subsequent spikes reflect oscillations of the cathode fall, which last until the end of the half-period. In each series, the amplitude of the spikes gradually decreases, starting with the highest spike. The barely visible trailing edge of the last spike in the series always occurs approximately at the peak of the applied voltage.

As the amplitude U_0 increases, the highest spike is displaced to the left from the peak of the applied voltage, so that, at large amplitudes U_0, it always occurs at the negative voltage phase. On the whole, regular current spikes of positive polarity always occur at the phase of the applied voltage at which the time derivative of the voltage amplitude is positive, $dU/dt > 0$, and vice versa.

The spikes of the total discharge current provide information on the magnitude of the active current component (i.e., the conduction current) in the discharge. The contribution of the active component to the total current increases with increasing U_0, thereby reducing the phase shift between the total discharge current and the applied voltage (the phase shift becomes smaller than 90°). Note that, between the successive spikes, the pulsed active current component decreases but does not vanish. This circumstance supports the above conclusion that the cathode fall always persists between the current spikes.

To conclude this section, we point out the following experimental observation. In discharges in helium with a very small (smaller than one percent) admixture of air, the number of current spikes was markedly (severalfold) larger, but their intensity was lower.

4. MATHEMATICAL MODEL OF A BARRIER DISCHARGE

Our experiments showed that, in the pulsed regime, barrier discharges in He are transversely homogeneous. Consequently, we can model the nonlinear discharge dynamics in the one-dimensional approximation, assuming that the discharge parameters inside a gas-filled capacitor changes only in the direction of the discharge current. Our model is based on the following familiar continuity equations describing the evolution of the electron and positive-ion densities, n_e and n_i:

$$\frac{\partial n_e}{\partial t} - \operatorname{div} \mathbf{j}_e = \alpha j_e + S^* - R, \qquad (1)$$

$$\frac{\partial n_i}{\partial t} + \operatorname{div} \mathbf{j}_i = \alpha j_e + S^* - R, \qquad (2)$$

where $\mathbf{j}_e$ and $\mathbf{j}_i$ are the electron and ion flux densities, α is the Townsend coefficient for gas (helium) ionization by direct electron impact, the ionization source term S^* describes the power of the processes of step ionization and Penning ionization, and R is the power of charged-particle losses in the discharge volume.

Equations (1) and (2) are supplemented with Poisson's and Kirchhoff's equations and the boundary conditions at the electrodes, which alternatively play the role of the cathode and anode during each half-period of the applied voltage:

$$\operatorname{div}\mathbf{E} = \frac{e(n_i - n_e)}{\varepsilon_0}, \tag{3}$$

$$U_0 \sin\omega t = U_d + U_b, \tag{4}$$

$$\gamma j_{ic} = j_{ec}, \quad j_{ia} = 0. \tag{5}$$

Here, e is the electron charge, ε_0 is the permittivity of free space, $\mathbf{E}$ is the electric field strength in the discharge, U_0 is the amplitude of the applied voltage, U_d is the voltage drop across the interelectrode gap, U_b is the voltage drop at the barriers, $\gamma \simeq 0.1$ is the total coefficient of secondary electron emission from the cathode caused by the ion flux j_{ec} (the electron emission from metastable helium atoms is neglected), j_{ic} is the flux of secondary electrons from the cathode, and j_{ia} is the ion flux emitted by the anode (which is assumed to emit no electrons). The quantities U_d and U_b have the form

$$U_d = \int_0^d E\,dx, \quad U_b = \frac{Q}{C}, \quad Q(t) = \int_0^t I\,dt, \tag{6}$$
$$I(t) = S(e\mu_e n_e E + e\mu_i n_i E + \varepsilon_0 \dot{E}),$$

where d is the length of the interelectrode gap, Q is the charge at the outer capacitor plates, C is the capacitance of the barriers, S is the cross-sectional area of the discharge column, μ_e and μ_i are the electron and ion mobilities, and $I(t)$ is the total discharge current with allowance for the displacement current (the contribution of diffusive processes to the current is ignored).

Equations (1)–(6) describe the discharge structure over the entire interelectrode gap and make it possible to follow the discharge evolution. Unfortunately, these integrodifferential equations are fairly difficult to solve numerically. That is why we tried to simplify the mathematical model by taking into account the following familiar features of the longitudinal structure of glow discharges at moderate pressures:

(i) The glow discharge can be described in terms of its main components—the cathode and anode falls and the plasma column between them.

(ii) The potential drop across the anode fall is small enough not to seriously influence the total voltage drop across the discharge.

(iii) The Faraday dark space in helium discharges at moderate pressures is, as a rule, sufficiently short, so that the entire plasma column can be regarded as being homogeneous (neglecting the Faraday space makes it possible to ignore the nonlocal nature of the electron distribution near the cathode fall).

(iv) Inside the cathode fall region, the electric field decreases almost linearly with distance from the cathode.

(v) The main contribution to the space charge inside the cathode fall region comes from positive ions, which are far less mobile than electrons.

(vi) As a rule, gas atoms inside the space-charge sheath near the cathode are ionized primarily by direct electron impact (the processes of step ionization and Penning ionization as well as charged-particle recombination are more important inside the plasma column).

(vii) Since the electrons are far more mobile than ions, the electron dynamics can be treated in the quasisteady approximation; i.e., the term $\partial n_e/\partial t$ in Eq. (1) can be neglected.

Hence, we can determine the longitudinal structure of a barrier discharge by analyzing, first, the cathode fall, in which the electric field decreases linearly with distance from the cathode, and, second, the quasineutral plasma column, in which the electric field is uniform. At certain times (immediately before breakdown), the cathode fall can extend over the entire interelectrode gap.

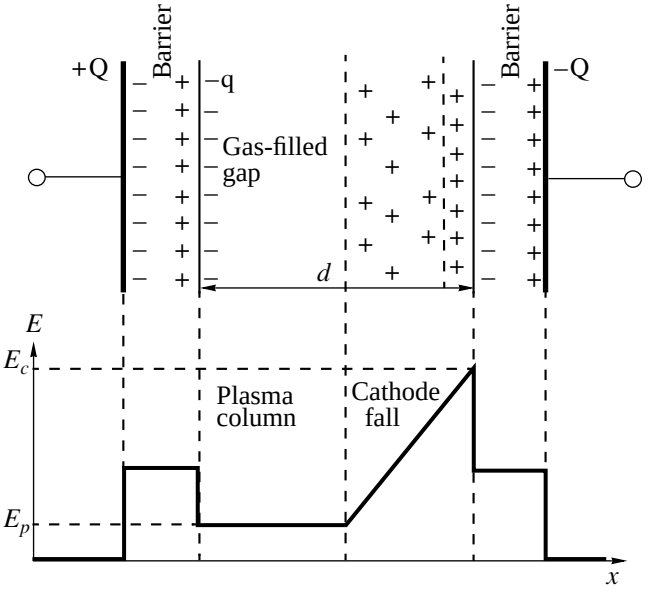

Fig. 5. Graphical illustration of the electric-field and charge distributions in a barrier discharge.

Taking into account the above properties of a glow discharge allows us to reduce integrodifferential equations (1)–(6) to a much simpler set of (formally) zero-dimensional differential equations for the variables Q, $-q$, q_s, q_v, d_c, E_c, and E_p. The physical meaning of these variables, which are illustrated in Fig. 5, is as follows: Q is the charge at the capacitor plates, $-q$ is the negative charge at the dielectric surface that currently plays the role of the anode, q_s is the positive charge at the dielectric surface that currently plays the role of the cathode, q_v is the total space charge inside the cathode fall region ($q = q_s + q_v$), d_c is the length of the cathode fall, and E_c and E_p are the electric fields at the cathode surface and inside the plasma column.

We integrate Eq. (2) along the cathode fall and, in accordance with property (vii), set $-\mathrm{div}\,\mathbf{j}_e \simeq \alpha j_e$. As a result, we obtain the equation

$$\frac{\partial q_v}{\partial t} = eS(j_{ip} + j_{ep} - j_{ic} - j_{ec}) \simeq \simeq eS(j_{ep} - j_{ic} - j_{ec}), \quad (7)$$

whose right-hand side contains charged-particle (electron and ion) fluxes through the boundary of the cathode fall from the plasma side and from the dielectric (cathode) surface. Without any serious loss of accuracy, we can neglect the ion flux j_{ip} from the plasma side.

The rate at which the total space charge inside the cathode fall region changes, $dq_v/dt = \dot{q}_v$, should be determined taking into account the time scale on which the length of the cathode fall varies periodically. Consequently, the final equation for $\dot{q}_v$ has the form

$$\dot{q}_v = eS(j_{ep} - j_{ic} - j_{ec} + n_p\dot{d}_c), \quad (8)$$

where the charged-particle density n_p in a quasineutral plasma is determined by the plasma field. At each instant, the electron flux in the cathode fall region with a linearly decreasing electric field is calculated from quasi-steady-state equation (1) in terms of the above variables:

$$j_{ep} \simeq \frac{\gamma}{1+\gamma} j_{ic} \exp\int_0^{d_c} \alpha(E(x))dx = \frac{\gamma}{1+\gamma}\frac{q_v}{d_c}\mu_i E_c \exp\int_0^{d_c} \alpha(E(x))dx,$$

where $E(x) = E_c - \dfrac{x}{d_c}(E_c - E_p)$.

Hence, the final set of equations can be written as

$$U_0 \sin\omega t = \frac{E_c + E_p}{2} d_c + \frac{Q}{C} + E_p \cdot (d - d_c), \quad (9)$$

$$\frac{\dot{Q}}{S} = \varepsilon_0 \dot{E}_p + e\mu_e n_p E_p, \quad (10)$$

$$\frac{\dot{q}_v}{S} = en_p\dot{d}_c + \frac{q_v}{d_c}\mu_i E_c\left(\frac{\gamma}{1+\gamma}\exp\int_0^{d_c}\alpha(x)dx - 1\right), \quad (11)$$

$$e\mu_e n_p(Q - q) + en_p\dot{d}_c = \frac{\gamma}{1+\gamma}\mu_i E_c \frac{q_v}{d_c}\exp\int_0^{d_c}\alpha(x)dx, \quad (12)$$

$$E_c = \frac{Q - q + q_v}{\varepsilon_0 S}, \quad E_p = \frac{Q - q}{\varepsilon_0 S}. \quad (13)$$

At the stage at which the cathode fall region extends over the entire interelectrode gap, these equations are solved under the conditions $d_c = d$ and $\dot{d}_c = 0$. At the contraction stage ($d_c \le d$), the equations are solved with the quantity q_v/d_c in place of en_p.

The simplified basic model as formulated was somewhat extended to describe effects related to the delay in the decay of the cathode fall by the time at which the electric field in the interelectrode gap reverses polarity. Since these effects were found to play an insignificant role, we do not describe them here. The basic set of equations was solved together with the balance equations for different charged particles and particles in different excited states. For this reason, our model can also be applied to gas mixtures containing excimer molecules in order to estimate the efficiency of, e.g., barrier discharge–based generators of vacuum ultraviolet (VUV) radiation.

We assumed that, in the cathode fall region, He^+ ions dominated over the ions of other species. As a function of the reduced electric field E/N, the ionization coefficient α was approximated by the dependence $\alpha(E/N) = A\exp(-B/(E/N) - C/(E/N)^2)$, which is close to the experimental dependence presented in [9]. Here, $A = 50\ \mathrm{cm^{-1}\ atm^{-1}}$, $B = 4.8 \times 10^{-16}\ \mathrm{V\ cm^2}$, $C = 4.8 \times 10^{-32}\ \mathrm{V^2\ cm^4}$, and the reduced electric field E/N is expressed in units of $10^{-16}\ \mathrm{V\ cm^2}$.

5. NUMERICAL RESULTS AND COMPARISON WITH THE EXPERIMENT

We tested our simplified model against the discharge parameters calculated from complete one-dimensional model equations (1)–(6). Thus, we simulated ac discharges in nitrogen under the conditions corresponding to those in [3] and also compared our numerical results with the results obtained by N.A. Dyatko from a complete one-dimensional model of a helium discharge. Test simulations revealed good agreement between the results from simplified and

complete models. As an example, Fig. 6 illustrates our results and the results obtained by Barkalov *et al.* [3] using a complete model.

Comparing the calculated waveforms of the current (Fig. 7) with numerous oscilloscope traces obtained in experiments, we found that our numerical model is capable of capturing the above main features of the barrier discharges. Hence, we can conclude that the simplified model realistically reflects the physical essence of the processes occurring in the pulsed regime of a barrier discharge. The only inaccuracy is associated with the quantitative characteristics of current pulsations and may stem not only from the simplifying model assumptions but also from an incomplete set of elementary processes incorporated into the model and an uncertainty in their rate constants. In order to illustrate the evolution of the longitudinal discharge structure within one half-period of the applied voltage that corresponds to a positive electric field in the interelectrode gap, in Figs. 8–10, we present some of the numerical results obtained for $f = 7$ kHz and $U_0 = 1.9$ kV.

From Fig. 8, we can see that, under the parameter values adopted for simulations, the discharge voltage after breakdown drops preferentially across the cathode fall, which almost always occupies the entire interelectrode gap until it decays by the end of the half-period. The plasma in the discharge is produced over a very short time interval, when the discharge current is the highest during the breakdown.

We can also see that the cathode fall is in a quasisteady state and experiences damped oscillations. In the pulsed mode, the space charge in the cathode fall region changes almost in phase with the current pulsations (Figs. 7, 8), while the pulsations of the voltage drop across the cathode fall and the pulsations of the positive space charge inside the cathode fall region are almost in antiphase (Fig. 8).

The voltage across the cathode fall varies periodically between its maximum and minimum values, at which the factor $\Phi = \frac{\gamma}{1+\gamma}\exp\int_0^{d_c}\alpha(x)dx$ characterizing electron production inside the cathode fall region is either larger or smaller than unity. Figure 9 shows that the factor Φ rises above and falls below unity very quickly (almost instantaneously) in comparison with the characteristic period of the applied voltage.

Hence, the pulsed regime is typical of the active phase of a barrier discharge (the phase in which the conduction current is nonzero). The above features of the pulsed regime make it possible to construct a simple analytic model of the current pulsations under investigation. We can draw an analogy between a barrier discharge and a dc electric circuit consisting of a load resistor R and a nonlinear element both connected in parallel with a voltage source with constant amplitude U_0. The resistance R is close to the impedance of the capacitor plates at the frequency of the applied voltage,

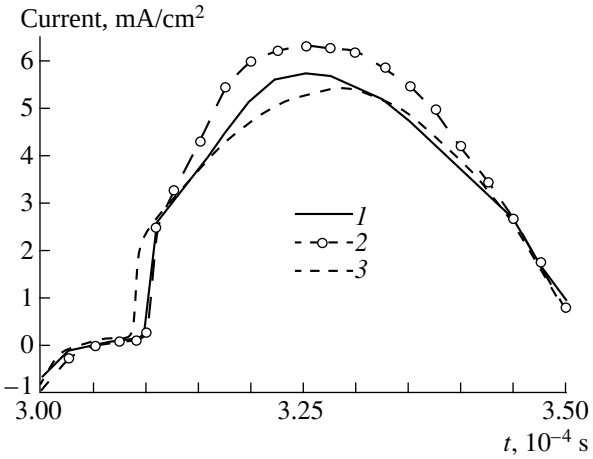

Fig. 6. Comparison of the results from (*3*) simplified and (*2*) complete models with (*1*) experimental data.

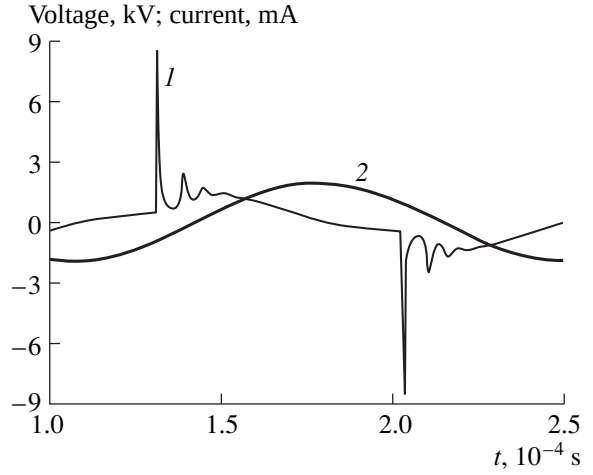

Fig. 7. Calculated waveforms of (*1*) the current and (*2*) voltage.

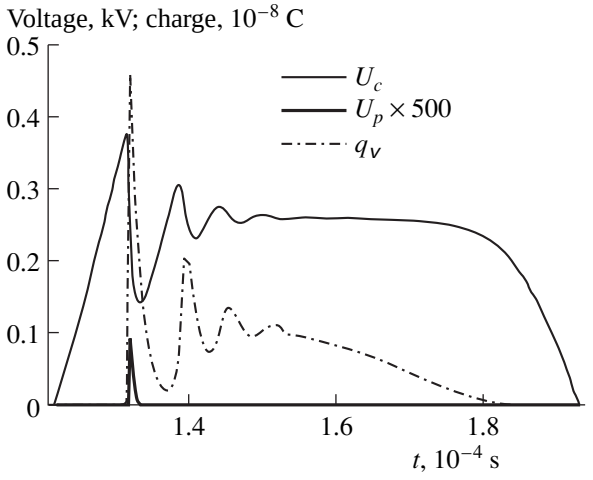

Fig. 8. Results of calculations for $f = 7$ kHz and $U_0 = 1.9$ kV: U_c is the voltage drop across the cathode fall, U_p is the voltage drop across the plasma column, and q_v is the space charge inside the cathode fall region.

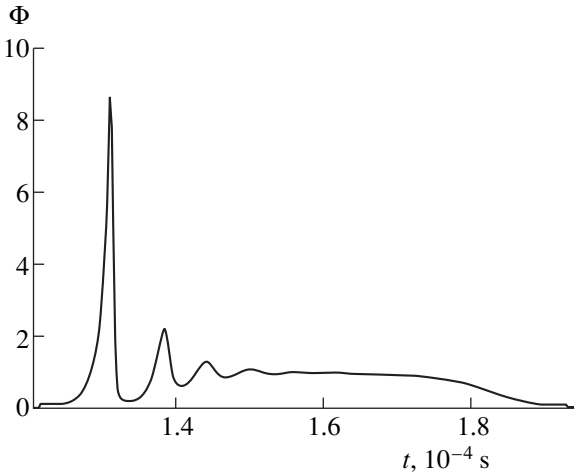

Fig. 9. Waveform of the electron production factor $\Phi = \frac{\gamma}{1+\gamma}\exp\int_0^{d_c}\alpha(x)dx$ in the cathode fall region for $f = 7$ kHz and $U_0 = 1.9$ kV.

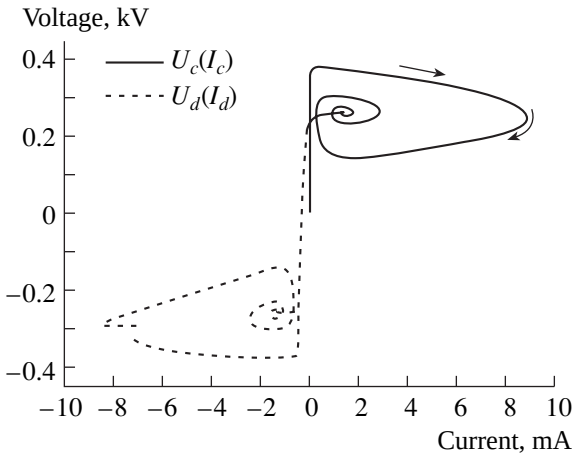

Fig. 10. Phase (or dynamic current–voltage) characteristic of the pulsed regime of a barrier discharge for $f = 7$ kHz and $U_0 = 1.9$ kV: U_c is the voltage drop across the cathode fall, U_d is the voltage drop across the interelectrode gap, I_c is the conduction current in the cathode fall region, and I_d is the total discharge current.

and the nonlinear element models the cathode fall. Such an electric circuit is described by the equations

$$U_0 = IR + U_c, \tag{14}$$

$$I = \dot{q}_v + \frac{\mu_i}{\varepsilon_0 Sd} q_v^2, \tag{15}$$

$$\dot{q}_v = \frac{\mu_i}{\varepsilon_0 Sd} q_v^2 (\Phi - 1), \tag{16}$$

which can be derived from Eqs. (9)–(13) under the assumption that $d_c \simeq d$.

For simplicity, we assume that the electron production factor changes in a steplike fashion; i.e., it instantaneously rises to Φ_{max} ($\Phi_{max} > 1$) when the voltage drop U_c across the cathode fall becomes equal to U_{max}, remains at the same level as the voltage decreases, instantaneously falls off to Φ_{min} ($\Phi_{min} < 1$) when the voltage becomes equal to U_{min}, remains at the same level until the voltage increases to U_{max}, and so on. With such a production factor, Eqs. (14)–(16) have a simple analytic solution. However, we do not write out the resulting formulas, because the analogy with the model based on Eqs. (14)–(16) was drawn merely for illustrative purposes. Note only that, for $\Phi > 1$, the current in the circuit increases explosively according to the law $\sim(1 - t/\tau_1)^{-1}$, and, for $\Phi < 1$, it decreases gradually due to recombination according to the law $\sim(1 + t/\tau_2)^{-1}$, where τ_1 and τ_2 are the characteristic rise and fall times of a current pulse, respectively. Qualitatively, this result agrees with both the experiment and simulations.

An analysis of the solution to Eqs. (14)–(16) enables us to draw the important conclusion that, in the model electric circuit, the time over which the current grows explosively corresponds to a decrease in the voltage across the cathode fall; in other words, the differential resistance of the growing cathode fall should be negative. This conclusion is supported by our calculations of the phase trajectories in the pulsed regime of a barrier discharge, or, equivalently, the dynamic current–voltage characteristics of the cathode sheath and interelectrode gap, $U_c(I_c)$ and $U_d(I_d)$. From Fig. 10, we can clearly see that, for each current pulse, an increase in the conduction current I_c inside the cathode fall region (or in the total discharge current I_d) is accompanied by a decrease in the voltage U_c across the cathode fall (or the voltage U_d across the interelectrode gap). Consequently, the fact that the differential resistance of the cathode fall evolving into a subnormal state after uniform breakdown is negative can be regarded as the main physical cause of the onset of the pulsed regime of a barrier discharge at small values of the parameter *Pd*, in which case the current pulsations are very similar in nature to those in a negative corona discharge, known as Trichel pulses [10, 11].

ACKNOWLEDGMENTS

We are grateful to A.P. Napartovich and N.A. Dyatko for helpful discussions of the results obtained. This work was supported by the Russian Foundation for Basic Research, project no. 99-02-16545.

REFERENCES

1. B. Eliasson and U. Kogelschatz, IEEE Trans. Plasma Sci. **19**, 309 (1991).

2. V. G. Samoĭlovich, V. I. Gibalov, and K. V. Kozlov, *Physical Chemistry of Barrier Discharge* (Mosk. Gos. Univ., Moscow, 1989).
3. A. D. Barkalov, V. D. Gavrilyuk, G. G. Gladush, *et al.*, Teplofiz. Vys. Temp. **16**, 265 (1978).
4. R. Bartnikas, IEEE Trans. Electr. Insulat. **El-6**, 63 (1971).
5. S. Okazaki, M. Kogoma, M. Uehara, and Y. Kimura, J. Phys. D **26**, 889 (1993).
6. F. Massines, R. Messaourdi, and C. Mayoux, Plasma Polym. **3** (1), 43 (1998).
7. I. Brauer, C. Punset, H.-G. Purwins, and J. P. Boeuf, J. Appl. Phys. **85**, 7569 (1999).
8. Yu. S. Akishev, A. V. Dem'yanov, V. B. Karal'nik, *et al.*, in *Proceedings of the XXIV International Conference on Phenomena in Ionized Gases, Warsaw, Poland, 1999*, Vol. 2, p. 137.
9. V. L. Granovskiĭ, *Electric Current in a Gas: Steady-State Current* (Nauka, Moscow, 1971).
10. G. V. Trichel, Phys. Rev. **54**, 1078 (1938).
11. A. P. Napartovich, Yu. S. Akishev, and A. A. Deryugin, J. Phys. D **30**, 2726 (1997).

Translated by G.V. Shepekina

Plasma Physics Reports, Vol. 27, No. 2, 2001, pp. 172–177. Translated from Fizika Plazmy, Vol. 27, No. 2, 2001, pp. 184–189.
Original Russian Text Copyright © 2001 by Antonov, Kovpik, Kornilov.

LOW-TEMPERATURE PLASMA

Excitation of RF Oscillations in a Discharge with Negative Differential Conductivity

A. N. Antonov, O. F. Kovpik, and E. A. Kornilov

Kharkov Institute of Physics and Technology, National Science Center, Akademicheskaya ul. 1, Kharkov, 61108 Ukraine

e-mail: antonov@kipt.kharkov.ua

Received February 16, 2000; in final form, June 26, 2000

Abstract—The excitation of oscillations in a discharge with negative differential conductivity is studied experimentally. The possibility is demonstrated of amplifying oscillations in the cathode dark space at frequencies close to the electron plasma frequency of the positive-column plasma. The phase velocities of waves at these frequencies are determined. When the waves pass from the cathode dark space to the discharge positive column, their phase velocities decrease; the closer the frequency is to the electron plasma frequency, the more pronounced the decrease in the phase velocity. As the intensity of oscillations increases, the discharge becomes non-steady-state. This is confirmed by the time evolution of the current–voltage characteristic. The shape of the current–voltage characteristic, its splitting, and the rate at which it varies depend on the input RF power. The decrease in the cathode dark space indicates that the ionization processes in the discharge are strongly influenced by electron plasma oscillations excited due to the collective interaction of the electron beam formed at the cathode with the discharge plasma. It is these processes that determine the maximum values of both the frequency of the excited oscillations and the power that can be withdrawn from the discharge.
© 2001 MAIK "Nauka/Interperiodica".

The idea of using a gas discharge with negative differential conductivity to create an RF oscillator has been repeatedly proposed since the first studies of gas discharges [1, 2]. After the invention of powerful triode tubes, this idea partially lost its attractiveness. However, the successful development of semiconductor oscillators, which have current–voltage characteristics with negative differential conductivity (the so-called Gunn oscillator [3, 4]) and can operate in the gigahertz frequency range, has refreshed the idea of creating a powerful and simple RF oscillator.

A gas discharge with negative differential conductivity can carry a relatively high current; hence, the power of a gas-discharge RF oscillator is expected to be much higher than that achieved in solid-state semiconductor oscillators.

As compared to a semiconductor plasma, gas discharge plasmas have some specific features that may affect the excitation of oscillations. Thus, in a gas discharge with negative differential conductivity,

$$\sigma_{\text{dif}} = \frac{\partial j_0}{\partial E} < 0, \quad \mathbf{j} = \sigma(E) \cdot \mathbf{E},$$

where E is the electric field, j_0 is the current density, and σ is the conductivity, the excitation of oscillations is related to the development of the beam-drift instability [5]. Due to this instability, the excited waves can be converted into shock waves with an oscillating front and then be damped. Generally, this occurs when the field gradient in the region with negative conductivity is high enough. As a result, the energy of an electron beam that is formed at the cathode may be spent on plasma heating rather than converted into oscillation energy, which may be withdrawn from the discharge [6]. As early as Langmuir's classical work [7], it was pointed out that the oscillations should be strongly damped in the region of the electron plasma resonance. Hence, it is expected that oscillations with a sufficiently large amplitude will strongly affect the current–voltage characteristic of the discharge.

In connection with this, it is of interest to study the excitation of oscillations in a gas discharge with negative differential conductivity, determine the relation between the frequency and intensity of oscillations and their dispersion characteristics, and find out how the oscillations influence the discharge. Such investigations may help reveal the role of collective processes in the development of a dc discharge. The purpose of this study is to experimentally investigate the above problems. The experiments were carried in the device shown schematically in Fig. 1.

We operated with an anomalous glow discharge with a cold cathode [8]. Such a discharge has the longest cathode region (in our case, it was longer than 10 cm). It is expected that the field of oscillations excited in this region will lead to the bunching of electrons. Due to the large size of the cathode region, it is possible to set many probes there and place a grid near the cathode, which allows us to excite the discharge current oscillations at the required frequency.

1063-780X/01/2702-0172$21.00 © 2001 MAIK "Nauka/Interperiodica"

A pumped-out glass bulb 40 mm in diameter was used as a discharge tube. The pressure of the working gas (air, argon, or hydrogen) was kept in the range 10^{-1}–10^{-4} torr. A voltage of up to 10 kV was applied to disk iron electrodes 30 mm in diameter placed at the bulb ends. The anode was grounded through the noninductive resistor R2 = 0.5 Ω (Fig. 1). The discharge current ranged within 0.5–50 mA. The bulb length was varied in a wide range; most of the experiments were carried out with a 300-mm-long bulb.

A set of Langmuir probes placed along the axis and radius of the bulb was used to measure the profiles of dc and ac electric fields, the main discharge parameters, and current fluctuations. Simultaneously, electromagnetic oscillations outside the bulb were recorded. For this purpose, we used oscillographs, spectrum analyzers, and a set of P5 radioreceivers.

The grid was made of a molybdenum wire 0.2 mm in diameter, the grid cell size being 5×5 mm. The grid was set 6 mm away from the cathode and fully shaded it. An ac voltage of 0–120 V at frequencies of 0.03–500 MHz was applied to the grid from an external oscillator. At a plasma density of up to 5×10^9 cm^{-3}, the frequency of the voltage applied to the grid might exceed the electron plasma frequency. The low density of the discharge plasma enabled fair matching of the grid to the RF oscillator.

In this type of discharge, the current is rather low, which facilitates the problem of heat removal from the discharge bulb and the probes placed therein.

Both the wavelength and dispersion characteristics of the excited oscillations were determined from the profiles of the oscillation amplitude along the discharge axis and radius and from the oscillation phases at the probes, measured with an FK2-12 phase meter. Simultaneously, both the discharge voltage and current were also measured. The current–voltage characteristic was recorded with a divider formed by resistors R4 and R5 (Fig. 1) connected between the cathode and ground. The voltage from the divider was applied to the horizontal amplifier of an oscillograph, whereas the voltage drop across resistor R2, which is part of the main discharge circuit, was applied to the vertical amplifier.

The main discharge characteristics measured in this study are presented in Figs. 2 and 3.

Figure 2 shows the profile of the potential in the cathode region for a discharge in air at a pressure of 1.4 mtorr. It is seen that the electric field occurs within a 12-cm region near the cathode (the cathode dark space).

Figure 3 shows typical averaged current–voltage characteristics recorded with a two-coordinate plotter H306 under smooth variations in the voltage for argon pressures of (*1*) 1.6, (*2*) 1.4, and (*3*) 1.2 mtorr (the recording time step is no more than 0.05 s). The measurements revealed two specific features of the current–voltage characteristics:

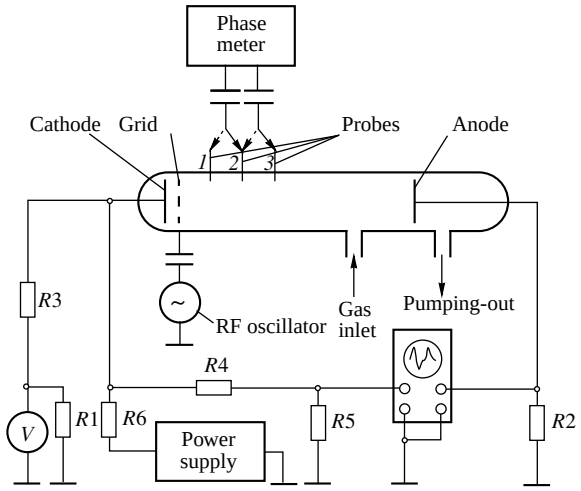

Fig. 1. Schematic of the experimental facility.

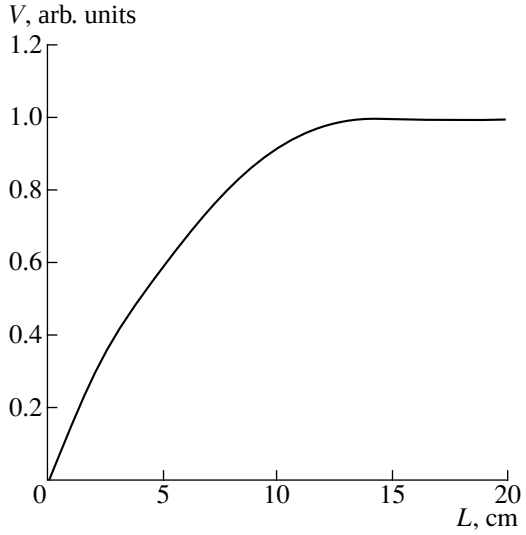

Fig. 2. Profile of the plasma potential (with respect to the cathode) along the discharge excited in air at a pressure of 1 mtorr and applied voltage of 6 kV.

(i) At a constant discharge voltage, the region of negative differential conductivity expands as the pressure decreases.

(ii) At a constant discharge current and voltage, the hysteresis effect covers the entire region of negative conductivity.

As was expected, under conditions of negative differential conductivity (Fig. 3), applying an RF signal to the grid resulted in its amplification, which manifested itself in an increase in the modulation depth of the discharge current at the given frequency. The oscillations excited in the discharge almost did not radiate, which

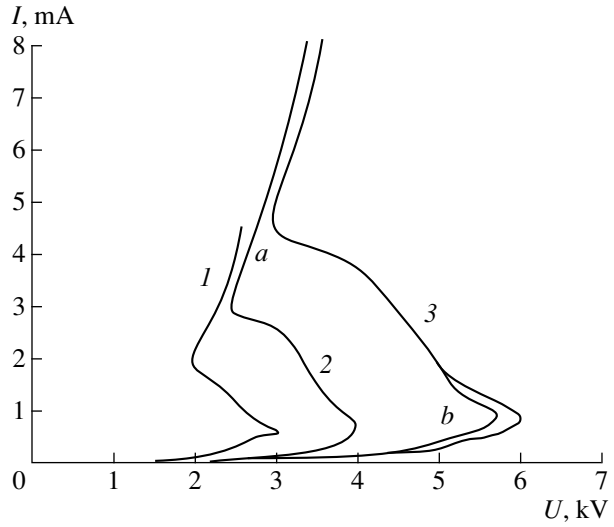

Fig. 3. Current–voltage characteristics of the discharge in argon at pressures of (*1*) 1.6, (*2*) 1.4, and (*3*) 1.2 mtorr.

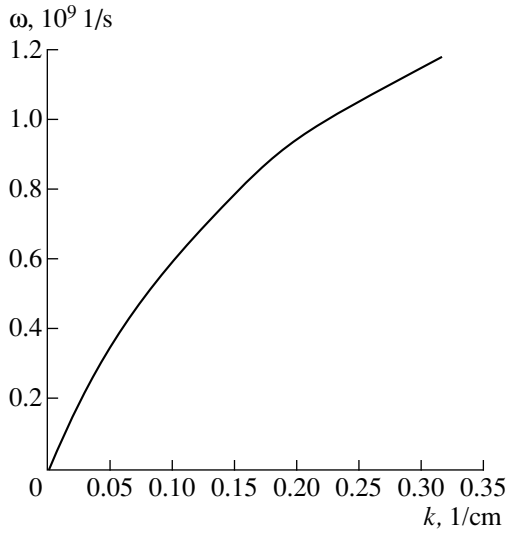

Fig. 4. Dispersion curve of the oscillations in the discharge dark space.

indicated that they were electrostatic in nature. The amplification maximums corresponded to the upper (*a*) and lower (*b*) kinks of the current–voltage characteristics. The maximum amplification occurred at the lower kink (*b*), where all the measurements were carried out.

The dispersion curve for the waves that are excited in the discharge dark space in the frequency range up to 200 MHz is shown in Fig. 4. It resembles the dispersion curve for waves in a plasma waveguide in the absence of a magnetic field [9]. The upper frequency of these waves tends to the electron plasma frequency in the discharge positive column ω_{pe} (Langmuir plasma frequency). The frequencies of the long-wavelength oscillations depend linearly on the wavenumber k:

$$\omega = kV_p,$$

where $V_p = (eE/2m)n^{-1}$; e and m are the electron charge and mass, respectively; E is the electric field in the cathode dark space; and n is the electron–neutral collision frequency.

At the interface between the dark space and positive plasma column, the phase velocities and amplitudes of waves decrease. This can be related to the efficient wave damping. The damping rate depends on frequency: the higher the frequency, the higher the damping rate.

Figure 5 presents the frequency dependences of the wave phase velocities within the frequency range under consideration. The dependences were determined from the phase differences of oscillations measured with three identical probes positioned consecutively in two discharge regions (Fig. 1). Probe *1* was set in the dark space, at a distance of 3 cm from the cathode; probe *2* was set 1.9 cm away from the first one, at the interface between the dark space and positive column (at the boundary of the discharge glow); and probe *3* was located in the discharge glow region, 2.1 cm away from probe *2*. In Fig. 5, curve *1* corresponds to the phase velocity in the region between probes *1* and *2* and curve *2* corresponds to that in the region between probes *2* and *3*. It is seen that, when the short-wavelength oscillations (with $\omega > \omega^*$) enter the positive column, their phase velocities decrease about twofold. For waves with frequencies

$$\omega > \omega^* = (1/4 - 1/5)\omega_{pe},$$

this is accompanied by an increase in the damping rate.

The frequency region where the oscillations are excited can be divided into two ranges: $\omega < \omega^*$ and $\omega_{pe} > \omega > \omega^*$. In these ranges, the excitation of oscillations and their influence on the discharge have some specific features.

When long-wavelength oscillations at frequencies from the first range are excited, the amplification occurs throughout the entire region between the anode and the cathode space. The oscillation amplitude increases proportionally to the amplitude of the signal applied to the grid. When the RF voltage at the grid is $\sim U = 50$ V, the modulation depth of the discharge current is 50%. The electric field caused by the signal $\sim U$ from the RF oscillator in the gap between the cathode and grid is about 100 V/cm. At the discharge voltage $U_d = 6$ kV (in this case, the dc electric field in the cathode dark space is 600 V/cm), the ratio $\sim U/U_d$ amounts to ~0.01.

The oscillations at frequencies $\omega > \omega^*$ are amplified only in the cathode dark space. They begin to influence the discharge at small values of the grid signal $\sim U$, when the ratio $\sim U/U_d$ is much less than in the previous case and amounts to about 0.001. Thus, when the RF

grid voltage was varied in the range $\sim U$ = 1–2 V (the dc discharge voltage being U_d = 6 kV), we observed variations in the size of the cathode dark space. As the amplitude of the grid voltage increased, the interface between the cathode dark space and plasma column started approaching the cathode so that the cathode dark space shrank. An increase in the gas pressure led to the same result. Figure 6 presents the profiles of the amplitude of the probe current oscillations at a frequency of 200 MHz along the discharge gap for pressures of 1.4 and 1.2 mtorr, the amplitude of the grid signal being constant. The vertical bars mark the boundary of the dark space. It is seen from Fig. 6 that, as the pressure increases by 0.2 mtorr, the dark space reduces by 2.5 cm. At a constant pressure, the increase in the grid voltage from 2 to 2.5 V leads to the same result. The increase in the grid voltage $\sim U$ from 1.8 to 4.5 V results in a decrease in the dark space width from 12 to 3 cm.

Applying an RF signal to the grid changes the discharge current–voltage characteristic. It is found that the effect of hysteresis in the discharge current–voltage characteristic (Fig. 3, curve *3*, zone *b*) stems from the existence of low-frequency oscillations at frequencies up to 1 MHz, which manifest themselves in the modulation of the discharge current. The modulation depth is determined by the current and may be as high as several tens of percent. The amplification of RF oscillations is accompanied by the amplification of low-frequency oscillations and the expansion of the hysteresis area over the entire region with negative differential conductivity.

It is seen from the oscilloscope traces of the discharge current and voltage that, when the amplitude of the RF grid voltage is higher than 0.5–1 V, the discharge operating point steadily circulates up and down along the current–voltage characteristic, thus tracing a closed cycle with a period of low-frequency oscillations. Hence, the current–voltage characteristic may be treated here as a dynamic one. Figure 7 presents the waveforms of the ac components of the discharge current and voltage and the dynamic current–voltage characteristic at an RF grid voltage of 0.5 V.

A further increase in the grid voltage ($\sim U \gg 2$ V) changes the shape of the hysteresis loop from a triangle into an ellipse. Then, the local loops and oscillations arise on the ellipse. Finally, the ellipse breaks into two or three smaller ones with a shorter repetition period (Fig. 8). The changes in the hysteresis loop correlate with changes in the shape of current pulsations and the decrease in both the pulse duration and pulse-repetition period.

In our opinion, the results obtained allow us to draw several important conclusions.

A gas discharge with a current–voltage characteristic that has negative differential conductivity stimulates the amplification (generation) of RF oscillations. This phenomenon is related to the onset of an instability caused by the passage of an electron beam formed at the cathode through the cathode dark space.

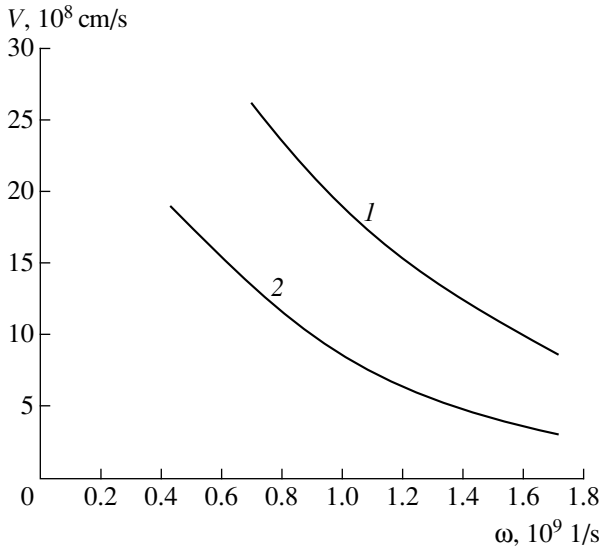

Fig. 5. Phase velocities of oscillations (*1*) at the interface between the dark space and plasma column and (*2*) in the plasma column.

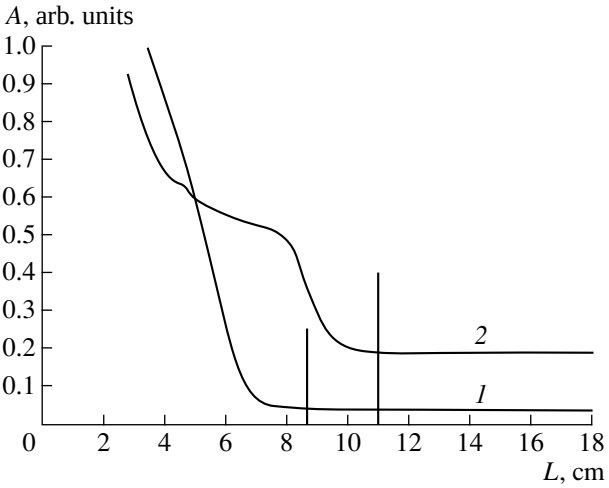

Fig. 6. Profiles of the amplitudes of the excited oscillations along the discharge at pressures of (*1*) 1.4 and (*2*) 1.2 mtorr. The vertical bars mark the boundary of the dark space.

The discharge in question can be used to generate RF oscillations with frequencies $\omega \ll \omega_{pe}$ (1/4 – 1/5), where ω_{pe} is the electron plasma frequency of the positive-column plasma. Since these oscillations are revealed in the discharge current, it is possible to efficiently withdraw the oscillation energy by incorporating a feedback in the electric circuit of the discharge power supply. The estimates show that the oscillation

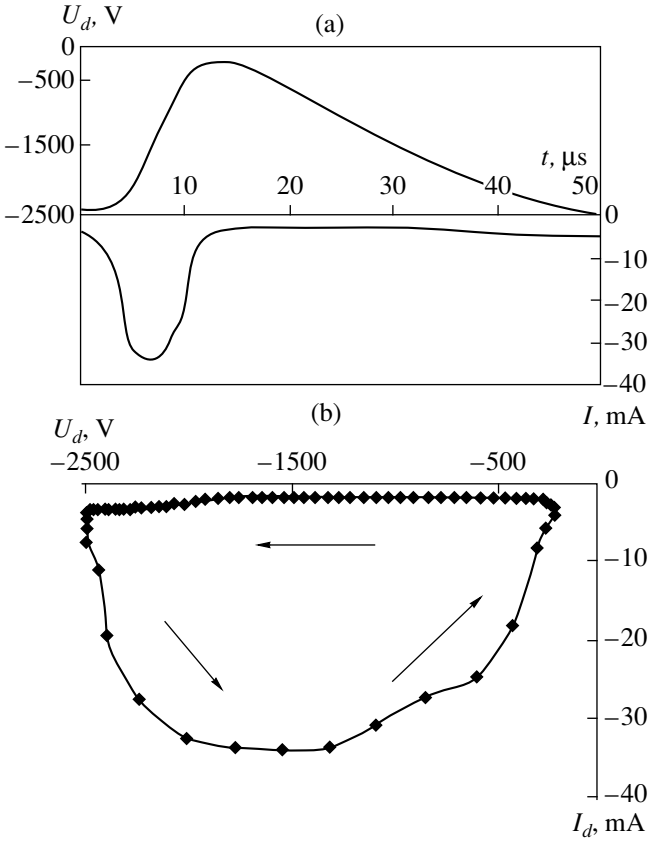

Fig. 7. Waveforms of (a) the discharge voltage (upper curve) and current (lower curve) pulsations during one period of low-frequency oscillations and (b) the dynamic current–voltage characteristic of the discharge in argon at a pressure of 2 mtorr for a dc discharge voltage of 3 kV and amplitude of the RF grid voltage of 0.5 V. The time interval between the labels is 1 μs; the arrows show the direction of evolution of the discharge voltage and current during one oscillation period (50 μs).

power can attain 10–20% of the dc power input in the discharge.

Most likely, the frequency of an oscillator based on the grid-controlled gas discharge with negative differential conductivity cannot exceed several hundreds of megahertz. This limitation is related to the strong damping of oscillations, as their frequency approaches the electron plasma frequency of the positive-column plasma.

On the whole, the experimental data indicate that the oscillations amplified (excited) in the cathode dark space of an anomalous glow discharge at frequencies near the electron plasma frequency of the positive-column plasma strongly influence the parameters of the current–voltage characteristic. The Shottky noise at the cathode can act as a seed fluctuation signal. The oscillation frequency and output power of the oscillator are largely governed by the rate and amplitude of the changes in the discharge parameters.

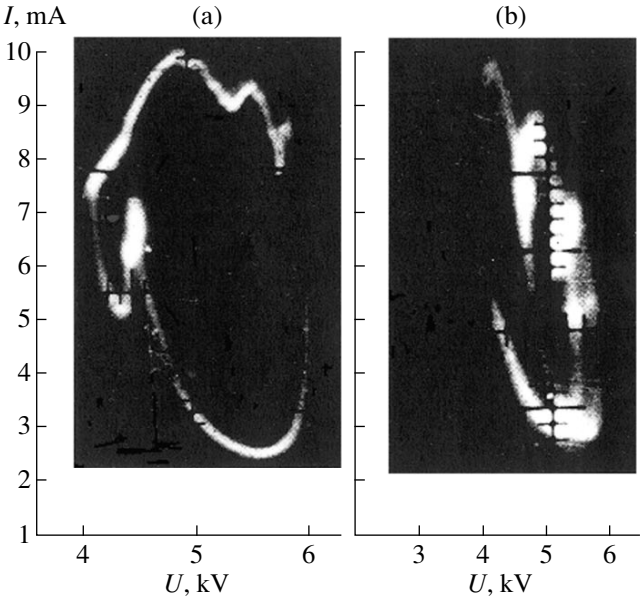

Fig. 8. Dynamic hysteresis fragments of the current–voltage characteristic at high RF grid voltages: U = (a) 3 and (b) 4 V.

The decrease in both the phase velocity and amplitude of the oscillations at the interface between the dark space and discharge positive column (at a distance comparable to or less than the oscillation wavelength) allows us to assume that the excited waves transform into nonlinear (shock) waves, which are then damped when propagating in the plasma column.

When the parameters of the given discharge are kept constant, the width of the cathode dark space is inversely proportional to the average electron ionization coefficient β [8]. Consequently, the decrease in the width of the dark space after the excitation of oscillations at frequencies $\omega \geq \omega_{pe}$ can only be explained by an increase in β. It is reasonable to assume that the electric field of the oscillations affects the electron energy distribution function in the dark space in such a way that the ionization ability of the electron beam per unit length increases. This assumption is confirmed by the dependences of the shape and size of the hysteresis loop and the depth and period of the discharge current modulations on the oscillation amplitude when the oscillations are excited at frequencies near the electron plasma frequency of the positive-column plasma.

ACKNOWLEDGMENTS

We are deeply grateful to Ya.B. Faĭnberg for fruitful discussions.

REFERENCES

1. A. von Engel and M. Steenbeck, *Elektrische Gasentladungen, ihre Physik und Technik* (Springer-Verlag, Berlin, 1934; ONTI, Moscow, 1936), Vol. 2.

2. N. A. Kaptsov, *Electronics* (Gostekhteorizdat, Moscow, 1953), p. 332.
3. *Microwave Devices*, Ed. by M. Howes and D. Morgan (Wiley, London, 1976; Mir, Moscow, 1979).
4. J. Gann, Usp. Fiz. Nauk **89**, 147 (1966).
5. A. N. Antonov, O. F. Kovpik, E. A. Kornilov, *et al.*, Report No. 1602 (Kharkov Institute of Physics and Technology, Kharkov, 1980); Report No. 1673 (Kharkov Institute of Physics and Technology, Kharkov, 1981).
6. M. V. Babykin, E. D. Volkov, A. N. Gavrin, *et al.*, Discovery No. 112, Byull. Izobret., No. 32 (1972).
7. I. Langmuir, Phys. Rev. **26**, 585 (1925); Z. Phys. **46**, 271 (1927).
8. A. von Engel, *Ionized Gases* (Clarendon, Oxford, 1955; Fizmatgiz, Moscow, 1959).
9. A. F. Alexandrov, L. S. Bogdankevich, and A. A. Rukhadze, *Principles of Plasma Electrocdynamics* (Vysshaya Shkola, Moscow, 1978; Springer-Verlag, Berlin, 1984).

Translated by N.N. Ustinovskiĭ

Plasma Physics Reports, Vol. 27, No. 2, 2001, pp. 178–179. Translated from Fizika Plazmy, Vol. 27, No. 2, 2001, pp. 190–191.
Original Russian Text Copyright © 2001 by Avrorin, Balebanov, Boyarchuk, Velikhov, Galeev, Golant, Erokhin, Zheleznyakov, Zelenyĭ, Karas', Kardashev, Krokhin, Kurdyumov, Litvak, Managadze, Mikhaĭlovskiĭ, Moiseev, Oraevskiĭ, Pokhotelov, Rukhadze, Sagdeev, Stepanov, Faĭnberg, Chkhetiani, Shafranov.

Jumber Lominadze (In Honor of His 70th Birthday)

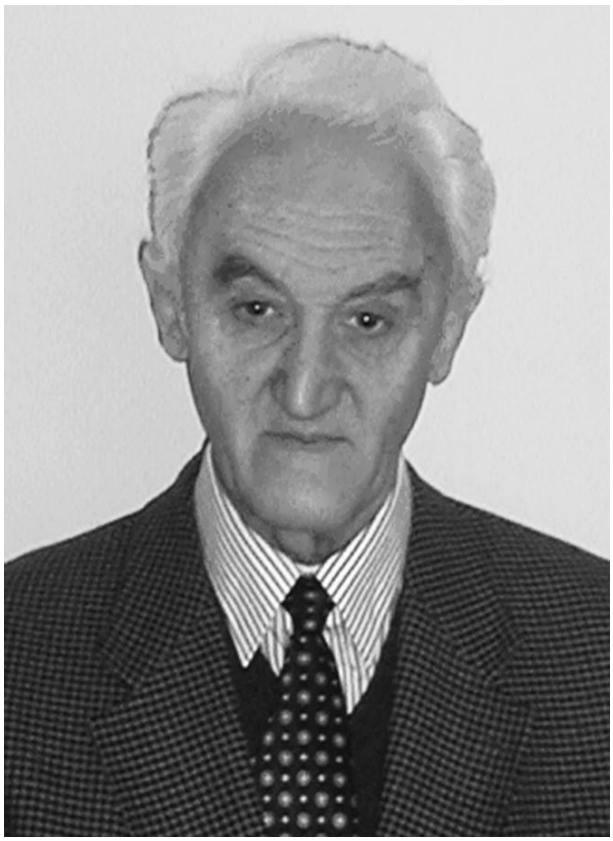

On September 20, 2000, we celebrated the 70th birthday of Jumber Lominadze, one of the first members of the Editorial Board of *Plasma Physics Reports* (1975–1987), academician of the Georgian Academy of Sciences, world-famous scientist, talented scientific administrator, and prominent political and public figure of the Republic of Georgia.

J. Lominadze was born in 1930 in Tbilisi. After graduating from Moscow State University, he worked in Chelyabinsk-70 (Snezhinsk), at the All-Union Research Institute of Technical Physics, where he developed a great interest in plasma physics and controlled nuclear fusion. In 1958, he returned to Georgia and was actively involved in the organization of these investigations at the Institute of Physics of the Georgian Academy of Sciences.

Being an open and friendly man, J. Lominadze established successful scientific contacts with physicists from the Kurchatov Institute of Atomic Energy, Lebedev Institute of Physics, and Kharkov Institute for Physics and Technology, as well as with American scientists from Princeton University, Oak Ridge, and the University of Maryland. The cycle of investigations on the propagation and absorption of cyclotron waves in a fully ionized plasma, which he carried out together with his Kharkov colleagues, was completed with the publication of his monograph *Cyclotron Waves in Plasmas* (Metsniereba, Tbilisi, 1975; Pergamon, New York, 1981), which became a handbook for many theorists and experimentalists.

In the 1980s, in connection with the rapid development of plasma astrophysics, J. Lominadze turned to this field of science. On the basis of the theoretical group founded in 1976 on his initiative at the Abastumani Astrophysical Observatory (AAO) of the Georgian Academy of Sciences, a famous scientific school of theoretical astrophysics was formed in a collaboration with various international science centers including the Institute of Space Research, Lebedev Institute of Physics, Sternberg Astronomical Institute, and Russian Research Centre Kurchatov Institute (Russia); the University of Maryland and California Technical College (USA); the Raman Research Center (India); Cambridge and Cardiff universities (United Kingdom); the International Center for Theoretical Physics (Italy); the Kepler Astronomical Institute (Poland); and the Ecole Polytechnique (France). Along with fundamental studies on the dynamics of perturbed continuous media, the members of the school investigated the processes occurring in various astrophysical objects, such as the accretion disks of black holes, active galactic nuclei, pulsar magnetospheres, the Sun, and the Earth's magnetosphere. J. Lominadze and his colleagues founded a new line of investigations—the electromagnetic theory of electron–positron plasma. They developed a theoretical model that explains the phenomenon of Crab pulsar emission. Since 1984, regular meetings of the International School and Workshop on Plasma Astrophysics organized on the initiative of J. Lominadze have been held. The 2000 International School, dedicated to 70th birthday of J. Lominadze, was held in Borzhomi.

The field of scientific interests of J. Lominadze has constantly grown. He investigated the hydrodynamics of a collisionless relativistic plasma with anisotropic pressure and relativistic self-focusing of electromagnetic beams in an inhomogeneous plasma. He contributed considerably to the laboratory modeling of vortices and solitons, a concept of which was developed by

1063-780X/01/2702-0178$21.00 © 2001 MAIK "Nauka/Interperiodica"

V.I. Petviashvili at the RRC Kurchatov Institute in the early 1980s. In cooperation with Russian scientists, a universal device for the modeling of vortices and sheared flows in planetary atmospheres and laboratory plasmas was created at AAO.

In recent years, J. Lominadze together with his pupils has developed new methods for analyzing processes occurring in accretion disks and jets. In particular, the resonance transformation of oscillations and conversion of vortices into waves have been investigated, and a nonmodal theory of dynamics of perturbed sheared flows has been developed. All this made it possible to substantially revise earlier concepts.

J. Lominadze has made an important contribution to the organization of science. He always promoted wide scientific contacts between Georgian scientists and scientists from other countries, which certainly assisted in maintaining the high level of Georgian science. Since 1982, he has been the academician–secretary of the Department of Mathematics and Physics of the Georgian Academy of Sciences. He was the director of AAO. At present, he is the head of the Center of Plasma Astrophysics (a branch of AAO). For more than thirty years, Professor J. Lominadze has given lectures at the Physics Department of Tbilisi State University. Under his supervision or with his active support, seven candidates and four doctors of science have defended their theses. J. Lominadze is a prominent political and public figure. Presently, he occupies the important position of the chairman of the Central Election Committee of the Republic of Georgia.

J. Lominadze is a man of encyclopedic knowledge and a connoisseur of music and art; he is also keen on artistic photography.

His friends and colleagues heartily congratulate Jumber Lominadze on his seventieth birthday and wish him robust health, happiness, further fruitful scientific activity, and success in all his initiatives.

On behalf of all of his friends and colleagues,

É.N. Avrorin, V.M. Balebanov, A.A. Boyarchuk, E.P. Velikhov, A.A. Galeev, V.E. Golant, N.S. Erokhin, V.V. Zheleznyakov, L.M. Zelenyĭ, V.I. Karas', N.S. Kardashev, O.N. Krokhin, S.P. Kurdyumov, A.G. Litvak, G.G. Managadze, A.B. Mikhaĭlovskiĭ, S.S. Moiseev, V.N. Oraevskiĭ, O.A. Pokhotelov, A.A. Rukhadze, R.Z. Sagdeev, K.N. Stepanov, Ya.B. Faĭnberg, O.G. Chkhetiani, and V.D. Shafranov

Plasma Physics Reports, Vol. 27, No. 2, 2001, p. 180. Translated from Fizika Plazmy, Vol. 27, No. 2, 2001, p. 192.
Original Russian Text Copyright © 2001 by the Editorial Board.

COMMENTS

Letter to the Editorial Board

In the seventh issue of *Plasma Physics Reports* for 2000, a comment made by me (together with V.I. Karas') was published about the book by A.F. Aleksandrov and A.A. Rukhadze *Course on Electrodynamics of Plasmalike Media* (Mosk. Gos. Univ., Moscow, 1999).

I will state the following. I generally confirm the high evaluation of this book, but I do not share the statements formulated in the second part of the comment, which were included in the text without consulting me.

Ya.B. Faĭnberg,
Academician of the National Academy of Sciences of Ukraine

Concerning the Inaccurate Account of Some Events in the Paper by A.F. Aleksandrov and A.A. Rukhadze "On the History of Fundamental Papers on the Kinetic Plasma Theory"

My attention was drawn to the inaccurate account of some events in the paper by A.F. Aleksandrov and A.A. Rukhadze "On the History of Fundamental Papers on the Kinetic Plasma Theory," Fiz. Plazmy **23**, 474 (1997) [Plasma Phys. Reports **23**, 442 (1997)]. The matter concerns the next to last paragraph of that paper. Having pointed out that N.N. Bogolyubov, in his monograph from 1946, gave a rigorous mathematical justification of the Vlasov kinetic theory, the authors of the paper wrote: "In this connection, the appearance of paper [5] in 1949 seems to be puzzling because of its sharp and unjustified criticism of Vlasov's studies and, especially, Vlasov's approach to the kinetic plasma theory. In that paper, the monograph by Bogolyubov [4] was not mentioned at all. This is even stranger as, by that time, this fundamental monograph, which was closely related to the kinetic plasma theory, was generally recognized and widely cited in the literature."

Here, the following events are inaccurately accounted:

1. In paper [5], the works by Vlasov from 1944–1945 on the generalized plasma theory and theory of solids, rather than his paper from 1938 (which was cited throughout the paper by Aleksandrov and Rukhadze as the basis of the kinetic plasma theory), were criticized. Paper [5] begins and ends by quoting just the above works from 1944–1945.

2. Paper [5] was published in 1946, not in 1949; therefore, it is not surprising that, "in that paper, the monograph by Bogolyubov was not mentioned at all." Analogously, "the discussion between Landau and Vlasov" cannot be dated as 1949 (as was done in the abstract of the paper by Aleksandrov and Rukhadze), because the paper by Landau in which he criticized Vlasov's studies, as well as Vlasov's reply [see A.A. Vlasov, Vest. Mosk. Univ., Ser. 3: Fiz., Astron., Nos. 3–4, 63 (1946)], was also published in 1946.

I extend my apologies for the overlooked distortion of facts in the paper by Aleksandrov and Rukhadze.

V.D. Shafranov, *Editor-in-Chief*

1063-780X/01/2702-0180$21.00 © 2001 MAIK "Nauka/Interperiodica"

Plasma Physics Reports, Vol. 27, No. 2, 2001, pp. 89–109. Translated from Fizika Plazmy, Vol. 27, No. 2, 2001, pp. 99–120.
Original Russian Text Copyright © 2001 by Aleksandrov, Branitskii, Volkov, Grabovskii, Zurin, Nedoseev, Oleinik, Samokhin, Sasorov, Smirnov, Fedulov, Frolov.

PLASMA DYNAMICS

Dynamics of Heterogeneous Liners with Prolonged Plasma Creation

V. V. Aleksandrov[1], A. V. Branitskii[1], G. S. Volkov[1], E. V. Grabovskii[1], M. V. Zurin[1], S. L. Nedoseev[1], G. M. Oleinik[1], A. A. Samokhin[1], P. V. Sasorov[1, 2], V. P. Smirnov[1], M. V. Fedulov[1], and I. N. Frolov[1]

[1]*Troitsk Institute for Innovation and Thermonuclear Research, Troitsk, Moscow oblast, 142092 Russia*
[2]*Institute of Theoretical and Experimental Physics, Bol'shaya Cheremushkinskaya ul. 25, Moscow, 117259 Russia*

Received May 23, 2000

Abstract—Prolonged plasma creation in heterogeneous liners, in which the liner substance is separated into two phase states (a hot plasma and a cold skeleton), is investigated both experimentally and theoretically. This situation is typical of multiwire, foam, and even gas liners in high-current high-voltage facilities. The main mechanisms governing the rate at which the plasma is created are investigated, and the simplest estimates of the creation rate are presented. It is found that, during prolonged plasma creation, the electric current flows through the entire cross section of the produced plasma shell, whose thickness is comparable with the liner radius; in other words, a current skin layer does not form. During compression, such a shell is fairly stable because of its relatively high resilience. It is shown that, under certain conditions, even a thick plasma shell can be highly compressed toward the discharge axis. A simplified numerical simulation of the compression of a plasma shell in a liner with prolonged plasma creation is employed in order to determine the conditions for achieving regimes of fairly compact and relatively stable radial compression of the shell. © *2001 MAIK "Nauka/Interperiodica"*.

1. INTRODUCTION

In recent years, significant progress has been achieved in generating high-power X-ray pulses in high-current high-voltage Z-pinch facilities [1, 2]. This progress has been made possible due to the implementation of the idea [3] of optimized radial collapse of a light liner onto a central target (the so-called double-liner scheme) under conditions typical of facilities with sufficiently high currents (such as Saturn and Z), when the light liner can be composed of many (up to 200–300) thin metal wires. Specifically, in the Z facility at Sandia National Laboratory (USA) [2], a 20-MA current with a rise time of 105 ns was switched on to a 2-cm-long and 4-cm-diameter cylindrical multiwire liner composed of 240 tungsten wires, each having a diameter of 7.5 μm. In a series of experiments carried out without a central target, 2-MJ X-ray pulses with a peak intensity of 200 TW and a full width at half-maximum (FWHM) of 5.5 ns were generated at the time at which the liner collapsed onto the discharge axis. One of the most important results obtained in those experiments was that of achieving such a relation between the current rise time and the FWHM of the generated X-ray pulse.

These experimental results motivated investigations of inertial confinement fusion (ICF) in Z-pinch facilities, the more so since facilities of this type are less expensive in comparison with, e.g., facilities for laser-driven ICF. Further progress in this field requires that the power of an X-ray pulse be made several times higher; such X-ray pulses could in principle be generated in machines that would be capable of operating with current pulses two to three times higher. Following from this, the question arises of how to scale the results obtained previously. To answer this question and, accordingly, to optimize the liner design and parameters, we must find the physical factors that govern such a symmetric and compact compression of multiwire liners in comparison with, e.g., gas liners with similar parameters [4, 5]. The renewed interest in the physical research on the compression of multiwire liners was a reaction to these important issues [6–14].

The main (and still undoubted) point in interpreting experimental data is that the multiwire structure of a liner leads to the compact compression of the produced plasma shell, thereby ensuring high densities of the kinetic and magnetic energies of the liner near the system axis. In attempting to explain such a compact compression of the plasma shell produced in a multiwire liner, most of the authors [6–13] assumed that a continuous cylindrical plasma shell with a fairly high degree of axial symmetry is formed on a sufficiently short time scale. According to this approach, it is the high symmetry of the produced plasma shell that ensures the symmetry and compactness of the liner plasma implosion and is responsible for the delayed onset of the Rayleigh–Taylor (RT) instability. In this case, the governing parameter of a multiwire liner is the ratio of the interwire gap to the diameter of the current-carrying

1063-780X/01/2702-0089$21.00 © 2001 MAIK "Nauka/Interperiodica"

plasma cylinder produced by an electric explosion of each individual wire [6, 11].

This paper is devoted to the experimental and theoretical justification of another approach to interpreting efficient compression of plasma shells formed in multiwire liners. We do not deny the importance of the symmetry of the initial state of a plasma liner, assuming, however, that it plays a secondary role. Our approach provides other ways of optimizing the compact compression of plasma liners.

The essence of our approach can be briefly described as follows. Multiwire liners ensure much more stable distributions of the produced current-carrying plasma in comparison with those in gas liners. This stems from both the heterogeneous nature of the liner (the presence of a hot plasma, which carries the main plasma current, and a relatively cold substance, which is produced directly by the electric explosions of the wires) and the associated prolonged plasma creation. Below, the term "plasma creation" does not mean a conventional ionization process but refers to the production of a plasma whose conduction is high enough for it to carry the bulk of the generator current and whose ohmic resistance is lower than the internal resistance of the generator and is comparable to or even lower than the impedance related to the change in the inductance of the liner. During prolonged plasma creation, the produced current-carrying plasma converges continuously toward the system axis, thereby giving rise to a plasma shell whose thickness is markedly larger than the skin depth, the magnetic field and current being, however, nonzero over the entire cross section of the shell. At the initial stages of compression, the plasma shell may even be discontinuous in the azimuthal direction. The convergence of a thick plasma shell toward the system axis is ensured by the spatially distributed Ampère force $j \times B/c$, which is almost uniform over the entire cross section of the shell, rather than by a magnetic piston, which acts on the outer surface of the liner and gives rise to strong instabilities. Such plasma liners are much less subjected to the RT instability as compared to thin plasma shells of thicknesses comparable to the skin depth.

At the same time, the plasma shell resilience caused by the frozen-in magnetic field may reduce the extent of radial compression. Obviously, there exists an optimum shell thickness that is small enough to ensure sufficiently compact compression, as if the instability were absent, and is large enough for the instability to be suppressed. We think that, in increasing the number of wires in the liner while keeping the liner mass fixed, the authors of [1, 2] groped experimentally for an optimum design for the given liner.

Here, we will not only attempt to validate some of the above assertions but also present arguments in favor of the fact that a relatively cold, thick plasma shell having a certain radial resilience caused by the frozen-in magnetic field can be highly compressed toward the system axis. In order to achieve such a high compression, the plasma pressure should be low enough and the initial current and mass densities should obey certain radial distributions. The analytic solutions presented below support this conclusion and disprove the widely accepted opinion that thick resilient plasma shells cannot be compressed effectively. Our results provide new ways of optimizing the design of multiwire liners.

The high-power pulsed electric energy sources in which we are interested here were designed and built in the 1970s with the purpose of generating megaampere relativistic electron beams with a duration of several tens of nanoseconds. Such generators were later used, in particular, to supply fast self-compressed plasma discharges. As a result, a qualitatively new situation arose that had never been encountered in classical megaampere Z-pinches and microsecond plasma foci. The essential features of this situation can be explained as follows. The requirement that the pinch compression rate be consistent with the much faster rise time of the discharge current necessitated a proportional (other conditions being the same) decrease in the initial pinch radius (to approximately one centimeter). Accordingly, the initial density of the plasma-producing substance to be compressed was increased by a factor of several tens or even several hundreds. Consequently, fundamentally new methods were developed to create substances with the desired initial density distributions. As a result, the final parameters of a compressed fast Z-pinch were found to depend critically on its initial shape and other characteristics. This is an important feature in which fast Z-pinch devices differ from plasma focus devices and which makes it possible to carry out experiments with fast pinches of complicated initial shapes, unachievable in classical devices [3, 15, 16], and subsequently with pinches whose heterogeneous substance contains a condensed plasma-producing component [1, 17, 18].

It was found that, under the "cold start" conditions of a fast pinch (when the plasma is created by the discharge current itself), the plasma creation process is spatially nonuniform. Using as an example foam and gas liners, Branitskiĭ *et al.* [18] thoroughly analyzed the cold-start effects, which result in nonuniform plasma creation in fast superterawatt self-compressed discharges. In gas liners, the appearance of a hot plasma component in an initial, almost uniform, cold substance most likely stems from thermal and ionization instabilities, which lead to plasma filamentation at the very beginning of the discharge. At later stages, the hot plasma component formation is probably maintained by various interchange instabilities (transverse stratification of the discharge), primarily, by the RT instability (here, we mean the second, strongly nonlinear stage of the RT instability, which was simulated in [10, 13, 19]). In foam liners, the plasma configuration is *a priori* heterogeneous because of the structure of the liner substance. Nevertheless, the filamentation and stratification instabilities peculiar to gas liners can also occur in

foam liners. Here, we are interested only in one aspect of the heterogeneous nature of plasma configurations originated from gas or foam liners; specifically, we will consider it as a cause of prolonged plasma creation—the most typical property of discharges initiated in heterogeneous plasma-producing media. In this sense, we can say that gas and foam liners resemble, to some extent, multiwire liners.

Hence, our study will cover not only multiwire liners but also other analogous heterogeneous structures, first of all, foam liners, which were thoroughly investigated by Branitskiĭ *et al.* [18]. After the discharge is initiated, "conventional" gas liners acquire a heterogeneous nature and, as was already noted, possess all of the properties of prolonged creation of a hot plasma. However, gas liners differ from multiwire and foam liners in that their heterogeneous nature stems from the onset of instabilities and, therefore, (like the plasma creation rate) is hard to control. Various heterogeneous liners can probably be classified by the extent to which their structures are regular and accordingly controllable, namely, gas, foam, and multiwire liners.

We can distinguish between the following three stages of compression of the plasma of a heterogeneous liner with prolonged plasma creation: the creation of a hot plasma, the convergence of a hot plasma toward the system axis, and the final stage of compact compression. Although our experiments were aimed at achieving the desired parameters of the compressed hot plasma at the final stage, in what follows we restrict ourselves to studying the first two stages of the dynamics of the plasma shell in a heterogeneous liner with prolonged plasma creation.

Our paper is organized as follows. In Section 2, we give a more detailed experimental and theoretical justification of the proposed scenario for compression of the plasma shell in a multiwire liner; in particular, in Section 2.2, we present new experimental data from the Angara-5-1 facility. In Section 3, we systematically describe the compression scenario. In Section 4, we theoretically examine different stages of this scenario. The most important point in our investigations is that plasma creation and plasma compression are analyzed separately. Specifically, taking into account the possibility of controlling the plasma creation process, we study the dynamics of a plasma shell in a liner with prolonged plasma creation by treating the creation rate as an independent external parameter, which is to be adjusted as necessary to optimize the compression of the shell toward the device axis. In Section 4.1, we make simple estimates of the plasma creation rate in heterogeneous plasma systems and determine how this rate depends on the current flowing through the plasma. In Section 4.2, we construct a simple model of the boundary layer near the plasma source. It is the structure of the boundary layer that governs the plasma creation rate. In Sections 4.3 and 4.4, we develop simple theoretical models of both the plasma dynamics in the presence of a continuously operating plasma source and the compression dynamics of a thick-walled current-carrying liner. In Section 4.5, we briefly discuss the stability of compression of a thick-walled current-carrying liner. In the Conclusion, we summarize our main results.

2. REVIEW OF EXPERIMENTAL AND THEORETICAL RESULTS ON HETEROGENEOUS LINERS

2.1. Exploding Wires and Early Experiments with Multiwire Liners

In the physics of Z-pinches, heterogeneous structures with prolonged plasma creation have been known for many years. Thus, heterogeneous structures are characteristic of the simplest dense Z-pinches produced by an electric explosion of metal or dielectric wires [20–25]. In the current range 10–300 kA, thermal instabilities [21, 24, 25] cause the discharge plasma of electrically exploded wires to separate into two phase states—a hot plasma corona with a temperature of 50–200 eV, which carries essentially all of the discharge current, and a cold substance, whose density is sometimes comparable with that of solids. In this respect, the most illustrative pinch is that formed as a result of the explosion of a cryogenic deuterium fiber [22–25], when the emitted radiation plays a negligible role. In this case, the electron heat flux from the hot corona toward the cold core of the pinch causes the core to "evaporate" progressively, so that the cryogenic fiber becomes a hot plasma within a time scale of 20–100 ns (depending on both the current magnitude and wire mass [23–25]). During this process, the plasma corona tied to its source remains globally stable, despite pronounced local instabilities.

Another example of heterogeneous structures with prolonged plasma creation is multiwire liners, which have been studied for a long time (see, e.g., [26, 27]). These early experiments differed from present-day experimental investigations [1, 2] in that they were carried out with liners comprised of a relatively small number of wires (usually, from 8 to 24), because, for relatively low currents switched on to the liners, the liner mass consistent with the desired compression rate (see below) was too small (and the technology for producing thin wires was far from being perfect at the time) in order to use a large number of wires (about several hundred). Also, in early experiments, there was no need to progress in this direction. Since the distances between the wires in such liners are large enough for an exploding wire to be insignificantly affected by the other exploding wires, each individual explosion can be regarded as being essentially independent of the others and can be described by the above approach: at the initial stages of explosion, a small-mass hot plasma corona surrounds a relatively cold and dense vapor of the exploding wires, in which case the bulk of the cur-

rent should flow in the coronal plasma because of its much larger transverse cross section and much lower specific resistance (due to much higher temperatures).

An important factor originating from the multiwire nature of the liner is the collective azimuthal field $\bar{B}_\varphi$, which accelerates each wire toward the liner axis. If each exploding wire with the complicated heterogeneous structure described above were accelerated as a single entity, then the acceleration would be equal to $g_r = I_1 \bar{B}_\varphi/(m_1 c)$, where I_1 is the current flowing in a wire and m_1 is the mass per unit length of a wire. However, for the core of the heterogeneous structure to move with such an acceleration, it should carry a current at least as high as $I_{\min} = m_1 c g_r/B_{\max}$, where $B_{\max} = 2I_1/(R_1 c)$ is the maximum magnetic field near the outer boundary of the plasma corona formed as a result of the explosion of a wire and R_1 is the radius of the dense part of the coronal plasma. Such compression rates can be achieved under the condition

$$\frac{R_0^2 \sigma_0}{R_1^2 \sigma_1} > 2\pi \frac{R_1}{\Delta}, \qquad (1)$$

where R_0 is the radius of the cold core; σ_0 and σ_1 are the conductivities of the coronal plasma and core substance, respectively; and Δ is the interwire gap. In the experiments performed up to now, this condition has not been satisfied even for $\Delta \gg R_1$, i.e., when the coronal plasma is expected to occur deep inside the regions bounded by the separatrices between the magnetic fields of the individual wires. This means that the coronal plasma accelerated toward the liner axis always remains separated from the essentially immobile exploding wire core, in which case the exploding wire substance cannot be accelerated as a whole toward the liner axis. Here, we have briefly reiterated (in the proper terminology) the analysis made by Bobrova *et al.* at the end of their paper [21],[1] which was aimed, in particular, at interpreting experiments carried out in [27]. In those experiments, it was found that the plasma "blown out" from a multiwire liner reached the discharge axis a fairly long time before the current had reached a maximum; this plasma formed a relatively stable pinch at the system axis. Then, the plasma produced by the explosions of the wires continued to flow toward the central pinch for a fairly long time after the current had reached a maximum. In [27], the properties of this radial plasma flow were studied both experimentally and theoretically. At that time, reducing the diameter of the wires while simultaneously increasing their number was not thought to be the best way of shortening the time required for the wires to become plasma and, accordingly, achieving more compact plasma shells at the final stage of radial compression of the explosion-produced plasma.

[1] This paper contains some misprints in the formulas.

2.2. Experiments on the Visualization of Prolonged Plasma Creation

In this section, we report the results of experiments with multiwire liners in the Angara-5-1 facility that provide clear evidence of the prolonged creation of a hot plasma through electric explosions of the wires. These experimental results, which were briefly described in [28], not only confirm but also significantly refine the results of earlier experiments carried out in [27] with liners comprised of a smaller number of wires. Note that the results of [27] clearly demonstrated the important role of prolonged plasma creation in multiwire liners.

Our experiments were performed with tungsten wires 6–10 μm in diameter placed along the generatrices of a cylinder 8–20 mm in diameter. The number of wires was varied from 8 to 120. The liner discharges were initiated by passing a 3–4-MA current with a rise time of 90–120 ns through the cylindrical multiwire liners. Before the main current pulse, a current prepulse heated the wires by no more than 10°C.

First, we report the results from our experiments with an 8-mm-diameter liner composed of 80 wires each having a diameter of 6 μm. Note that, since the liners in our experiments were smaller in diameter than the liners in the experiments of [1, 2], the interwire gap (about 300 μm) and the current per unit length of the circumference of the liner (about 1 MA/cm) are both fairly close to those in the experiments of [1, 2]. Accordingly, in our experiments, soft X-radiation (SXR) pulses were shorter than the current rise time by approximately the same factor (Fig. 1), the maximum achievable SXR power being 5 TW.

The plasma dynamics was experimentally visualized by laser shadowgraphy. A probing laser beam was first divided into three spatially separated rays, which were delayed with respect to each other in order to ensure probing over the desired time intervals. In experiments with laser shadowgraphy, we used liners without four "central" wires, in order to ensure the viewing of the central region of a liner through the vertical gap between the wires. These experiments were conducted with somewhat lower currents than the current in the experiment illustrated in Fig. 1. The representative laser shadowgraphs are shown in Fig. 2. We do not discuss here the pronounced axial inhomogeneity of the plasma. We draw attention to the quasi-planar plasma flows from each wire toward the liner axis. In Fig. 2, the most interesting phenomenon is the formation of a plasma prepinch (precursor) at the liner axis, which is distinctly seen in the second and third frames. These experimental results clearly indicate that the plasma flows toward the discharge axis for a relatively long time, while the liner periphery, which serves as a plasma source, remains immobile and contains most of the original liner mass.

We do not focus on the interferometric images of the plasma flows in the plane parallel to the discharge axis

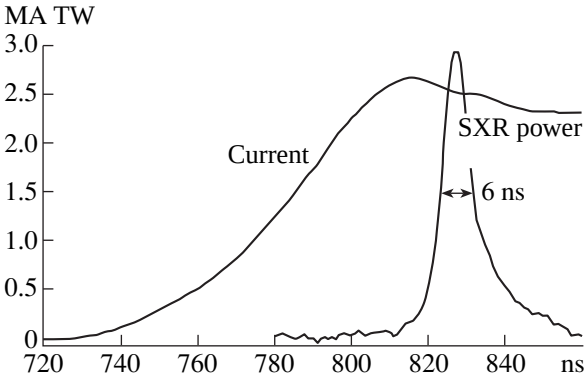

Fig. 1. Time evolutions of the SXR power and the current flowing through an 8-mm-diameter liner composed of 80 tungsten wires each having a diameter of 6 μm (shot no. 3594).

[28]. In experiments carried out in the MAGPIE facility at the Imperial College of Science and Technology (London, UK) [8], such plasma flows were visualized by interferometric measurements along the discharge axis. Recent MHD simulations carried out by Chittenden *et al.* [12] for liners comprised of a small number of wires and treated using cylindrical geometry (the coordinates being r and φ) confirm the qualitative analysis that was performed about ten years ago and was briefly repeated in the previous section and also agree with the experimental data presented here.

In our experiments, prolonged plasma creation was also studied with the help of fast scanning photometry combined with X-ray frame-by-frame photography. The experimental data on an electrical discharge in an 8-mm-diameter liner composed of 32 wires each having a diameter of 10 μm are demonstrated in Fig. 3. The upper frame of the figure presents the time evolutions of the total current and SXR intensity. The middle frame shows an optical image of the liner plasma scanned in time through a slit perpendicular to the discharge axis. The four lower frames are photos of the SXR from the liner.

Fast scanning photometry of the SXR from the liner clearly shows that the wires are immobile for a long time, while the plasma flows (in the form of narrow strips) from the wires toward the liner axis. The dynamics of the development of plasma flows is also seen in X-ray frame-by-frame photographs. The plasma is seen to fill the liner interior so that the pinch at the axis grows from the prepinch, which is maintained by the plasma inflow. The wires remain immobile for about 130 ns. The current per wire increases to 50–55 kA. Only the last X-ray photograph shows that the wires evaporate completely, although the X-ray image of the plasma is only slightly smaller in size than the original liner. At the original positions of the wires, the optical luminosity of the plasma starts to decrease 130 ns after the beginning of the current pulse. The residual plasma converges toward the discharge axis at a velocity of about $\sim 10^7$ cm/s.

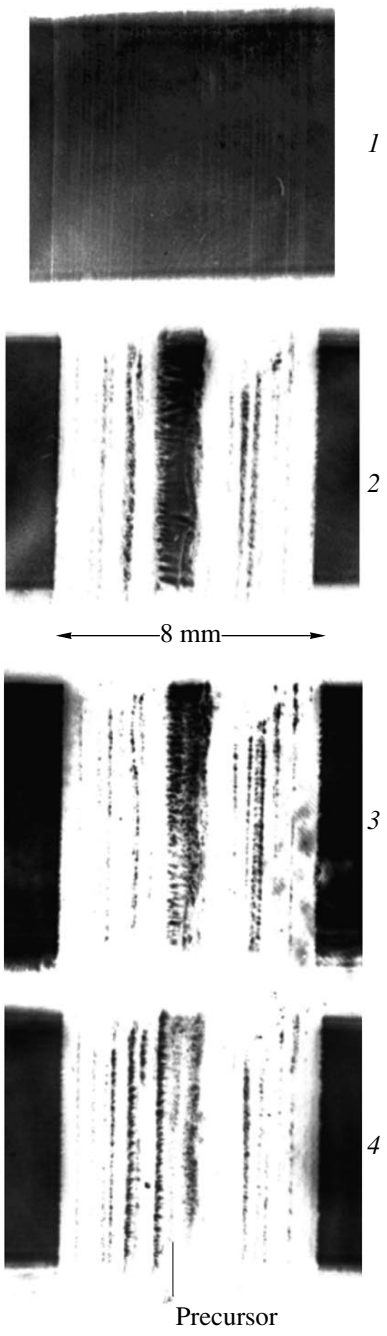

Fig. 2. Laser shadowgraphs of an 80-wire liner (shot no. 3205): (*1*) before the current pulse, (*2*) 87 ns after the beginning of the current pulse (the current per wire being 9 kA), (*3*) 100 ns after the beginning of the current pulse (the current per wire being 12 kA), and (*4*) 113 ns after the beginning of the current pulse (the current per wire being 15 kA). The prepinch (precursor) is seen to form in the central region of the initially empty diagnostic gap.

Hence, we can conclude that the liner consists of a plasma flowing toward the axis and a dense substance,

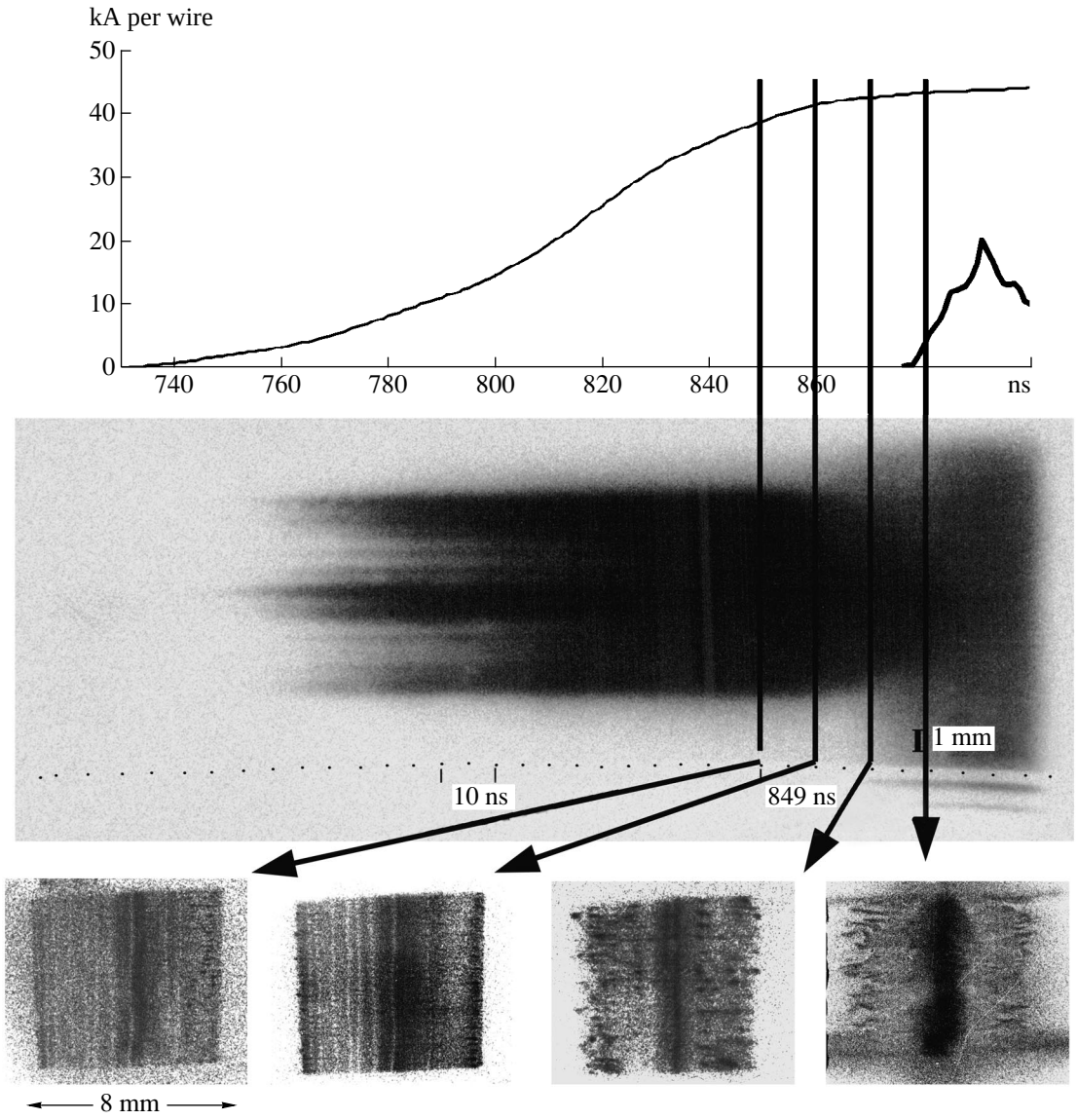

Fig. 3. Compression of a 32-wire liner (shot no. 3623).

which serves as a plasma source. This can naturally be attributed to the fact that a highly conducting plasma is produced from the substance of the exploding wires almost throughout the current pulse.

2.3. Other Examples of Liners with Prolonged Plasma Creation

Another example of heterogeneous liners with prolonged plasma creation is foam liners prepared by drying agar-agar gel [18]. A foam liner is composed of dry agar fibers and plates distributed randomly in space, the characteristic size of a spatial cell being 50 μm. Such a liner is uniform on spatial scales longer than 100 μm. An important distinctive feature of the foam liner is that the diameter of the corona that can form around each fiber is markedly larger than the size of an elementary spatial cell. Therefore, we can assume that the skeleton of the heterogeneous liner is immersed entirely in a hot plasma. Although, at the initial discharge stages, the mass of the hot plasma is substantially smaller than the total liner mass, it carries essentially all of the discharge current, while the current carried by the cold skeleton is negligible. For this reason, the hot plasma accelerates toward the axis at a much higher rate than a liner with a uniform current distribution over mass. Although the Ampère force causes the hot plasma to converge toward the axis, the liner skeleton always remains inside the hot plasma component (in the presence of a strong axial electric field whose strength is proportional to $\approx v_r B/c$) due to prolonged plasma creation via the evaporation of the liner substance. Hence, in the experiments of [18],

a heterogeneous liner consisting of two components—a cold skeleton immersed in a hot plasma—also serves as a long-term source of hot plasma, which accelerates toward the discharge axis. The radial size of such a plasma (with a frozen-in magnetic field) can substantially exceed the skin depth.

As was noted in the Introduction, due to the cold-start effects, the gas liner also evolves into a heterogeneous structure with prolonged plasma creation.

An important feature of foam liners (as well as gas liners) is current filamentation at the initial discharge stages [18]. Presumably, the current filamentation results from the thermal–ionization instability, which occurs on spatial scales from one millimeter to fractions of a millimeter (in the azimuthal direction). However, this instability is likely to be suppressed in multiwire liners comprised of periodically spaced wires, the interwire gap (fractions of a millimeter) being of the same order as the instability scale length; at the very least, the cited papers, as well as other papers devoted to multiwire liners, contain no information on the thermal–ionization instability, which, however, may develop in liners composed of a larger number of more closely spaced wires.

3. SCENARIO OF THE EVOLUTION OF A HETEROGENEOUS LINER WITH PROLONGED PLASMA CREATION

Summarizing the above considerations, we propose the following scenario of the evolution of heterogeneous liners. As an example, we analyze a multiwire liner composed of wires that are equally spaced over a circle and are oriented perpendicular to it. Nevertheless, the proposed scenario refers to a far larger class of liners.

Heterogeneous liners are those in which, immediately after breakdown, the substance separates into two phase states—a relatively cold skeleton with a density close to that of solids and a hot plasma with a temperature of several tens of electronvolts. The cold liner skeleton always remains immersed in the hot plasma, which, however, may not form a continuous shell in the azimuthal direction. The plasma carries almost all of the discharge current and thus is Joule-heated to high temperatures. The electron heat flux and radiation flux from the hot plasma cause the cold liner skeleton to evaporate continuously. Under the action of the Ampère force, the hot plasma converges toward the discharge axis, while the massive skeleton, which carries a much smaller fraction of the total current, is almost immobile. When a portion of the hot plasma gets displaced toward the axis by a distance large enough for it not to interact with the skeleton, the processes of evaporation, ionization, and heating of the liner substance at the skeleton surface give rise to the next portion of hot plasma. We are thus dealing with the continuous creation of new portions of hot plasma, which are accelerated toward the axis. At the same time, the converging hot plasma carries a frozen-in magnetic field (magnetic flux); consequently, the electric current parallel to the discharge axis flows through it. Below, we will refer to this plasma as a converging current-carrying plasma flow with a frozen-in magnetic field. The frozen-in field gives rise to plasma flow resilience. If the elements of the liner skeleton are separated by large distances, then each element gives rise to its own plasma jet accelerated toward the discharge axis. In the axial region, individual converging jets can merge into a continuous ringlike flow. This processes is captured well by the two-dimensional modeling (in cylindrical r–φ geometry) of a multiwire liner [12]. If the skeleton elements are sufficiently close to each other, then the hot plasma forms a continuous shell around the liner skeleton. In our scenario, the difference between these two cases is not of crucial importance.

The process just described lasts until the liner skeleton evaporates completely. An important question then arises concerning the evaporation rate or the time required for the liner skeleton to evaporate completely, under the assumption that the liner mass is matched with the rise time of the current pulse in the sense that a liner with a uniform current distribution over the mass should stagnate near the discharge axis some time after the current has reached a maximum. If the hot plasma is created at a slow rate, the plasma continues to be created after the current has reached a maximum. Since the mass of the hot plasma is smaller than the matched liner mass, the portions of hot plasma that are produced at the very beginning of the pulse arrive at the discharge axis a long time before the current has reached a maximum. Thus, we are dealing with a long-term and almost steady-state hot-plasma flow from the peripheral regions where the hot plasma is continuously created toward the discharge axis. In this case, the recorded X-ray pulse from the central dense pinch is greatly smoothed and has nothing in common with the desired pulse. Otherwise, if the hot plasma is created at a very fast rate, then the plasma creation process terminates a long time before the current has reached a maximum. In this case, the plasma shell turns out to be thin in the radial direction, the frozen-in magnetic flux is far less intense, and the plasma itself is far less resilient. A further increase in the current gives rise to a magnetic piston, which leads to even stronger compression of the hot plasma into a thin shell that is rapidly destroyed due to the RT instability. This situation is analogous to a thin-walled plasma liner, which is less attractive from the standpoint of the parameters of the generated X-ray pulse. A comparison between these somewhat unfavorable limiting cases provides evidence for the existence of the optimum plasma creation rate. If the plasma production comes to an end approximately at the time when the current reaches its maximum, then the effect of the magnetic piston, which should come into play at a later time and may be dangerous due to the possible onset of the RT instability, is insignificant, the more so

because the substantial frozen-in magnetic flux makes the converging plasma flow highly resilient in the radial direction. On the other hand, by that time, a liner whose mass is matched with the current rise time is displaced toward the axis only slightly. Consequently, the thickness of the hot plasma shell can be appreciably smaller than the liner radius. Presumably, this situation provides the possibility of achieving highly compressed plasma pinches and, accordingly, generating short high-power X-ray pulses. This means that, for a liner with a matched mass, the optimum time for finishing the plasma creation process is about the time during which the current reaches its maximum.

Hence, we can see that the plasma creation rate is a key parameter for heterogeneous liners with prolonged plasma creation. It is important to investigate the plasma creation rate as a function of both the current per unit length of the liner in the azimuthal direction and the interwire gap at a prescribed surface mass density of the liner.

A comparison between the old experimental data [27] and the new results presented here and in [1, 2] clearly indicates that the plasma creation rate increases with decreasing interwire gap, the remaining parameters of the liner (in particular, its mass) being fixed, at least until the distance between the wires is larger than the transverse dimensions of the individual converging plasma jets. This important conclusion requires additional experimental and numerical verification. If this conclusion is in fact valid, then the published data from the experiments carried out by Sanford *et al.* [11] in order to investigate how the number of wires in a liner affects its dynamics might be reinterpreted in a radically different manner.

4. SIMPLEST THEORETICAL MODELS OF THE DYNAMICS OF A LINER WITH PROLONGED PLASMA CREATION

In this section, we consider the simplest theoretical models suitable for describing the dynamics of a liner with prolonged plasma creation. It is convenient to investigate the dynamic problem in two steps, i.e., to study the plasma creation process and the dynamics of the produced plasma shell separately. Although the plasma shell may have an inverse effect on plasma creation, we start by investigating the shell dynamics, assuming that the plasma source is prescribed. Moreover, in this work, we will often choose the plasma creation rate so as to satisfy the requirement that the radial structure of the plasma shell should be fairly homogeneous. We also simplify the problem under discussion by averaging over the internal spatial structure of a heterogeneous liner. This approach leads to a volume plasma source whose intensity depends only on the radius and time. The related MHD equations, which are rather difficult to find in the literature, are presented in the Appendix. Meanwhile, we begin by estimating the plasma creation rate.

4.1. Estimation of the Plasma Creation Rate

In a hot plasma flow formed by a liner with prolonged plasma creation, we can distinguish between two regions. In the first region, which is located at a large distance from the liner skeleton, the magnetic field can be assumed to be frozen in the plasma, the heat transport due to thermal conduction can be neglected, and the azimuthal structure of the heterogeneous liner is of secondary importance. In the second region, which is immediately adjacent to the skeleton of a heterogeneous liner, the above processes are important and the magnetic field is not yet frozen in the plasma. This region can naturally be called the "boundary layer," in view of its small thickness, which is determined by the largest of the following spatial scales:

(i) the characteristic period δ of the heterogeneous structure (e.g., the interwire gap in a multiwire liner composed of wires positioned along the generatrices of the cylinder),

(ii) the radial thickness δ_r of the liner skeleton (e.g., the thickness of the foam liner), and

(iii) the skin depth $\delta_s = \nu_m/c_A$ (where $\nu_m = c^2/4\pi\sigma$ is the magnetic viscosity, σ is the plasma electric conductivity, and c_A is the local Alfvén velocity).

In this section, we discuss the simplest estimate of the plasma creation rate in order to introduce the physical processes underlying plasma creation and provide at least a rough insight into the dependence of the plasma creation rate on the current flowing through the liner.

We estimate the hot-plasma creation rate $\dot{m}$ in units of mass per unit area of the side surface of the liner, assuming that $\delta_s \gg \delta, \delta_r$. Under these conditions, we are dealing with an azimuthally homogeneous and infinitely thin plasma source. We also neglect radiation from the plasma and direct Joule heating of the cold substance of the liner skeleton. In the problem as formulated, the plasma can be produced from a relatively cold substance only via the heat flux from the hot plasma. Consequently, the plasma creation rate is determined exclusively by the heat transfer from the hot plasma toward the region immediately adjacent to the liner skeleton. Under the above assumptions, the only process responsible for such a heat transfer is electron thermal conduction. Since the hot plasma is accelerated toward the discharge axis predominantly by the Ampère force, the plasma near the source flows at a velocity close to the Alfvén velocity and the thermal component of the energy density in the plasma flow is approximately the magnetic field energy density. Thus, we have

$$v \sim c_A \sim \frac{B_0}{\sqrt{4\pi\rho}}, \tag{2}$$

$$\frac{\gamma}{\gamma - 1} p \sim \frac{B_0^2}{8\pi}. \tag{3}$$

Here, v and c_A are the radial plasma velocity and characteristic Alfvén velocity in the boundary layer, respectively; the magnetic field B_0 at the outer surface of the liner is uniquely determined by the total current and liner radius; ρ and p are the typical plasma density and pressure inside the boundary layer; and γ is the adiabatic index. The left-hand side of Eq. (3) represents the specific plasma enthalpy. The numerical coefficient on the right-hand side of this equation is fairly small (about 0.1–0.2, see the next section). Nevertheless, we can use these relationships to obtain order-of-magnitude estimates and to establish the qualitative dependence of the plasma creation rate on the discharge parameters (primarily, on the discharge current).

The thickness of the boundary layer, where the magnetic field becomes frozen in the converging plasma flow, is determined by the skin depth

$$\delta_s \sim \frac{\nu_m}{v}. \tag{4}$$

Since, under the above simplifying assumptions, the electron thermal conduction serves as the main mechanism for heat transfer inside the boundary layer, the contribution from electron heat conduction should be comparable with the Joule heating effect:

$$\kappa\frac{T}{\delta_s^2} \sim \frac{j^2}{\sigma} \sim \frac{B_0^2}{\delta_s^2}\nu_m, \tag{5}$$

where T and j are the characteristic plasma temperature and electric current density in the boundary layer, respectively, and κ is the thermal conductivity.

Relationships (2)–(5) make it possible to estimate the four main parameters of the boundary layer—specifically, ρ, T, ν, and δ_s—as functions of B_0 or, equivalently, the total current flowing through the liner of given radius. Assuming the Coulomb logarithms to be constant, we turn to conventional expressions for the plasma electric and thermal conductivities:

$$\sigma \propto \frac{T^{3/2}}{z}, \tag{6}$$

$$\kappa \propto \frac{T^{5/2}}{z}. \tag{7}$$

We also assume that the mean ion charge number z is a power function of temperature,

$$z \propto T^{\alpha},$$

where α lies between 0 and 1, depending on the liner substance. As a result, we arrive at the following dependence of the plasma creation rate ($\dot{m} \sim \rho v$) on the total current flowing through the liner of given radius:

$$\dot{m} \propto \sqrt{AB_0^{(11-5\alpha)/(3-\alpha)}}, \tag{8}$$

where A is the atomic weight of the liner substance. We can see that, as α increases from 0 to 1, the power index of B_0 decreases from 1.866 to 1.5. The remaining parameters of the boundary layer depend on the liner current and the atomic weight of the liner substance as follows:

$$\rho \propto AB_0^{(5-3\alpha)/(3-\alpha)}, \quad T \propto B_0^{1/(3-\alpha)},$$
$$v \propto \sqrt{\frac{B_0^{(1+\alpha)/(3-\alpha)}}{A}}, \quad \delta_s \propto \sqrt{\frac{A}{B_0^{(4-\alpha)/(3-\alpha)}}}. \tag{9}$$

Note that, according to relationships (3) and (5), the ratio of the electron gyrofrequency ω_{Be} to the electron collision frequency ν_e is on the order of unity and, in our approximation, does not depend on B_0. This circumstance justifies the use of relationships (6) and (7), which are valid for ω_{Be}/ν_e = const. The numerical coefficients in formulas (8) and (9) will be discussed at the end of the next section.

4.2. Steady Plasma Flow near a Heterogeneous Liner with Prolonged Plasma Creation (Boundary Layer Structure)

Recall that, in a plasma flow formed by a heterogeneous liner with prolonged plasma creation, there exists a boundary layer in which an important role is played by the azimuthal liner structure and the processes of heat transport, Joule heating, and plasma diffusion transverse to the magnetic field. The boundary layer is thin enough to assume (at least, in the first approximation) that the plasma flow is steady and to neglect the cylindrical character of the flow. In contrast, in the bulk of the flow, the above processes are of secondary importance, whereas the unsteady nature of the plasma flow and its cylindrical geometry play a governing role. In this section, we completely discard the azimuthal inhomogeneity of the liner and take into account only diffusion, heat transport, and Joule heating. In other words, we treat the problem in slab geometry. In order to provide a qualitative (for the most part, analytic) consideration of the problem, we will adopt the simplest form of the equation of state and dissipative coefficients of the plasma.

The above simple estimates imply that the plasma creation rate is governed by both Joule heating and heat transport, which occur against the background of the hydrodynamic plasma flow and plasma diffusion across the magnetic field. The related set of MHD equations, which takes into account volume plasma sources, is presented in the Appendix. Disregarding the cylindrical geometry of the problem, we consider a one-dimensional planar steady plasma flow in the presence of a plasma source, which may be arbitrarily distributed in space. In this approximation, all of the quantities depend only on $x = r_L - r$ (where r_L is the outer radius of the liner) and the only nonzero components are the x-component of the plasma velocity, the y-component of the magnetic field, and the z-component of the elec-

tric field. Since the flow is steady-state, the electric field does not depend on x. Under the assumptions that the x-component of the initial momentum of the produced plasma is zero and the energy expended on creating the plasma is ensured by the heat flux from the already produced hot plasma, the steady nature of the plasma flow also implies that the momentum and energy flux densities are constant. Hence, we have

$$\rho v^2 + p + \frac{B^2}{8\pi} = \text{const} = \frac{B_0^2}{8\pi}, \tag{10}$$

$$\rho v W + \frac{1}{2}\rho v^3 - \frac{c}{4\pi}E_z B - \kappa\frac{\partial T}{\partial x} = \text{const} = -\frac{c}{4\pi}E_z B_0, \tag{11}$$

$$cE_z = \nu_m\frac{\partial B}{\partial x} - vB = \text{const}, \tag{12}$$

$$\frac{\partial}{\partial x}\rho v = q(x). \tag{13}$$

Here, v is the x-component of the plasma velocity; ρ, T, p, and W are the density, temperature, pressure, and specific enthalpy of the plasma, respectively; $q(x)$ is the intensity of the plasma source averaged over its spatial structure; κ is the thermal conductivity; $B(x)$ is the magnetic field; the magnetic field B_0 at the outer surface of the liner is uniquely determined by the total current and liner radius; and E_z is the z-component of the electric field. Consider an infinitely thin (in the radial direction) plasma source. Integrating Eq. (13) yields the relationship

$$\rho v = \text{const} = Q_m, \tag{14}$$

which is valid in the region enclosed by a cylindrical plasma source ($x > 0$), while outside of this region ($x < 0$), there is a vacuum.

Equations (10)–(12) and (14), which describe the plasma flow in the entire region enclosed by the cylindrical source ($x > 0$), should be supplemented with the boundary conditions

$$v(0) = 0, \quad T(0) = 0. \tag{15}$$

We also assume that, as $x/d \longrightarrow \infty$, all of the quantities approach their finite asymptotic values, which correspond to as-yet unknown plasma parameters on the outside of the boundary layer. The second condition in (15) stems from neglecting the temperature of the cold liner skeleton in comparison with the temperature of the hot plasma. With the prescribed electric-field component E_z, which, strictly speaking, cannot be determined in this problem (see below for details), Eqs. (10)–(12) and (14) with the boundary conditions (15) have a solution only for a certain Q_m value, which is thus an eigenvalue of the problem and determines the self-consistent creation rate of the hot plasma.

In order to make the formulation of the problem as simple as possible, we turn to an elementary but quite realistic description of the plasma parameters. We represent the pressure and specific enthalpy of the plasma as $p = G\rho T$ and $W = \frac{\gamma}{\gamma - 1}\frac{p}{\rho}$, where the parameter G and adiabatic index γ are both assumed to be constant. We also assume that the plasma electric conductivity σ and, accordingly, the magnetic viscosity ν_m are constant and write the thermal conductivity as $\kappa = \kappa_0 T$ with $\kappa_0 = \text{const}$.

We switch to the dimensionless variables

$$B(x) = B_0 b(\varsigma), \quad E_z = -E_0\varepsilon_z, \quad v(x) = v_0 w(\varsigma), \quad \rho(x) = \rho_0 R(\varsigma), \quad T(x) = T_0\tau(\varsigma), \quad Q_m = Q_0\tilde{Q}, \tag{16}$$

where

$$\varsigma = \frac{x}{d_0}, \quad d_0 = (8\pi)^{1/4}\nu_m^{3/4}\kappa_0^{1/4}G^{-1/2}B^{-1/2}\tilde{Q}\left(\frac{\gamma - 1}{\gamma}\right)^{1/2},$$

$$E_0 = \frac{1}{(8\pi)^{1/4}c}\nu_m^{1/4}\kappa_0^{-1/4}G^{1/2}B_0^{3/2}\tilde{Q}^{-1}\left(\frac{\gamma}{\gamma - 1}\right)^{1/2},$$

$$v_0 = \frac{1}{(8\pi)^{1/4}}\nu_m^{1/4}\kappa_0^{-1/4}G^{1/2}B_0^{1/2}\tilde{Q}^{-1}\left(\frac{\gamma}{\gamma - 1}\right)^{1/2},$$

$$\rho_0 = (8\pi)^{-1/2}\nu_m^{-1/2}\kappa_0^{1/2}G^{-1}B_0\tilde{Q}^2\frac{\gamma - 1}{\gamma},$$

$$T_0 = (8\pi)^{-1/2}\frac{\gamma}{\gamma - 1}\nu_m^{1/2}\kappa_0^{-1/2}B_0\tilde{Q}^{-2},$$

$$Q_0 = (8\pi)^{-3/4}((\gamma - 1)/\gamma)^{1/2}\nu_m^{-1/4}\kappa_0^{1/4}G^{-1/2}B_0^{3/2}, \tag{17}$$

and obtain the set of equations

$$\frac{db}{d\varsigma} = -\varepsilon_z + wb, \tag{18}$$

$$\frac{d\tau}{d\varsigma} = \frac{\tilde{Q}^4}{\tau}\left[-2\varepsilon_z(1 - b) + \tau + \frac{1}{2}w^2\right], \tag{19}$$

$$Rw = 1, \tag{20}$$

$$w + b^2 + \frac{\gamma - 1}{\gamma}R\tau = 1. \tag{21}$$

We express w and R in terms of τ and b and substitute w into Eqs. (18) and (19) to arrive at an autonomous set of differential equations for b and τ. This set of equations, supplemented with the obvious boundary conditions, constitutes an eigenvalue problem (the eigenvalue being $\tilde{Q}$) with the as-yet unknown parameter ε_z, which can be obtained by solving a problem on the outside of the boundary layer. Below, we consider a fairly realistic limiting case, which provides an essentially complete analytic treatment.

Before proceeding with a qualitative analysis of this limiting case, note that ε_z and γ are the only parameters that enter Eqs. (18) and (19). Therefore, the eigenvalue $\tilde{Q}$ should be fairly close to unity (for ε_z of order unity). To within a factor on the order of unity, this circumstance, together with formulas (16) and (17), determines both the self-consistent plasma creation rate and its dependence on the liner discharge parameters—first of all, the generator current or equivalently B_0 (in our formulation of the problem).

We will use a simplifying assumption that the ionization energy required to produce both dense-liner and forerunner plasmas is substantially (by a factor of 5–10) higher than the thermal energy of the free electrons, which govern the plasma pressure. Under this assumption, we can examine the limiting case $\gamma \longrightarrow 1$. In the limit of infinitely large ς values, the left-hand side of Eq. (19) approaches zero, indicating that the specific enthalpy is on the order of the magnetic field energy $B^2/8\pi$. Since, in this limit, the plasma pressure is markedly lower (by a factor of $1/(\gamma - 1)$) than the magnetic field pressure, it can be neglected, at least, in the first approximation. In other words, on the left-hand side of Eq. (21), we can omit the term proportional to $R\tau$. As a result, Eqs. (18)–(21) become independent of the temperature and can be rewritten as

$$\frac{db}{d\varsigma} = -\varepsilon_z + b(1 - b^2), \tag{22}$$

$$w = 1 - b^2, \tag{23}$$

$$R = \frac{1}{1 - b^2}. \tag{24}$$

We can see that Eq. (22) is a closed differential equation for $b(\varsigma)$. The remaining parameters of the plasma flow can be expressed in terms of $b(\varsigma)$ by using Eqs. (23) and (24).

The solutions to Eq. (22) with the boundary condition $w(0) = 0$ can be parameterized by the ε_z value. The condition $\varepsilon_z > 0$ corresponds to the plasma motion from the source toward the region $\varsigma > 0$. The solutions with $\varepsilon_z > 2/(3\sqrt{3})$ cannot be continued through the entire region $\varsigma > 0$, because, for finite ς values, the magnetic field b approaches $-\infty$. Consequently, physically meaningful solutions to the problem of a steady plasma flow from the source are those with $0 < \varepsilon_z \le 2/(3\sqrt{3})$. For $\varsigma \longrightarrow \infty$, the plasma flow velocity depends on ε_z and is determined by the condition for the right-hand side of Eq. (13) to vanish. Thus, to find the flow velocity, we must solve a cubic equation. The dependence $w(\varsigma \longrightarrow \infty)$ on ε_z is shown in Fig. 4. The highest flow velocity, which is reached at $\varepsilon_z = 2/(3\sqrt{3})$, is equal to the local Alfvén velocity. At lower ε_z values, the plasma flow velocity at large distances from the source is lower than the Alfvén velocity and decreases monotonically with decreasing ε_z. The value of ε_z cannot be specified by solving the time-independent problem in slab geometry. To do this requires solving the time-dependent problem with consideration of the geometric structure of the plasma flow at large distances from the source. The plasma flow with the highest possible velocity, which can be referred to as a critical flow, occupies a special place and is the most important for our purposes. It is this solution that we are going to analyze, keeping in mind that any solution in the range $0 < \varepsilon_z < 2/(3\sqrt{3})$ is qualitatively analogous to the solution with $\varepsilon_z = 2/(3\sqrt{3})$.

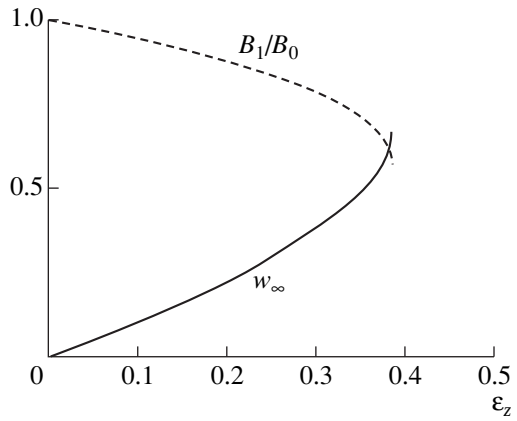

Fig. 4. Dimensionless plasma flow velocity at the inner surface of the boundary layer and the ratio of the magnetic fields at the inner surface of the boundary layer and at the outer surface of the liner as functions of the dimensionless electric field ε_z.

To obtain the critical solution, we can integrate Eq. (22) implicitly by quadratures,

$$\varsigma = \frac{b}{b - b_\infty} + \frac{1}{3}\ln\frac{(b - b_\infty)(1 + 2b_\infty)}{(b + 2b_\infty)(1 - b_\infty)} - \frac{1}{1 - b_\infty}, \tag{25}$$

in which case we have

$$b(\varsigma \longrightarrow \infty) = b_\infty = \frac{1}{\sqrt{3}},$$

$$w(\varsigma \longrightarrow \infty) = 1 - b_\infty^2 = \frac{2}{3},$$

$$R(\varsigma \longrightarrow \infty) = \frac{1}{1 - b_\infty^2} = 1.5,$$

$$\tau(\varsigma \longrightarrow \infty) = \frac{(1 - b_\infty)(1 - b_\infty^2)(3b_\infty - 1)}{2}$$

$$= \frac{2}{3}\left(\frac{2}{\sqrt{3}} - 1\right) \approx 0.103.$$

The resulting functions $b(\zeta)$, $w(\zeta)$, and $R(\zeta)$ are presented in Fig. 5. To determine the plasma temperature, we need to solve Eq. (19) with the already known w and b.

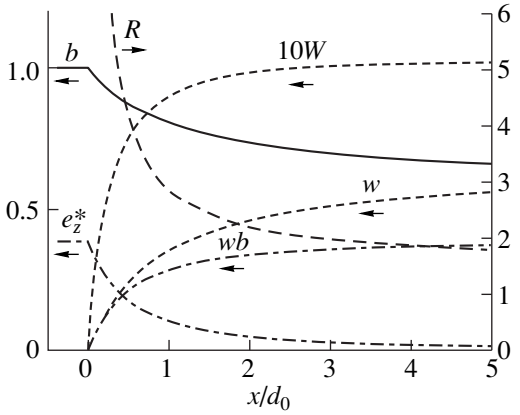

Fig. 5. Boundary layer structure near the plasma source: the dimensionless magnetic field b, plasma density R, plasma velocity w, electric (ohmic) field e_z^* in the comoving frame of reference, inductive electric field wb (in dimensional units, it is equal to vB/c), and tenfold specific plasma enthalpy W in the limit in which the adiabatic index γ tends to unity.

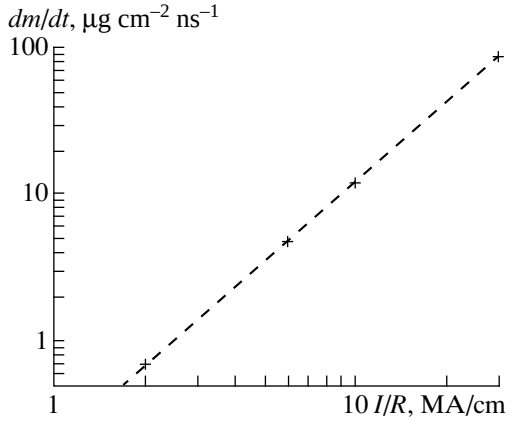

Fig. 6. Dependence of the steady-state rate at which a tungsten plasma is produced from a unit area of the side surface of the liner on the ratio of the total current flowing in the liner to its radius. The dependence was estimated from formulas (28). The calculated points (crosses) were used to obtain the power fit $\dot{m} = 0.2\left(\frac{I[\mathrm{MA}]}{R[\mathrm{cm}]}\right)^{1.8}$ μg cm^{-2} ns^{-1} (dashed curve).

Solving the eigenvalue problem (19) numerically with the boundary conditions $\tau(0) = \tau'(\infty) = 0$ yields

$$\tilde{Q} \approx 0.965. \tag{26}$$

The dimensionless plasma enthalpy $W(\varsigma) = \tau(\varsigma)$ computed in this way is also plotted in Fig. 5. In physical units, the self-consistent plasma creation rate is equal to

$$Q_m = 0.965\sqrt[4]{\frac{\kappa_0 B_0^6(\gamma-1)^2}{(8\pi)^3\nu_m G^2\gamma^2}}. \tag{27}$$

Note that the dimensionless enthalpy of the plasma flow is fairly low (about 0.1). Since the dimensionless plasma pressure is even lower (e.g., at $\gamma \approx 1.2$, it is lower by a factor of approximately 5), we can see that it does not exceed several percent of the magnetic field pressure $B_0^2/8\pi$. This circumstance mostly validates the corresponding simplifying assumption.

Using the above solution to the boundary layer problem, we can rewrite Eqs. (2)–(5) in the form

$$v = \frac{B_0}{\sqrt{12\pi\rho}}, \quad \frac{\gamma}{\gamma-1}p = 0.155\frac{B_0^2}{8\pi}, \qquad \kappa T = 1.14\times 10^{-2}\frac{B_0^2}{8\pi}\nu_m, \tag{28}$$

where v, ρ, T, and p are now the plasma parameters at the inner surface of the boundary layer. The boundary layer thickness δ corresponding to the radius at which the ohmic component of the electric field is weaker than the total electric field by a factor of approximately 3.8 is given by the relationship

$$\delta_s = d_0 = \frac{2}{3}\frac{\nu_m}{v}. \tag{29}$$

In the model adopted in this section, reducing Eqs. (2)–(5) to Eqs. (28) and (29) makes it possible to reconstruct the boundary layer parameters exactly. In more general cases, Eqs. (28) and (29) will probably give fairly good estimates.

The characteristic feature of the boundary layer structure analyzed in this section (Fig. 5) is that the heat conduction–driven energy flux starts to play an important role only in the region of sufficiently small ς values, where the plasma still remains fairly dense and cold. Therefore, in this region, the electrons are unmagnetized, $\omega_{Be}/\nu_e \ll 1$, so that we are justified in using the above relationship between the electric and thermal conductivities. For this reason, when obtaining estimates, the electric and thermal conductivities in Eqs. (28) and (29) should be taken not from the general expressions, for which the adopted relationship between the thermal and electric conductivities fails to hold, but from the formulas in which the electron plasma component is assumed to be unmagnetized.

This approach was used to calculate the dependence of the rate $\dot{m}$ at which a tungsten plasma is produced from a unit area of the side surface of the liner on the ratio of the total current flowing in the liner to its radius. The dependence illustrated in Fig. 6 was calculated under the assumption of the thermodynamically equilibrium degree of ionization of the tungsten atoms at the inner surface of the boundary layer. The expressions for the kinetic coefficients of the plasma were taken from [29]. Now, we can say that, within the accuracy

adopted in our study, this estimate of the plasma creation rate contradicts neither the experimental data from the Angara-5-1 facility nor those from the Z and Saturn facilities. The calculated plasma production rate can be estimated accurate to a numerical factor on the order of 2–3. This error stems from the simplifying assumptions made in deriving the simple formulas that describe the plasma properties; neglecting the original azimuthal structure of the liner; and neglecting the discharge axial structure, which occurs spontaneously and is distinctly seen in the photographs taken in experiments. To refine this estimate and to systematically compare it with the experimental data requires a separate study.

4.3. Numerical Simulation of the Dynamics of a Liner with a Plasma Source (Acceleration and Convergence of the Plasma Shell toward the Discharge Axis)

In this section, we report the results of the numerical simulation of the acceleration of the produced plasma shell toward the discharge axis. Here, we neglect the radial thickness of the boundary layer, whose structure was analyzed above, and/or the radial thickness of the plasma source. Accordingly, we can also ignore Joule heating, heat conduction, and plasma diffusion across the magnetic field, because these processes are only important inside the boundary layer or inside the plasma source, provided that its radial thickness is larger than that of the boundary layer. On the other hand, we systematically take into account the unsteady nature of the discharge and its cylindrical geometry. We also perform averaging over the azimuthal structure of a heterogeneous liner, assuming, e.g., that the interwire gap is smaller than the spatial resolution achievable in both the experimental investigations of the plasma flow and the present theory. Since the plasma pressure in the converging flow is lower than the magnetic field pressure (see above), we take into account only the Ampère force and discard the thermal flow parameters in the plasma shell accelerated toward the liner axis. An important feature of the problem that we are going to solve in this section is that the plasma creation rate is to be chosen so as to satisfy the conditions for the formation of the most suitable plasma shell. Thus, the problem becomes non-self-consistent. This is adopted intentionally because we do not wish to concentrate on the specific multiwire liner design for which the plasma production rate has been estimated in the previous sections. This approach makes our problem more universal.

The dynamics of the produced plasma shell can be described by the equations (see Appendix)

$$\frac{\partial}{\partial t}v + v\frac{\partial}{\partial r}v = -\frac{1}{8\pi r^2\rho}\frac{\partial (Br)^2}{\partial r}, \tag{30}$$

$$\frac{\partial B}{\partial t} + \frac{\partial}{\partial r}vB = 0, \tag{31}$$

$$\frac{\partial \rho}{\partial t} + \frac{1}{r}\frac{\partial}{\partial r}(\rho v r) = 0. \tag{32}$$

The plasma source at the cylindrical surface $r = R_{ex}$ is incorporated into the boundary conditions as follows:

$$(\rho v)|_{r = R_{ex}} = -\dot{m}(t), \tag{33}$$

$$\left(\rho v^2 + \frac{B^2}{8\pi}\right)\Bigg|_{r = R_{ex}} = \frac{[B_0(t)]^2}{8\pi}, \tag{34}$$

$$-v|_{r = R_{ex}} \le \frac{|B|}{\sqrt{4\pi\rho}}\Bigg|_{r = R_{ex}}. \tag{35}$$

Here, $\dot{m}$ is the plasma creation rate (in terms of mass) near the cylindrical surface $r = R_{ex}$ per unit area of its side surface and $B_0(t) = 2I(t)/cR_{ex}$, where $I(t)$ is the total discharge current. If, in the region near the cylindrical surface $r = R_{ex}$, the plasma flow is subsonic (i.e., the flow velocity is below the Alfvén velocity), then two characteristics of the hyperbolic set of equations (30)–(32) come from this surface inward in the positive direction along the time axis. In this case, we need to impose two boundary conditions on this surface and the boundary condition (35) actually places no additional constraints. If, in this region, the flow velocity is above the Alfvén velocity, then there are three characteristics that come from this surface inward in the positive direction along the time axis. In this case, the only constraint placed by the boundary condition (35) is the fact that, in our approximation, the flow velocity in the immediate vicinity of the plasma source should be exactly equal to the Alfvén velocity, because the solution on the inside of the boundary layer (see the previous section) exists only when the flow velocity on the outside of the boundary layer is lower than or equal to the Alfvén velocity.

Equations (30)–(32) with the boundary conditions (34) and (35) and with the boundary condition $v(0, t) = 0$ at the axis were solved numerically using a modified version of the Richtmyer difference scheme (see Section 3 of Chapter V in [30]). The difference scheme was modified to keep both the mass and magnetic flux unchanged and to satisfy the radial momentum conservation law when the time step approaches zero and the spatial gradients are sufficiently high in comparison with the inverse radius. In connection with this, we note that the boundary condition (34) is a consequence of the constancy of the radial momentum flux through an infinitely thin plasma source under the assumption that the plasma is produced with zero momentum.

The results of numerical simulations carried out with

$$I(t) = I_m t^2 \frac{(3t_j - 2t)}{t_j^3} \tag{36}$$

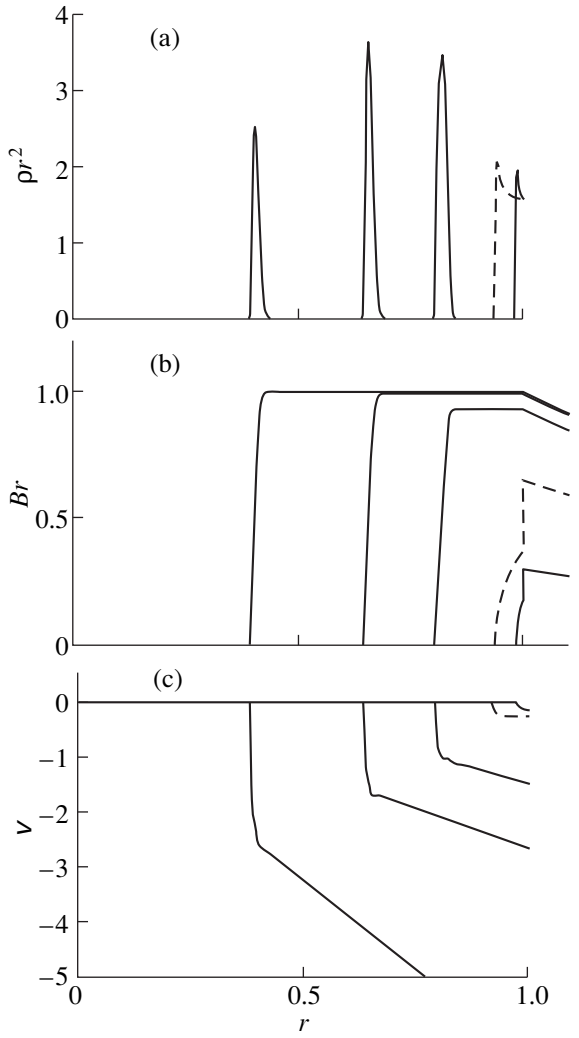

Fig. 7. Simulation of the dynamics of the plasma shell in a liner with prolonged hot-plasma creation for $t_q = 0.6t_j$: the radial profiles of (a) the plasma density multiplied by the squared radius, (b) the electric current flowing inside a cylindrical surface of radius r (i.e., the product of the magnetic field and the radius, Br), and (c) the radial plasma velocity at the times 0.36, 0.6, 0.84, 0.96, and 1.08 of the current rise time t_j. The profiles are presented in the units introduced in the text.

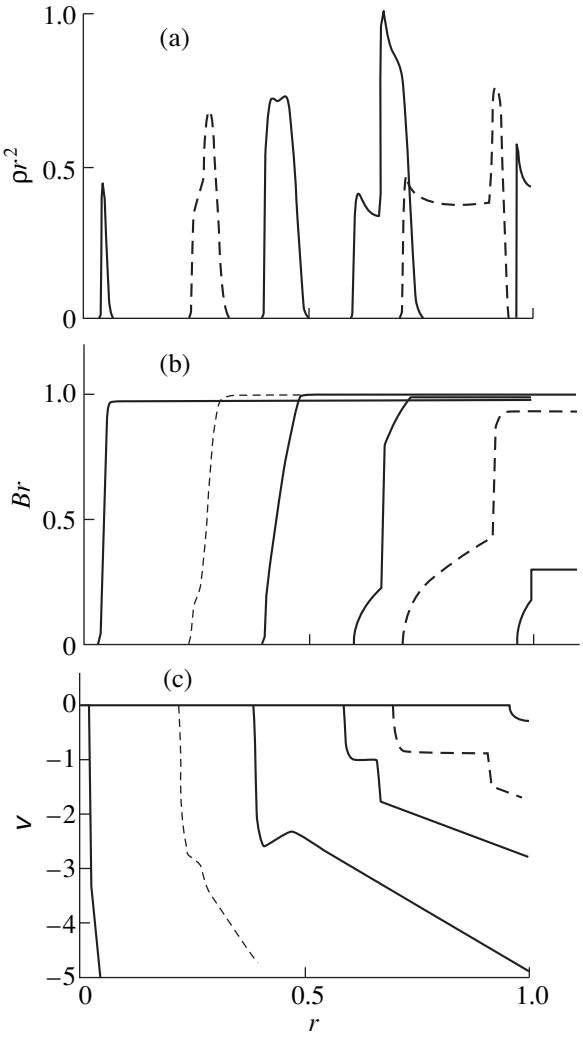

Fig. 8. Simulation of the dynamics of the plasma shell in a liner with prolonged hot-plasma creation for $t_q = 0.8t_j$: the radial profiles of (a) the plasma density multiplied by the squared radius, (b) the electric current flowing inside a cylindrical surface of radius r (i.e., the product of the magnetic field and the radius, Br), and (c) the radial plasma velocity at the times 0.36, 0.84, 0.96, 1.08, 1.14, and 1.2 of the current rise time t_j. The profiles are presented in the units introduced in the text.

and

$$\dot{m}(t) = \frac{M_L}{2\pi R_{ex}} \frac{t^2(3t_j - 2t)}{t_q^3(t_j - 0.5t_q)}\theta(t_q - t), \qquad (37)$$

and for different ratios $t_q/t_j = 0.6$, 0.8, and 1 are shown in Figs. 7–9. Here, I_m is the maximum current achieved at the time $t = t_j$ after the discharge begins, M_L is the total mass per unit length of the liner, and $t = t_q$ is the time at which the plasma source ceases. In order to make the number of free parameters as small as possible, in this series of simulations, we assumed that the plasma source depletes instantaneously at the time when the entire cold liner substance becomes the plasma. The depletion of the plasma source was modeled using the Heaviside step function θ in Eq. (37).

The simulations described below were performed with the same liner mass, which was chosen to achieve a complete collapse at the time $t = 1.2t_j$ (in the zero-dimensional model) and was found to be $M_L \approx 0.234(I_m t_j/cR_{ex})^2$. This duration of liner compression was chosen to be close to the optimum duration, i.e., to ensure the highest efficiency of conversion of the magnetic energy of an inductive storage into the kinetic energy of the liner. We stopped the calculations at the

time $t = 1.2t_j$, i.e., before the discharge current started to fall off significantly.

The problem under consideration is a scale-invariant one. If we express the radius in units of R_{ex}, the time in units of t_j, the magnetic field in units of $2I_m/cR_{ex}$, the plasma density in units of $I_m^2 t_j^2/(\pi c^2 R_{ex}^4)$, and the plasma velocity in units of R_{ex}/t_j, then the set of equations and the boundary conditions both rewritten in terms of these variables involve a single parameter, specifically, the ratio t_q/t_j. However, note that the solutions should also depend on the shape of the current pulse and the plasma creation rate. The profiles plotted in Figs. 7–9 were rescaled in the units introduced above.

We emphasize that the plasma source intensity was chosen to be proportional to the current throughout the current pulse. According to our test simulations, this is the case when the plasma mass is distributed most uniformly over the transverse cross section of the shell. For a weaker dependence of the plasma creation rate on the discharge current, the plasma will be concentrated near the inner boundary of the plasma shell, and, for a stronger dependence, it will accumulate near the outer boundary. It was found that, in the first case, the plasma flow velocity near the plasma source is below the Alfvén velocity, and, in the second case, it is above the Alfvén velocity. In this sense, our reference parameter values (for which, at any instant of plasma production, the plasma flow velocity at the outer boundary of the plasma flow near the plasma source is exactly equal to the Alfvén velocity) correspond to an intermediate version between these two cases. When the plasma flow velocity is equal to the Alfvén velocity, Eq. (34) shows that the plasma in the boundary layer carries a fraction of $1 - 1/\sqrt{3} \approx 42\%$ of the total discharge current.

At the time at which the source stops producing plasma (in our model, the source depletes instantaneously), the magnetic field undergoes a jump at the outer boundary of the source, thereby giving rise to a shock wave, which propagates through the forerunner plasma and converges toward the discharge axis. The shock wave, which acts to additionally compress the plasma shell to a smaller thickness, is clearly shown in Figs. 8 and 9. The effect of additional compression of the forerunner plasma is a common feature of heterogeneous liners: it occurs regardless of the rate at which the plasma production terminates. However, if this rate is sufficiently low, the additional compression is not accompanied by the onset of a shock wave.

For $t_q = 0.6t_j$, i.e., at the time when the formation of the plasma shell has come to an end, the shell itself remains essentially immobile. This situation may also be captured by a zero-dimensional model of the compression of a liner as a single entity. Consequently, for this value of the ratio t_q/t_j, the radial thickness of the produced plasma shell is very small and the compression of the shell can be described in precisely the same way as in the zero-dimensional model for the compression of a thin-walled liner as a whole (Fig. 7). At first glance, it is surprising that this situation already occurs at the relatively large value $t_q/t_j = 0.6$. Such compression conditions may be favorable for the onset of strong RT instability.

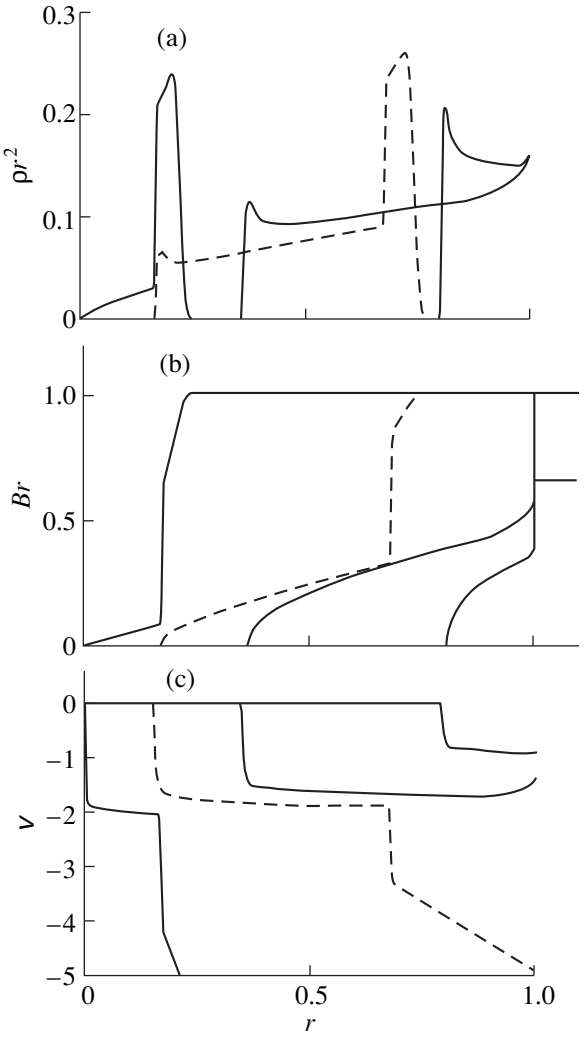

Fig. 9. Simulation of the dynamics of the plasma shell in a liner with prolonged hot-plasma creation for $t_q = t_j$: the radial profiles of (a) the plasma density multiplied by the squared radius, (b) the electric current flowing inside a cylindrical surface of radius r (i.e., the product of the magnetic field and the radius, Br), and (c) the radial plasma velocity at the times 0.6, 0.96, 1.08, and 1.2 of the current rise time t_j. The profiles are presented in the units introduced in the text.

For $t_q = t_j$, i.e., when the plasma production time is exactly equal to the current rise time, the leading edge of the forerunner plasma reaches the discharge axis earlier than the compression (shock) wave (Fig. 9). Consequently, the plasma shell collapses over a time insufficiently short to achieve the optimum duration of an X-ray pulse generated in the stage of collapse, when the

kinetic energy of the plasma shell and the magnetic field energy are converted into thermal energy.

Among the versions that we have simulated in this study, the version with $t_q = 0.8t_j$, which is illustrated in Fig. 8, is optimum in many aspects. By the time the source stops producing plasma, the leading edge of the forerunner plasma has traveled a distance approximately equal to 0.3 of the original liner radius. After the source is depleted, the trailing edge of the plasma shell starts to catch up with its leading edge, the radial velocity of the trailing edge being higher than that of the leading edge by a factor of approximately 2. In this stage, the plasma shell is being strongly compressed in the radial direction. The front of the compression wave reaches the leading edge of the plasma shell at the time at which the shell is at a radius about halfway between its original position and the discharge axis, the shell thickness being about 1/5 of its radius. Then, the plasma shell continues to converge toward the axis, keeping its relative thickness almost unchanged and experiencing slight radial oscillations due to the finite resilience associated with the frozen-in magnetic field. In other words, the plasma shell is compressed almost in a self-similar manner. This feature of compression will be thoroughly investigated in the next section, where we construct the related self-similar solutions. Presumably, such a plasma shell is, on the one hand, compact enough to generate a fairly short X-ray pulse when collapsing toward the discharge axis, and, on the other hand, it is sufficiently resilient and extended in the radial direction to substantially suppress its instabilities.

As was mentioned above, in order to reduce the number of free parameters of the problem, we have assumed that the plasma source depletes instantaneously and that, until this instant, the plasma production rate depends on the current only. However, in reality, the cold liner substance is depleted gradually, so that $\dot{m}(t)$ vanishes some time after it reaches its maximum. The law by which $\dot{m}(t)$ approaches zero determines the plasma distribution outside the main pinch, which forms at the system axis. In other words, the character of the source depletion process may govern the extent to which the compressed liner plasma is compact and stable.

4.4. Self-Similar Dynamics of a Thick-Walled Current-Carrying Liner Plasma with a Frozen- in Magnetic Field

The above results of the modeling of plasma shell compression in a liner with prolonged plasma creation show that, under certain conditions, the plasma shell is compressed approximately in a self-similar manner. In this section, we construct the related self-similar solution in order to illustrate that such a compression process is in fact possible. Hence, we consider the compression of the already produced plasma shell with a frozen-in magnetic field, using a one-dimensional ideal MHD model and assuming the generator current to be constant. The corresponding equations (in a more general form) were written above [see Eqs. (30)–(32)]. We will seek their solutions with separable variables in the form

$$B(r,t) = \frac{2I}{cr_0(t)}b(\xi), \quad v_r(r,t) = \frac{r}{r_0(t)}\frac{d}{dt}r_0(t), \qquad \rho(r,t) = \frac{\mu}{r_0^2(t)}R(\xi), \tag{38}$$

where

$$\xi = \frac{r}{r_0(t)}, \tag{39}$$

and $r_0(t)$ is a characteristic time-dependent radial scale of the problem. Assuming that this scale is equal to the outer radius of the plasma shell yields the boundary conditions

$$b(1) = 1. \tag{40}$$

We choose the mass parameter μ to satisfy the normalization condition

$$2\pi\int_0^1 R(\xi)\xi d\xi = 1, \tag{41}$$

in which case μ is the total mass of the plasma shell per unit length.

On the one hand, such a solution, which actually corresponds to uniform deformation, is a generalization of the results obtained by Kulikovskiĭ [31]. On the other hand, it extends the zero-dimensional theory of the compression of thin-walled liners (see, e.g., [32]) to the case of finite-thickness liners.

The conditions under which we can look for the desired solutions can be obtained by substituting the assumed dependences (38) and (39) into Eqs. (30)–(32):

$$\frac{1}{\xi^3 R}\frac{d}{d\xi}(b\xi)^2 = C, \tag{42}$$

$$r_0(t)\frac{d^2}{dt^2}r_0(t) = -\frac{I^2}{2\pi\mu c^2}C, \tag{43}$$

where C is a positive constant, which is determined from condition (41). We can see that the functional dependences in these solutions are specified with some freedom. Notably, the time dependence of the inner radius of the shell is in fact almost the same as that for a thin-walled liner [see Eq. (43)].

As an example, we present the solution with a piecewise constant function R, which is nonzero only over the interval $1 > \xi > \xi_1$ (Fig. 10). In this case, we have

$$R = \frac{1}{\pi(1-\xi_1^2)} \tag{44}$$

for $1 > \xi > \xi_1$,

$$C = \frac{4\pi}{1+\xi_1^2}, \tag{45}$$

$$b(\xi) = \frac{1}{\xi}\sqrt{1-\frac{1-\xi^4}{1-\xi_1^4}} \tag{46}$$

and the function $r_0(t)$ satisfies the equation

$$r_0(t)\frac{d^2}{dt^2}r_0(t) = -\frac{2I^2}{\mu c^2(1+\xi_1^2)}. \tag{47}$$

These self-similar solutions, describing the compression of a plasma shell with a frozen-in magnetic field, show that, despite the finite thickness of the shell and its radial resilience, it is possible to achieve compact radial compression such that, in the approximation at hand, the plasma shell collapses almost instantaneously. This conclusion seems to be very important for the theory of liners with prolonged plasma creation: the finite thickness characteristic of liners with prolonged plasma creation is not, generally speaking, an obstacle to achieving very rapid conversion of the kinetic energy of a plasma shell to heat and X radiation.

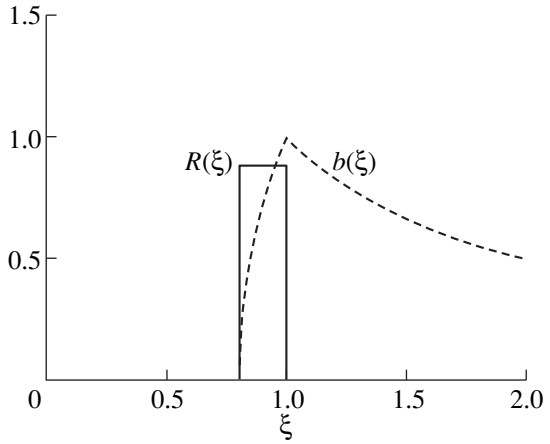

Fig. 10. Radial profiles of the dimensionless plasma density $R(\xi)$ and the dimensionless magnetic field in a plasma shell converging in a self-similar manner for a piecewise constant density, which is nonzero within the interval $1 > \xi > \xi_1 = 0.8$.

4.5. Stability of a Thick-Walled Current-Carrying Liner

4.5.1. Instability of the body of the plasma shell. In this section, we consider the acceleration-driven interchange instability of the body of the plasma shell. The next section will be aimed at an analysis of the RT instability of the outer boundary of the shell. In the stability problem, we adopt the unperturbed state that is characterized by the self-similar solutions, which were constructed in Section 4.4 and describe the compact compression of a plasma shell. The axial wavenumber k_z of perturbations remains unchanged during compression. In the geometrical-optics approximation, the short-wavelength instability of perturbations with the radial wavenumber $k_r = 0$ (and with $m = 0$ for the interchange mode) can be studied under the assumption $|k_z|(r_0 - r_1) \gg 1$. Hence, we can specify the perturbations of the plasma density, azimuthal magnetic field, and two flow velocity components v_r and v_z as $a(t)f(\xi)e^{ik_z z}$, where $\xi = r/r_0(t)$ and the time-dependent radial scale of the problem, $r_0(t)$, was introduced above. Because of the magnetic field–induced resilience of the plasma shell, the perturbations under consideration (specifically, those with frequencies much lower than $k_z c_A$) should not disturb the magnetic field. In other words, the perturbed magnetic field in such relatively slow perturbations can be neglected in our approximation. On the other hand, since the magnetic field is frozen in the plasma, the quantity $B/\rho r$ should be constant along the streamlines of the plasma flow. Consequently, the perturbed plasma density $\tilde{\rho}$ and perturbed radial flow velocity $\tilde{v}_r$ are related by the equation

$$-\frac{d}{dt}\frac{\tilde{\rho}B}{\rho^2 r} + \tilde{v}_r\frac{\partial}{\partial r}\frac{B}{\rho r} = 0, \tag{48}$$

which follows from the continuity and frozen-in conditions. Here, the unperturbed quantities, namely, those that are not identified by a tilde, refer to the self-similar solutions constructed in the previous section. For instance, the total plasma density is equal to $\rho + \tilde{\rho}$. The derivative $d/dt = \partial/\partial t + v_r\partial/\partial r$ corresponds to the Lagrange derivative along the unperturbed trajectories of the volume elements of the plasma. Recall that the unperturbed plasma parameters are z-independent. From Eq. (48), we obtain

$$\frac{d}{dt}\frac{\tilde{\rho}}{\rho} = -\tilde{v}_r\frac{\partial}{\partial r}\ln\frac{B}{\rho r}. \tag{49}$$

Linearizing the Euler equation for the radial flow velocity component yields

$$\frac{d}{dt}\tilde{v}_r + \tilde{v}_r\frac{\partial}{\partial r}v_r = \frac{\tilde{\rho}}{\rho}\frac{B}{4\pi\rho r}\frac{\partial(Br)}{\partial r} = -\frac{\tilde{\rho}}{\rho}\xi\frac{d^2}{dt^2}r_0(t) \tag{50}$$

or, equivalently,

$$\frac{1}{r_0}\frac{d}{dt}r_0\tilde{v}_r = -\frac{\tilde{\rho}}{\rho}\xi\frac{d^2}{dt^2}r_0. \tag{51}$$

Equations (49) and (51) can be reduced to the following second-order linear differential equation for the relative perturbed plasma density:

$$\frac{d}{dt}r_0^2\frac{d}{dt}\frac{\tilde{\rho}}{\rho} = -\frac{\tilde{\rho}}{\rho}\frac{\partial\ln(B/\rho r)}{\partial\ln\xi}r_0\frac{d^2}{dt^2}r_0, \tag{52}$$

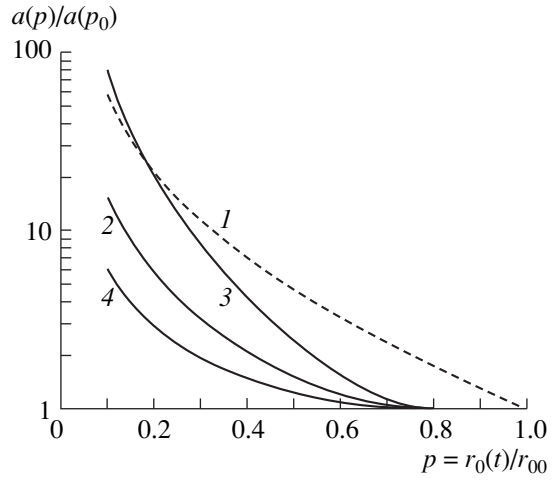

Fig. 11. Growth of the relative density perturbations during compression for (*1*) $K = 1.8$ and $p_0 = 1$, (*2*) $K = 1.8$ and $p_0 = 0.8$, (*3*) $K = 4.3$ and $p_0 = 0.8$, and (*4*) $K = 1$ and $p_0 = 0.8$. Profiles *1* and *2* correspond to a plasma shell whose radial thickness is about 1/5 of its radius.

where, by virtue of Eq. (43), we have

$$r_0 \frac{d^2}{dt^2} r_0 = -\frac{I^2 C}{2\pi\mu c^2}. \tag{53}$$

We denote the radius at which the derivative $dr_0(t)/dt$ vanishes by r_{00} and pass over from the time t to the new variable $p(t) = r_0(t)/r_{00}$, which has the meaning of the time-dependent degree of compression of the plasma shell. Then, we arrive at the following equation for the amplitude $a(p, \xi)$ of the relative density perturbations:

$$\sqrt{\ln\frac{1}{p}}\frac{d}{dp}p^2\sqrt{\ln\frac{1}{p}}\frac{d}{dp}a = \frac{1}{2}a\frac{\partial\ln(B/\rho r)}{\partial\ln\xi}. \tag{54}$$

As was noted above, the frozen-in condition implies that the factor $\partial\ln(B/\rho r)/\partial\ln\xi$ on the right-hand side of this equation is actually dependent only on ξ. We can see that, for

$$\frac{\partial\ln(B/\rho r)}{\partial\ln\xi} = \frac{\partial\ln(B/\rho r)}{\partial\ln r} > 0 \tag{55}$$

the perturbation amplitude increases during compression. According to Eq. (54), the characteristic time required for the instability to develop is proportional to the square root of the shell thickness. From this point of view, thicker plasma shells are more preferable.

To be specific, let us turn to self-similar compression and consider how the perturbations grow in the vicinity of a cylindrical surface of radius $\xi = \sqrt{(1+\xi_1^2)/2}$, which divides the plasma shell into two parts of equal mass, assuming the rectangular plasma-density profile [see formulas (44)–(47)]. We treat the case $\xi_1 = 0.8$, because this ξ_1 value corresponds to the relative shell thickness, which was calculated for $t_q = 0.8t_j$ in Section 4.4 and for which the radial thickness of a completely compressed shell (after the plasma creation process terminates) is about 1/5 of its radius. In this case, the coefficient $K = (1/2)\partial\ln(B/\rho r)/\partial\ln\xi$ on the right-hand side of Eq. (54) is approximately equal to 1.8. We also present some other values of this coefficient for other values of ξ: $K(\xi_1 = 0.7) \approx 0.76$, $K(\xi_1 = 0.85) \approx 2.4$, and $K(\xi_1 = 0.9) \approx 4$. Equation (54) was solved numerically with the initial condition $\tilde{v}_r(p = p_0) = 0$. We calculated the amplification coefficient of the relative amplitude $a(p)/a(p_0)$ of the density perturbations for $p < p_0$. For $K \approx 1.8$ and $p_0 = 1$, the amplification coefficient is shown by the dashed curve in Fig. 11. One can see that, by the time when the original liner is compressed tenfold, the seed perturbation amplitude increases by a factor of about 100. However, we stress that, according to the results from numerical simulations of the compression of a plasma shell in a liner with prolonged plasma creation (Fig. 8), the radial shell thickness at the time when the cold liner substance has been completely evaporated is still appreciably larger than that after the compression by the shock wave (and, accordingly, the gradient $B/\rho r$ is appreciably smaller than the final one). That is why, before compression, the instability is suppressed to a markedly greater extent than after the compression by the shock wave. Consequently, it is more expedient to choose $p_0 = 0.8$. By almost the same time, the front of the compression wave reaches the middle of the shell. The profiles displayed in Fig. 11 were obtained precisely for $p_0 = 0.8$ and for the three parameter values $K = 0.76$, 1.6, and 4, for which the relative radial thickness of the plasma shell equals 1/3, 1/5, and 1/10, respectively.

Hence, when the plasma creation process terminates at a time equal to 0.8 of the current rise time (in which case the thickness of the shell after the compression by the shock wave will be approximately equal to 1/5 of its radius), the relative amplitude of the seed density perturbations increases (due to the internal interchange instability) by a factor of about 20 by the time the original liner is compressed nearly tenfold. This result allows us to hope that seed perturbations with relative amplitudes of no more than 5% will not destroy the plasma shell as it is compressed tenfold. This rough analysis was performed under the assumption that, before the cold liner substance evaporates completely, the plasma creation rate is proportional to the current flowing through the liner, in which case the mass of the plasma shell is fairly uniformly distributed over its transverse cross section. A weaker or stronger dependence of the plasma creation rate on the total current will cause the plasma to be concentrated either near the leading or trailing edge of the plasma shell, so that the role played by the internal interchange instability may become more important.

4.5.2. Role of the instability of the outer boundary of the shell. While the body of the plasma shell is subject to interchange instability, which was analyzed

in the previous section, the outer boundary of the shell may experience conventional RT instability [33].

The compression under discussion differs from ordinary liner compression in that, before the plasma creation process has come to an end, the outer boundary of the plasma shell is not a freely moving boundary, because it is attached to the immobile cold dense liner skeleton. The liner skeleton is in turn immobile because it carries a small fraction of the total current. Just after the plasma source stops producing plasma (provided that the final stage of plasma production is sufficiently short), the fraction of the total current that flowed through the boundary layer when the plasma was still being produced and then accelerated the plasma to the Alfvén velocity gives rise to a converging compression wave, which starts to propagate through the plasma flow. Before the compression wave reaches the leading edge of the plasma flow, the plasma is accelerated only at the front of the compression wave, while the plasma behind the front converges with an almost constant velocity. Consequently, before the compression wave reaches the leading edge, the ordinary RT instability cannot occur, which indicates that the compression of the outer boundary of a light liner with prolonged plasma creation is more stable in comparison with what is usually expected.

Another distinctive feature of the compression process under discussion is that the plasma shell is fairly thick because of its resilience associated with the frozen-in magnetic field. For this reason, the time required for the RT instability to destroy such a shell is fairly long. The results of recent ICF-related theoretical and experimental investigations of the RT instability (see, e.g., [34–36]) show that, during the development of the three-dimensional RT instability on scale lengths comparable with the thickness of a thin plasma shell, the distance that the accelerated shell can travel is roughly seven times its thicknesses (provided that there are no additional stabilizing factors). Since the liner under consideration is accelerated under the action of the magnetic field, the development of the RT instability is partially suppressed in one direction due to the anisotropy of the instability. For this reason, the plasma shell accelerated by the magnetic field is presumably somewhat more stable than that accelerated by the pressure of a light gas.

Hence, we can suppose that the plasma shell with a frozen-in magnetic field and with a thickness of about 1/5 of its radius can be successfully compressed (without complete destruction) to a radius of about 1/10 of the original liner radius. We speak of self-similar compression, which was considered at the beginning of this section. Achieving such a stable compression of thinner plasma shells may turn out to be problematic.

Summing up the results of our study of the instabilities of a compressed plasma shell, we can say that the plasma shell formed during prolonged plasma creation can be compressed fairly efficiently under the conditions that the plasma creation rate is approximately proportional to the total current, the cold liner substance evaporates completely some time before the current reaches its maximum, and the plasma compression comes to an end some time after the current reaches its maximum. After the beginning of the current pulse, the plasma creation process should optimally terminate at a time equal to 0.8–0.9 of the current rise time, the compression time being 1.2 times as long as the current rise time.

5. CONCLUSION

We have shown that, in high-current high-voltage facilities, multiwire, foam, and even gas liners are characterized by prolonged plasma creation, which can last almost throughout the current pulse. The Ampère force causes the rarefied hot plasma produced to converge toward the liner axis, giving rise to the radial plasma flow, while the liner skeleton, which carries a small fraction of the total current, is almost immobile. This phenomenon is independent of whether or not the produced hot plasma forms a continuous shell in the azimuthal direction. This can result in the formation of a fairly thick current-carrying plasma shell with a frozen-in magnetic field, the shell thickness being much larger than the skin depth. We have studied the main factors that govern the rate at which the hot plasma is produced. We have developed the simplest theoretical model, which allows us to estimate the plasma creation rate and to analyze the structure of the boundary layer near the plasma source.

A thick current-carrying plasma shell with a frozen-in magnetic field is characterized by a certain resilience, which makes liner compression more stable against the RT instability in comparison with plasma liners whose thickness is about the skin depth and which are accelerated by a magnetic piston. We have constructed self-similar solutions and have simulated the dynamics of a plasma shell formed by a liner with prolonged plasma creation in order to show that fairly thick shells can also be compressed into a very compact pinch at the device axis. This conclusion rejects the widely accepted objection that the compact compression of such a plasma shell is unlikely to be achieved. The main obstacles that may hamper compact compression are the high plasma pressure in the shell and plasma instabilities. For the liners under consideration, both of these obstacles are avoided by composing the liners of chemical elements that are heavy enough for the plasma creation process to terminate a short time before the current reaches its maximum, the liner mass being such that the plasma shell is compressed completely some time after the current reaches its maximum. Under the assumption that the plasma creation rate is proportional to the total discharge current until the plasma source is depleted, we have shown that the optimum time for the complete evaporation of the cold liner is approximately equal to 0.8 of the current rise

time, the compression time being approximately equal to 1.2 of the current rise time. After the plasma source ceases, additional compression makes it possible to achieve a plasma shell with a thickness of about 1/5 of its radius, thereby facilitating further fairly stable collapsing of the liner.

Presumably, the authors of [1, 2] grasped the experimental way to achieve the optimum parameter range for the assumed design of multiwire liners, namely, liners composed of identical wires placed along the generatrices of a cylinder with a given radius. According to our simple estimates, for a very narrow interwire gap, such a multiwire liner design leads to a stronger dependence of the plasma production rate on the current than desired. We think that this fact opens new possibilities for refining the already obtained results by making the liner design more complicated in order to further optimize the time dependence of the plasma creation rate.

Production of a new plasma at the discharge periphery (or, more precisely, at the inner surface of the insulator) also occurs in explosion magnetic generators. There are publications on this subject (see [37] and the literature cited therein) in which the density of the plasma flow from the insulator into the discharge chamber is estimated. Under these conditions, the radiative energy transfer toward the insulator surface is of great importance. In [37], the value of $\dot{m}$ was estimated for a Plexiglass insulator with allowance for the above effect, but without taking into account electron heat conduction. In our notation, this estimate takes the form $\dot{m} = 0.17(I[\text{MA}]/R[\text{cm}])^{1.7}$ μg cm^{-2} ns^{-1}. This formula may be compared with the result obtained in Section 4.2 for tungsten (see Fig. 6). The fact that these formulas, which were obtained under very different assumptions, are similar speaks well for their reliability.

ACKNOWLEDGMENTS

We are grateful to S.V. Bulanov, S.V. Zakharov, and I.V. Glazyrin for fruitful discussions. This work was supported in part by the Russian Foundation for Basic Research, project nos. 99-02-17952, 99-02-16471, and 00-02-16177.

APPENDIX

Set of Equations for a Cylindrical MHD Problem with a Plasma Source

In the absence of an axial magnetic field, cylindrically symmetric plasma flows with spatially averaged plasma-source terms are described by the following set of modified MHD equations:

$$\frac{\partial}{\partial t}\rho v + \frac{1}{r}\frac{\partial}{\partial r}\rho v^2 r = -\frac{\partial p}{\partial r} - \frac{1}{c}jB, \tag{A.1}$$

$$\frac{\partial B}{\partial t} + \frac{\partial}{\partial r}vB = c\frac{\partial}{\partial r}\left(\frac{j}{\sigma}\right), \tag{A.2}$$

$$\frac{\partial \rho}{\partial t} + \frac{1}{r}\frac{\partial}{\partial r}(\rho v r) = q(r,t), \tag{A.3}$$

$$\frac{\partial}{\partial t}\rho\varepsilon_e + \frac{1}{r}\frac{\partial}{\partial r}\rho\varepsilon_e v r + \frac{p_e}{r}\frac{\partial}{\partial r}v r = -\frac{1}{r}\frac{\partial}{\partial r}r q_{Te} + \frac{j^2}{\sigma} + C_{ei}(T_i - T_e) - Q_r, \tag{A.4}$$

$$\frac{\partial}{\partial t}\rho\varepsilon_i + \frac{1}{r}\frac{\partial}{\partial r}\rho\varepsilon_i v r + \frac{p_i}{r}\frac{\partial}{\partial r}v r = -\frac{1}{r}\frac{\partial}{\partial r}r q_{Ti} - C_{ei}(T_i - T_e) + \frac{v^2}{2}q(r,t) \tag{A.5}$$

or by the set

$$\rho\frac{d}{dt}v = -\frac{\partial p}{\partial t} - \frac{1}{c}jB - vq(r,t), \tag{A.6}$$

$$\frac{\partial B}{\partial t} + \frac{\partial}{\partial r}vB = c\frac{\partial}{\partial r}\left(\frac{j}{\sigma}\right), \tag{A.7}$$

$$\frac{\partial \rho}{\partial t} + \frac{1}{r}\frac{\partial}{\partial r}(\rho v r) = q(r,t), \tag{A.8}$$

$$\rho\frac{d}{dt}\varepsilon_e + \frac{p_e}{\rho}\frac{\partial}{\partial r}v r = -\frac{1}{r}\frac{\partial}{\partial r}r q_{Te} + \frac{j^2}{\sigma} + C_{ei}(T_i - T_e) - Q_r - \rho\varepsilon_e q(r,t), \tag{A.9}$$

$$\rho\frac{d}{dt}\varepsilon_i + \frac{p_i}{r}\frac{\partial}{\partial r}v r = -\frac{1}{r}\frac{\partial}{\partial r}r q_{Ti} - C_{ei}(T_i - T_e) + \left(\frac{v^2}{2} - \varepsilon_i\right)\rho q(r,t). \tag{A.10}$$

Here, ρ is the plasma density; v is the radial component of the plasma velocity; B is the azimuthal component of the magnetic field; j is the axial component of the electric current density,

$$j = \frac{c}{4\pi}\frac{1}{r}\frac{\partial}{\partial r}Br, \tag{A.11}$$

$T_{e,i}$ are the electron and ion plasma temperatures; $p_{e,i}$ are the electron and ion pressures; $\varepsilon_{e,i}$ are the specific energies (per unit mass) of the electrons and ions; r is the radial coordinate; and $d/dt = \partial/\partial t + v\partial/\partial r$. The modified MHD equations are supplemented with the simplified Ohm's law for the axial component of the electric field, $E = -\frac{1}{c}vB + \frac{j}{\sigma}$, and with the simplified expressions for the electron and ion heat fluxes,

$$q_{Te,i} = -\kappa_{e,i}\frac{\partial T_{e,i}}{\partial r}. \tag{A.12}$$

The continuity equations (A.3) and (A.8) incorporate the plasma source intensity. The plasma is assumed to be created with a zero momentum exclusively at the expense of the energy of the plasma already produced.

Otherwise, the right-hand sides of Eqs. (A.1), (A.4), and (A.5) should be supplemented with the corresponding source terms. It is assumed that $p_{e,i}$, $\varepsilon_{e,i}$, $\kappa_{e,i}$, C_{ei}, and σ are functions only of ρ, T_e, and T_i; and that $\kappa_{e,i}$ and σ also depend on $|B|$. In the above equations, the effects of viscosity are discarded, because they are most likely of secondary importance in the problem under study.

Many problems can be solved by assuming $q = 0$ and by incorporating the plasma source only into the boundary conditions. Notably, if the radius of the plasma source is much larger than its radial thickness, then integrating Eq. (A.1) over the radius shows that the quantity $\rho v^2 + p + B^2/8\pi$ is continuous at the cylindrical surface corresponding to the source.

REFERENCES

1. T. W. L. Sanford, G. O. Allshouse, B. M. Marder, *et al.*, Phys. Rev. Lett. **77**, 5063 (1996).
2. R. B. Spielman, C. Deeney, G. A. Chandler, *et al.*, Phys. Plasmas **5**, 2105 (1998).
3. V. P. Smirnov, E. V. Grabovskii, V. I. Zaitsev, *et al.*, in *Proceedings of the 8th International Conference on High-Power Particle Beams (BEAMS-90), Novosibirsk, 1990*, Ed. by B. N. Breizman and B. A. Knyazev (World Scientific, Singapore, 1991), Vol. 1, p. 61.
4. C. Deeney, P. D. LePell, T. Nash, *et al.*, in *Proceedings of the 9th International Conference on High-Power Particle Beams (BEAMS-92), Washington, 1992*, Ed. by D. Mosher and G. Cooperstein (NTIS, Springfield, 1992), Vol. 1, p. 159.
5. A. V. Branitskii, V. D. Vikharev, S. V. Zakharov, *et al.*, Fiz. Plazmy **17**, 531 (1991) [Sov. J. Plasma Phys. **17**, 311 (1991)].
6. M. G. Haines, IEEE Trans. Plasma Sci. **26**, 1275 (1998).
7. S. V. Lebedev, R. Aliaga-Rossel, J. P. Chittenden, *et al.*, Phys. Plasmas **5**, 3366 (1998).
8. S. V. Lebedev, I. H. Mitchell, R. Aliaga-Rossel, *et al.*, Phys. Rev. Lett. **81**, 4152 (1998).
9. B. M. Marder, T. W. L. Sanford, and G. O. Allshouse, Phys. Plasmas **5**, 2997 (1998).
10. T. W. Sanford, R. C. Mock, R. B. Spielman, *et al.*, Phys. Plasmas **5**, 3737 (1998).
11. T. W. Sanford, R. C. Mock, T. J. Nash, *et al.*, Phys. Plasmas **6**, 1270 (1999).
12. J. P. Chittenden, S. V. Lebedev, A. R. Bell, *et al.*, Phys. Rev. Lett. **83**, 100 (1999).
13. R. Benattar, S. V. Zakharov, A. F. Nikiforov, *et al.*, Phys. Plasmas **6**, 175 (1999).
14. V. V. Branitskii, E. V. Grabovskii, I. N. Frolov, *et al.*, in *Proceedings of 12th International Conference on High-Power Particle Beams (BEAMS-98), Haifa, 1998*, Ed. by M. Makkovits and J. Shilon (Rafael, Haifa, 1998), Vol. 2, p. 599.
15. A. V. Batyunin, A. N. Bulatov, V. D. Vikharev, *et al.*, Fiz. Plazmy **16**, 1029 (1990) [Sov. J. Plasma Phys. **16**, 597 (1990)].
16. A. V. Branitskii, S. A. Dan'ko, A. V. Gerusov, *et al.*, Fiz. Plazmy **22**, 307 (1996) [Plasma Phys. Rep. **22**, 277 (1996)].
17. I. K. Aĭvazov, M. B. Bekhtev, V. V. Bulan, *et al.*, Fiz. Plazmy **16**, 645 (1990) [Sov. J. Plasma Phys. **16**, 373 (1990)].
18. A. V. Branitskii, E. V. Grabovskii, M. V. Zurin, *et al.*, Fiz. Plazmy **25**, 1060 (1999) [Plasma Phys. Rep. **25**, 976 (1999)].
19. D. L. Peterson, R. R. Bower, K. D. McLenithan, *et al.*, Phys. Plasmas **5**, 3302 (1998).
20. L. E. Aranchuk, S. L. Bogolyubskiĭ, G. S. Volkov, *et al.*, Fiz. Plazmy **12**, 1324 (1986) [Sov. J. Plasma Phys. **12**, 765 (1986)].
21. N. A. Bobrova, T. L. Razinkova, and P. V. Sasorov, Fiz. Plazmy **14**, 1053 (1988) [Sov. J. Plasma Phys. **14**, 617 (1988)].
22. J. D. Sethian, A. E. Robson, K. A. Gerber, and A. W. DeSilva, Phys. Rev. Lett. **59**, 892, 1790 (1987).
23. I. R. Lindemuth, G. H. McCall, and R. A. Nobel, Phys. Rev. Lett. **62**, 264 (1989); P. Shehey, J. Hammel, and I. R. Lindemuth, Phys. Fluids B **4**, 3698 (1992).
24. N. A. Bobrova, T. L. Razinkova, and P. V. Sasorov, Fiz. Plazmy **18**, 517 (1992) [Sov. J. Plasma Phys. **18**, 269 (1992)].
25. N. A. Bobrova, V. V. Neudachin, T. L. Razinkova, and P. V. Sasorov, in *Proceedings of the 3rd International Conference, London, 1993*, Ed. by M. Haines and A. Knight (AIP, New York, 1994), p. 10.
26. C. Stallings, K. Childers, I. Roth, *et al.*, Appl. Phys. Lett. **29**, 404 (1976); F. Burkhalter, J. Davis, J. Rauch, *et al.*, J. Appl. Phys. **50**, 705 (1979).
27. M. V. Bekhtev, V. L. Vikharev, S. V. Zakharov, *et al.*, Zh. Éksp. Teor. Fiz. **95**, 1653 (1989) [Sov. Phys. JETP **68**, 955 (1989)]; I. K. Aĭvazov, V. D. Vikharev, G. S. Volkov, *et al.*, Fiz. Plazmy **14**, 197 (1988) [Sov. J. Plasma Phys. **14**, 110 (1988)].
28. V. V. Alexandrov, A. V. Branitskii, G. S. Volkov, *et al.*, in *Proceedings of 1st International Conference on Inertial Fusion Sciences and Application (IFSA-99), Bordeaux, 1999*, Ed. by C. Labaune, W. J. Hogan, and K. A. Tanaka (Elsevier, Paris, 1999), p. 591.
29. N. A. Bobrova and P. V. Sasorov, Fiz. Plazmy **19**, 789 (1993) [Plasma Phys. Rep. **19**, 409 (1993)].
30. R. D. Richtmyer, *Difference Methods for Initial-Value Problems* (Interscience, New York, 1957; Inostrannaya Literatura, Moscow, 1960).
31. A. G. Kulikovskiĭ, Dokl. Akad. Nauk SSSR **114**, 984 (1957) [Sov. Phys. Dokl. **2**, 269 (1958)]; F. S. Felber, Phys. Fluids **25**, 643 (1982).
32. L. A. Artsimovich, *Controlled Thermonuclear Reactions*, Ed. by A. Kolb and R. S. Pease (Fizmatgiz, Moscow, 1961; Gordon and Breach, New York, 1964).
33. N. F. Roderic, T. W. Hussey, R. J. Faehl, and R. W. Boyd, Appl. Phys. Lett. **32**, 273 (1978).
34. D. L. Youngs, Physica D (Amsterdam) **12**, 32 (1984).
35. K. I. Read, Physica D (Amsterdam) **12**, 45 (1984).
36. M. M. Basko, Phys. Plasmas **1**, 1270 (1994).
37. S. F. Garanin, E. S. Pavlovskiĭ, and V. B. Yakubov, Prikl. Mekh. Tekh. Fiz., Nos. 2, 9 (1984).

Translated by G.V. Shepekina